Swift heavy-ion track formation and metal nanoparticle shaping in silicon dioxide, silicon nitride and silicon oxynitride layers

Pablo E. Mota Santiago

A thesis submitted for the degree of
Doctor of Philosophy
The Australian National University

May, 2019

Declaration

I certify that, to best of my knowledge, this thesis represents my original work; except where due mention is made in the text. It contains no material previously submitted for a degree or diploma at any University.

Pablo E. Mota Santiago

December, 2018

Acknowledgements

First of all to my family. To my parents, from who I received nothing but unconditional love and support during this long journey. And to my brothers, their advice and support helped me stay a float in more than one occasion. Muchas gracias.

I would like to extend my infinite gratitude to my former supervisor Dr. Alejandro Crespo, for encourage me to cross the world and pursuit my dreams. To the late Prof. Mark Ridgway for giving me the opportunity of being part of his amazing group. And to A/Prof. Patrick Kluth, for taking me under his supervision, without his support, encouragement and freedom this thesis would have not been possible.

To my co-supervisory panel, Dr. Matias Rodriguez, Dr. Felipe Kremer and Dr. Christian Notthoff not only for their guidance and endless patience but also for their friendship. Their ideas and support made a significant impact in this thesis and on my person.

This research project was conducted in close collaboration with different research groups; I would like to thank:

- The materials physics simulations group of Prof. Kai Nordlund and Prof. Flyura Djurabekova from the University of Helsinki, in particular to Dr. Aleksi Leino and Henrique Vasquez Muinos, for their molecular dynamics simulations;
- The Materials Research Department, leaded by Dr. Christina Trautmann, at the GSI Helmholtz Center for Heavy Ion Research in Darmstadt (Germany) for performing the ion irradiations with high energies; and
- Dr. Giancarlo Rizza from the Laboratoire des solides irradieś at Ecole Polytechnique in France, and to Dr. Christian Dufour from Universitéde Caen

for the code to model the three dimensional version of the inelastic thermal spike.

Similar thanks go to the technical and practical support received during the realisation of the experiments relevant to this research project. I would like to express my gratitude to:

- the SAXS/WAXS beamline scientists at the Australian Synchrotron, Dr. Nigel Kirby, Dr. Stephen Mudie, Dr. Adrian Hawley and Dr. Timothy Ryan for their assistance with our SAXS measurements;
- Prof. Rob Elliman, Dr. Kidane Belay, Dr. Tom Ratcliff and Tom Kitchen from the Department of Electronic Materials Engineering at ANU, for the training and technical assistance at the high energy implanter and RBS accelerator;
- Dr. Fouad Karouta and Dr. Kaushal Vora from the Australian National Fabrication Facility ACT node, for their training, technical support and troubleshooting with the PECVD, optical ellipsometer, rapid thermal annealer, thermal evaporator and ICP etching; and
- Dr. Nikolai Lobanov, Dr. Dimitrios Tsifakis and other staff from the Department of Nuclear Physics at ANU for their support at the 14 UD accelerator.

A special thanks go to friends and colleagues Dr. Daniel Schauries, Allina Nadzri, Dr. Thomas Bierschenk, Dr. Sahar Mirzaei, Dr. Ruixing Feng, Andrea Hadley, and the people at the Department of Electronics Material Engineering at ANU, with a special mention to Julie Arnold. And to my friends, Allan, Tan, Juan, Alex, Ben and Julie. Thanks to you I have so many fond memories of ANU and Canberra.

Finally, to Andrea, who witness all the struggles and challenges I had to overcome during this research project. Thank you.

Abstract

Amorphous silicon dioxide (a-SiO_2) and silicon nitride (a-Si_3N_4) are key dielectric materials in current Si-based microelectronics, optical fibres and integrated optical devices, and many other applications. Silicon dioxide has an optical band gap around 8 eV, is thermally stable, and exhibits a tetrahedral structure making it an adequate material to study the behaviour of ceramics and glasses. Silicon nitride on the other hand, possesses good mechanical resistance, thermal stability, a lower band gap ($\sim$5 eV), a higher refractive index and chemical inertness, and is widely used in industry for photovoltaic, light-emitting and optoelectronic devices, among others. Recently, ternary alloys known as silicon oxynitrides (a-SiO_xN_y) have become more interesting for Si-based device fabrication as they combine properties of silicon dioxide and silicon nitride with the additional benefit that they can be tuned by adjusting their composition.

Ion irradiation has been extensively studied for the characterization, fabrication and modification of materials and nanostructures, and is an industrial method in mainstream microelectronics industries for the introduction of dopants into semiconductors. The range of applications often varies with the ion energy and depends on the interaction between the incoming energetic ions and the target nuclei and electrons. For energies below 0.1 MeV/u, elastic collisions with the target nuclei dominate the interaction, resulting in material modification such as displacement cascades and chemical modifications. This is the common energy range for applications such as ion implantation or doping, ion mixing, elastic recoil or backscattering spectroscopies, among others. On the other hand, at energies exceeding 1 MeV/u, the energetic ion interacts predominantly via inelastic collisions with the target electrons, forming an energetic electronic cloud around the ion trajectory, where the incident ion direction is largely retained. The excited electrons can interact with the target nuclei via

the electron-phonon coupling. If the energy deposited by the atom surpasses a material dependent threshold, the coupling can lead to heating above melting, known as thermal spike, and can lead to the formation of few nanometres narrow and micrometers long defect structures aligned to the ion beam direction, so called 'ion tracks'. Theses ion tracks have numerous applications in nanotechnology such as the formation of optical waveguides in insulating materials, including a-SiO_2 and a-Si_3N_4, and selective chemical etching to create well defined nano-channels for filtration and sensor applications. Ion tracks are also important in areas such as geochronology, nuclear physics, and interplanetary science.

This work provides a systematic study of ion irradiation to tailor the physical and chemical properties of a-SiO_2, a-Si_3N_4 and a-SiO_xN_y materials with a particular focus on three specific areas: (i) the formation of ion tracks by swift heavy-ion (SHI) irradiation in a-SiO_2, a-Si_3N_4, and a-SiO_xN_y, (ii) the ion beam synthesis of Au nanoparticles (NPs) in a-SiO_2 and a-Si_3N_4; and (iii) the ion shaping process of embedded metallic NPs in a-Si_2, a-Si_3N_4 and at the interface of the two materials.

(i) Ion tracks were created by SHI irradiation of a-SiO_2, a-Si_3N_4 and a-SiO_xN_y of different composition, with 185 MeV and 2.2 GeV Au ions at fluences between 1×10^{11} - 1×10^{13} cm^{-2}. Synchrotron based small-angle X-ray scattering (SAXS) revealed a cylindrical ion track morphology which resembles, for all materials and compositions considered, an under-dense core surrounded by an over-dense shell with a smooth transition between the two regions, in good agreement with molecular-dynamics (MD) simulations. A decrease in the ion track dimensions for samples with higher nitrogen content was determined, accompanied by an increased density change. The latter is attributed to the short-lived thermal spike resulting from the higher thermal conductivity associated with a-Si_3N_4. Infrared spectroscopy analysis shows a region of high radiation damage region within the ion track core for a-SiO_2 and a-Si_3N_4. In addition, the role of residual H in the form of Si-H and N-H bonds was studied. While N-H bands monotonically decrease with increasing fluence, Si-H appears to be highly resilient to ion irradiation. The results suggest that the density

variations originate from freezing in the local viscous flow arising from the non-uniform temperature profile in the radial direction of the ion path. The concomitant drop in viscosity mediated by the thermal conductivity appears to be the main driving force.

(ii) To study the synthesis of metallic NPs, a-SiO_2 and a-Si_3N_4 were implanted with 2 MeV Au ions at a fluence of 5×10^{16} cm^{-2}. The synthesis and growth was promoted by thermal annealing for 60 minutes in either air or N_2 gas at temperatures between 1000 and 1100°C. Characterization with SAXS and transmission electron microscopy (TEM) of a-SiO_2 showed that the Au NP growth rate exhibits very little difference between thermally grown and plasma enhanced chemical vapour deposited (PECVD) thin layers. In the case of a-Si_3N_4, when deposited by PECVD the NP growth is very limited, accompanied by the formation of voids at the depth of maximum implantation damage and the formation of NPs with a mean diameter of 3 nm while the a-Si_3N_4 layer remains amorphous. Fourier transform infrared (FTIR) spectroscopy showed the presence of Si-H absorbance bands after annealing suggesting a high thermal stability. When the a-Si_3N_4 layer is deposited by low pressure chemical vapour deposition (LPCVD), the layer undergoes an amorphous-to-poly-crystalline phase transformation accompanied by the diffusion of the implanted Au ions through the whole layer. For the study of the ion shaping process of Au NPs embedded in a-SiO_2, a-Si_3N_4 and at the interface of a-SiO_2 and a-Si_3N_4 a good control of the initial NPs size is required. To achieve that, Au NPs were synthesised by depositing two layers of a-SiO_2 (or a-Si_3N_4) of few hundred nanometres in thickness with a 5 nm thick Au layer in-between, followed by subsequent rapid thermal annealing (RTA). This results in a single layer of Au NPs with a mean diameter of $\sim$ 20 $\pm$ 5.5 nm exhibiting a weak dependence on the composition of the surrounding medium.

(iii) The ion-irradiation induced elongation of embedded Au NPs was carried out by SHI irradiation with 185 MeV Au ions. TEM revealed different elongation rates in a-SiO_2 and a-Si_3N_4. For the former, an evolution from sphere to rod-like NPs with increasing fluence was observed, while for the latter, the Au NPs evolved towards faceted prolate NPs with smaller aspect ratios. When NPs are located at the interface between

a-SiO_2 and a-Si_3N_4, preferential elongation towards the a-SiO_2 layer was observed with a limited elongation towards the a-Si_3N_4 layer. Numerical simulations based on the three-dimensional thermal spike (3D-TS) model showed, in the single layer case, a thermal spike duration of about 20 and 10 ps for a-SiO_2 and a-Si_3N_4, respectively. The shorter lifetime and the thermal profile calculated for a-Si_3N_4 agree with the reduced efficiency of the elongation process observed. In the case of Au NPs located at the interface, the preferential diffusion of Au towards the ion track formed in a-SiO_2 can also be explained by the difference of the thermal spike life-time between the two materials, and the reduced efficiency of the elongation process in a-Si_3N_4. High angular annular dark field (HAADF) in STEM mode revealed the formation of porous Au NPs in the ion-shaping process for a-Si_3N_4.

Contents

List of Figures

List of Tables

Chapter 1

Introduction

1.1 Project overview

Ion irradiation is a well-established and powerful technique for materials processing, and has gathered great interest for more than 50 years. Its applications can be divided in two groups according to their main effects: the introduction of foreign atoms and the energy deposition into a material [3]. The former has the potential to locally change the composition and structure, providing great control over the physical and chemical material properties. The latter focusses on the controlled and highly localized energy deposition into the material of interest, which can lead to anisotropic deformation, defect annealing, radiation damage or a phase transition [18–20]. Besides materials modification, ion irradiation has also applications in unique analytical techniques using specific ion beams as a probe to study the material properties, such as nuclear reaction analysis (NRA), Rutherford backscattering spectroscopy (RBS), elastic recoil displacement analysis (ERDA) [21]. Ion irradiation possesses a broad range of applications with commercial use in the semiconductor industry [22, 23]. Recently, novel applications have been reported in photonics [24], photovoltaics [25] and nonlinear optics [26], making ion irradiation a valuable tool for new technology developments. Application of the ion irradiation technique requires a solid knowledge of the specific ion-matter interactions, many of which are not yet fully understood due to the complex interactions taking place.

When an energetic ion penetrates a solid, it interacts predominantly via elastic collisions with the target nuclei and excitation of electrons through inelastic collisions.

As a result, the ion deposits energy into the target during its passage, ranging from a few eV/nm to tens of keV/nm. This is known as the energy loss rate, where its magnitude and the dominant interaction process are dependent on the kinetic energy of the ion. For energies below 0.1 MeV/u, elastic collisions with the target nuclei dominate the interaction. At energies exceeding 1 MeV/u, the energetic ion interacts predominantly via inelastic collisions with the target electrons. Elastic collisions with the target nuclei can directly produce structural transformation of the atomic lattice by atomic displacements, while the electronic interactions require the transfer of energy from the electrons to the lattice atoms to induce structural modifications, the latter known as ion tracks [27]. In composite materials, such as embedded metallic NPs, interesting effects have been observed, governed by the difference in the energy transfer efficiency between the electronic and atomic system and the materials physical properties. This is the case of Au NPs embedded in a-SiO_2, where elongation along the beam direction was observed. Such elongation has been previously ascribed to the expansion of the transiently molten Au NP along the beam direction through the under-dense ion track form in a-SiO_2 yet, it is still not well understood.

There are specific interest in the formation of ion tracks in insulating materials, for example, as the ion track region is highly susceptible to chemical etching it is possible to selectively remove the material within the formed ion tracks with little effects on the bulk material, this process is known as 'track-etching'. As a result, cylindrical or conical hollow regions or pores with diameters between few nanometres up to micrometers are created. Track-etching is an industrially compatible and applicable in a variety of materials such as minerals [28], polymers [29] and other insulating materials [30]. Among the range of applications are micro/nano-filtration [31], particle separation [32], chemical and biological sensing [33], as well as host for secondary materials. The latter results in templates for nanowires [34], micro-capacitors [35], diodes and sensors [36]. On the other hand, ion tracks also play a key role in material engineering, for example, they are used to formed high aspect-ratio defective regions in high-temperature superconductors to tune the magnetic-flux pinning [37]. Furthermore, SHI irradiation is capable of induce porosity in semiconductors, which

differ significantly in their properties from their bulk counterparts [38]. Also, the study of ion track formation and thermal annealing in minerals has gain relevance as a tool for thermochronology. Annealing of ion tracks in minerals lead to a self-recovery process which results in shrinking or contraction of the track, behaviour that can be related to the geological history of the specific mineral or geographical region [28]. While the applications of ion tracks rather broad [3], the presented examples aim to highlight the relevance of understand their formation in specific materials and their morphology as such characteristics drive the applicability and tune of the properties of the bulk material.

Amorphous silicon oxynitrides (a-SiO_xN_y) are materials whose composition ranges from SiO_2 to Si_3N_4 [39–41], with a network formed by five types of tetrahedrons: $SiO_\nu N_{4-\nu}$ for ν=0,1,2,3 and 4, determined by the O and N content [42, 43]. They have received interest given their potential to replace SiO_2 as a gate dielectrics in MOS devices due to their ability to remove Si-Si bonds at the SiO_2/Si interface [44]. They also have applications as anti-reflection coatings, passivation layers and tunnel dielectrics in Si-based photovoltaic cells [17, 45], in the fabrication of waveguides integrated in SiO_2 environments or as yellow LED emitters [46–48], among others. An advantage of a-SiO_xN_y compared to SiO_2 and Si_3N_4 is the possibility to continuously adjust the physical properties to those in between the two binary materials such as the refractive index (1.4-2.0), dielectric constant (3.8-7.5), optical band gap (4.5-9.0 eV), thermal expansion (0.5 - 1.6$\times10^{-6}$/K), and hardness (635-3200 kg/mm) [41, 43]. It is also possible to adjust the chemical inertness, characteristic of Si_3N_4, to prevent B and water diffusion in photovoltaic devices [49].

In order to assess the potential of ion irradiation to tailor the physical and chemical properties of a-SiO_xN_y materials, it is meaningful to study the material response of their binary components (SiO_2 and Si_3N_4) before looking into the composition dependence of the radiation effects. Because of its tetrahedral structure, a-SiO_2 has been studied under multiple irradiation conditions due to its similarities to the glass structure and because is a material commonly found in optical and electronic devices.

It is one of the most studied materials [27]. Yet, very little work has been carried out in a-Si_3N_4 in comparison. Furthermore, radiation effects are largely unknown when the composition deviates from the ideal stoichiometry, which is common in thin films from many new deposition methods such as LPCVD, PECVD, atomic layer deposition (ALD) [43].

From the technological point of view, the engineering of parallel anisotropic metallic nanostructures embedded in dielectric materials via irradiation with swift heavy-ions, also known as ion shaping, has been of particular interest in recent years because of their potential applications in linear and nonlinear optics, photovoltaics and magneto-optics [26, 50]. The properties of the NPs and suitability for the applications are strongly determine by their geometry, dimensions and surrounding medium. Similar to ion track formation, the ion shaping process has been studied predominantly using a-SiO_2 as the host matrix, where the ion track morphology and dimensions as well as the NP size has been found to be of fundamental relevance for the process. Little work has been done in materials other than a-SiO_2. Due to the relationship between the ion track fine structure and the ion shaping process [51, 52], it is important to study the ion track formation process in other amorphous insulators to extend the current understanding developed for a-SiO_2.

1.2 Aims

The research in this thesis aims to:

- the study of the ion track morphology and formation process in a-SiO_xN_y while varying the stoichiometry from a-SiO_2 to a-Si_3N_4;
- the determination of a synthesis method to control the spatial and size distribution of metallic (Au) NPs (MNPs) embedded in a dielectric medium; and
- the swift heavy-ion irradiation induced shape transformation of MNPs embedded in a-SiO_2, a-Si_3N_4 and at the interface of the two materials.

In amorphous materials, the lack of contrast previously limited the characterization of ion tracks to indirect techniques such as infrared spectroscopy [53, 54] or ion track etching [55], where no direct information about the ion track inner fine structure can be obtained. Recently, the ion track morphology of thermally grown SiO_2 was determined by synchrotron based small angle X-ray scattering, where an under-dense core surrounded by an over-dense shell was reported, yet the absolute density change was not determined [56]. Furthermore, the question remained open if the observed core-shell structure can be ascribed to the density anomaly of SiO_2 above 1800 K [57]. For amorphous silicon nitride (a-Si_3N_4), a similar structure comprised of an under-dense core and an over-dense shell was observed by HAADF-STEM for very thin films [58]. However, the nature of the core and shell regions were ascribed to the quenching of the boiling and melting phase, respectively, also known as the two-threshold model [59]. The determined ion track radius is matched with the numerical calculation of the molten region by choosing the appropriate value of the electron mean-free path, thus the boundary of the core region defines the boiling energy. By considering the current knowledge of ion tracks in amorphous materials, the first part of the study aims to determine the local density variations resulting from the ion track formation process. By combining synchrotron-based SAXS measurements with FTIR Spectroscopy it is possible to construct a more accurate interpretation of the fine structure within the ion track, while extending the study to a-SiO_xN_y. These results will help to understand the nature of the under-/over-dense ion track configuration and demonstrate if it can be related to a density anomaly or if there are other processes involved. Complementary MD simulations are carried out to explain the adequate under-/over-dense configuration and analyse the coordination defects induced in the matrix. This helped to develop an atomistic and more comprehensive model to explain the origin of the under-/over-dense ion track morphology.

Furthermore, the methodology was extended to a-SiO_xN_y, where two different models exist to understand their structure [43]. The first suggests a random mixture of two tetrahedrons corresponding to SiO_4 and SiN_4. The second considers the structure to be formed by five kinds of tetrahedrons, where their distribution can be related to

the corresponding chemical composition. Thus, the ion track formation process can provide valuable insights into the local structure of a-SiO_xN_y by comparing the ion track morphology to the results of a-SiO_2 and a-Si_3N_4.

Ion beam synthesis of MNPs is a well-established process often studied in a-SiO_2 [60–62] but to lesser extent in a-Si_3N_4 [63, 64]. a-Si_3N_4 is a good diffusion barrier for metals [65], and the synthesis of MNPs in this material remains difficult. Previous comparisons between a-SiO_2 and a-Si_3N_4 with high concentrations of implanted Ge have shown a remarkable difference in interfacial energy and diffusivity [64]. Au has been employed widely for ion beam synthesis of MNPs because of its chemically inertness. In this work the synthesis of Au NPs in a-Si_3N_4 is investigated and compared to the results in a-SiO_2 at different annealing atmospheres to study the role of reduced diffusion on the NPs dimensions. This is done by combining SAXS measurements and TEM. The former provides a size distribution averaged over a large volume of the MNPs, while the latter permits to determine the formation of voids and information regarding depth distribution of the MNPs and voids. In addition, an alternative technique involving the thermal deposition of very thin Au layers, instead of ion beam synthesis is explored. This technique provides good control over the MNPs mean size and size dispersion, especially for a-Si_3N_4, allowing the synthesis of Au NPs with dimensions comparable to the ion track diameter for the two materials, paramount for the study of the ion shaping process.

A systematic study of the shape transformation, from gold NPs to high aspect-ratio nanowires, by swift heavy-ion irradiation when embedded in a-Si_3N_4, a-SiO_2 and at the interface of the two materials provides new and important information to better understand the processes operational in the shape transformation. The study is carried out by using a combination of TEM with HAADF. The former provides information regarding the NPs shape and size after irradiation and presence of voids. The latter takes advantage of the high contrast present between gold and the two substrates and provides with further information regarding the shaping process at the interface of the two materials. The current understanding of the ion-shaping process presumes that

the existence of an energy deposition threshold, the formation of a molten track with dimensions related to those of the NPs, as well as the presence of an under-dense core in the ion track play a key role in the ion shaping process [4, 66–68]. Such studies have been conducted predominantly with a-SiO_2 as the host matrix, yet little work has been done in other materials [3]. As a-Si_3N_4 exhibits a higher dielectric constant, density, melting point and thermal conductivity while exhibiting an optical band gap of nearly half the value of a-SiO_2, it is a suitable material to test the validity of the current understanding as well as leading to new insights.

1.3 Thesis structure

This thesis is divided into eight chapters as follows:

- **Chapter 2** outlines the theoretical background of ion-matter interactions and discusses the existing models regarding ion irradiation at low and high energies. In particular, the theoretical aspects involving ion implantation and ion beam synthesis, ion track formation in amorphous dielectric materials, and ion shaping of Au NPs embedded in a-SiO_2 are summarized.

- **Chapter 3** explains and describes the laboratory-based experimental techniques employed in the present work.

- **Chapter 4** describes the theory and physical principles of synchrotron-based small angle X-ray scattering as well as the analysis methodology.

- **Chapter 5** shows the characterisation of ion tracks formed in a-SiO_2, a-Si_3N_4 and a-SiO_xN_y, as well as a proposed model to explain the resulting morphologies.

- **Chapter 6** discusses the synthesis of metallic NPs using two different approaches: (i) ion implantation followed by thermal annealing, and (ii) thermal deposition of a very thin metallic layer between two CVD deposition processes followed by a rapid thermal annealing. The results on the dimensions and size distributions of the corresponding MNPs inform the approach selected for the shaping experiments.

- **Chapter 7** contains the results on ion beam shaping of MNPs embedded in a-SiO_2 and a-Si_3N_4, and at the interface of a-SiO_2/a-Si_3N_4 multi-layer configurations.

- **Chapter 8** contains the conclusions of this thesis and outlines future work.

Chapter 2

Background

To elucidate the potential structural modifications a solid target can undergo when irradiated with energetic ions, it is necessary to understand the fundamental interactions occurring between the ion and the solid. This chapter presents a summary of these fundamental interactions. It also contains a brief description of the applications such as the ion beam synthesis of metallic nanoparticles (MNPs), followed by a through description of the processes involving swift heavy-ion matter interactions, which can lead to the formation of damaged trails known as ion tracks. Lastly, the role of ion tracks in the shape transformation of MNPs, so called 'ion shaping', is discussed.

2.1 Ion-matter interactions

During the passage of an energetic ion through a solid material, the ion will lose its kinetic energy predominantly via elastic collisions with the target atoms by means of screened Coulomb interactions, and due to inelastic collisions with the electrons [3,19]. The ion can also lose energy by means of nuclear reactions with the target elements, however, the energy required for that to take place surpasses the energy regime considered in this work and thus, their effect in this study can be considered negligible. The decrease of the ions kinetic energies as they penetrate the solid target is known as 'energy-loss rate' or 'stopping power'. The rate at which an incident ion loses energy given the distance travelled in the target (measured perpendicular to the target's surface) or depth is commonly denoted $\frac{dE}{dx}$. Furthermore, the corresponding interactions between the ion with the target atoms (elastic collisions) and electrons (inelastic collisions) are commonly considered independent interactions. Thus, it is

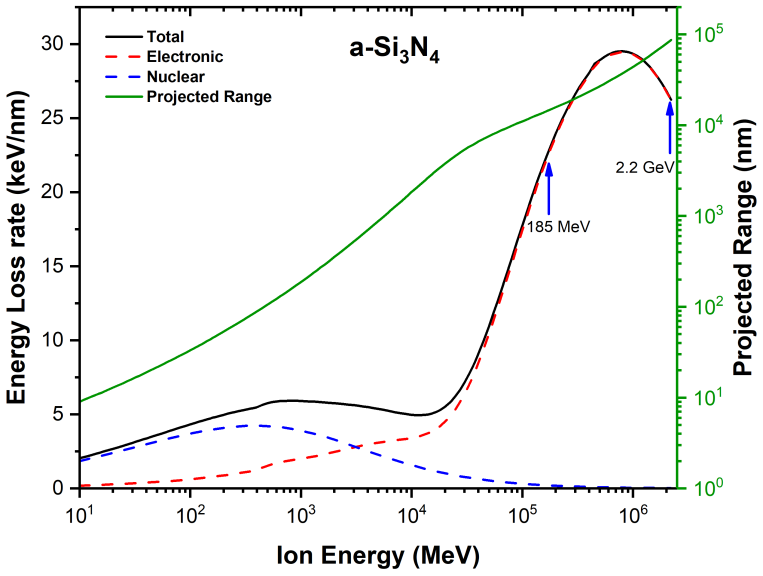

Figure 2.1: *Total stopping power (black line) of Au ions in a-Si_3N_4 as well as the nuclear and electronic components (blue and red dashed lines, respectively) as a function of the initial ion energy calculated by the SRIM2013 code. The corresponding projected range is presented as a green line.*

possible to express the total energy-loss rate as the sum of both contributions,

$$\frac{dE}{dx} = \left.\frac{dE}{dx}\right|_n + \left.\frac{dE}{dx}\right|_e \tag{2.1}$$

where the terms n and e correspond to the nuclear and electronic energy-loss rate, respectively. The magnitude of the nuclear and electronic interactions depends mainly on the ion velocity, mass and charge state. This is exemplified for the case of irradiation of amorphous silicon nitride with Au ions in Figure 2.1. In this thesis, the units of kilo-electron-volt per nanometre $\frac{keV}{nm}$ are used for the energy-loss rate.

For the nuclear contribution, the kinetic energy transferred can lead to atomic displacements in the material, deflection of the incident ion and generation of collision cascades. On the other hand, inelastic interactions arise from changes to the electronic configuration of the ion and the target atom by excitation and ionization and only

leads to negligible change in the ion trajectory.

2.1.1 Nuclear stopping power

The nuclear stopping power is the average energy-loss rate experienced by a moving particle due to elastic collisions with the target atoms. After each collision, the incident ion is deflected while transferring energy to the target nuclei. Its determination depends mainly on the ion species and kinetic energy, as well as on the target composition. For a particle with energy E, travelling a distance dx, there is a probability of undergoing a collision that results in an energy transfer T between T and $T + dT$. Thus, the average energy loss requires to integrate over all possible events or possible values of T:

$$S_n(E) = \frac{1}{N}\frac{dE}{dx} = \frac{1}{N}\langle dE \rangle = \int_{T_{min}}^{T_M} T \frac{d\sigma_n(E)}{dT} dT. \tag{2.2}$$

The lower integration limit T_{min} is the minimum energy transferred (not necessarily zero), which under certain circumstances is defined as the minimum energy required to displace an atom from its equilibrium position inside the lattice, or by defining an impact parameter comparable to the screening length of the interatomic potential (cut–off energy). The upper limit T_M is the maximum transferred energy and is determined by the kinematic factor for a head-on collision (see section 3.4.1). The term $\frac{d\sigma_n(E)}{dT}$ corresponds to the differential nuclear energy-transfer cross-section.

Equation 2.2 can be express in terms of center-of-mass coordinate system from the theory of binary elastic collisions. This approach has the advantage that, in the absence of transverse forces, the motion of the two particle system can be simplified as a single particle moving within an interatomic potential centered at the origin of the coordinate system besides the complexity of the acting force. The aim is to simplified the description in terms of the interatomic potential $V(r)$ which depends only on the absolute value of the interatomic separation r, the ion energy E and the impact pa-

rameter b[1] by considering conservation of momentum in a center of mass coordinate system [69].

The first goal is to determine the energy transferred to the target atom. This can be done from the velocity vector diagram for the laboratory and center-of-mass coordinate systems and the relationships between the scattering angles [69]. This leads to the relation: $v_2 = 2v_0 \frac{M_c}{M_2} \cos\phi$, which relates the recoil velocity v_2 as a function of the incident ion velocity v_0 and the recoil angle ϕ and being M_c the reduced mass. The next step requires to use the relation between ϕ and the recoil angle in the centre-of-mass system θ_c: $\phi = \frac{\pi - \theta_c}{2}$, and that of the kinetic energy: $E = \frac{1}{2} M_2 v_2^2$. Such considerations allow to express the energy transferred from the ion to the target nuclei in terms of the scattering angle θ_c:

$$T = E = T_M \sin^2\left(\frac{\theta_c}{2}\right) = \gamma E \sin^2\left(\frac{\theta_c}{2}\right), \tag{2.3}$$

where $\gamma = \frac{4M_1M_2}{(M_1+M_2)^2}$ and M_1 and M_2 correspond to the mass of the target atoms and the projectile ion, respectively.

The scattering angle θ_c can be expressed following the theory of motion under a central force [69]. This allows to express the scattering angle as a scattering integral dependent on the central interatomic potential $V(r)$, ion energy E and impact parameter b as:

$$\theta_c = \pi - 2b \int_0^\infty \frac{dr}{r^2 \left[1 - \frac{V(r)}{E} - \left(\frac{b}{r}\right)^2\right]^{1/2}}. \tag{2.4}$$

The scattering integral 2.4 can be solved by considering an appropriate interatomic potential, which in turn allows the determination of the corresponding impact parameter.

[1]The impact parameter is the offset distance from a parallel line of the initial particle's direction moving through a central force, and is directly related to the centrifugal energy and the angular orbital momentum [19].

Finally, it is important to outline the equivalence between the energy transfer differential cross-section and the impact parameter. This means that integrating the energy-transfer differential cross-section over all possible energy transfers is equivalent as integrating over all range of impact parameters [21]. This can be express by using the identity

$$\int_{T_{min}}^{T_M} \frac{d\sigma_n(E)}{dT} dT = \int_{T_{min}}^{T_M} \frac{4\pi}{T_M} \frac{d\sigma(\theta_c))}{d\Omega} = \int_0^{b_M} \frac{4\pi}{T_M} \frac{b}{\sin\theta_c} \left| \frac{db}{d\theta_c} \right| = \int_0^{b_M} 2\pi b db, \quad (2.5)$$

the integration parameters account for a head-on collision ($b = 0$) and the maximum impact parameter b_M, commonly set to infinity. Thus, the differential energy-transfer cross-section can be expressed by the impact parameter b and the scattering angle θ_c in the center of mass coordinate system as follows:

$$\int_{T_{min}}^{T_M} T \frac{d\sigma_n(E)}{dT} dT = \gamma \pi E \int_0^{\infty} \sin^2\left(\frac{\theta_c}{2}\right) d\left(b^2\right). \quad (2.6)$$

The evaluation of equation 2.6 requires the selection of an appropriate interatomic potential to simultaneously solve equation 2.4 and 2.6. As there is no single interatomic potential function that appropriately describes all binary interactions between the ion and the target nuclei, empirical parameters are often employed based on existing interatomic potentials. The most commonly used is the universal ZBL screening function proposed by Ziegler, Biersack and Littmark and is based on the numerical solution to the average of multiple screening functions of different two-atom configurations [70]. This yields the best agreement to experimental values over other classical screening potentials. It is worth to mention that such general methods developed to evaluate equation 2.6 take into consideration only statistical models of the atom without considering the exchange energy of the quasi-molecule formed during the nuclear interactions. The presented approach is valid for amorphous materials, however, when dealing with a single- or poly-crystalline material it is necessary to consider structural effects such as ion channelling [3] (Lindhard theory [71]).

2.1.2 Electronic stopping power

The second mechanism of energy-loss corresponds to the energy transferred from the ion to the target electrons. This mechanism is strongly dependent on the ion velocity and its charge state, where two different processes can be distinguished. At low ion velocities, $\beta = \frac{v}{c} \leq 0.01$, where v is the ion velocity and c the speed of light, the ion carries most of its electrons and can capture electrons from the target to neutralize, as their interaction time increases. At higher velocities, electron loss by collisions with the target electrons dominates and an ion with atomic charge Z can be deprived from all electrons. It will then exhibit an effective charge Z^* following the relationship $Z^* = Z\left(1 - e^{-125\beta Z^{-2/3}}\right)$, losing energy by electron excitation and ionization of the target [72].

In the low velocity regime, the interaction time between the ion and the target atom lasts long enough to permit the formation of a quasi-particle, therefore, the energy loss process is not the product of binary collisions. Instead, it is the result of an exchange of electrons in the quasi-particle in an attempt to neutralize the charge state of the incident ion. The electrons transferred from the atom to the ion require a certain energy to be accelerated from their equilibrium position, and this amount of energy is supplied by the ion, contributing to its slowing. This was first considered by Firsov [73] and later modified by Lindhard and Scharff [74]. Firsov considered the slowing process of the incident ion as the result of the interaction between two Thomas-Fermi atoms, showing good agreement for the cases where the ratio of the two atomic numbers is less than or equal to four, but limiting its applicability. Lindhard and Scharff instead, suggested that the interaction should be mediated by a screened Coulomb potential given by the geometrical mean of the corresponding Coulomb fields, leading to the electronic stopping power at low energies expression:

$$S_e(E) = 38.45 \frac{\zeta_L Z_1 Z_2}{\left(Z_1^{2/3} + Z_2^{2/3}\right)^{3/2}} \left(\frac{E}{M_2}\right)^{1/2}, \tag{2.7}$$

where Z_1 and Z_2 are the atomic numbers of the target atoms and the projectile ion, respectively. $\zeta_L = Z_2^{1/6}$ is the correction factor derived from the numerical fit of experimental data and M_2 the mass (in a.m.u.) of the ion. The slope $E^{1/2}$ is characteristic for ion velocities $\beta \leq 0.01$.

When the ion velocity increases, the electronic stopping power can be determined by pure Coulomb interactions with high accuracy. During the ion passage, the net component of the Coulomb force on the target electrons along the path is zero, although, a momentum Δp is transferred to the electron in the perpendicular direction. The transferred transverse momentum can be determined in terms of the impact parameter b and the Coulomb force F_c as: [3, 19, 75]

$$\Delta p = \frac{1}{v} \int_{-\infty}^{\infty} F_c dx = \frac{2 Z_1 Z_e e^2}{bv}, \tag{2.8}$$

where its important to note that eZ_1 corresponds to the charge of the incoming ion and the $Z_e = 1$ for the electron.

Thus, the energy T transferred to the electron of mas m_e and lost by the ion is:

$$T = \frac{\Delta p^2}{2m_e} = \frac{2 Z_1 e^4}{m_e v^2} \left(\frac{1}{b^2}\right). \tag{2.9}$$

The energy-loss rate can then be determined in an analogous fashion as for the nuclear stopping power by substituting the mass of the target with the electron mass. The electronic stopping power can then be expressed as follows:

$$S_e(E) = \int_{T_{min}}^{T_{Max}} T\frac{d\sigma_e(E)}{dT}dT = 4\pi\frac{Z_1^2e^4}{m_ev^2}\int_{b_{min}}^{b_{Max}}\frac{1}{b^2}d(b^2) = 4\pi\frac{Z_1^2e^4}{m_ev^2}ln\frac{b_{Max}}{b_{min}}. \quad (2.10)$$

Equation 2.10 diverges as b_{min} decreases, thus, a minimum impact parameter is required to be defined. Under the assumption that the electron mass is much smaller than the mass of the incident ion, it is possible to use Rutherford's elastic scattering theory to estimate the closest approach during a head-on collision, which leads to $b_{min} \sim \frac{Z_1e^2}{m_ev^2}$ [19]. On the other hand, the smallest energy that can be transferred from the ion to a target electron should be enough to reach an excited state thus, $b_{max} = \frac{2Z_1e^2}{(2m_ev^2I)^{1/2}}$, where the average ionization energy I follows the approximate relationship $I \approx (10eV)Z_2$, where Z_2 corresponds to the atomic number of the target atom. The combination of both results leads to the well-known Bethe-Bloch formula for the electronic stopping power: [76–79]

$$S_e = \frac{4\pi Z_1^2Z_2e^4}{m_ev^2}ln\left(\frac{2m_ev^2}{I}\right), \quad (2.11)$$

for a projectile ion and a target atom with atomic numbers Z_1 and Z_2, respectively.

Corrections have been made to the Bethe-Bloch formula to take into consideration relativistic effects at very high energies and the electronic structure of the target atoms: [75]

$$S_e = \frac{4\pi Z_1^2Z_2e^4}{m_ev^2}\left[ln\left(\frac{2m_ev^2}{I(1-\beta^2}\right) - \beta^2\right]. \quad (2.12)$$

2.1.3 Bragg's rule

The principle of additivity of stopping cross-sections for compound targets is commonly known as Bragg's rule [80]. It assumes that the stopping power results from the sum of a sequence of binary collisions between the energetic ion and the target's

atomic nuclei or electrons, regardless of the surrounding atomic bonding. Therefore, the net stopping power of a compound can be expressed as a linear combination of the stopping cross-section S_i (S is defined as: $S \equiv \frac{1}{N}\frac{dE}{dx}$, where N is the atomic density) of its individual elements, weighted by the relative abundance of the constituents of the compound n_i i.e. in terms of the stoichiometric composition of the target. Bragg's rule can be expressed as:

$$\frac{dE}{dx} = \Sigma_i n_i S_i = \Sigma_i n_i \left(S_{n,i} + S_{e,i}\right), \tag{2.13}$$

such that $\Sigma_i n_i = 1$.

While Bragg's rule offers a good estimate with less than 20% deviation from experimental values for most compounds, the accuracy decreases for estimating the electronic stopping power of compounds involving light elements such as H, C, N, O, F, S, etc. For such compounds, the expected values involving Bragg's rule show large discrepancies, well above 20% compared to experiments, highlighting the relevance of the atomic bonding configuration for the stopping power of organic and molecular targets.

2.1.4 Ion range and range distribution

During the passage through a solid target, an energetic ion will deviate from its original trajectory as a result of the stopping processes involved before coming to rest. At high energies (or ion velocities), inelastic collisions with the electronic subsystem are the predominant interaction, where the electron mass is small in comparison with the ion mass, resulting in negligible deviation of the projectile ion from its original trajectory. In contrast, at lower energies nuclear interactions become more relevant and dominate the energy-loss process. Multiple binary collisions between the ion and the target atoms can occur, each of them involving an energy transfer that can cause the ion to change direction and lead to large angular deflections.

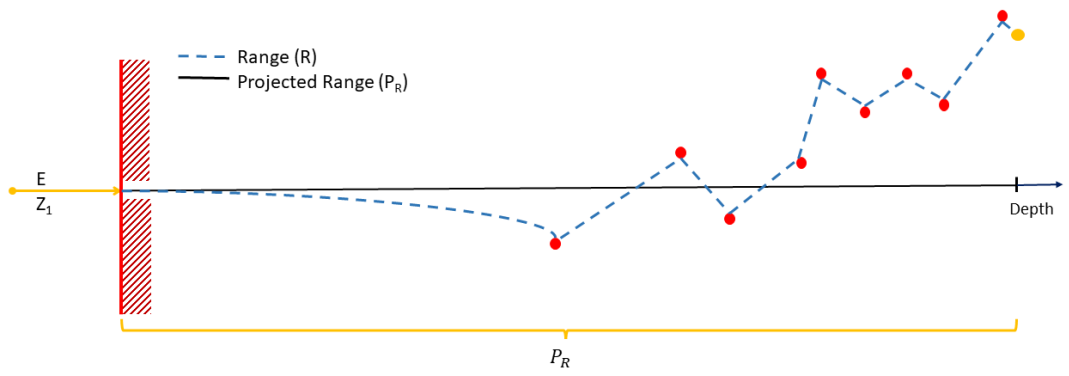

Figure 2.2: *Schematic of the range and projected range of an ion implanted into a solid target.*

For the distance an ion travels through a target before coming to rest, two definitions are of particular interest: the range R and the projected range R_P. The first corresponds to the net distance travelled by the ion from the surface until it comes to rest, while the projected range is the length of a perpendicular line with respect to the surface connecting the surface and the position of the ion at rest (Figure2.2). This is equivalent to the penetration depth of the ion. The range can be expressed from the elementary principle of energy loss as: [3, 19]

$$R = \int dR = \int_{E_0}^{0} \left(\frac{dE}{dx}\right)^{-1} dE = \int_{E_0}^{0} \frac{dE}{NS(E)}, \tag{2.14}$$

for an incident ion with initial energy E_0 and total stopping cross-section $S(E) = S_n(E) + S_e(E)$, where the subscripts n and e correspond to the nuclear and electronic contributions, respectively.

For a set of ions of the same species, energy and incidence angle, the trajectory and thus the projected range is not necessarily the same due to the stochastic nature of the stopping process. Consequently, the projected range can be described by a Gaussian statistical distribution. The distribution function of the implanted ions can be express as:

$$N(x) = \frac{\phi_i}{\Delta R_P (2\pi)^{1/2}} exp\left[-\frac{1}{2}\left(\frac{x - R_P}{\Delta R_P}\right)^2\right]. \quad (2.15)$$

The projected range distribution $N(x)$ is often referred to as the range distribution or depth profile distribution, where the term R_P is the mean, also referred as the projected range. The standard deviation of the Gaussian distribution ΔR_P represents the so called 'straggling'. The distribution is commonly normalized to the irradiation or implantation fluence ϕ_i.

2.1.5 Damage cascades

At low energies, the ion will transfer energy mainly to the target nuclei by elastic collisions, which can lead to three different behaviours depending on if the transferred energy E_T is lower, higher or several times higher than the energy required to remove an atom from its bound position, also called displacement energy E_d [81].

When the transferred energy is lesser than the displacement energy ($E_T < E_d$), the atom is incapable of overcoming the potential well of its bond configuration and it will remain in its position and dissipate the energy received through lattice vibrations. In the second case, when the transferred energy is larger than or equal to the displacement energy but less than twice its value ($E_d \leq E_T \leq 2E_d$), the target atom gains enough energy to become free but with limited kinetic energy to interact with other atoms along its path. In crystalline materials, the empty place left by the displaced atom is called a vacancy, while for amorphous materials it is called a coordination defect [82]. In this case, the displaced atom has enough energy to produce a vacancy but not enough to keep interacting with the neighbouring atoms, occupying an interstitial site in the lattice. The remaining interstitial-vacancy pair is also known as a Frenkel-pair or Frenkel-defect. In amorphous materials, radiation-induced defects create dangling bonds or coordination defects [42]. In general, the atoms displaced by energetic ions due to nuclear interactions are called a primary knock-on atoms or PKAs. A secondary knock-on atom is a displaced atom from a collision with a PKA, continuing in hierarchy until the displaced atom exhibits a kinetic energy lower than

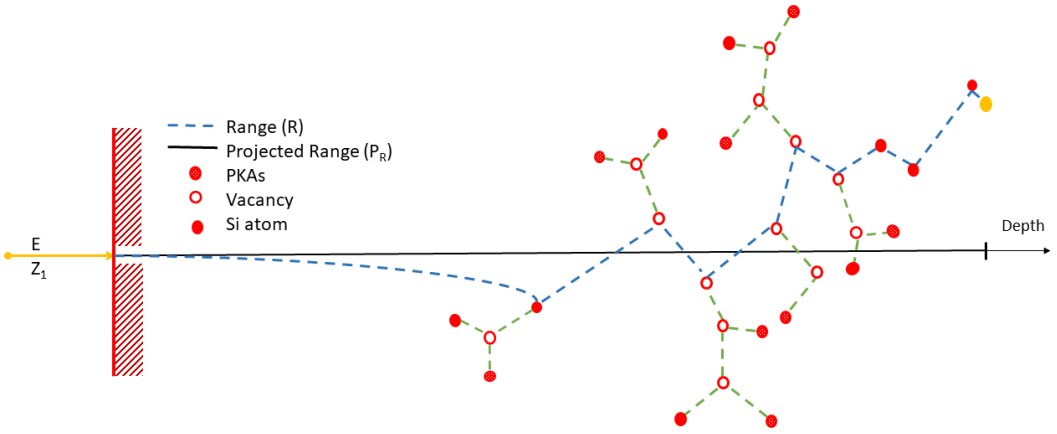

Figure 2.3: *Schematic of the damage cascade process for an energetic ion. When the electronic stopping power dominates the interactions, we can observe only small deviations from the initial trajectory. As the kinetic energy decreases, interactions with the target nuclei becomes relevant. Such interactions can lead to high ion deflection and atomic displacements, which can result in damage cascades.*

$2E_d$.

For this to happen, the energy transferred to the PKA needs to be several times larger than the displacement energy ($2E_d << E_T$). The PKA then has enough kinetic energy to produce a ballistic collision cascade (Fig.2.3), with the mean displaced atoms being produced during a cascade determined by the displacement damage function. Radiation damage cascades are matter of concern in the case of semiconductor doping [3], as they are capable of inducing effects such as chemical disorder, phase-transformations or structural disorder. They also deliberately used for material modification such as irradiation-induced amorphisation [83, 84], and layer intermixing [85].

2.1.6 Non-additive effects

As mentioned before, when an energetic ion penetrates a solid target, its energy-loss rate is considered the sum of two independent contributions (equation 2.1). As a consequence, two clear domains have been identified: the low energy range, where

nuclear interactions dominate the interactions between the ion and the target and the high energy range, where pure electronic interactions lead to material modifications. However, more recent experiments show that additive, competing or synergistic effects may play an important role, in particular where both contributions are of similar magnitude [86–91].

2.1.7 SRIM code

The SRIM package (Stopping and Range of Ions in Matter) is a Monte Carlo-based code used to simulate the path of energetic ions travelling through a specific target [70, 92, 93]. The simulation of a significant number of ions allows to build up sufficient statistics permitting the estimation of the ion distribution, straggling and radiation damage. SRIM also allows to calculate stopping power tables for a given energy/species and target combination for a broad energy range. It provides high accuracy numerical values thanks to its more than 28000 experimental stopping power datasets in over 300 elemental and compound targets. The code also includes a correction known as the Core and Bond approach (CAB) to include atomic bonding effects [75, 92], yielding an accuracy of under 10 % with respect to experimental values. The nuclear interactions are calculated considering binary collisions between the ion and the target nuclei (equations 2.6 and 2.4) using an approximation based on diffusion equations, known as the 'Magic Formula' [93] and the PRAL algorithm [94], which provide high computational efficiency and accuracy. The electronic interactions are calculated by extrapolation from tabulated experimental values while considering a straight trajectory between each nuclear collision under continuous interaction with the target electrons (Eq. 2.12). It is worth to mention that SRIM does not consider compositional changes and treats all targets as amorphous materials, disregarding channelling effects or orientation.

2.2 Swift heavy-ion irradiation

At high ion energies, processes are predominantly based on the interaction of the projectile ions with the electrons in the target material as the interaction cross-section for nuclear collisions dramatically decreases with increasing ion energy, $S_n << S_e$ [95]. Ion tracks are the residual damage along the largely strained ion trajectory [56, 96]. Energies higher or equal than 1 MeV/u are commonly used as they induced continuous ion tracks of several micrometers in length; however, ions of lower energies may still deposit enough energy to create continuous tracks of shorter lengths [97–99] (in a-SiO_2 this can be as low as 0.1 MeV/u [100, 101]). To highlight the difference of the interaction processes, irradiation with ions of mass greater than He and energies close to or above 1 MeV/u is referred as swift heavy-ion irradiation (SHI) and is a requirement for certain processes to take place, as it will be explained in this subsection.

When a swift heavy-ion penetrates a solid, it will interact predominantly with valence and core electrons, leading to the charge redistribution resulting from the production of energetic electrons called δ-electrons, as the result of the deposition of large amounts of energy into the electronic system. The overall movement of the energetic electrons leads to a radially symmetric charge separation perpendicular to the ion trajectory, producing secondary ionization, positive holes, and the corresponding formation of a transverse electric field. Auger transitions and secondary ionization occur within a few femtoseconds and a trace of energetic electrons and holes is formed within the δ-electron range, up to a few hundreds of nanometres from the ion trajectory [102, 103]. This leads to a radially polarized region comprised of a positive inner region populated by valence-band holes and energetic electrons in the outer region. Yet, the transient electric field vanishes rapidly, earlier than atomic motion can occur in most materials, due to depolarization. Depolarization leads to the recovery of spatial net charge neutralization, although the electrons remain excited [102]. This can be considered a preamble for the rapid increase of the lattice temperature, known as the thermal spike that will cause the main structural modifications in the material [4, 101, 102].

The highly localized energy is transferred from the energetic electrons to the lattice by electron-phonon coupling leading to a rapid increase in temperature within a few nanometres of the ion trajectory, a so called "thermal spike" that can by far exceed the melting temperature of the material. This heating produces a shock wave associated with the thermal expansion, followed by energy dissipation through the lattice and fast quenching of the thermal spike. The following rapid resolidification can leave a trail of permanent damage a so called 'ion track' [95]. An ion track can be broadly defined as the local structural modification of the target material resulting from the collective interactions linked to the passage of a swift heavy-ion [102].

The timescale of the heating in the thermal spike is dependent on the lattice specific heat and the electron-phonon coupling strength but commonly lasts up to a few picoseconds. This stage defines the energy deposition threshold required to surpass the melting (and boiling) points that are believed to produce a molten phase[2]. The threshold energy is also modified by the material relaxation and depends on the self-trapping of excitons, the formation of an amorphous structure or pre-existing defects. By the end of this stage, the excited electrons reach local thermal equilibrium with the lattice.

In the last stage, the atoms cool down and reach thermal equilibrium with the environment in a process of heat conduction that can last up to hundreds of picoseconds. For the structural modification created during the lattice relaxation and heating to become permanent, the temperature should decrease quickly enough so the modified structure quench-in as the system tends to return to their initial equilibrium configuration [104]. Thus, the timescale of the cooling stage is of high relevance.

[2]Because of the non-equilibrium nature of the process, the term 'melting' should be understood in a broader context as there are several forms of dynamic disorder and energy transfer and redistribution rates, which vary with position and timescale [102]

2.2.1 Ion track morphology in amorphous silicon dioxide and silicon nitride

Different models have been proposed to explain the mechanisms of the ion track formation process. Historically, one of the first proposed models suggested that the main structural modification occurred during the charge redistribution stage [105]. The remaining positive cores located near the ion path experience a repulsive Coulomb field that can exceed the lattice bonding forces. This is known as the Coulomb explosion model and estimates the magnitude of the forces generated to produce atomic displacements, if comparable to the bulk Young modulus. However, it was shown that the neutralization of the atoms can occur within few femtoseconds, much faster than the lattice relaxation times, as in the case of Si [106]. Thus, this model was unable to explain the radial dimensions of ion tracks observed by electron microscopy in many crystalline materials [101].

The most common approaches to explain the experimental data regarding the radial dimensions of the ion tracks are based on so called 'thermal spike models'. These models assume that the dimensions of the modified structure is related to the region that surpasses the melting point during the heating stage [101,102]. While the thermal spike models attempt to quantitatively describe the ion track dimensions in terms of the molten region formed during the relaxation and heating stage, they cannot describe the atomic response of the material. Alternatively, molecular dynamics (MD) numerical simulations were developed to study the atomic behaviour of matter under electronic excitations, such as swift heavy-ion irradiation [107]. Initially, the electronic excitations were simulated as cylindrical spikes whose energy is directly transferred to the atomic system. In this first approach, the simulations did not consider the influence of the ion velocity on the energy deposition, and the complex interaction related to the energy deposition and transfer by the electron-phonon coupling. Nevertheless, the main challenge remained the transfer of the energy from the electronic to the atomic subsystem, to get a more realistic heat spike.

For crystalline dielectrics, it has often been found that the ion track morphology resembles an amorphous cylinder, resulting from the fast re-solidification of the molten region into an amorphous or defective zone. This zone is often surrounded by a halo exhibiting a large stress field based on high resolution transmission electron microscopy (HR-TEM) [67, 101, 108, 109]. Similar results were reproduced by MD simulations for tracks formed in materials such as $Gd_2Ti_2O_7$ and Gd_2TiZrO_7 [110], where the energy was deposited directly into the atoms, considering a reduced effective energy loss. In agreement with experiments, the MD showed the formation of an amorphous core surrounded by a defective shell. In addition, novel results were achieved for crystalline SiO_2 and ZnO showing the amorphisation of the former while track recrystallize for the latter [104].

On the other hand, experimental observations of ion tracks in amorphous materials have been limited to macroscopic measurements such as change in electrical conductivity or infrared spectroscopy, as they do not exhibit sufficient contrast to be observed by electron microscopy techniques [27, 54, 89]. The first attempts to characterise ion track formation and dimensions in a-SiO_2 were based on indirect measurements such as Fourier transformation infrared spectroscopy (FTIR) [53, 111] or from chemical etching [98, 112]. In the FTIR analysis, a-SiO_2 exhibits a main absorbance band at 1080 cm^{-1} attribute to the TO3 band and a secondary absorbance signal at 1185 cm^{-1}. After irradiation, a shift towards lower wavenumbers was observed for the main band while exhibiting an increase in absorbance intensity for the second band. This behaviour was explained as resulting from the transformation of the normal six-member rings of tetrahedral SiO_4 to planar three-member rings but without providing information regarding the ion track dimensions [53]. In the second case, the size of the pore was extrapolated to the dimensions of the ion track in a crude approximation but lacking any structural information about the track region. Recently, the ion track morphology of thermally grown a-SiO_2 was determined by synchrotron based small angle X-ray scattering (SAXS), where an under-dense core surrounded by an over-dense shell was reported, yet the absolute density change was not determined [56]. In the same work, MD simulations were carried out showing good

agreement with the proposed ion track morphology and dimensions. Here, the energy deposition profile was determined from thermal spike calculations. Nevertheless, the question remained open if the observed core-shell structure can be ascribed to the density anomaly of SiO_2 above 1800 K [57].

For a-Si_3N_4, the morphology of ion tracks was initially characterized by FTIR [54], where the decrease of the main absorbance peak was related to the ion track dimensions by a Poisson law and without any information regarding the morphology. Recently, very thin (30 nm) layers grown by low pressure chemical vapour deposition (LPCVD) [58] were irradiated with C_{60} molecules and Au ions. The track structure comprised of an under-dense core and an over-dense shell observed by HAADF-STEM, similar to a-SiO_2. In this case, the nature of the core and shell regions were ascribed to the quenching of the boiling and melting phase as calculated by the inelastic thermal spike model, respectively [59]. This is also known as the two-threshold model. From their experimental results, the ion track radius agrees with the numerical calculation of the molten region by choosing the electron-phonon coupling such that the calculations agree with the experimental value, thus the boundary of the core region defines the boiling energy, which for a-Si_3N_4 was determined to be 2.5 eV/atom.

2.2.2 Thermal spike models

Currently, two versions of the thermal spike model are discussed, the inelastic (i-TS) [108, 109] and the analytical (ATS) [113] thermal spike model. The i-TS model describes the temporal evolution of the ion-induced thermal spike while the ATS disregards the temporal dependency of this stage and only determines the maximum temperature reached during the thermal spike. In both models, the ion track dimensions are defined by the region that exceeds the melting temperature of the material. In the following, a brief discussion of the approaches adopted by each model and their applicability and agreement with experimental observations are presented.

The inelastic thermal spike

The inelastic thermal spike (i-TS) model, originally proposed for metals by Lifshitz *et al.* [114, 115] and later reconsidered for insulators and semiconductors [1, 101, 102, 108, 109, 116], describes the transport of the energy deposited by the ion through electron-electron and electron-atom interactions. It assumes that such interactions are described mathematically in terms of two coupled Fourier heat equations, which is the reason why it is sometimes called the two-temperature model (TTM). It assumes a local equilibrium in the electron and lattice systems, characterized by their corresponding temperatures and heat flow between the two. The energy deposition is assumed to be constant along the ion's path in an isotropic medium, thus, the coupled Fourier equations can be expressed in a cylindrical geometry as:

$$C_e(T_e)\frac{\partial T_e}{\partial t} = \nabla[K_e(T_e)\nabla T_e] - g(T_e - T_i) + A(r,t) \quad (2.16)$$

$$C_l(T_l)\frac{\partial T_l}{\partial t} = \nabla[K_l(T_l)\nabla T_l] + g(T_e - T_l) \quad (2.17)$$

where $C_{e,l}(r,t)$, $K_{e,l}(r,t)$ and $T_{e,l}(r,t)$ represent the heat capacity, thermal conductivity and temperature for the electronic and lattice subsystems, respectively, at a radial distance r from the ion trajectory at a given time t. The input energy is defined by the electronic energy loss in the functional form of the radial and time distribution $A(r,t) = A_0 D(r)G(t)$ [2, 103, 117]. The temporal function represents a normalized time pulse ($G(t) = \frac{1}{\sqrt{2\pi}\sigma} exp\left(\frac{-(t-t_0)^2}{2t_0^2}\right)$) of few femtoseconds duration, where t_0 is the mean flight time of the delta electrons ($t_0 \approx 1 \times 10^{-15} s$). On the other hand, the spatial function is defined by the corrected formula for the dose radial distribution by Waligorski *et al.* [103] and will be explained in more details in the following section. The term A_0 represents the normalization constant such that:

$$A_0 \int_{t=0}^{\infty}\int_{r=0}^{R} \frac{1}{\sqrt{2\pi}\sigma} exp\left(\frac{-(t-t_0)^2}{2t_0^2}\right) D(r) 2\pi r dr dt = S_e. \quad (2.18)$$

The electron-phonon coupling g is estimated in terms of the electron mean-free path (λ) as:

$$g = \frac{K_e(T_e)}{\lambda^2}. \tag{2.19}$$

Here, the only free parameter is the electron mean-free path λ, which can be approximated using its empirical dependence on the optical band gap E_g in amorphisable insulators [1]. It can also be estimated by varying the magnitude of the electron-phonon coupling term to match the ion track dimensions found by experimental methods with the analytical solution provided by the model.

The ion track is then assumed to be the cylindrical region where the lattice temperature exceeds the melting point of the material. As explained by Wang *et al.* [108], the application of the current model in insulating materials is carried out using equilibrium thermodynamic parameters where the effect of pressure appears to have no or little effect on them. The radial dimension of an ion track is defined by the molten region, not only by reaching the melting temperature but also the heat of fusion, in the heating stage. This model provides a useful relationship between the electronic stopping power and the ion track radius for a given material. Following the definition of the electron-phonon coupling in terms of the electron mean-free path, it can explain the difference in the ion track dimensions found between crystalline and amorphous materials by the smaller λ-values in the amorphous phase.

In addition, the i-TS model can be used to explain the so called 'velocity effect', which is related to the formation of ion tracks of different radial size in insulators when irradiated with ions at two different energies but exhibiting the same stopping power. Specifically, smaller track radii are generally observed at the higher ion energies. In Figure 2.1 the stopping power is plotted against the irradiation energy. In the plot, the stopping power increases gradually with increasing ion energy, when dominated by nuclear interactions which is followed by an abrupt increase, when the electronic

stopping power begins to dominate. As the energy keeps increasing, the stopping power reaches a maximum value, known as the Bragg peak, which is followed by a slow decrease for further increasing energies. The comparison between the two irradiation energies, one below and the other above the Bragg peak but with the same stopping power (low- and high-velocities), suggested that the evolution of the damage trail left by the ion's passage is not solely dependent on the stopping power S_e [99].

As mentioned above, the spatial energy distribution in the i-TS model is predicted by an analytical formula of the radial distribution of the deposited energy, determined by Waligorski *et al.* [103]. The proposed radial energy distribution (equation 2.25) shows a dependence on the ion velocity and predicts an increase of the δ-electrons range with increasing velocity. This is reflected in the integration of the radial energy distribution considering a cylindrical geometry. The resulting radius R in which the energy is deposited increases for the high-velocity ion. This can be seen in Figure 2.4, where the radial distribution is plotted for two ion velocities in a-SiO_2 and a-Si_3N_4 and the above mentioned differences become clear. As a consequence, the decrease of the energy deposited within the first few nanometres is responsible for the velocity effect.

The analytical thermal spike model

In the ATSM, the time-evolution of the lattice relaxation and heating stage is considered irrelevant as it assumes that the maximum lattice temperature is reached within 1 picosecond. Therefore, the main ion-induced physical effects are determined by the maximum temperature reached which only decreases and broadens due to heat conduction [113, 118]. Here, the increase in the system's temperature is approximated by a Gaussian distribution at the maximum peak temperature T_p ($t = 0$) by the following form:

$$\Delta T(r,0) = \frac{\gamma S_e}{\pi \rho c a^2(0)} exp\left(-\frac{r^2}{a^2(0)}\right), \tag{2.20}$$

where the terms ρ and c are the material density and heat capacity defined by the Neumann-Kopp's rule, γ is the efficiency of the electronic energy loss S_e deposited in the thermal spike[3], and $a(0)$ the initial width of the Gaussian distribution in the lattice system. The two only free parameters of the model are the energy deposition efficiency and the initial width of the distribution.

The effective ion track radius R_e can then be estimated in terms of the sample temperature during irradiation T_{irr} as:

$$\Delta T(R_e,0) = T_m - T_{irr} \tag{2.21}$$

$$R_e^2 = \begin{cases} a^2(0) ln(\frac{S_e}{S_{et}}) & for\ S_e\ <\ 2.7\ S_{et} \\ \frac{a^2(0) S_e}{2.7 S_{et}} & for\ S_e\ >\ 2.7\ S_{et} \end{cases} \tag{2.22}$$

where S_{et} represents the electronic stopping power threshold for track formation [113].

In this simple formalism, there is no defined mechanism that quantifies the energy deposited in the lattice, and it determined by fitting the radius of the molten region to the radius of ion tracks determined by experimental methods. The ion track dimensions correspond to the maximum melt volume, defined by the melting point (T_m) while ignoring the heat of fusion. It also explains the velocity effect as the decrease in energy transfer efficiency with higher irradiation energies. Although the ATS model can be used to describe most of the experimental data, it is of particular relevance when studying materials where an elliptical ion track cross-section is formed, as in the case of high T_C superconductors [118]. This is because it is not a basic

[3]this relates to the electron-phonon coupling in the i-TS model

assumption the necessity of an underlying isotropic thermal conductivity, offering a better interpretation of the flux of charge carriers and their contribution with the beam direction.

2.3 Inelastic thermal spike calculations

The thermal spike calculations performed as part of this thesis aim to estimate the energy exchanged between the ions and the materials and use the previously described i-TS model for the experimental irradiation conditions involved. In particular, we are interested in the time-evolution of the temperature [119, 120] and the effect of the difference in thermo-physical properties such as thermal conductivity and melting point between a-SiO_2 and a-Si_3N_4.

The calculations based on the i-TS model provide a good estimate of the time-evolution of the lattice temperature at different radial distances from the ion path. The selection of the i-TS over the ATS model lies in the fundamental hypothesis that the ion track formation and the ion beam shaping processes are not only dependent on the energy deposition, but also on the timescale required to reach melting. The time-evolution is mediated by the equilibrium thermodynamic parameters of the material of interest, which in the case of a-SiO_2 and a-Si_3N_4, are significantly different.

It is important to discuss the limitations of the model. It only provides an estimate of the time-evolution of the temperature profile around the ion path, from which we infer the possible material response, but does not yield information regarding the remaining material modification. The main approximation that has drawn some criticism is the use of equilibrium values due to the highly non-equilibrium nature of the thermal spike [118]. As mentioned in the previous sub-section, the use of equilibrium values, and without considering the effect of pressure, is supported by the timescale required for the thermalization of electrons and the target atoms, comparable to the thermal spike timescales. Also, comparison with experimental

results at different irradiation energies in a-SiO_2 are in good agreement with the temperature time-evolution defined by the i-TS model.

The i-TS model was implemented to simulate the time-evolution of the temperature profile of two different phenomena, the ion track formation process in a-SiO_2 and a-Si_3N_4, and the ion shaping process of Au nanoparticles embedded in the two dielectric materials. For the ion track formation process, the two-dimensional version was used as only the radial dimension is required to define the region that reaches melting. The three-dimensional version of the i-TS model provided by Dufour *et al.* [2] was used to model the temperature profile when the ion passes through an embedded Au nanoparticle. Both codes are based on the same physical principles, hence, a through description of only the two-dimensional version is presented in this subchapter while briefly explaining the extension required for a three-dimensional system.

Two-dimensional inelastic thermal spike

In the i-TS model, the energy transferred from the energetic ion into the sample is modelled by two coupled Fourier heat equations describing the electronic and the lattice subsystems (Equation 2.17). The coupling factor is known as the so-called electron-phonon coupling factor. In the two-dimensional version, the assumption of a homogeneous target (e.g. amorphous material) allows to express the coupled equations in cylindrical coordinates system assuming rotational symmetry around the trajectory:

$$C_e(T_e)\frac{\partial T_e}{\partial t} = \frac{1}{r}\frac{\partial}{\partial r}\left(rK_e(T_e)\frac{\partial T_e}{\partial r}\right) - g(T_e - T_l) + A(r,t) \tag{2.23}$$

$$C_l(T_l)\frac{\partial T_l}{\partial t} = \frac{1}{r}\frac{\partial}{\partial r}\left(rK_l(T_l)\frac{\partial T_l}{\partial t}\right) + g(T_e - T_l), \tag{2.24}$$

in this model $A(r,t)$ models the energy deposition from one ion at a time. the terms C, K and T correspond to the specific heat, thermal conductivity and temperature for the electronic and lattice, subscript e and l respectively.

The energy deposition function can be separated in terms of its spatial and a temporal variables by: $A(r,t) = A_0 D(r) G(t)$, where A_0 is a normalization factor to the electronic stopping power (equation2.18). The temporal function $G(t)$ represents a normalized time pulse of few femtoseconds duration, as described in the previous subsection. The spatial function $D(r)$ is defined by the corrected formula for the radial dose distribution by Waligorski *et al.* [103] which has the form:

$$D(r) = \frac{Ne^4 Z^{*4}}{\alpha mc^2 \beta^2 r} \left[\frac{\left(1 - \frac{r+\theta}{R+\theta}\right)^{1/\alpha}}{r+\theta} \right] \left[1 + A \left(\frac{r-B}{C} \right) exp \left(-\frac{r-B}{C} \right) \right], \qquad (2.25)$$

where N is the electron density of the target, e is the electron charge in cgs units, and Z^* ($Z^* = Z[1 - exp(-125\beta Z^{-2/3})]$) is the effective charge of an ion of elemental charge Z moving with velocity $\beta = \frac{v}{c}$. A power law to describe the range of electrons θ in aluminium is assumed ($\theta = kI^\alpha$), where k is the constant value (k= $6{\times}10^{-6}$ g·cm^{-2}·keV$^{-\alpha}$) for atoms with an ionization potential I. The value of the exponent α depends on the ionization potential fo the target: $\alpha = 1.079$ for $I < 1$ keV, or $\alpha = 1.667$, otherwise. The variable R corresponds to the maximum range of the δ-electrons, determined in terms of the kinematically maximal δ-electron energy $W = \frac{2mc^2\beta^2}{(1-\beta^2)}$ and can be calculated as: $R = kW^\alpha$. The assumed value for α in this case depends on the ion velocity, being $\alpha = 1.079$ for $\beta < 0.03$ or $\alpha = 1.667$ for $\beta > 0.03$.

The last term of the radial dose function is a semi-empirical expression that corrects for the underestimated energy deposition within the first nm, observed in Monte Carlo simulations in liquid water for protons of different energies, in the region determined between 1 and 10 nm [103]. For $r > 0.1$ nm, $B = 0.1$, $C = 1.5{+}5{\cdot}\beta$;

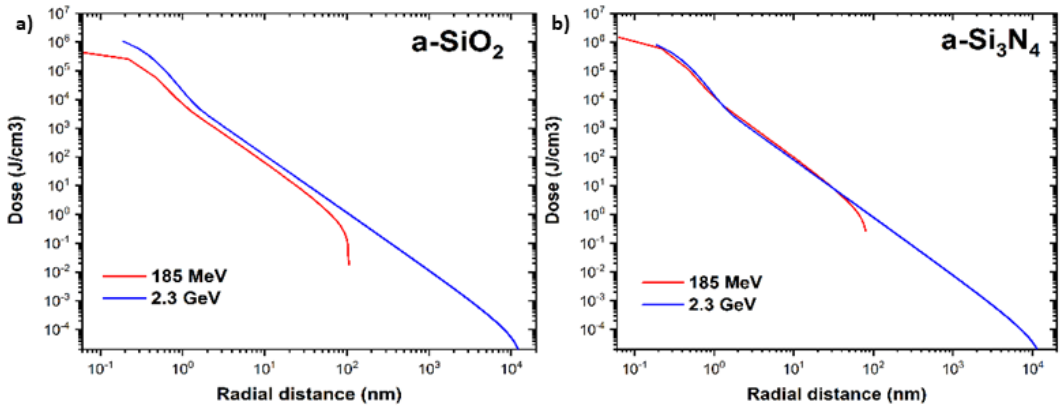

Figure 2.4: *Radial dose distribution of Au ions in a-SiO_2 (a) and a-Si_3N_4 (b).*

A=8·$\beta^{1/3}$ for $\beta < 0.03$, otherwise A=19·$\beta^{1/3}$. For $r < 0.1$ nm, the expression reduces to unity.

The radial dose distribution is given in units of the ionization radiation dose (Gy), and can be transformed into energy density by multiplying it with the target density (1 Gy has units of joules per kg), which is more appropriate for the thermal spike calculations. Figures 2.4 (a) and (b) shows the calculated radial dose distributions for 185 MeV and 2.3 GeV Au ions in PECVD a-$SiO_{1.9}$ and a-$SiN_{1.06}$ in units of energy per volume [$J \cdot cm^{-3}$]. For 2.3 GeV, which is above the Bragg peak, the maximum range of delta electrons is larger than for 185 MeV (below the Bragg peak Fig. 2.4), and the electronic stopping power rate is higher than its lower energy counterpart, resulting in the energy density being distributed in a larger volume. The latter leads to a decrease in the energy density around the ion path, which can influence the resulting ion track dimensions, also referred to as the velocity effect [108].

As mentioned before, in the i-TS model the material is considered to be isotropic (without preferential orientations for thermal conductivity or electron mobility). For this reason, the coupled equations 2.24 are solved assuming a cylindrical region 0 ≤ r ≤ R_M; 0 ≤ θ ≤ 2π; 0 ≤ z ≤ Z_M, considering the ion passage through the center of the disk (r = 0). R_M corresponds to the maximum radius of the simulated cell and is

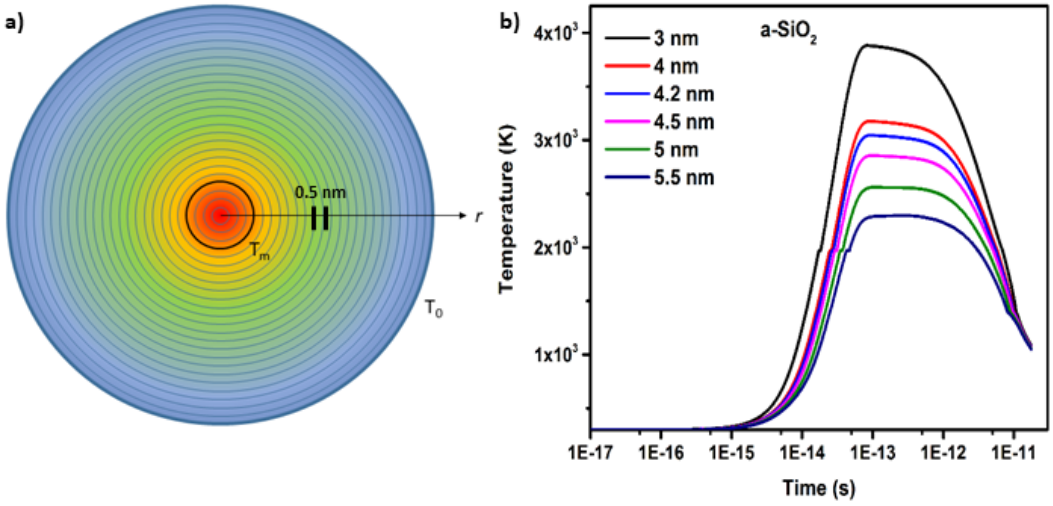

Figure 2.5: *Discretization of the cylindrical cell around the ion track (a). Due to the symmetry present, the height of the cylindrical cell remains irrelevant for the calculation because the stopping power is constant along the sample thickness and energy is diffused radially only. Spatiotemporal evolution of the radial temperature for selected radial distances for a-SiO_2 (b).*

set such that $R_T << R_M$, where R_T is the track radius. To minimize boundary effects such as over-cooling we set $R_M = 50$ nm. Due to the symmetry in angle and along the ion path the heat is exchanged only in the radial direction and no special conditions are required for the angular and height variables, thus we set their values to 2π and 1 nm, respectively for simplicity.

The numerical calculation of the spatiotemporal thermal distribution was carried out by discretization of the radial distance of the cylindrical region, where it is defined a single temperature at each concentrically ring defined, as exemplified in Figure 2.5 (a). In Figure 2.5 (b) the corresponding evolution with time is plotted for a selected radial distances for a-SiO_2. The determination of the temperature for each concentrical ring was carried out by solving the coupled heat equations by the finite difference method [121, 122]. The continuous coupled partial differential equations are then expressed by discrete steps, and solved in terms of the energy deposition per time-step with regards to the system at the previous time-step. Thus, the partial differential equations can be approximated as follow:

$$\frac{\partial f(t)}{\partial r} \approx \frac{f_{i-1}(t_j) - f_i(t_j)}{\Delta t}. \tag{2.26}$$

The terms on the numerator on the right-hand side correspond to the function defined on the i-th ring of the discrete cell at the time-step t_j. Δr corresponds to the width of the uniformly spaced cylindrical cell, such that:

$$r_i = (i + 1/2)\,\Delta r, for i = 0, 1, 2, \cdots, N. \tag{2.27}$$

In the cylindrical grid, the radial step was set to 0.1 nm. Similarly, the time dependency is defined as:

$$t_{n+1} = t_0 + (n + 1)\Delta t = t_n + \Delta t, for\, n \geq 0. \tag{2.28}$$

The selection of the time-step is based on the stability condition of the solution to the discrete version of the Fourier heat equations [122], establishing an upper boundary for the time-step Δt:

$$\Delta t \leq \frac{(\Delta r)^2}{2K^2}, \tag{2.29}$$

where K corresponds to the thermal conductivity of the lattice. The term on the right-hand side is of the order of $\sim 10^{-16}$ s. Thus, by defining the time-step as $\Delta t \sim 10^{-18}$ s, the stability of the calculations is warranted for all systems considered.

The boundary conditions are set as:

$$T|_{r=0, r=R_M} = T_0 = 300K. \tag{2.30}$$

We require the condition $\frac{\Delta r}{R_M} << 1$ to minimize thermalization effects or the boundary to act as an energy sink.

The system is initialized at $t_0 = 1 \times 10^{-17}$ s, with $T_{e,l}(r_i, t_0) = T_0 = T_{room} = 300$ K for $\forall i$. The transformation from differential to finite difference equations involve the integration of the right and left parts within each ith-cell and time interval: $[t_n, t_{n+1}]$.

$$\frac{1}{\Delta t \cdot V_i} \quad \int_{t_n}^{t_{n+1}} \int_{r_{i-1/2}}^{r_{i+1/2}} \left[C(T)\frac{\partial T}{\partial t}\right] 2\pi \cdot z \cdot r dr dt = C_i^n \cdot \frac{T_i^{n+1} - T_i^n}{\Delta t}$$

$$\frac{1}{\Delta t \cdot V_i} \quad \int_{t_n}^{t_{n+1}} \int_{r_{i-1/2}}^{r_{i+1/2}} \left[A(r,t) - g(T_e - T_l)\right] 2\pi \cdot z \cdot r dr dt = A_i^n - g_i^n (T_{e,i}^n - T_{l,i}^n)$$

$$\frac{1}{\Delta t \cdot V_i} \int_{t_n}^{t_{n+1}} \int_{r_{i-1/2}}^{r_{i+1/2}} \frac{1}{r}\frac{\partial}{\partial r}\left[rK(T)\frac{\partial T}{\partial r}\right] 2\pi \cdot z \cdot r dr dt = \frac{1}{\Delta r}\left[r_{i+1/2}K_{i+1/2}(T_{i+1}^n - T_i^n) - r_{i-1/2}K_{i-1/2}(T_i^n - T_{i-1}^n)\right]$$

The same transformation can be applied to the electronic subsystems by taking into consideration the appropriate sign of the electron-phonon coupling strength and by excluding the energy deposition function. The superscript n represents time integrals while the subscript i corresponds to space integrals evaluated at the center of the cell.

The boundary conditions require that the heat flow normal to the surface is the same on both sides of the interface on each cell:

$$(K\nabla T, \mathbf{n})\,|_{r^+} = (K\nabla T, \mathbf{n})\,|_{r^-}$$

The adopted equilibrium thermodynamic parameters for the i-TS calculations are

based on the approach used by Dufour *et al.* [2]. The electronic subsystems of a-$SiN_{1.06}$ and a-$SiO_{1.9}$, behave as a free electron gas above their bandgap temperature due to their insulating nature. Under the assumption that below the bandgap temperature, the number of hot electrons is proportional to the electronic temperature, the specific heat of the electronic system can be expressed by:

$$C_e(T_e) = \begin{cases} \left(\frac{\pi^2 k_B n_e}{2}\right) & T_e \leq \frac{3}{\pi^2} \\ \frac{3k_B n_e}{2} & T_e > \frac{3}{\pi^2} \end{cases}, \tag{2.31}$$

where k_B is the Boltzmann constant and n_e the electron density, T_g is the corresponding bandgap temperature for the respective bandgap energy, $E_g = k_B T_g$. The values used to determine the bandgap temperature were obtained by ellipsometry techniques and amount to $E_{g-SiN_x} = 4.5$ eV, and $E_{g-SiO_x} = 9$ eV. For the electronic thermal conductivity, the relationship $K_e(T_e) = C_e(T_e)D_e(T_e)$ is used, where the last term is the electronic diffusivity, which can be expressed as:

$$D_e(T_e) = \begin{cases} 300 \cdot \left(\frac{D_{300}}{T_e}\right) & T_e \leq T_g \\ D_{min} & T_e > T_g \end{cases}, \tag{2.32}$$

with $D_{300} = 150$ cm^{2}s^{-1} and $D_{min} = 1$ cm^{2}s^{-1}.

In the case of Au, we apply the free-electron gas model to model the electronic thermal conductivity and heat capacity, which have the same form as in the case of insulators with the difference of being determined in terms of the Fermi temperature (T_F) rather than the bandgap temperature.

For metals, the electron-phonon coupling exhibits a dependence on the electronic temperature, a behaviour expected in insulating materials too. However, in the approximation of the i-TS model, we consider it to be temperature independent. For Au and a-SiO_2, values for the electron-phonon coupling have been reported: $g_{Au} = 0.91 \times 10^{-11}$ W·cm^{-3} K^{-1} [108] and $g_{a-SiO_2} = 3.2 \times 10^{-13}$ W·cm^{-3} K^{-1} [53]. In the

case of a-$SiN_{1.06}$, the relation between the electron mean-free path λ and electronic thermal conductivity with the electron-phonon coupling has been adopted:

$$g = \frac{D_e C_e}{\lambda^2}. \tag{2.33}$$

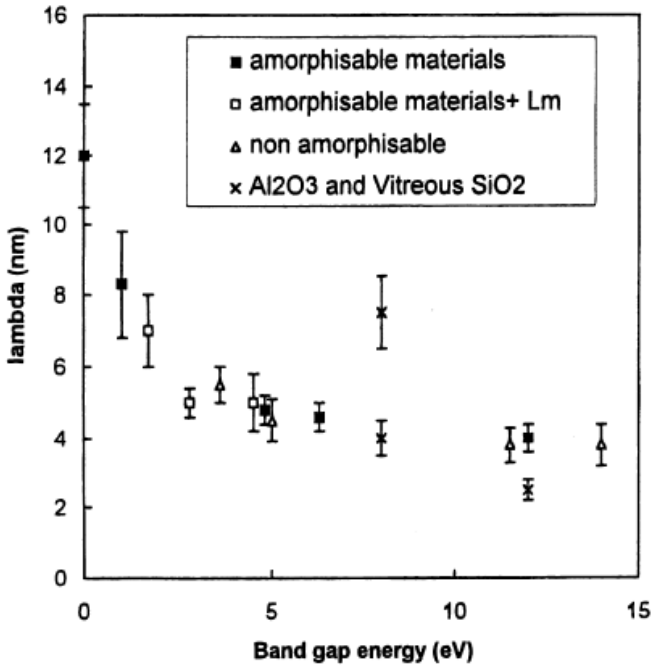

Figure 2.6: *Electron-lattice interaction mean-free path λ versus bandgap for amorphizable and non-amorphizable materials [1].*

In the past the electron mean-free path has been treated as a free variable to adjust the strength of the electron-phonon coupling and match the melting region with the experimentally determined ion track dimensions. For a-Si_3N_4, the value $\lambda =$ 3 nm has been proposed [58]. This value contrasts with the expected approximated value of 4.3 nm, based on a bandgap of 4.5 eV, which can be determined using the empirical correlation between the electron-mean-free path and the optical bandgap. The empirical correlation, plotted in Figure 2.6, was proposed by Toulemonde *et al.* [1] and considers λ as an adjustable parameter that affects the value of the

electron-phonon coupling as expressed by equation 2.33. They used the experimental values obtained for ion tracks formed in insulating crystalline, amorphisable and non-amorphisable materials, were used to determine the corresponding value of λ and thus, the electron-phonon coupling. This was done by varying the value of the electron-phonon coupling to match the radius of the molten region to the experimental ion track radius. As a result, a clear correlation between the optical bandgap and λ for a broad selection of materials was found. For this thesis, i-TS calculations for a-$SiN_{1.06}$ with the two values of λ were carried out. Figure 2.5 (b) shows the spatiotemporal temperature profile for selected radial distances considering the value of $\lambda = 4.3$ nm, in good agreement with the radius determined by experimental means. When considering $\lambda = 3$ nm, the resulting molten area correspond to a radius significantly larger ($r \sim 5$ nm), supporting the adoption of the value determined by the empirical correlation between the experimentally determined optical bandgap and λ.

2.3.1 The three-dimensional version of the i-TS model

For the description of the ion-shaping process of Au NPs located at the interface of a-Si_3N_4 and a-SiO_2 the three-dimensional version of the i-TS model was employed. Its superior capacity to qualitatively explain such process has been demonstrated over the two-dimensional version [2, 117, 123].

Here, we consider a two-component system within a three-dimensional cell in Cartesian coordinates. The incident ion energy deposition $A(\vec{r}, t)$ exhibits the same form and normalization procedure as for the two-dimensional version yet, the radial dose distribution $D(\vec{r})$ (Equation 2.25) is modified to account for the two components present at the metal/dielectric boundary.

To do so, the electronic density $\nu(x, y, z) = \rho Z/A$ considered for each cell slice (Figure 2.7), where a metal/dielectric boundary is present, is averaged as:

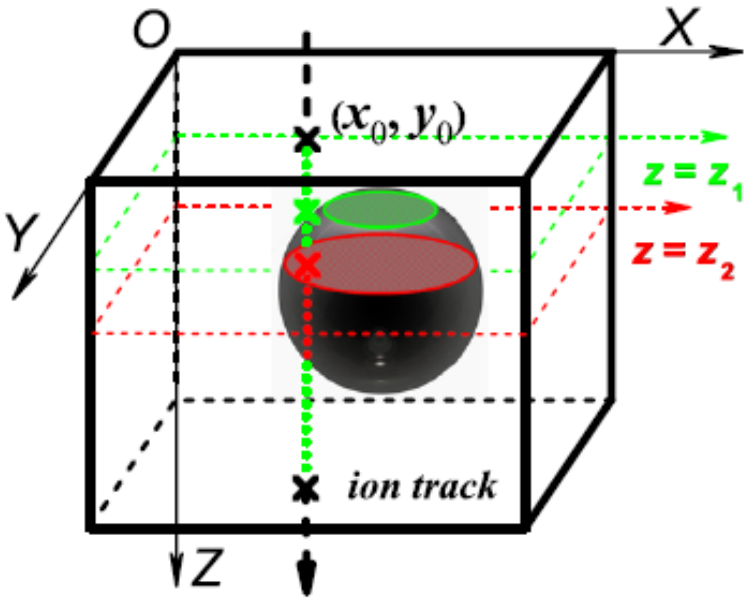

Figure 2.7: *Geometry of the calculation cell for the 3D-iTS model [2].*

$$\bar{\nu} = \int_0^1 \nu[\xi(\upsilon), \eta(\upsilon), z] d\upsilon,$$

where the spatial dependence of the electron density is calculated as $\xi(\upsilon) = x_0 + (x - x_0)\upsilon$ and $\eta(\upsilon) = y_0 + (y - y_0)\upsilon$. x_0 and y_0 correspond to the (x, y) coordinates of the incident ion, as shown in Figure 2.7.

The δ-electron range r in equation 2.25 is replaced by an effective range $r(x, y, z) = \vec{\nu}\sqrt{(x - x_0)^2 + (y - y_0)^2}$ weighted by the mean electron density, defined in units of $[g \cdot cm^{-2}]$ [2].

The lattice thermophysical parameters are calculated in the same fashion as for the two-dimensional version. For simplicity, the case of an energetic ion passing through the center of the cubic cell was the only case studied. The amorphous condition of the system allows the simplification of the thermal diffusion process whereas instead of looking into the nine components of the thermal conductivity tensor, we can use its diagonal expression with only one central value, *i.e.* considering an isotropic medium.

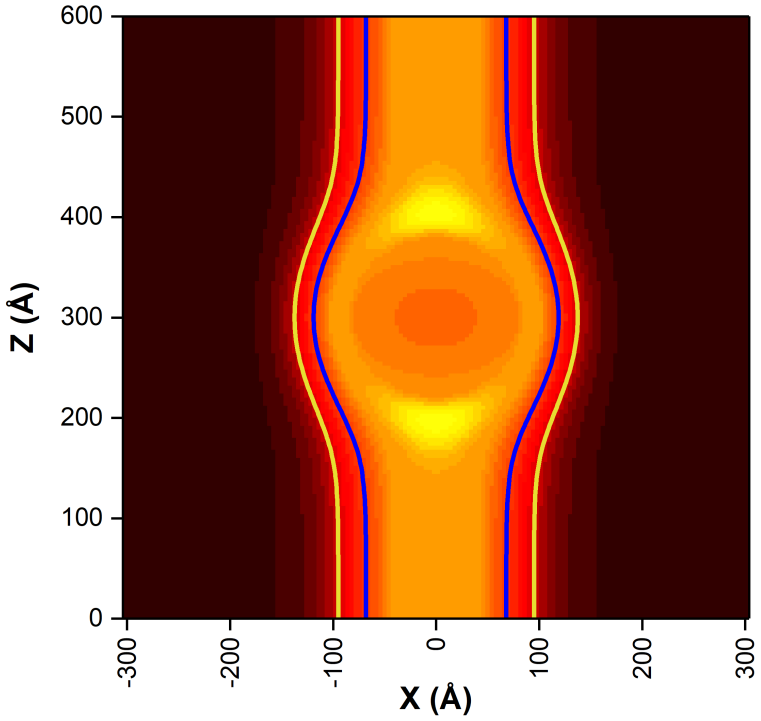

Figure 2.8: *Snapshot at t = 1 ps of the X-Z cut of the tree-dimensional i-TS model of one Au NP embedded in a-Si_3N_4 after irradiation with one 185 MeV Au ion. The continuous lines corresponds to the melting point of a-Si_3N_4 (blue) and Au (yellow), respectively.*

$$\vec{K}_{e,l} = \begin{pmatrix} K_{xx} & K_{xy} & K_{xz} \\ K_{yx} & K_{yy} & K_{yz} \\ K_{zx} & K_{zy} & K_{zz} \end{pmatrix} = \begin{pmatrix} K & 0 & 0 \\ 0 & K & 0 \\ 0 & 0 & K \end{pmatrix} \tag{2.34}$$

Instead of solving the coupled heat equations in a disk as in the two-dimensional version, in the three-dimensional case the equations are solved using Cartesian coordinates in a cell defined by: $\{0 \leq \mathrm{x} \leq \mathrm{x}_M; 0 \leq \mathrm{y} \leq \mathrm{y}_M; 0 \leq \mathrm{z} \leq \mathrm{z}_M\}$, choosing the ion's passage parallel to the z-axis through the centre $\{\mathrm{x}_0 = \mathrm{x}_M/2; \mathrm{y}_0 = \mathrm{y}_M/2\}$ of the cell. Figure 2.8 shows a snapshot of a cut along the xz-plane of the three-dimensional calculations of the temperature profile for one Au NP of 20 nm in diameter embedded in a-Si_3N_4. The equilibrium thermodynamic parameters are the same as for the

two-dimensional version.

2.3.2 Molecular dynamics simulations

Commonly, the formation of ion tracks resulting from the passage of an energetic ion in solid materials has been explained in terms of the i-TS model, where the ion track width has been associated to the dimensions of the simulated molten region. Numerical calculations based on the i-TS model provide with a crude approximation of the time-evolution of the thermal environment due to the passage of the energetic ion, however, it does not provide any information regarding the remaining structural modification. On the other hand, molecular dynamics (MD) simulations are capable of integrating the energy deposition based on the i-TS model to simulate the atomic motion during the ion track formation and ion-shaping processes but require high computational resources and large simulation cells due to the spatial extend of the thermal spike.

As already mentioned, MD simulations calculate the time evolution of the atomic motion resulting from the thermal spike. It was first proposed in the late 50's to simulate the elastic collisions in a many particle system mediated by a hard-sphere interatomic potential, where the number of particles is limited mainly by computational power [124, 125]. It follows the evolution of the many particle system by calculation of the net force acting on each particle due to the influence of its neighbours, given by the initial conditions (position and velocities). The calculated net force allows to determine the trajectory of each atom considering the motion under a constant force in a short time-interval. At the end of the time-step, a new force is calculated for the following time-interval, resulting in an iterative process to determine the motion of atoms in the system. The accuracy of the calculations are determined by the selection of realistic interaction potentials and appropriate time-intervals [125]. These need to ensure energy conservation as well as efficient use of computer time. In the case of swift heavy-ion irradiation, the selection of the time step is an adaptive process limited by a maximum allowed atomic travelled distance, set commonly at 0.1 $\mathring{A}$ [126].

A realistic interatomic potential is crucial for the calculations, where it should be able to correctly describe the ground state of the atom, the cohesive energy, crystal structure, describe all relevant phases, melting, and defect energetics. In the case of compounds, segregation can occur thus it is necessary to model each element separately. The forces acting on each particle can be determined after the selection of an appropriate interatomic potential, where the choice is dominated by 3-body potentials of the Tersoff-like class [127], which explicitly include an angular contribution to the force. For Tersoff-like potentials, the parameters defining the interatomic potentials are typically determined by comparison to different experimental or density-functional theory values of the ground state and different phases present, which is not a trivial task.

The two-temperature molecular dynamics model (2T-MD) was used to analyse ion tracks produced in a-Si_3N_4 and a-SiO_2 after ion irradiation with 185 MeV Au ions [95, 128]. The simulations were carried out at the Materials Science simulations groups of Prof. Kai Nordlund and Prof. Flyura Djurabekova at the University of Helsinki, Finland. The atomic motion is solved by combining the spatiotemporal evolution of the electronic temperature given by the i-TS continuum model (equation 2.24) and MD in the following way: [128]

$$m_i \frac{\partial v_i}{\partial t} = F_i(t) + \xi m_i v_i, \tag{2.35}$$

where the term $F_i(t)$ represents the net force acting on the i=eth atom, calculated using the MD interatomic potential, and $\xi m_i v_i$ is a driving force proportional to the energy transferred from the electronic system via the electron-phonon coupling. The magnitude ξ is defined such that energy conservation is guaranteed.

In this thesis, calculations were carried out up to 100 ps. The electron energy distribution was calculated based on the Waligorski formula for electrons emitted

perpendicularly to the ion trajectory (equation 2.25). To calculate the electronic parameters it was initially proposed to use density functional theory (DFT) [128] however, in the current case we adopted the free electron gas approximation instead, as in Dufour *et al.* [2]. As it is shown in section 5.3.2, this approach has produced good agreement with experimental observations. For a-SiO_2 we considered the electron-phonon coupling to be $g = 1.25 \times 10^{13}$ W·cm^{-3}K^{-1} [117], while for a-Si_3N_4 it was estimated from the expression $g = k_e/\lambda^2$ for the $\lambda = 4.3$ nm (estimated from the bandgap according to Toulemonde *et al.* [1])and $\lambda = 3$ nm (the same value as a-SiO_2). For the lattice physical properties of a-Si_3N_4, we used the lattice thermal conductivity $K_l = 6$ E·m^{-1}K^{-1} [129–131] and the heat capacity from Ben-Hai *et al.* [132]; for a-SiO_2 the parameters are the same as in Dufour *et al.* [2]. The de Mota MD potential [133] was applied for our simulations for a-Si_3N_4, and the many-body Watanabe-Samela potential for a-SiO_2 [134, 135]. The Munetoh potential was also used to confirm the absence of artefacts due to the potential selected and showed agreement with the other potentials [136]. Nonetheless, it is well-known that all three potentials fail to reproduce the melting point of the studied materials sufficiently close to the experiment [137]. To overcome this problem, the deposited energy was scaled by a factor obtained from the ratio of the MD melting temperature and the experimental one. We applied the Berendsen boundary temperature control [138] and the dimensions of the cells employed were 263 $\mathring{A}\times$ 258 $\mathring{A}\times$38 $\mathring{A}$ for a-Si_3N_4 and 241 $\mathring{A}\times$ 227 $\mathring{A}\times$ 46 $\mathring{A}$ for a-SiO_2. To account for statistical uncertainties, the presented simulations were averaged over 5 simulation runs for each material.

2.4 Ion beam synthesis

Ion implantation is a non-equilibrium process used to introduce foreign atoms into a host material above their solubility limit. It is a process dominated by nuclear interactions leading not just to the addition of the implanted species but also the production of radiation damage, which can act as nucleation seeds, or even amorphisation in the case of crystalline materials. The process from the introduction of foreign

species to the formation of metallic NPs in dielectric materials can be described by thermodynamic and kinetic processes, defined in the classical nucleation and growth theory [139, 140].

During the ion implantation process, the solute concentration increases in the implanted region as a function of time, from under- to super-saturated. The change in concentration plays an important role in the nucleation and growth process (Figure 2.9) and can be described by the supersaturation parameter $S(t)$, defined as: [62]

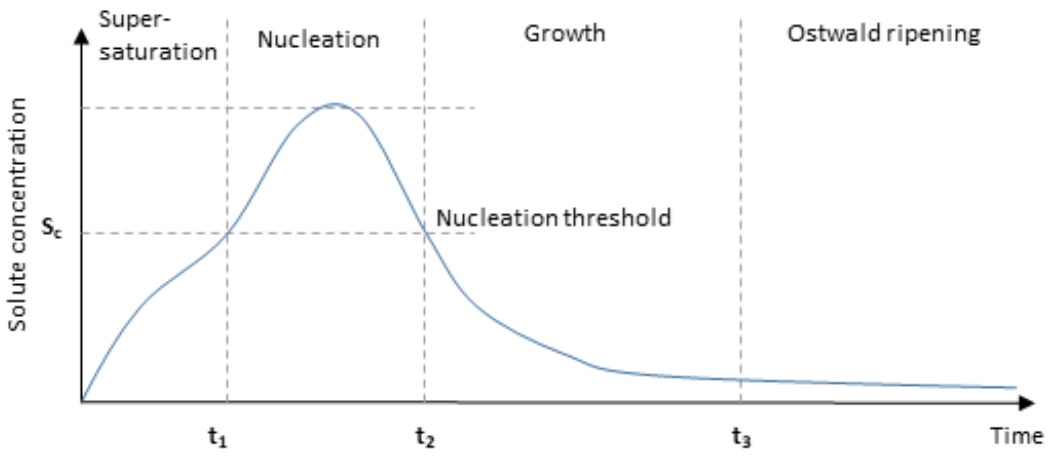

Figure 2.9: *Time-evolution of the supersaturation parameter $S(t)$ and the different stages involved in the NP synthesis [3].*

$$S(t) = \frac{C(t)}{C_\infty} \tag{2.36}$$

where $C(t)$ is the concentration of the solute[4] at a given time and C_∞ represents the bulk solubility (5.9×10^{28} atoms·cm^{-3} for Au in a-SiO_2) [61].

After a certain period of time during the ion implantation, the solute concentration $C(t)$ will reach and exceed the bulk solubility limit, resulting in $S(t)$ surpassing unity,

[4]proportional to the ion fluence

defining a supersaturated mixture. Supersaturated mixtures constitute a metastable state that can be described in terms of the Gibbs free energy by pressure, temperature and solute concentration. Due to their metastable state, their evolution should minimize Gibbs free energy. This occurs through the nucleation of small NPs, which evolve in size via growth and Ostwald ripening. Therefore, the synthesis of metallic NPs by ion implantation is considered a process under mass conservation conditions and governed by the Gibbs-Thomson principle [139, 140].

The stability of the newly formed NPs is directly linked then to their corresponding dimensions as their Gibbs free energy is given by two competing contributions: a negative term related to the formation of the new phase commonly regarded as a volumetric force, and a positive term arising from the surface energy of the NP. A critical radius for the NPs is related to the point where both contributions to the energy terms are equal. This means that NPs with a radius smaller than the critical radius R^* will disappear while NPs with radius greater or equal will increase in size. The energy ΔG^* related to the critical radius scales with temperature as well as the supersaturation condition and it can be approximated by [3,139,140]:

$$\Delta G^* \propto \frac{1}{T^2 \cdot ln(S(t)^2)}, \tag{2.37}$$

and the critical radius by:

$$R^* \propto \frac{1}{T \cdot ln(S(t))}. \tag{2.38}$$

The inverse proportionality with temperature and supersaturation plays an important role in the synthesis process as the number density of NPs formed during this step increases with a decreasing critical radius. Due to the dependency of ΔG^* and R^* on the supersaturation and temperature, they can be tuned by the different parameters involved during the ion implantation process such as the ion energy, fluence, implantation temperature and flux [3]. The ion energy controls not only

the deposition depth but also the straggling, which in combination with the fluence will determine the spatial distribution of the supersaturation function [141]. For sufficiently low fluences, the supersaturation condition is not met and the implanted ions can be considered as isolated, relevant for example for doping of semiconductors. Intermediate fluences (10^{14} - 10^{17} cm^{-2}) are thus commonly used for the synthesis of NPs. At higher fluences, the precipitates can coalesce, leading in certain cases to the formation of a continuous layer at the projected range. For single ion implantation, due to the inherent Gaussian depth distribution, the concentration varies with depth during the synthesis process, generally leading to a broad size distribution of NPs.

Ion implantation is a process where the monomer supply is fixed and proportional to the fluence, thus it is considered a closed system where $S(t)$ reaches its maximum value at the end of the ion implantation process [3]. This is commonly followed by a post-thermal annealing process. At the beginning of the annealing process, nucleation takes place[5]. During this step, the newly formed NPs behave as sinks to the solute, leading to a local decrease of $S(t)$. This results in an increase of ΔG^* and R^*, reducing the rate of NP formation until $S(t)$ decreases back to unity.

When $S(t)$ reaches unity the formation of new NPs stops, however, there is still a large amount of remaining monomers in the medium, which can attach to the existing NPs so they can continue growing. This stage is characterized by a constant NP number. The growth process reduces $S(t)$ to much smaller than unity, and leads to a consequent significant increase of R^*. As a result, NPs with a radius smaller than R^* become unstable, dissolve and are eventually absorbed by larger NPs. This stage is known as Ostwald ripening, originally described by Lifshitz, Slyozov and Wagner (LSW theory) [114, 142]. As mentioned before, the system evolves towards its state of minimal Gibbs free energy. This is achieved by increasing the size of the NPs. As monomer supply has ceased, this can only occur at the expense of NPs with radii smaller than R^*. Hence, conservation of the number of NPs is no longer valid and

[5]nucleation can also take place during the ion implantation process near the upper limit of the intermediate fluence range

decreases with time [62].

In particular, the growth and ripening process in a solid matrix are limited by the atomic diffusion of the solute [62, 143], *i.e.* the diffusion of Au in a-Si_3N_4 or a-SiO_2, which is temperature dependent [143]. Such dependencies have been studied for Au implantation in a-SiO_2 at different temperatures and in an oxidizing atmosphere by Miotello *et al.* [144]. In their work, they showed the formation of a buried layer of NPs with diameters larger than 10 nm after annealing for seven hours at 900 C, with sizes increasing with further annealing. It is worth to mention that the selection of annealing atmosphere can have significant influence on the growth process. For example, in the case of Au implanted in a-SiO_2 faster growth and ripening rate has been observed in oxidizing ambients [64]. The latter was ascribed to an enhanced Au diffusion due to the excess of oxygen.

Studies of ion beam synthesis in a-Si_3N_4 are rather scarce. Only few works have been published, with a focus on the synthesis of semiconductor NPs [63,64]. In the case of Au, the synthesis and growth of NPs has only been reported by electron irradiation of Au implanted samples [145]. In the present thesis, it is not the scope to directly compare the growth and ripening process of Au NPs between a-Si_3N_4 and a-SiO_2. Instead, the focus is to survey the potential application of ion beam synthesis of Au NPs in a-Si_3N_4 for the study of the ion-shaping process, where the initial dimensions of the NPs play a key role in the final geometry, as it will be explained in the next section.

2.5 Ion shaping of metallic nanoparticles

Metals are characterised by exhibiting a low energy transfer efficiency, an electron-phonon coupling typically three orders of magnitude lower than the dielectric case, accompanied by a high electron diffusion thus, the formation of a thermal spike may not reach temperatures as hot as in the dielectric case [67].

When the two are combined, *i.e.* the irradiation with a highly energetic ion of a metallic NP embedded in an amorphous matrix, the passage of the energetic ion creates an ion track around the NP, along or near its axis [123]. Inside the NP, the energetic electronic cloud diffuses radially outwards from the ion trajectory reaching the dielectric boundary. At the interface, due to the stronger electron-phonon coupling of the surrounding dielectric matrix, the temperature increases at the metal/dielectric boundary leading to an outer-boundary heating scenario followed by a partial or total melt of the NP [2, 52]. If the energy deposited by the ion surpasses a material-dependent threshold, the metallic NP is expected to experience a change in its original geometry. In particular, the dimensions of the NPs parallel to the ion beam increase while the perpendicular dimensions shrink, a phenomenon known as 'ion shaping'.

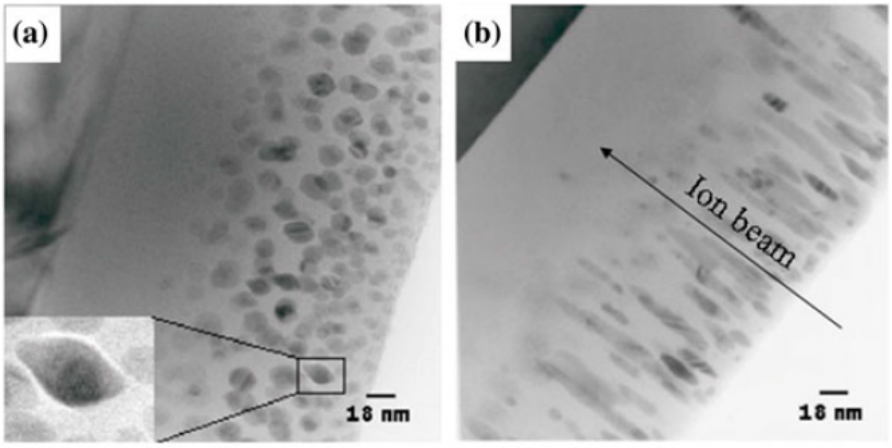

Figure 2.10: *Ion-shaping of Co NPs embedded in a-SiO_2 after irradiation with 200 MeV I ions at 10^{13} cm^{-2} (a), where NPs with a lemon shape were observed, and 10^{14} cm^{-2} (b) [4].*

The first study on ion-shaping was carried out for ion beam synthesized Co NPs in a-SiO_2, where the shape transformation was induced by irradiation with 200 MeV I ions at different fluences [4]. In this first work, TEM images of embedded NPs showed an increase in the mean size after irradiation with 10^{12} cm^{-2}, while remaining spherical in shape. Increasing the fluence to 10^{13} ions·cm^{-2}, the NPs exhibited

an anisotropic shape described as a lemon-like shape (Figure 2.10 (a)), while the formation of anisotropic NPs with high aspect-ratios was observed after irradiation with 10^{14} ions·cm^{-2} (Figure 2.10 (b)). In their interpretation, the relevance of the initial size of the NPs was outlined and three regions were proposed to understand the process. For small NPs ($r \leq 6$ - 8 nm), the typical range of energy deposited by a swift heavy-ion would suffice to induce not only the melting but the vaporization of the NP resulting in its dissolution. When the dimension of the NP is large enough ($r \geq 18$ - 20 nm), the deposited energy is not sufficient to induce melting of the NP thus, no shape transformation is expected. Nonetheless, when NP dimensions lay within the two, the deposited energy is sufficient for the NP to melt without reaching boiling. As a result, Co NPs were found to elongate in the beam direction. The observations were explained using the i-TS model, where the estimated temperature within the ion track surpassed the melting temperature of the NP. Thus, the ion shaping process was proposed to be due to the difference in temperature, combined with differences in thermal expansion and compressibility that should induce a creep deformation of the NP and corresponding freeze-in of the anisotropic NP.

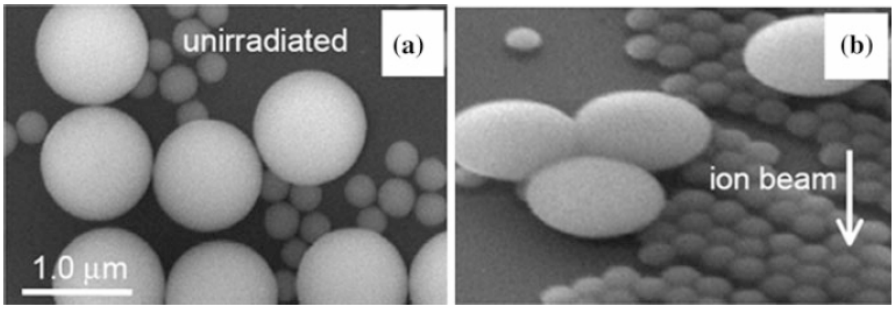

Figure 2.11: *Colloidal SiO_2 NPs prior to (a) and after irradiation with 4 MeV Xe ions (b) [5].*

The requirement for the NP to melt in order to modify its morphology was supported by successive experimental work; nevertheless, the distinctive controlled orientation exhibited by the NPs suggested a metal flow process due to the in-plane stress generated between the molten NP and the 'solid' dielectric boundary [146].

It is important to mention that such first work followed the ion-induced shape transformation of colloidal SiO_2 spherical NPs [5]. In their work, the a-SiO_2 NPs elongated in the direction perpendicular to the ion beam, in contrast to the Co NPs embedded in a-SiO_2 (Figure 2.11). This difference suggested that in the ion-shaping process, the matrix plays a relevant role and it should be connected to an effect known as ion hammering [146]. This process is characterised by an increase of the dimensions perpendicular to the ion beam for irradiated materials, while the dimensions parallel to the ion beam shrink [67]. However, it was soon demonstrated that the in-plane stress is not sufficient to induce the deformation of Co NPs, supporting the idea of NP melting and flow into the ion track [67]. In addition, further experiments showed the existence of a threshold electronic energy-loss for deformation [147], which is not required for ion hammering [148].

To better understand the ion-shaping process, experiments were carried out to systematically study the dependence on NP size by Dawi *et al.* [68, 149, 150], following on the observations of Awazu *et al.* [117] and Oliver *et al.* [66]. In particular, Awazu *et al.* [117] tried to explain the deformation of Au NPs embedded in a-SiO_2 using i-TS calculations of the NP and matrix system. However, according to their calculations, Au NPs of 10 nm should not reach melting because of the low electron-phonon coupling resulting in an inefficient energy transfer. To explain the contradictory results, the tree-dimensional inelastic thermal spike (3D-iTS) model was developed by Dufour *et al.* [2]. They demonstrated that the energy deposited into the electronic system of the NP was able to diffuse to the metal/dielectric boundary, where the significantly higher electron-phonon coupling strength in a-SiO_2 results in a heating process from the boundary towards the centre. The results from Dawi *et al.* were interpreted using the 3D-iTS model and rationalized by Rizza and collaborators [123]. From the 3D-iTS calculations the molten volume for NPs of different sizes was estimated and compared to the experimental observations. As seen in Figure 2.12, the three regions originally proposed by D'Orleans *et al.* [4] can be extended to four, adding the case of NPs that partially melt, which results in a facetted-like geometry. These investigations demonstrated that the dimension of the NPs play one of the central roles in the shape

transformation process.

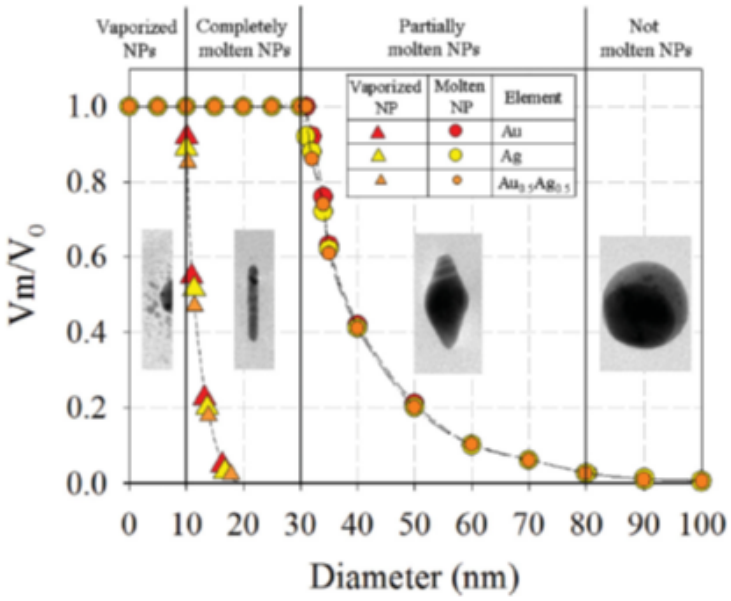

Figure 2.12: *Diagram showing the shape modification of Au NPs in terms of the original dimensions and the relative molten volume as determined by 3D-iTS calculations [2].*

The ion-induced shape transformation process of MNPs has been studied predominantly with a-SiO_2 as the host matrix for various metallic NP species such as Au [117, 123, 146, 150–152], Ag [66, 153], Co [4], Ni [154, 155], Zn [156–158], V [159], alloy NPs [160, 161], and Ge [162]; however, Au remains one of the preferred material because of its chemical inertness in a-SiO_2 [61].

While the 3D-iTS model helped to explain the heating scenario of Au NPs, the underlying process for the shape modification remained unclear. In particular, following reports from Amekura *et al.* [52, 100, 156–158] who showed by optical dichroism that Zn NPs become anisotropic at fluences lower than those where ion hammering has been reported in a-SiO_2. Furthermore, Kluth *et al.* [152] and Ridgway *et al.*] [155] showed the existence of a saturation width for the elongation process comparable to the ion track dimensions, as well as the necessity of a molten track.

Based on the good agreement of MD simulations with the experiments to describe the ion track formation process, Leino *et al.* [51] simulated the shape transformation of 10 nm Au NPs embedded in a-SiO_2 after the passage of up to 12 ions. Among the most relevant findings, it was suggested that the elongation process takes place by diffusion of the Au NP into the under-dense core region of the ion track surrounding the NP. It was also found that the process occurs within the first 20 ps after the passage of the ion in the time where the ion track and the NP are molten, and NP recrystallization plays an important role in the elongation process.

The interpretation of the MD simulation results has still left a number of questions open regarding the relevance of the parameters involved in the ion-shaping process: the relationship of NP/ion track dimensions [123, 155], the formation of an ion track exhibiting an under-dense core region [51, 100], and the time/temperature evolution of the molten ion track/NP system. An example contributing to this discussion is the recent results that have shown that the formation of a vapour phase inside the ion track in silica is not necessary for the ion-shaping process to take place [100]. This was initially proposed as a pre-requisite for the observation of an under-dense core in a-SiO_2 [59].

Chapter 3

Experimental methods

The following chapter introduces the main experimental methods used for synthesis, characterization and modification of a-Si_3N_4, a-SiO_2 and a-SiO_xN_y layers using ion beams. The thin layers were predominantly deposited on c-Si (100) wafers by PECVD. Additionally, nearly stoichiometric silicon nitride, deposited by LPCVD, and thermally grown a-SiO_2 (silica) were used. Physical properties such as thickness, refractive index and optical band gap were determined by optical ellipsometry. The layer deposition and optical characterization were carried out at the Australian National Fabrication Facility (ANFF). The chemical composition and depth profile of ion implanted species were determined by Rutherford backscattering spectroscopy (RBS) where, in combination with the thickness determined by optical means, the density of the material can be determined. Complementary elastic recoil detection analysis (ERDA) was used to provide a good estimation of the H content and depth profile. FTIR spectroscopy was employed to characterize the bond density and configuration before and after SHI irradiation to characterize the structural evolution as a function of ion fluence.

The majority of the SHI irradiation was carried out at the Heavy Ion Accelerator Facility at the Australian National University while for higher irradiation energies, the UNILAC facility was used at GSI in Darmstadt, Germany. The comparison between irradiation energies was of particular interest to study the 'velocity effect' in amorphous a-Si_3N_4 and a-SiO_2. To form metallic NPs, two methods were employed: (i) Au ion implantation was carried out at the ion accelerator facility at the Electronic Materials Engineering department followed by a post-annealing process under varying conditions; (ii) thermal evaporation of a thin Au layer (5 nm thickness) followed by a

rapid thermal annealing (RTA) step. Transmission electron microscopy (TEM) and high angular annular dark field (HAADF) techniques were employed to characterize NP synthesis and the ion shaping process, conducted at the Centre for Advance Microscopy (CAM) at the Australian National University.

SAXS was the main technique used for the characterization of the ion track morphology, density change and ion beam synthesis. It was carried out at the SAXS/WAXS beamline at the Australian Synchrotron in Melbourne. Because SAXS was the central technique used for characterization, it is described in more detail in a separate chapter.

3.1 Plasma enhanced chemical vapour deposition

The thin layer and layered systems studied in this work were deposited on c-Si (100) by plasma enhanced chemical vapour deposition or PECVD, with exception of an almost stoichiometric silicon nitride sample deposited by low pressure CVD (LPCVD) and thermally grown silicon dioxide films used for comparison. CVD techniques are standard techniques for deposition of dielectric layers such as a-SiO_x, a-SiN_y, a-SiO_xN_y and a-Si, at a relatively low thermal budget cost. For example, growth of thermal oxides generally involves temperatures above 1000 °C, in contrast to CVD processes such as LPCVD, carried out in the range between 600 - 800 °C or PECVD, typically performed around 400 °C but capable of deposition at room temperature (20 °C). Besides the greatly reduced temperature process, their low thermal budget permits the integration into optical and electrical devices [43, 47], CVD techniques provide highly homogeneous depositions over large areas with high control of the stoichiometry of the deposited layers [163].

The main principle of CVD deposition methods involves the decomposition of a gas mixture on a sample (wafer) surface. The deposition of amorphous silicon nitride by LPCVD is largely driven by thermal decomposition and requires wafer temperatures

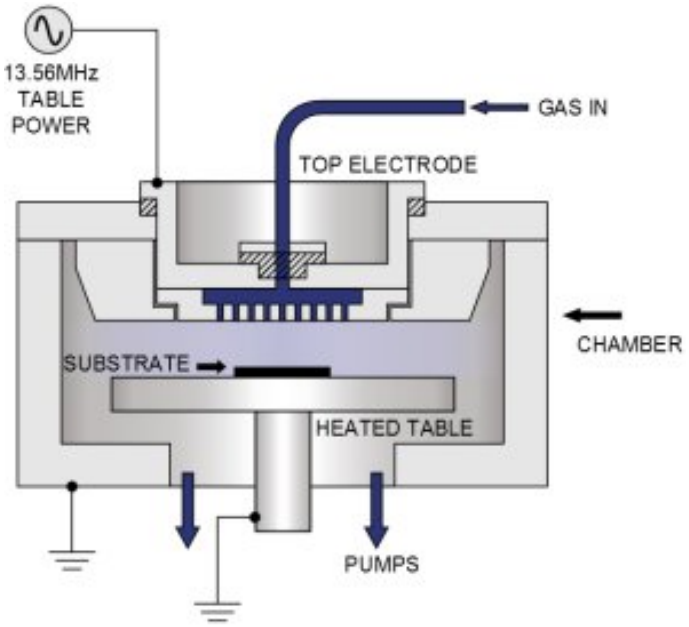

Figure 3.1: *Basic PECVD reactor configuration.*

between 600 - 800 °C. A gas mixture of dichlorosilane ($SiCl_2H_2$) and ammonia (NH_3) is used as the source of Silicon (Si) and Nitrogen (N_2), respectively. LPCVD enables the deposition of amorphous silicon nitride layers close to stoichiometric Si_3N_4.

In contrast, the deposition temperature is greatly reduced in the PECVD process by using a plasma source to lower the reaction activation energy. The PECVD deposition system available at the ANFF is a PlasmaPro 100 PECVD system from Oxford Instruments. It constitutes an RF driven top electrode and a heated grounded electrode, where the sample (wafer) is located (Figure3.1) [164]. The gas mixture is injected into the process chamber through a shower-head gas inlet in the top electrode at working pressure between 0.5 - 1 Torr.

The PECVD system allows control over the stoichiometry of the silicon oxynitride (a-SiO_xN_y) materials by varying the process conditions and gas mixture. Due to the involvement of Silane (SiH_4) and the low temperature processing, PECVD deposited layers are well-known for containing residual H. For example, the deposition

of a SiN_y layer involves complex reactions between SiH_4, NH_3 and N_2 due to the low-temperature process: [164, 165]

$$SiH_4 + 4NH_3 \xrightarrow{plasma} Si(NH_2)_4 + 4H_2 \tag{3.1}$$

$$3Si(NH_2)_4 \xrightarrow{Heat} Si_3N_4 + 8NH_3. \tag{3.2}$$

However, these reactions are commonly incomplete leading to amorphous, non-stoichiometric layers containing residual H. In the present work, the deposition of a-SiO_xN_y layers was carried out using a gas mixture of SiH_4, NH_3, N_2 and nitrous oxide (N_2O) at different ratios to control the stoichiometry at 600 °C with a RF of 60 MHz at a pressure of 650 mTorr. The deposition details can be found in Table3.1. The supply of SiH_4 was done using N_2 as an inert carrier gas. The temperature deposition was selected to keep the H content below 10 atomic percent, instead of the typical 15 - 30 % at lower deposition temperatures. The chemical reactions involved can be summarized as follows:

$$\begin{aligned} SiN_x &: SiH_x + NH_x \rightarrow SiN_x(+H_2) \\ SiO_x &: SiH_x + N_2O \rightarrow SiO_x(+N_2 + H_2) \\ SiO_xN_y &: SiH_x + N_2O + NH_3 \rightarrow SiON_x(+N_2 + H_2) \end{aligned} \tag{3.3}$$

3.2 Spectral ellipsometry

Ellipsometry measures and analyses the change in polarization of an incident, linearly polarized beam upon incidence and reflection from a flat sample. The reflected beam is elliptically polarized, thus the name ellipsometry [166–169]. The analysis of the reflected beam can be used for a very accurate determination of the physical properties of thin layers, such as thickness, refractive index, absorption coefficient, conductivity, porosity, etc.

Sample/Gas flow (sccm)	SiH_4	NH_3	N_2	N_2O	T (°C)
$SiN_{1.06}$	8	14	980	0	600
$SiO_{0.26}N_{1.0}$	8	13.5	965	15	600
$SiO_{0.45}N_{0.99}$	8	13	950	30	600
$SiO_{1.05}N_{0.48}$	8	12	910	70	600
$SiO_{1.38}N_{0.25}$	8	10.5	790	190	600
$SiO_{1.59}N_{0.15}$	8	5.6	525	455	600
$SiO_{1.9}$	8	0	270	710	600

Table 3.1: *Gas flux and processing temperature for PECVD silicon oxynitrides deposition processes. The gas flow values are given in standard cubic centimetres per minute units (sccm). The listed chemical composition of the deposited silicon oxynitride layers (a-SiO_xN_y) correspond to the values determined by RBS.*

A typical ellipsometry set-up consists of a light source (it can be monochromatic or a white light source for spectral experiments), a polarizer (defines the incident polarization state), the sample, an analyzer (to study the change in polarization state), and a detector (Figure 3.2). For the current experiments, the ellipsometry measurements were performed with a J. A. Woollam Co. M-2000 spectroscopic ellipsometer. The set-up is based on a rotating compensator ellipsometry (RCE) design for spectral range resolution between 400-1600 nm and detection at three angles: 55°, 65° and 75°.

When a linearly polarized light beam is incident at an oblique angle on the interface between two media, the reflected light beam is commonly elliptically polarized. The resulting state of polarization of the reflected light is then measured by the ellipsometer, characterized by the complex amplitude reflection ρ, commonly expressed in terms of the two angles ψ and Δ:

$$\rho = \tan\psi e^{i\Delta} \tag{3.4}$$

where ψ is the relative attenuation and Δ is the relative phaseshift of the two polarization eigenstates. The value of ψ and Δ are determined by rotating the compensator and analyzer until the light intensity reaching the detector is minimal [167].

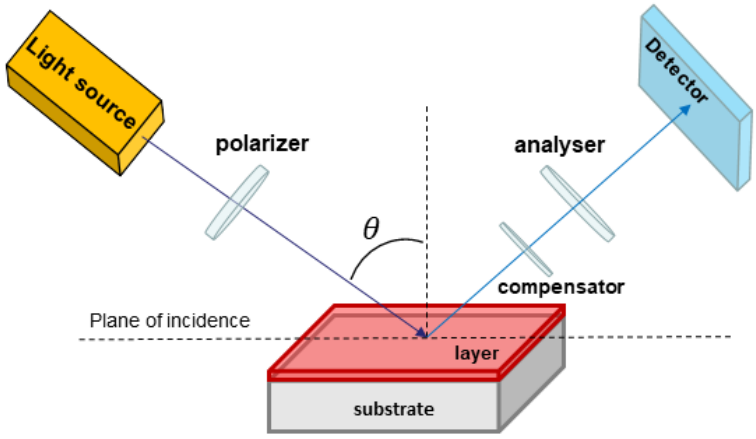

Figure 3.2: *Rotating ellipsometry set-up. The beam coming from the light source passes through the polarizer, is reflected by the sample entering a compensator and analyzer consecutively before reaching the detector.*

The ellipsometry parameters ψ and Δ do not yield direct information of the material of interest and require an appropriate model to interpret them. From such model it is possible to determine the physical properties of the material and thus, ellipsometry measurements are model dependent [167–169]. The modelling is based on Maxwell's equations considering that the incident and the reflected beam form a plane of incidence (POI). The incident linearly polarized light can be expressed as a linear combination of two polarization eigenstates: one parallel (E_p) and another perpendicular (E_s) to the plane of incidence, with the same amplitude and phase, and an angle of incidence (θ_i). After reflection, the angle of the incident beam reflected by the sample θ_r is the same as the incident angle θ_i, however, the amplitude and phase do not necessarily remain the same resulting in an elliptical polarization. If the sample is isotropic, boundary conditions at the interface are defined by Maxwell's equations to calculate the complex reflection coefficients: $r_s \equiv \frac{E_{rs}}{E_{is}}$, and $r_p \equiv \frac{E_{rp}}{E_{rs}}$. In the case of a single interface, the complex reflection coefficients can be expressed as:

$$r_s = \frac{N_1 \cos\theta_1 - N_2 \cos\theta_2}{N_1 \cos\theta_1 + N_2 \cos\theta_2}$$
$$r_p = \frac{N_2 \cos\theta_2 - N_1 \cos\theta_1}{N_2 \cos\theta_2 + N_1 \cos\theta_1} \tag{3.5}$$

where incident and reflected angles are calculated by Snell's law $n_1 \sin\theta_1 = n_2 \sin\theta_2$, where the subindex 1 and 2 represent the incident and the transmitted medium, respectively. Absorption effects are included using the complex expression of the refractive index $N = n + ik$, where n is the refractive index and k the extinction coefficient. When a single layer is deposited on top a substrate, as shown in Fig. 3.3, the incident light will face multiple internal reflections within the thin film with a number of these reflections contributing to the measured signal. At the interface between air and the thin layer, part of the incident beam is reflected (r_{01}) while the rest is transmitted (t_{01}). The reflected and transmitted coefficients can be calculated by applying equation 3.5 at each interface. The transmitted beam travels a distance $d \cdot \cos\theta_1$, for a layer of thickness d while reaching the layer/substrate interface. At the interface, part of the beam is transmitted through the substrate (t_{12}) and part reflected (r_{12}). The reflected beam travels a distance $d \cdot \cos\theta_1$, and reaches the air/layer interface where it is again transmitted t_{10} and reflected r_{10}. Thus, the beam transmitted from the layer/substrate interface will contribute to the net reflected beam by the thin layer after travelling an even number of times through the layer. Thus, the reflected coefficient can be expressed as: $R = r_{01} + t_{01}t_{10}r_{12}e^{-2i\beta} - \ldots$, which has been calculated from the Airy formula [170] and can be expressed as:

$$r_{s,p} = \frac{r_{1s,p} + r_{2s,p}e^{-2i\beta}}{1 + r_{1s,p}r_{2s,p}e^{-2i\beta}}, \tag{3.6}$$

with the film phase thickness $\beta = 2\pi\left(\frac{d}{\lambda}\right) n_1 \cos_t$. The coefficients are correlated to the complex amplitude reflection by the expression:

$$\rho = \frac{r_p}{r_s}, \tag{3.7}$$

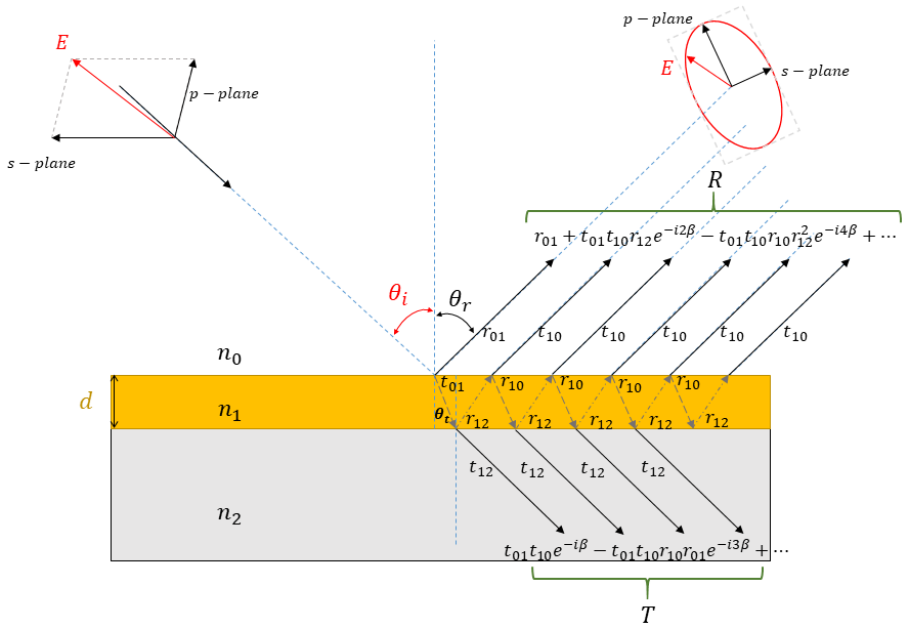

Figure 3.3: *Multiple-internal reflection in a thin film.*

r_p and r_s are two complex expressions, that can be directly related to ψ and Δ as follows:

$$\begin{aligned} \tan\psi &= |\frac{r_p}{r_s}| \\ \Delta &= \theta_{rp} - \theta_{rs}, \end{aligned} \tag{3.8}$$

where θ_{rp} and θ_{rs} are the phases corresponding to r_p and r_s.

In the current case, the thin layers were deposited on a c-Si (100) substrate with a thickness of ∼500 μm, for which the parameters are known. Hence, the values required to calculate are the thickness of the thin layer d and the real and imaginary part of the complex refractive index. This was carried out combining variable angle spectroscopic ellipsometry (VASE) and adopting the Tauc-Lorentz dispersion function for the a-SiO_xN_y layers [171, 172]. The latter combines the Tauc joint density of states and the Lorentz oscillator model to determine the real and imaginary part

of the dielectric function ($n = \sqrt{\epsilon} = \sqrt{\epsilon_0 + i\epsilon_i}$, where ϵ_0 and ϵ_i are the real and imaginary parts of the dielectric function) in the approximation of parabolic bands while describing inter-band transitions above the band edge as:

$$\epsilon_i \propto \begin{cases} A_T \cdot \left[\frac{(E-E_g)^2}{E^2}\right] & for E > E_g \\ 0 & for E \leq E_g \end{cases}, \tag{3.9}$$

where A_T is the Tauc coefficient, E is the photon energy and E_g is the optical band gap. The real part ϵ_0 is calculated using the complete analytical solution to the Kraemers-Kronig integral of ϵ_i. It is noteworthy that the Tauc-Lorentz model does not take into account intra-band absorption thus, requires the imaginary part of the dielectric function to be zero for energies below the band gap.

3.3 Ion accelerators

Ion accelerators are machines capable of producing and accelerating beams of selected charged atoms via electrostatic forces to controlled kinetic energies that can range several orders of magnitude, i.e. between few eV's and GeV's depending on the type of accelerator. They are used for adding impurities to materials over a specific area with depth control and minimal contamination due to the high vacuum involved, promoting nuclear reactions and elastic-inelastic interactions for elemental characterization, amongst other uses. Their types vary according to their purpose, ion species and energies required [173].

In this thesis three electrostatic accelerators of the tandem pelletron type, and one linear accelerator (LINAC) were used for the modification and characterization of a-SiO_x, a-SiN_y and a-SiO_xN_y thin layers. An ion implanter with a maximum potential of 1.7 MV with a SNICS source was used to add gold into a-SiO_x and a-SiN_y above the natural solubility to synthesise NPs. The elemental depth profile of pristine and ion implanted samples was measured using a dedicated 5SDH 1.7 MV ion beam analysis

system, with a radio frequency source for Rutherford backscattering spectroscopy (RBS) and elastic recoil detection analysis (ERDA). The swift heavy-ion irradiation of the samples was carried out at the 16.7 MV Heavy Ion Accelerator at ANU and the Universal Linear Accelerator (UNILAC) at GSI (Germany), with energies of nearly 1 MeV/u and 11.1 MeV/u, respectively. Thus, the present section is subdivided in the working principles of electrostatic accelerators followed by a brief description of the UNILAC.

3.3.1 Electrostatic ion accelerators

'Electrostatic' ion acceleration refers to the use of an electrostatic system to charge a high voltage terminal, responsible for the acceleration of an ion beam. These kind of ion accelerators comprise the following general components: an ion source, an acceleration stage, beam optics and diagnostic system, a mass/charge electromagnetic analyser, a beam scanning system and a target chamber. The ANU ion implanter and the Heavy Ion Accelerator possess the type of same ion source, a source of negative ions by Cs sputtering SNICS, used to produce negative ions from solid elements and mixtures, while the ion beam analysis system makes use of a radio frequency ion source, for the production of negative ions from gases such as hydrogen and helium. The three electrostatic accelerators share similar beam optics and diagnostic system, a mass/charge electromagnetic analyser and the acceleration system, which consists of a tandem configuration using pellet chains to transport the electrostatic charge to the high voltage terminal.

In this subsection first the two kinds of ion sources used by the three electrostatic accelerators, i.e. SNICS and radio frequency, are explained. This is followed by the description of the ANU ion implanter, where the tandem acceleration system will be explain in detail. Then, the dedicated ion beam analysis accelerator will be briefly described, as the two have the same acceleration capabilities and beam optics. Finally, details of the Heavy Ion Accelerator, where the beam optics system is more robust due to the energies involved, are described.

The ion sources

The ion implanted and the Heavy Ion Accelerator use a 'Source of Negative Ions by Caesium Sputtering', or SNICS [6,174]. A schematic of the SNICS source is presented in Figure 3.4. Here, Caesium is heated in a reservoir to form a stream of Cs vapour which rises up into the source chamber. Some of the Cs adheres to the tip of the cathode (which is cooled) while the rest gets in contact with the hot ionizer surface, at about 1100 °C. When in contact with the ionizer, which has the shape of a cone with an aperture in the center that allows the ions to be transmitted through it, Cs vapour is ionized forming Cs^+ and accelerated towards a negatively biased Cu cathode (∼5 kV). The cathode has an opening on the end facing the Cs^+ flow, which is filled with compacted powder containing a reasonable amount of the desired beam material. The Cs^+ sputters the cathode material via nuclear interactions. The presence of minimal amounts of Cs on the surface of the cathode enhances the probability to form negative ions as the Cs helps to decrease the work function while being highly electro-positive. Thus, the sputtered particles pick up electrons from the cold Cs, which are then accelerated through the aperture of the ioniser towards the positively-biased extractor (∼ 13 kV). An Einzel lens assembly is used to focus the extracted negative ion beam before entering the pre-acceleration section or source bias stage (∼ 42 kV).

The ion beam analysis system uses an *Alphatross* radio frequency (RF) source instead of a SNICS source to produce ions from gas sources, such as H and He [7,174]. A diagram of the ion source is presented in Figure 3.5. The H^- and He^- are produced via a two-step process involving the production of positive ions followed by a charge exchange step using an alkali metal vapour. The desired element is selected from two pressured bottles containing H or He, connected by a fine metering valve to a quartz bottle coupled to an RF oscillator where a plasma is generated from the neutral gas mixture (Figure 3.5). A bias voltage is applied across the quartz bottle to select and inject the now positive ions into a Rb vapour exchange cell through a Ta canal. Rb has the highest charge exchange efficiency among the

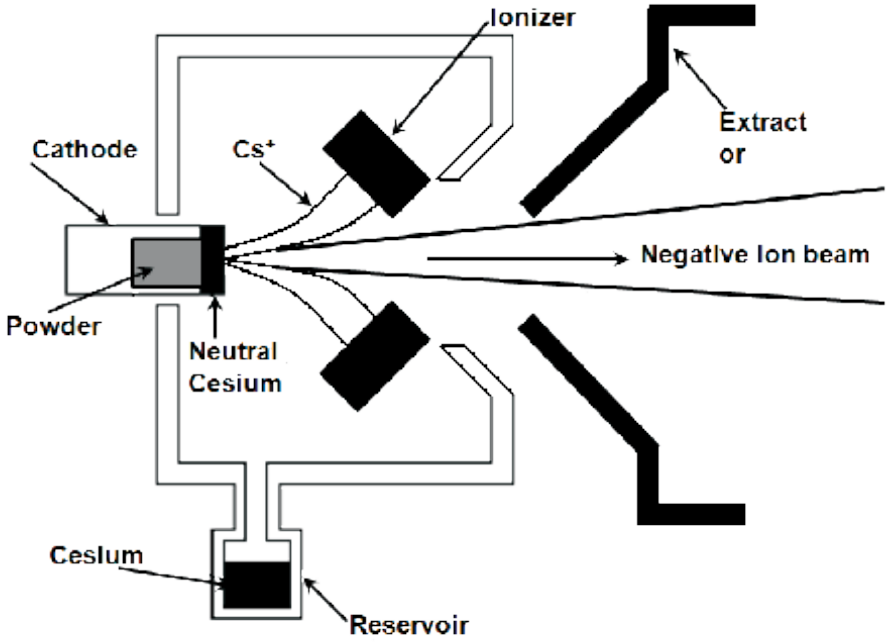

Figure 3.4: *Schematic showing the production of negative ions by a SNICS source [6].*

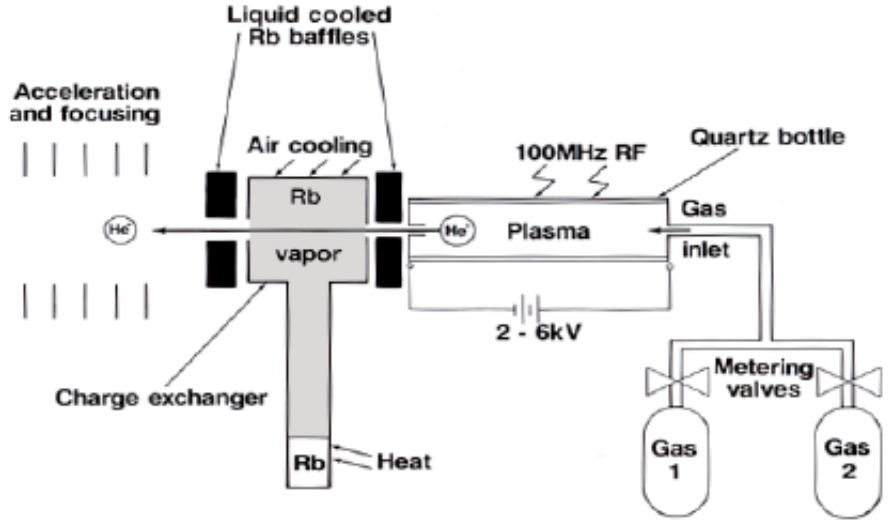

Figure 3.5: *Schematic of the Alphatross RF ion source by NEC [7].*

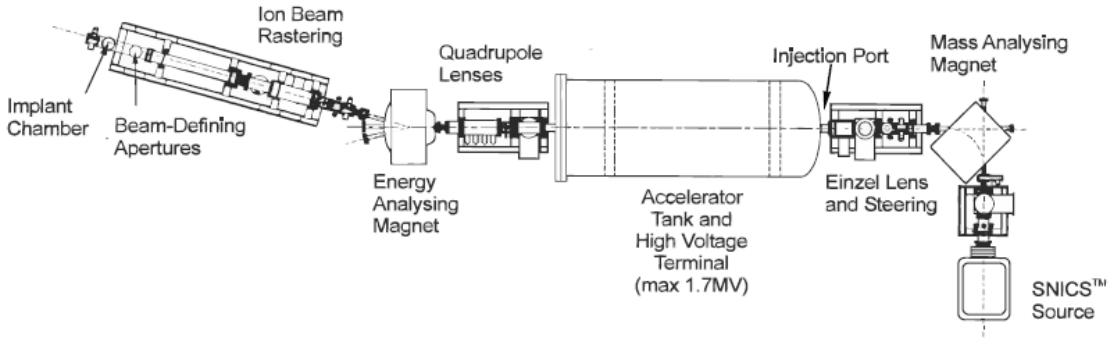

Figure 3.6: *Schematic of the high energy implanter at the Department of Electronic Materials Engineering, ANU [8].*

alkali metals, as well as a lower operating temperature compared to Na and K. The positive ions will exchange electrons with Rb during its path along the cell before exciting the ion source. Rb vapour condenses on the cell walls thanks to a liquid cooling system for reuse. Similar to the SNICS source, the negative ions are accelerated by an extractor bias voltage ($\sim$ 18 kV) towards the acceleration section.

The high energy implanter

The high energy implanter is part of the Department of Electronic Materials Engineering, at the Research School of Physics and Engineering at ANU. It is a 5SDH-4 pelletron tandem accelerator from National Electrostatics Corp. (NEC) connected to a SNICS source with a maximum terminal voltage of 1.7 MV [175]. The high energy implanter was used for the ion implantation with 2 MeV Au^+ with fluences of $5{\times}10^{16}$ cm^{-2} into a-SiO_x and a-SiN_y.

A schematic of the ion implanter and its components is presented in Figure 3.6. The beam formed by the negative ions, produced by the SNICS source, passes through a tunable electromagnetic (90° magnet) to select the required mass to charge ratio from the ion beam. The beam energy of at least 60 keV permits the required species resolution by the magnet. The resulting beam proceeds to a second Einzel lens and an

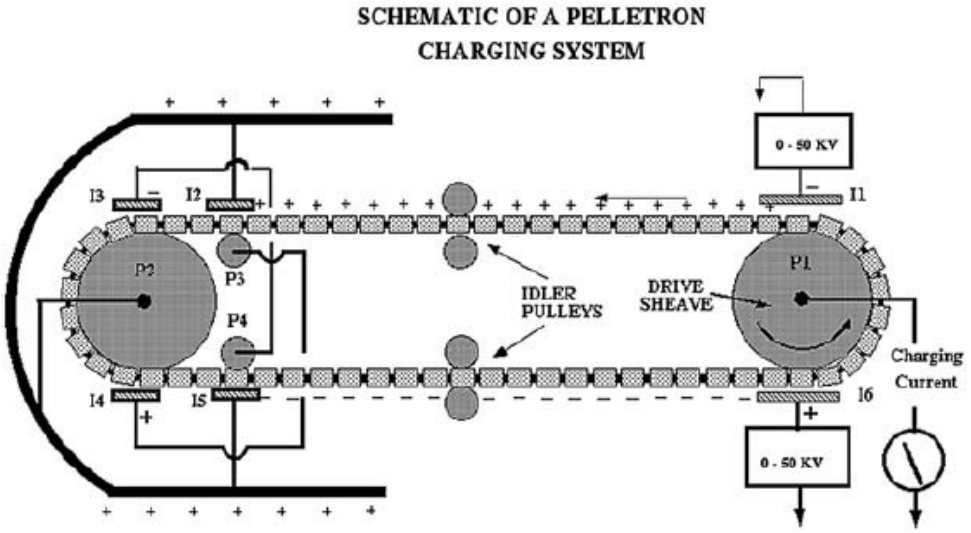

Figure 3.7: *Schematic of the pelletron positive charge system, taken from [9].*

(x, y) electrostatic steerer system prior to injection into the acceleration stage. The latter consists of a tandem acceleration system. It utilizes the terminal voltage twice by changing the charge state of the ions from negative to positive half way through the acceleration system.

The terminal is positively charged using two charging 'pelletron' chains [7, 9, 176, 176]. Pelletron chains are made of metallic pellets connected by insulating nylon links. The metal pellets are charged by an electric filed generated between the negatively charged biased inductor electrode and the drive pulley, pushing electrons out of the pellets while in contact with the grounded drive pulley (Fig. 3.7). The chain transports the charge to the high-voltage terminal, where the reverse process takes place. An accelerator column, made of insulating ceramics , surrounds the ion accelerator tube before and behind the high-voltage terminal. The electrodes are connected to equipotential rings in the acceleration column to maintain a uniform potential distribution along the acceleration stage (Fig. 3.8) [177]. This voltage grading system is also aimed to spread the electric stress among each subdivision to minimize discharges to the terminal which permits to achieve higher voltages. Such

discharges occur inside the acceleration tube or between the external region of the acceleration tube and the tank. For the former, the breakdown occurs in vacuum while for the latter it occurs in the high-pressure insulating environment. Stabilization of the terminal voltage is carried out by a combination of a generating voltmeter (GVM) at the acceleration tank and a slit feedback system at the analysing magnet. The acceleration tank is filled with pressurized Sulphur hexafluoride (SF_6) gas to provide electrical insulation between the high voltage terminal and the walls of the acceleration tank.

The incoming negative ion beam is accelerated towards the positively-charged terminal, localized at the middle of the acceleration stage. At the high voltage terminal, the negatively charged ions pass through a column of N_2, known as the stripper gas [9,178]. The interaction with N_2 leads to a collisional electron-detachment from the negative ions where the cross-section is dependent on the flow rate and ion species. This leads to a distribution of neutral, as well as negative and positive ions of various charge states. The positively-charged ions are then repelled by the positive high voltage terminal, experiencing a second boost of acceleration while travelling towards the high-energy end of the acceleration stage, with a final energy:

$$E = V_i + (1 + q) \cdot V_t, \tag{3.10}$$

where V_i is the pre-acceleration potential considering an initial charge state of -1, q is the charge state of the positive ion, and V_t the potential at the high voltage terminal.

After exiting the acceleration stage, the now positive ions pass through a magnetic quadrupole arrangement to re-focus the beam and continue towards a 15° switching magnet for the selection of the desired charge state and therefore, ion energy. At the end of the high-energy implanter beamline, the sample is mounted onto a Ni block with vertical and rotational movement control. In order to carry out homogeneous implantation over a selected area, the ion beam is electrostatically scanned with

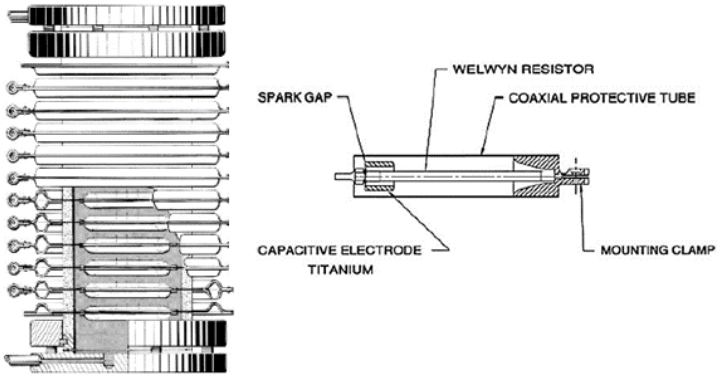

Figure 3.8: *Schematic of the NEC acceleration tube. The Ti electrodes are bonded to ceramic insulators protected by annular spark gaps and support a triplet of a corona points in the acceleration tube.*

an (x,y) scanning system located before the sample supplied by an AC frequency generator at a fixed frequency. The beam is scanned across the desired implanted area, which is defined by an appropriate aperture located closely in front of the sample at the entrance of the target chamber. The available sample holders are capable of carrying out the ion implantation at temperatures between liquid N_2 (LN) and 500 °C. The Au ion implantation performed for this thesis took place at room temperature. The implantation fluence was determined using a charge integrator connected to the sample holder and a secondary electron suppression Cu cage, which surrounds the sample.

Ion beam analysis accelerator

The RBS and ERDA analysis systems are part of a dedicated ion beam analysis 5SDH pelletron tandem accelerator from NEC at the Department of Electronic Materials Engineering [175]. It shares the elemental working principles with the ion implanter and their components can be identified in Figure 3.6. Among the main differences to the ion implanter are the ion source, which is an *Alphatross* RF source to produce ions from gas sources, which cannot be produced by a SNICS source, and the absences of a mass/charge selector electromagnet (90° magnet) and scanning system.

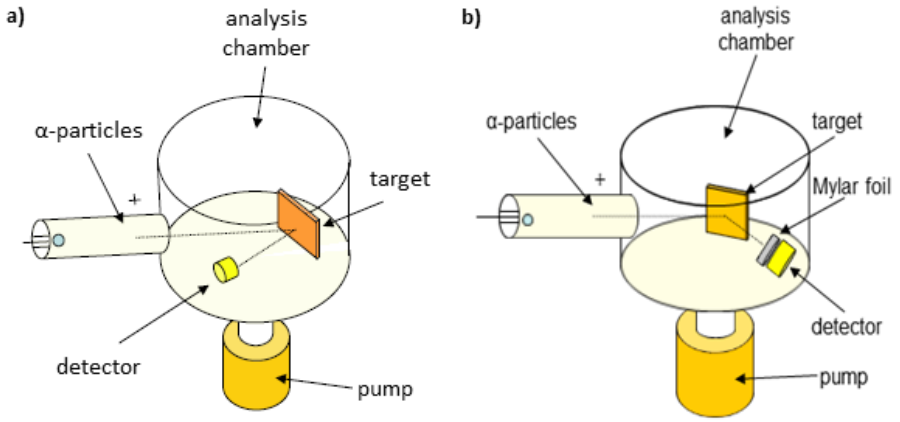

Figure 3.9: *Schematic of the RBS (a) and ERDA (b) analysis chamber.*

After exiting the ion source, a velocity selector is located to single out the correct ion species. This is done by a 4° kink in the beamline and an electrostatic steerer. Before the acceleration section, the beam is focussed by a set of Einzel lenses. The acceleration section is comprised of a tandem pelletron system with a maximum voltage of 1.7 MV similar to the ion implanter. The negative ions are accelerated towards the positive high voltage terminal where a charge exchange takes place via a perpendicular N_2 flow. The now predominantly positive ions are accelerated away from the high voltage terminal towards the end of the acceleration stage.

After the acceleration stage, the beam passes through a quadrupole focusing arrangement before entering a switching magnet. The switching magnet selects the appropriate beam energy and steers the beam into one of the two existing beamlines, RBS and ERDA, respectively.

Before the analysis chamber, the incident ion beam passes through four slits, resulting in a cross-sectional area of approximately 1 mm^2. For RBS analysis, the collimated beam is focused to the center of a goniometer where the sample is placed. The goniometer possess four degrees of freedom, two translational (x,y) and two rotational (along the x- and y- axis). The analysis chamber contains a surface barrier detector for backscattered particles (165° from the incident beam), Figure 3.9 (a). For the RBS measurements in this thesis, alpha particles of 2.4 MeV energy were used.

For ERDA analysis, the sample is mounted on a sample holder that allows two translational (x,y) degrees of freedom. The beam is incident at 80° off the sample surface normal. The surface barrier detector is located at 65°, opposite to the incident beam (Fig. 3.9 (b)), and is covered by a Mylar layer of 12 μm thick to absorb the scattered alpha particles. For this case, alpha particles with 2.8 MeV energy were used.

The heavy ion accelerator

The ion irradiation required for the formation of ion tracks in silicon oxynitrides and ion beam shaping of MNPs, was carried out at the Heavy Ion Accelerator Facility (HIAF) at the Department of Nuclear Physics at ANU. The irradiation was performed using the 14 UD (14 Unit Double) ion accelerator for irradiations with 0.95 MeV/u (185 MeV) Au^{13+} [179, 180]. A schematic of the design of the 14 UD is presented in Figure 3.10. The 14 UD is a pelletron tandem accelerator capable of reaching 16.7 MV at the high voltage terminal [181]. The acceleration stage is 21.9 m long and 5.5 m in diameter with a weight of 150 t, connected to 10 separate beamlines, including a superconducting booster linear accelerator (LINAC). The swift heavy-ion irradiations took place at line '0'.

The 14 UD has the capability of produce negative ions from two ion sources, a gas cathode assembly (gas insertion occurs through the center of a cathode) SNICS II [182] and a multi-sample SNICS source [183] with capacity for 40 cathodes with a working principle similar to the single-cathode SNICS source at the ion implanter. The ion sources supply a high-resolution injector system where the negative ions are pre-accelerated up to 150 keV by the source bias and focused by the pre-accelerator tube and an Einzel lens before reaching the single-focusing injection magnet (90° magnet). After exiting the injection magnet, the selected beam is then coupled to a programmable chopper, as can be seen in Fig. 3.10, which consists of a pre-tandem buncher system [184] that allows to compress the continuous beam produced by the SNICS source into variable pulse widths (in the ns scale) and pulse repetitions between

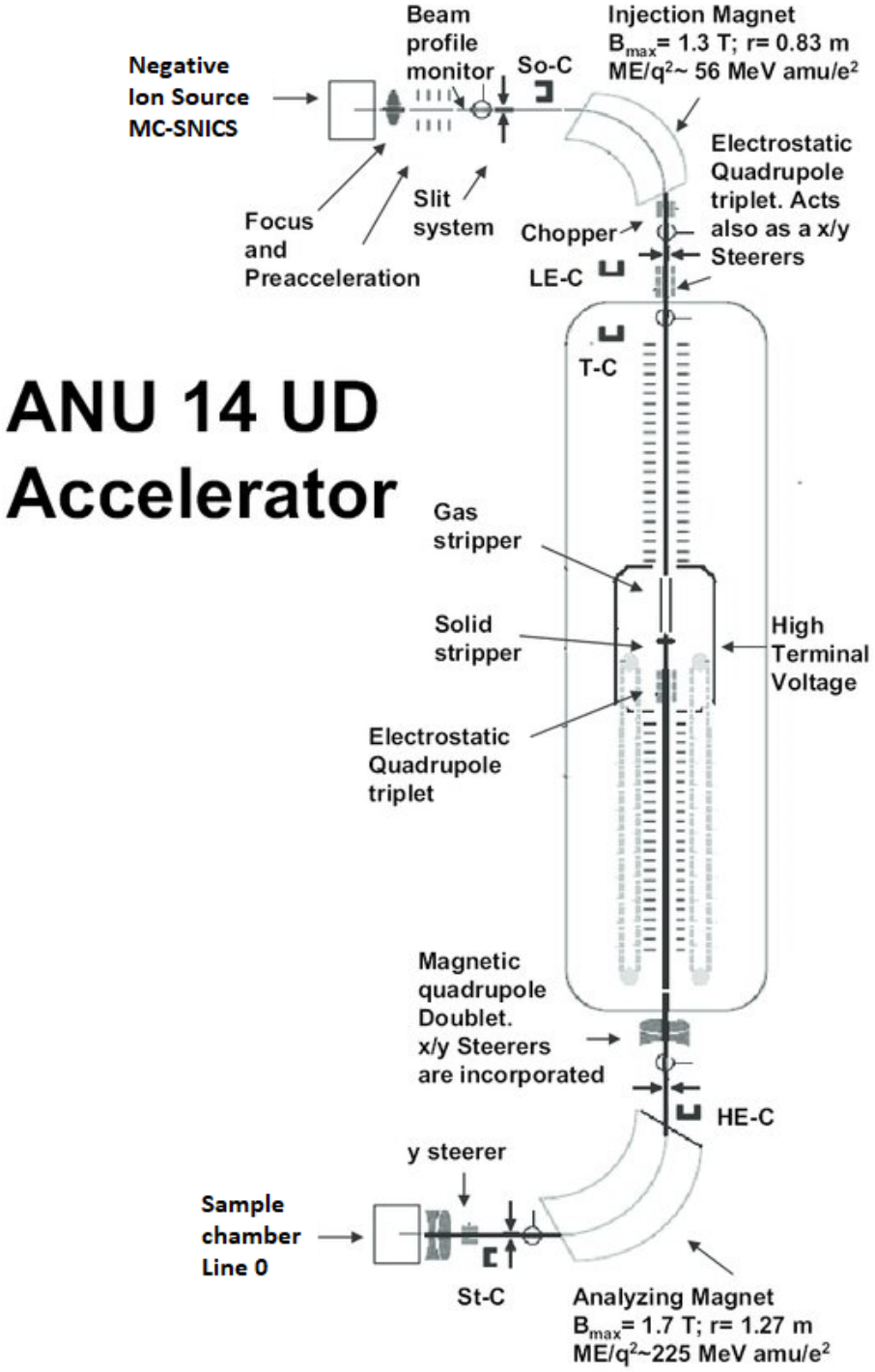

Figure 3.10: *Diagram of the heavy ion accelerator '14 UD' at the Department of Nuclear Physics, ANU, modified from [10].*

0.1 μs and 500 ms[1].

After passing through the pulsed beam system, the beam is again focused by a triplet quadrupole lens before entering the acceleration stage. The acceleration stage has a tandem pelletron configuration with the high terminal voltage supplied by three pelletron chains able to reach up to 16.7 MV. To achieve voltage stability, the acceleration line is divided into 14 acceleration tube segments (Fig.3.10) before and after the HV terminal (14UD) with electron traps formed by 45° V shaped electrodes and vacuum chemistry treatment of those electrodes to reach gradients slightly above 1 MV/unit. The stage is immerse in pure pressurized SF_6 for electrical insulation. At the HV terminal, a foil-gas stripping assembly is available using either N_2 or carbon foils to strip electrons from the negative ions. For the acceleration of Au^{13+} the carbon stripper foils were used. Carbon is the material with the lowest atomic number that can be fabricated into a very thin foils to reduce multiple scattering and energy straggling, as well as achieving higher charge states, suitable for generating high charge states [9]. The HV terminal is comprised of a terminal quadrupole lens for beam focusing after the charge stripping step. The now positive ions continue being accelerated towards the end of the acceleration stage. After exiting the acceleration stage, the ion beam passes through a y-steerer before being focussed by a quadrupole lens into an analyzing magnet to select the appropriate beam energy.

The selected energy is then steered into beamline '0', passing through an x-y raster system to scan a 3 $\times$ 6 mm^2 aperture located 10 cm in front of the target, in the irradiation chamber. The irradiation fluence is calculated with a charge integrator connected to a secondary electron suppression cage.

[1]During the SHI irradiation experiments carried out at the 14 UD, the chopper was used to produce an ion beam pulse with a width of 10 μs and a repetition between 100 and 200 μs when the current measured right before the acceleration staged surpassed 80 nA. Such high currents lead to very swift degradation of the solid stripper system and instability of the high terminal voltage. The ideal input current should not be higher than 60 nA for optimal conditions.

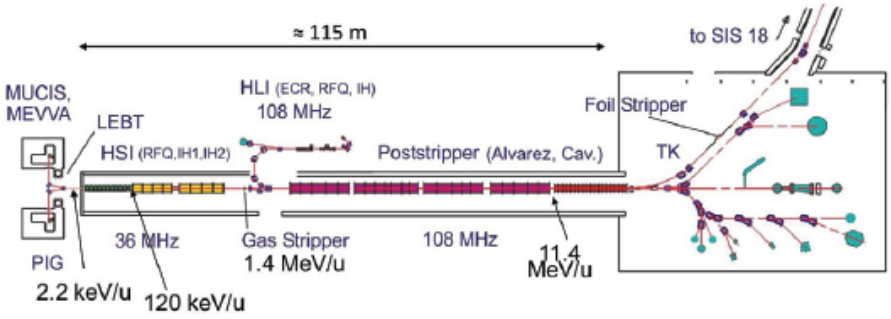

Figure 3.11: *Diagram of the UNILAC at GSI [11].*

3.3.2 GSI UNILAC

Ion track formation with ion energies above the Bragg peak requires kinetic energies above 4 MeV/u. Such kinetic energies are not achievable by electrostatic ion accelerators, such as those available at the ANU. For this reason, irradiations with 11.1 MeV/u Au ions (2.2 GeV) were performed by our collaborators from the Department of Material Science, at the Helmholtz Centre for Heavy Ion Research (GSI) [185] in Darmstadt, Germany at the X0-branch of the Universal Linear Accelerator (UNILAC). This end station uses a defocused beam instead of a raster system to irradiate a target area of 5×5 cm^2.

Linear accelerators, such as the UNILAC, rely on a succession of drift tubes coupled to high-frequency power generators on a linear path instead of electrostatic fields for particle acceleration and are capable of producing ions with higher particle velocities [173, 186, 187]. Between the ion beam terminal, composed of low (Penning) or high current (MEVVA/MUCIS/VARIS) ion beam sources [11, 188–191], the beam is prepared for transfer between the source and the drift tube linear accelerator by a high current injector (HSI). The HSI allows an efficient preparation of the high-intensity low-energy beam, reaching a transfer efficiency of the initial beam above 90%. This is achieved by an initial RF quadrupole (RFQ) [192] (shown in green at the beginning of the beamline in Figure 3.11). The RFQ tackles the defocusing effect (at low velocities it is difficult to maintain high currents due to electrostatic

repulsion that leads to defocusing of the beam) thanks to its quadrupole transversal symmetry. Furthermore, its sinusoidal longitudinal design bunches and continuously accelerates the beam by a RF electric field up to 120 keV/u. The RFQ is followed by two interdigital H-type RFQs (IH-RFQs) for acceleration to 1.4 MeV/u. The first is known as the IH1 because works in the dipole magnetic mode TE_{110}, which is efficient to accelerate particles with initial velocities $\beta \leq 0.03$. Afterwards, the beam enters the IH2, which runs on a magnetic quadrupole TE_{210} (efficient for $\beta \leq 0.08$ [2]) [193]. At the exit of the IH2, the beam passes through a stripper gas and after dispersive selection, the desired charge state is injected into a subsequent post-stripper drift tube LINAC Alvarez-type, comprised of five tanks where particles can reach energies up to 11.4 MeV/u. The RF source feeds a series of drift tubes in such a way that while the particles are inside the drift tubes they are shielded from the external field thus, the acceleration occurs in between the tubes. Therefore, the beam produced at LINAC accelerator is a high rate discontinuous beam, in contrast to electrostatic accelerators. To prevent the system from radiating large amounts of energy at high frequencies, the gap between the drift tubes is enclosed in a cavity, where by inductive load, the resonant frequency of the cavity matches that of the accelerating field, thus, each cavity is fed individually. Such design is known as the Alvarez structure, where ions reach relativistic velocities (Shown in red in Figure 3.11).

3.4 Ion beam analysis

The characterization of thin films using ion beam analysis techniques is an active field in applied science. Rutherford backscattering spectroscopy (RBS) and elastic recoil detection analysis (ERDA) are two techniques that make use of energetic ion beams, commonly H or He^+, in the energy range between 0.5 - 3.5 MeV. The ion beam impinges on the sample where collisions with the target nuclei take place. From the elastic interactions, it is possible to accurately determine the stoichiometry, elemental density and impurity distribution as a function of depth in the near-surface region for

[2] $\beta = \frac{v}{c}$, where c is the speed of light and v the velocity of the ion

solid targets. RBS was used to quantify the Si, N and O content, to determine the stoichiometry for all materials considered in this thesis, and the depth profile in the case of Au implantations, prior to and post thermal annealing. ERDA was used to measure the H content and depth distribution for all a-SiO_xN_y thin layers deposited by PECVD.

3.4.1 Rutherford backscattering spectroscopy (RBS)

Quantification of the number and energy distribution of backscattered ions from the target atoms in the region close to the surface permits an accurate identification of atomic masses and the distribution of the target elements as a function of depth. Figure 3.12 shows a schematic of the RBS principle. The projectile ion with initial energy E_0 reaches the sample at almost normal incidence θ_1. As it penetrates the sample, the projectile loses energy due to the electronic energy loss, from E_0 at the surface to $E_0^{'}$ at a given penetration depth, before it is backscattered by a nucleus of one of the elements that comprises the target, and then loses energy on his way out of the target before reaching the detector. The energy of the backscattered particles is recorded by a surface barrier detector located a few degrees off from the target's normal.

The energy E_f^i of a projectile ion with initial energy E_0 after a binary collision with one of the target's atom is given by:

$$E_f^i = K_s^i E_0, \tag{3.11}$$

where the superscript term i is related to the target species (Si, N or O for silicon oxynitride targets), and K_s is the kinematic factor for scattering, defined as:

$$K_s = \left[\frac{(M_2^2 - M_1^2 \sin^2\theta)^{1/2} + M_1 \cos\theta}{M_1 + M_2} \right]^2 . \tag{3.12}$$

The terms M_1 and M_2 corresponds to the mass of the projectile ion and target nucleus, respectively, and θ is the backscattered angle as shown in Fig.3.12.

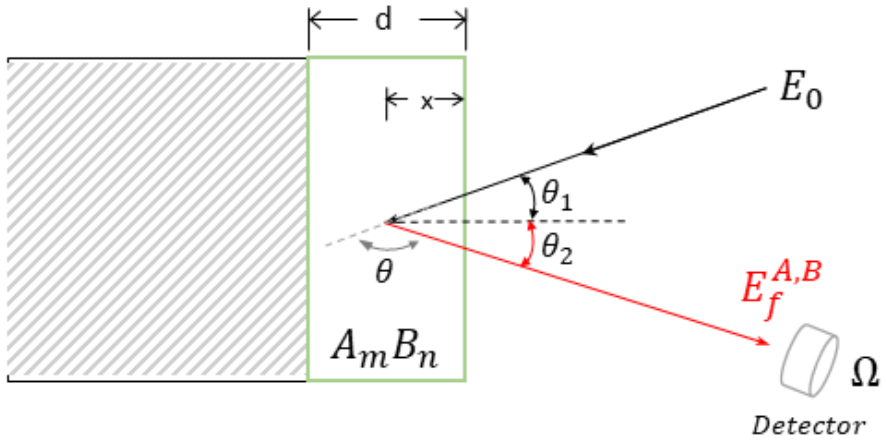

Figure 3.12: *The RBS principle: an ion projectile with energy E_0 approaches a binary target with an incident angle θ_1, it penetrates the sample to a depth x where it collides with one of the target nuclei. After impact, the ion is backscattered with an angle θ, with respect to the initial trajectory. The final kinetic energy of the ion projectile is then recorded by the detector for analysis.*

The probability of an alpha particle to be backscattered by a target nucleus and be detected is obtained by the product of the scattering cross-section $\sigma_s(E,\theta)$ with the solid angle of detection Ω, typically 10^{-2} sr [3]. For Rutherford scattering, $\sigma_s(E,\theta)$ can be calculated in the following form:

$$\sigma_s(E,\theta) = \left[\frac{Z_1 Z_2 e^2}{4E}\right]^2 \frac{4\left[(M_1^2 - M_1^2\sin^2\theta)^{1/2}) + M_2\cos\theta\right)^2}{M_2\sin^4\theta(M_2^2 - M_1^2\sin^2\theta)^{1/2}}, \tag{3.13}$$

where Z_1 and M_1, and Z_2 and M_2 correspond to the atomic number and mass of the projectile ion and target nucleus, respectively. The term E is the projectile ion energy before the binary collision. It is possible to relate the scattering cross-section to the count yield Y_s of backscattered particles per energy step ΔE using the following relationship:

[3] steradian is a measure of the solid angle in Si units. It is defined as the solid angle of a sphere subtended by a portion of the surface equal in area to the square of the radius

$$Y_s = \frac{Q\sigma_s(E_0^{'},\theta)\Omega N(x)\Delta E}{\cos\theta_1 \cdot \frac{\Delta E}{\Delta x}}, \tag{3.14}$$

where Q is the amount of alpha particles incident on the target (projectile fluence). The energy of the ion projectile at a distance x form the surface is then $E_0^{'} = E_0 - \frac{\Delta E}{\Delta x} \cdot x$, with an angle of incidence θ_1, and $N(x)$ the atomic density of a given region of thickness Δx. The energy step ΔE represents the energy resolution of the detector, commonly around 10 keV, and $\frac{\Delta E}{\Delta x}$ is the corresponding electronic energy loss rate of the ion projectile in the target.

The integrated count yield for a given species can be correlated with the actual elemental areal density N_i by:

$$N_i d_i = \frac{A_i \cos\theta_1}{Q\sigma_s(E_0^{'},\theta)\Omega}, \tag{3.15}$$

where A_i is the integrated yield and d_i the thickness of the region of interest.

Because only single scattering events are considered in RBS, the ion projectiles interact only with the electronic system prior to collision with the target nuclei, thus, the term $\frac{\Delta E}{\Delta x}$ or $\frac{dE}{dx}$ corresponds to the electronic energy loss rate. This means that the energy recorded from a backscattered particle comprises the loss of energy while it penetrates the sample before an event, the resulting energy due to scattering given by the corresponding kinematic factor and the energy loss resulting from the travel back, which can be expressed as:

$$KE_0 - E_f = \left[\frac{K}{\cos\theta_1}\frac{dE}{dx}\,|_{in} + \frac{1}{\cos\theta_2}\frac{dE}{dx}\,|_{out}\right] x. \tag{3.16}$$

If the energy loss rate is known, equation 3.16 can be used to determine the depth of the scattering event, leading to an expression for the depth scale.

For the case of binary or multi-elemental targets, the previous principles are valid and the final count yield at a specific energy is the superposition of the yield count for each element at that energy, following the Bragg rule (see section 2.1.3). Thus, the stoichiometry of multi-element samples can be determined by comparing the surface heights of the elemental peaks. The mean stoichiometry ration can be calculated by combining the previous equation for a binary compound (A_mB_n) leading to the expression:

$$\frac{m}{n} = \frac{A_B}{A_A}\frac{\sigma_m(E,\theta)}{\sigma_n(E,\theta)}, \tag{3.17}$$

where A_A and A_B correspond to the integrated yield for the element A and B, respectively.

Equations 3.15 and 3.17 can be combined to calculate the layer thickness d in terms of the layer density ρ_{AB}, thus:

$$d = \frac{N_A d_A}{N_A^{AB}} = \frac{N_B d_B}{N_B^{AB}}, \tag{3.18}$$

where N_A^{AB} and N_B^{AB} are the atomic densities ($N_A^{AB} = \frac{m\rho_{AB}N_0}{M_{AB}}$), N_A is Avogadro's number and M_{AB} the molecular weight of the binary compound ($M_{AB} = mM_A + nM_B$).

RBS analysis

For a typical data set, where the incident ion projectile mass, energy and backscattering geometry are known, two codes are commonly used: SIMNRA [194] and RUMP [195, 196]. For the analysis of RBS and ERDA spectra in this thesis, the RUMP code was used. For the numerical analysis of each spectrum, the thin layer is considered to be formed by a stack of sublayers of uniform composition. The selection of the thickness Δx of each sublayer is determined such that $\Delta E = \frac{\Delta E}{\Delta x} \cdot \Delta x$, where $\frac{\Delta E}{\Delta x}$ is the corresponding electronic energy loss at a given depth, for ΔE slightly larger than

or equal to the corresponding detector energy resolution. The requirement of homogeneity through the sample is necessary to consider a fixed energy loss for each sublayer.

The energy loss rate for each sublayer is evaluated using a fifth order polynomial of Ziegler's data for alpha particles [197], which is known for almost all elements in the energy range from 0.35 - 3.5 MeV. For multi-elemental compounds, Bragg's linear additivity fule for energy loss rate is used (see section 2.1.3). This permits a rapid and accurate estimation of the ion projectile final energy after travelling through a sublayer of thickness $N \cdot d$ with an incident angle θ_1. Thus, the simulated spectrum will be the superposition of the contribution from each elemental component of each sublayer of the sample.

If the thickness of each sublayer is comparable to the resolution of the detector, the corresponding RBS spectra would resemble a trapezoid shape typically defined by their front and back energies, however, if the thickness is much wider, the shape of its contribution to the spectra can produce kinks in the overall spectra and inaccuracies of the extrapolated area. The RUMP code solves these problems by approaching the height of the RBS spectra for of each sublayer by a parabola instead of a straight line. Because the area is proportional to Rutherford's backscattering cross-section (equation 3.13), for the simulated contribution, all terms are constant except for the energy, thus, it can be re-written as: $\sigma_s(E) = C \cdot E^{-2}$, leading to an integral that can be solved exactly:

$$area = \int_0^{Nd\sec\theta_1} \sigma_s(E(\xi))d\xi = C \cdot \int_0^{ND\sec\theta_1} E(\xi)^{-2}d\xi. \tag{3.19}$$

Equation 3.19 is solved by approximating the argument of the integral using a third order polynomial, yielding high accuracy for a broad range of energies and target atoms [195].

When the particle reaches the detector, the signal is pre-amplified before it reaches a multi-channel board. The multi-channel board then assigns one channel to

a specific energy range defined by a specific energy width ΔE following a linear scale as:

$$E = E_{off} + \Delta E \cdot \#channel, \tag{3.20}$$

where the first term corresponds to the energy of the backscattered particle, and E_{off} is the offset energy, also known as the energy of the first channel. An accurate determination of E_{off} and $\#channel$ is meaningful for a satisfactory analysis. The positive sign implies that higher channels correspond to higher energies, a rule employed to determine the expected position of the target species (*i.e.* Au appears on the right side of the spectra with respect to Si, O or N, see Figure 3.13). Figure 3.13 shows typical experimental and simulated RBS spectra of a-SiN_y implanted with 4.5 $\times$ 10^{16} cm^{-2} Au ions. The RBS experiment was carried out with 2.4 MeV He^+ particles at almost normal incidence ($\sim 3^\circ$ off the normal), where the detector was positioned at a backscattering angle $\theta = 165^\circ$ (Figure 3.12). The blue, yellow and orange dashed lines represent the yield edge (backscattering from the atoms at the surface) for N, Su and Au, respectively. The energy corresponding to the yield edge E_f^i is calculated using equation 3.11 and is E_f^N = 629.1 keV for N, E_f^{Si} = 1135.0 keV for Si and E_f^{Au} = 1846.4 keV for Au. The calibration of E_{off} and $\#channel$ was carried out using the energy and channel values of the yield edge of N and Si.

The simulated spectrum (red line) presented in Figure 3.13 corresponds to the a-SiN_y layer, without the contribution of the Si substrate. Because the thickness of the a-SiN_y layer is about 1 μm, the 2 MeV He ions can penetrate further into the sample, providing information about the entire layer. Between channels 152 and 292, the yield corresponds to Si only while between channels 116 and 152, the total yield corresponds to the superposition of the yield of N located at and near the surface of the layer, and the Si signal originated at the backside of the layer. The difference between the simulated and the experimental yield for channels below 120 corresponds to the contribution of Si from the substrate, which has not been taken into account for the simulation.

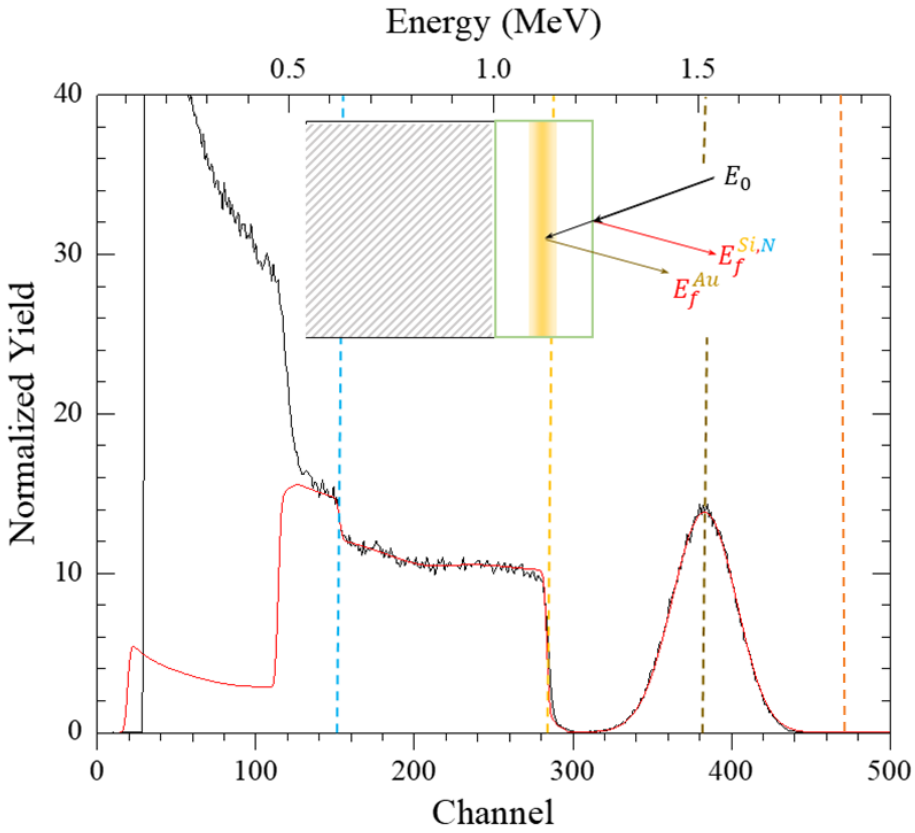

Figure 3.13: *RBS spectra of a-$SiN_{1.06}$ implanted with 4.6 × 10^{16} cm^{-2} Au ions. The black line represents the experimental data while the red line corresponds to the theoretical fitted spectra where Au has been modelled as an impurity. The coloured dashed lines represent the corresponding channel (energy) of backscattered alpha particles by Si (yellow), N (blue) and Au (orange) at the surface of the sample, as shown in the inset. The brown dashed line corresponds to the projected range of Au implanted with 2 MeV.*

The determination of the stoichiometry of a-SiO_x, a-SiN_y and a-SiO_xN_y thin layers was carried out with pristine samples. As pointed out in equation 3.18, if the density of the material is known, it is possible to integrate the total yield of Si, N or O for each deposited layer and thus, determine the corresponding thickness. In the current case it is the opposite, the stoichiometries and layer densities are unknown however, the thickness of each layer is known, independently determined by spectral ellipsometry. Thus, equations 3.17 and 3.18 were used to determine the stoichiometry and layer density, respectively.

The concentration of impurities added by ion implantation, as in Fig. 3.13, is calculated by RUMP using the sublayer approximation. For all Au implanted in a-SiO_x and a-SiN_y layers, the depth profile can be expressed by a Gaussian function centred at the projected range and a width dependent on the implanted energy. The RUMP code subdivides the Gaussian distribution into multiple sublayers, where a first estimation of the projected range, full width at half maximum (FWHM) and implanted fluence is required. Typically, the projected range and FWHM input values correspond to those determined previously by the SRIM code [92]. An initial estimation is carried out and is followed by the fitting of the parameters such that the Poisson maximum likelihood function χ^2 is minimized, following a non-linear least squares algorithm [20]. The region of interest is divided in sublayers and the yield height for each sublayer and thickness is calculated in the impurity approximation. For very low impurity concentrations, typically below 3 at. %, the contribution to the sample density and stopping power is so small that it can be neglected and thus, the values of the material sample can be used for the calculations. By combining equations 3.14 and 3.15 [20, 195, 196] the number of impurities per unit area can be determined, which in the case of Au in a-SiN_y has the form:

$$N_{Au}d_{Au} = \frac{A_{Au}}{\sigma_{Au}} \cdot \frac{\cos\theta_1}{Q \cdot \Omega} = \frac{A_{Au}}{\sigma_{Au}} \cdot \frac{\sigma_{Si} N_{Si}}{Y_{Si}} \cdot \frac{\Delta E}{(\Delta E/\Delta x)} = \frac{A_{Au}}{Y_{Si}} \cdot \frac{\sigma_{Si}}{\sigma_{Au}} \cdot \frac{\Delta E}{(\Delta E/\Delta x)} \cdot N_{Si}, \quad (3.21)$$

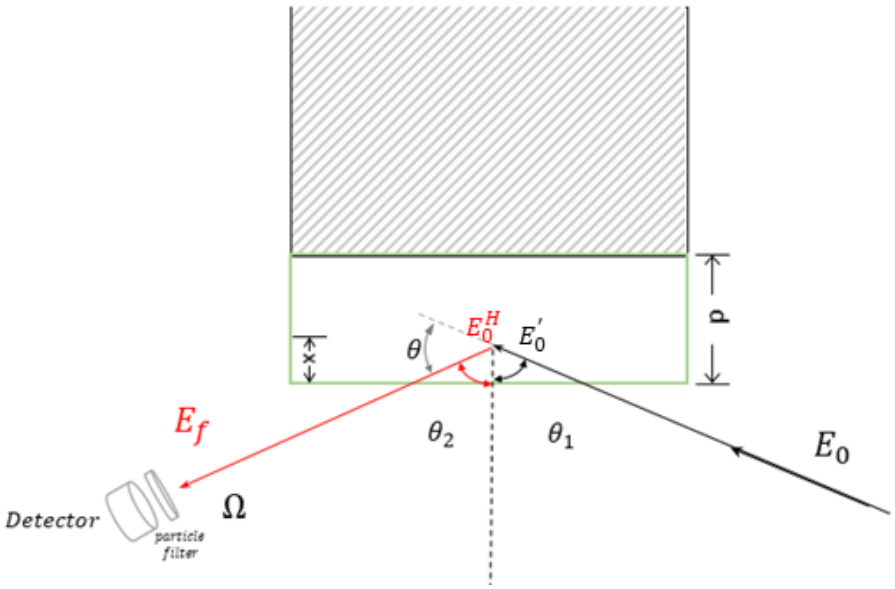

Figure 3.14: *The ERDA principle: an incident ion projectile with an energy E_0 reaches the target at nearly grazing incidence. The ion projectile travels through the sample before undergoing a collision with an H atom at a depth x. The ion projectile recoils an H atom with energy $E_0^H = K_r E_0'$, which also loses energy as it traverses the sample out before reaching the detector. A particle filter is placed at the surface of the detector to stop scattered ion projectiles.*

where A_{Au} is the area under the Au peak, θ_1 is the incidence angle, σ_{Au} is the corresponding Rutherford's cross-section. Y_{Si} is the yield edge of Si, N_{Si} is the atomic density of Si in a-SiN$_y$ and the term $(\Delta E/\Delta x)$ is the electronic energy-loss rate of He ions backscattered by Si in a-SiN$_y$.

3.4.2 Elastic Recoil Detection Analysis (ERDA)

Figure 3.14 shows the basic principle of ERD analysis, which can be related to the physical principles described for RBS. When an incident projectile ion, with energy E$_0$ and nearly grazing incidence reaches the target, the ion travels through the sample at shallower regions than at RBS before undergoing an elastic collision with a target atom at a depth x. During the collision, the projectile ion will transfer part of its kinetic energy into the target atom and can lead to the production of a free target

atom if the transferred energy surpasses its binding energy. This is known as a recoil atom. In ERD analysis, the forward recoil scattered target atoms are recorded by a detector located at an angle θ from the ion beam trajectory, as depicted in Figure 3.14. Target atoms with a mass lower than that of the projectile ion are more likely to be recoiled at the angles required to reach the detector, such as H in a-SiO_xN_y layers. In this case, after the collision the recoiled H atom possess an energy $E_0^H = K_r E_0^{'}$, where K_r is the kinematic factor (equation 3.22) for recoil atoms and $E_0^{'}$ is the energy of the projectile ion at a depth x. The projectile ion loses energy as it traverses the sample out until reaching the detector. The recoiled particle reaches the detector, which is covered with a particle filter (typically $\sim$ 12 μm Mylar film) aimed to stop heavier particles. Hence, information regarding the concentration and depth distribution of light elements is encoded in the number and energy of the recoiled atoms measured. ERDA and RBS are complementary as RBS has difficulties to resolve light elements in heavy targets ($Z \leq 11$),while ERD is capable of depth profiling elements lighter than the projectile ion (typically $1 \leq Z \leq 9$). ERDA is based on the elastic interaction between the projectile ion and the target's nuclei, like RBS. Thus, the energy transfer between the projectile and the target nucleus is defined by the kinematic factor of a classical binary collision. The probability for a collision to occur is determined by the differential scattering cross-section given by Rutherford's formula. The mean energy loses of the projectile and recoil atom are defined by the corresponding stopping power as they traverse the sample, and the statistical fluctuations in the energy loss, is given by the straggling [20,198,199].

Analogously to RBS,the kinematic factor for recoil can be expressed as:

$$K_r = \frac{4M_1M_2\cos^2\theta}{(M_1+M_2)^2}, \tag{3.22}$$

where M_1 and M_2 correspond to the mass of the projectile ion and target atom, respectively, with θ being the recoil angle, as defined in Figure 3.14. For recoiled atoms, Rutherford's scattering cross-section formula becomes:

$$\sigma_r(E,\theta) = \left(\frac{1}{(2M_2E)^2}\right) \cdot \frac{(Z_1 Z_2 e^2 (M_1 + M_2))^2}{\cos^3\theta}, \tag{3.23}$$

which can be used to calculate the count yield for recoiled atoms per energy step ΔE, as in equation 3.14, being Z_1 and Z_2 the atomic number of the projectile ion and target ion, thus:

$$Y_r = \frac{Q\sigma_r(E_0^{'},\theta)\Omega N(x)\Delta E}{\cos\theta_1 \cdot \Delta E/\Delta x}, \tag{3.24}$$

where the term ΔE/Δx represents the effective electronic energy loss rate, which takes into account the energy loss of the projectile ion while travelling through the thin layer before colliding with a light element and the energy loss rate of the recoiled light atom towards the detector. Because of their angle of incidence, ERDA possess higher sensitivity to light elements while RBS has better depth resolution.

Analysis of ERDA measurements

ERDA measurements were carried out with 2.8 MeV He^{2+} ion with an angle of incidence of $\theta_1 = 75°$ and scattering $\theta_2 = 65°$. The aim of the experiment was to quantify the residual H content in a-SiO_x, a-SiN_y and a-SiO_xN_y thin layers due to the deposition method. The normalization and analysis of the ERDA spectra was carried out with the RUMP software, as for RBS. The calibration of the ERDA spectra was done by carrying out measurements of Kapton polymide ($C_6HO_8N_7$, ρ = 1.42 g/cm^3) for different ion beam energies (E = 2.0, 2.5, 2.915 and 3.0 MeV). From the corresponding yield edge channel (# Channel = 123, 220, 264 and 277, respectively) and the use of the RUMP software it is possible to determine the energy of recoil atoms at each edge channel, and thus, the corresponding E_{off} and $\#channel$.

Because He^{2+} was the selected projectile ion, ERDA is restricted to the detection of H in the current case. The quantification of H in the samples was carried out

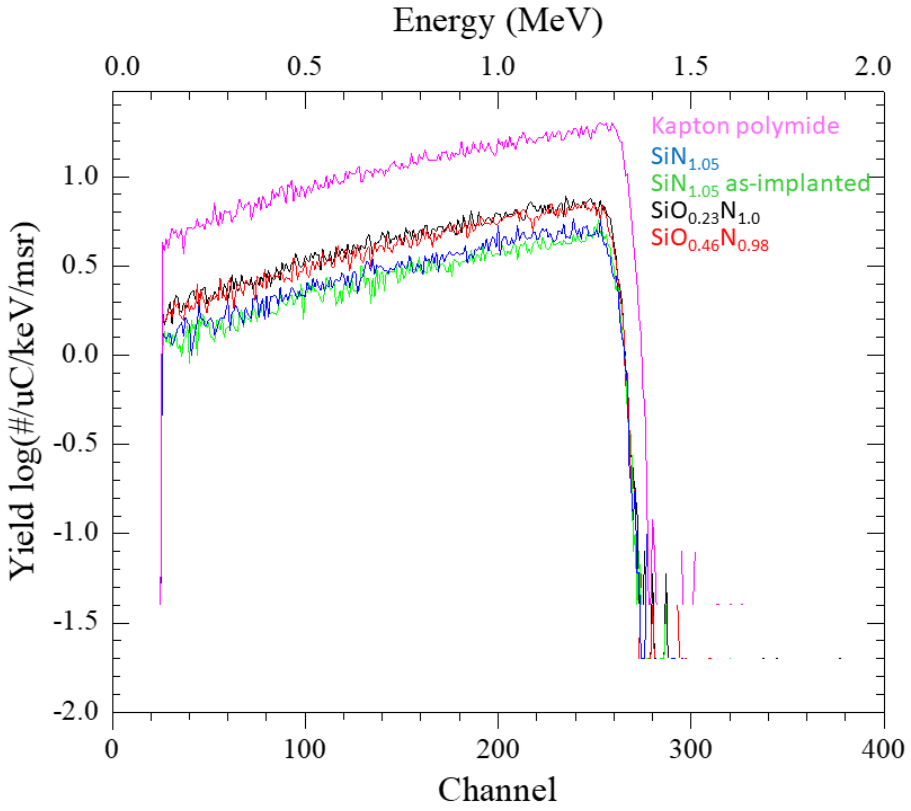

Figure 3.15: *ERDA spectra of selected a-SiO_xN_y thin layers compared with Kapton polymide. Kapton polymide is used as a reference, as the H content is known and homogeneous with depth. The yield ratio of a-SiO_xN_y layers with Kapton polymide is used to estimate the H content while the comparison of the slope spectra is used to determine the depth distribution of H.*

combining the principles depicted in equations 3.17 and 3.24. The corresponding spectra of selected a-SiO_xN_y thin layers are plotted with respect to Kapton polymide in Figure3.15. In the plot a similar slope for all samples is observed. This suggests that H is evenly distributed within the samples. Because the H content is known and homogeneously distributed within the Kapton polymide, it was used as reference to estimate the corresponding H content in the PECVD thin layers. The latter was carried out by determination of the integrated yield ratio between the PECVD layers and Kapton polymide, where the H content is 25.5 at. %. This method provides a reliable estimate of the H content, yet the errors are larger than those in RBS (up to 10%).

3.5 Infrared spectroscopy

A molecule is a group of two or more atoms with neutral charge connected by chemical bonds, where the atoms can vibrate around the center of their chemical bond. As the energy of those vibrational modes lies between 0.05 and 0.5 eV (400 - 4000 cm^{-1}), infrared spectroscopy can be used to obtain information about the chemical bonds by exciting theses modes. The technique is based on the absorption of infrared electromagnetic radiation at frequencies that matches the characteristic vibrational frequencies of specific chemical bonds within the molecule. The total energy of a molecule can be broken down into different contributions, each related to specific motions such as: vibrational, rotation and translational. Infrared spectroscopy takes advantage of the uniqueness of the vibrational modes of the component atoms in the molecule [200].

In order for a molecule to be 'infrared active' or exhibit absorption of infrared radiation, a net change of the electric dipole moment of the molecule should occur during the vibration. Whenever a molecule interacts with electromagnetic radiation, a quantum of energy is either absorbed or emitted. This includes those related to the change in rotational or vibrational modes. This is called the selection rule for infrared spectroscopy. Infrared spectroscopy is not the only vibrational spectroscopy, Raman

spectroscopy can be carried out for complementary analysis to infrared spectroscopy, yet it has different selection rules, where a net change in bond polarizability is required for a transition to be Raman active.

To understand the change of electric dipole in molecules, we can consider the molecule to be a system formed by masses joined by bonds with spring-like properties. Hence, models employed in infrared spectroscopy focus on the description of the molecular vibrations in terms of the normal modes, which are the minimum set o fundamental vibrations that can describe the system.

Since the atoms are bonded together, the molecule exhibits only 3 degrees of freedom due to translational motion. For linear molecules, which exhibit 180 angles, only 2 degrees of freedom exists due to rotational motion (for example CO_2, O=C=O) as the rotational axis along the molecular axis leaves the molecule unchanged. On the other hand, non-linear molecules possess 3 rotational degrees. Therefore, the number of normal modes of vibration of a molecule formed by N atoms can be estimated by the following formulas:

$$\begin{aligned} Linear\, molecule\, vibrational\, modes = &\quad 3N-5 \\ Non-linear\, molecule\, vibrational\, modes = &\quad 3N-6 \end{aligned}$$

where the term $3N$ constitutes the total degrees of freedom (translational, rotational and vibrational) and N the number of atoms contained in the molecule.

The previous equations to determine the total number of vibrational modes present in a molecule do not take into account degenerated states, i.e. vibrational modes with the same frequencies. It is thus common to observe less absorbance peaks in the infrared spectra than expected. The vibrational modes can be separated in two main groups, in-plane and out-of-plane vibrations. Among the in-plane modes we can find

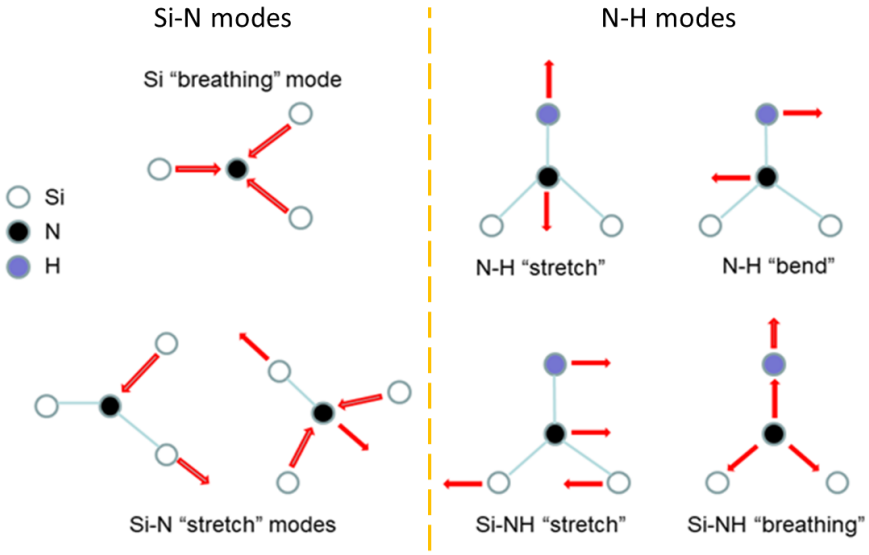

Figure 3.16: *Vibrational modes present in silicon nitride layers deposited by PECVD.*

stretching (change in bond length) which can be symmetrical (in-phase) or asymmetrical (out-of-phase), and bending (change in bond angle) which constitutes deformation or rocking. In contrast, out-of-plane modes include wagging and twisting vibrational modes, and bending. Figure 3.16 shows the infrared active normal vibrational modes in Si_3N_4, two asymmetric stretching and one breathing (in-phase) modes. Furthermore, when H is present, four infrared active modes can be distinguished and are divided into the N-H (stretch and bend) and the Si-(NH) (symmetric and asymmetric stretching) vibrational modes, because of the different frequencies involved. It is important to clarify that H does not only bond to N but also to Si, and leads to several vibrational modes according to the molecule being formed (H-Si-Si_3, H-Si-HSi_2, among others). More information can be found in references [16,201,202] and are discussed in chapter 5.

The infrared spectrum can be divided in three regions: mid-, near- and far-infrared. Because information regarding the bonding configuration of a-SiO_xN_y materials is located at the mid-infrared, near- and far-infrared spectra will not be discuss further in this section. The mid-infrared spectrum (400 - 4000 cm^{-1}) is commonly subdivided into four regions, according to common group frequencies (absorbance bands

assigned to particular features of the molecule): the region between 2500 - 4000 cm^{-1} corresponds to the stretching vibrational modes of diatomic units involving H, such as Si-H, N-H and O-H. Around 2000 - 2500 cm^{-1} is the triple-bond region, followed by the double-bond region (1500 - 2000 cm^{-1}). Between 600 - 1500 cm^{-1} the fingerprint region is located, where the most characteristic vibrational modes of a molecule are present. In the near-infrared (4000 - 13000 cm^{-1}) region, overtones or combinations of the fundamental stretching bands are present, exhibiting weak intensities and overlap, becoming less suitable for quantitative analysis. In the far-infrared (100 - 400 cm^{-1}) region, the vibrational information concerns only molecules containing heavy atoms, molecular torsions or crystal lattice vibrations. The characteristic bending modes involving the whole molecule are also present in this region.

Infrared spectroscopy was carried out for a-SiO_xN_y layers deposited by PECVD, with a focus on the fingerprint region (400 - 4000 cm^{-1}) to characterize H-related bonds present in the oxynitride network as well as the transformation of the characteristic tetrahedra. While there are many methods available for the acquisition of an infrared spectrum, we utilize Fourier transform infrared (FTIR) spectroscopy as it is one of the common methods, with high flexibility and fast data recording in comparison with traditional dispersive instruments.

3.5.1 Fourier transform infrared spectroscopy

Fourier transform infrared (FTIR) spectroscopy is among the most common infrared techniques used to characterize a-SiO_xN_y layers and other infrared active materials. In FTIR, the sample is located in the light path of a globar source (U-shaped SiC piece) that emits between 400 and 12000 cm^{-1}. Light from characteristic wavelengths is absorbed by the sample while the rest is transmitted to the detector. The absorbance is related to the excitation of vibrational modes as discussed above. The location of each band allows the identification of the excited mode while the amplitude and width can be used to determine the bond density.

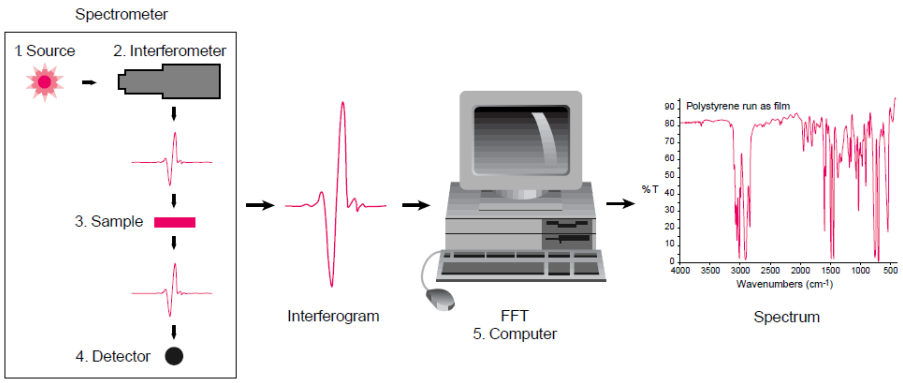

Figure 3.17: *FTIR working principle.*

FTIR spectroscopy offers high sensitivity, fast data acquisition and simplicity by measuring the complete infrared range of interest simultaneously. This is done by using an interferogram to produce a single signal composed of the infrared frequencies of interest. Thus, when the signal traverses the sample, the specific changes recorded in the single signal with respect to the original spectrum of the light source (reference) can be traced back to each infrared frequency by fast Fourier transformation of the signal (Fig. 3.17). Most FTIR set-ups employ a Michaelson interferometer. The beam is generated at the light source where a mirror configuration allows the beam to be divided by a KBr beam splitter (Fig. 3.18). One beam is reflected off to a fixed flat mirror. The second beam is reflected to a mirror connected to a motor that allows the mirror to move small distances (a few millimetres). Both beams are reflected and meet again at the beam splitter, where they recombine (interfere) creating a single signal called interferogram. The interferogram is then focus by a mirror into the sample chamber, where the sample is located and the transmitted interferogram is latter collected by the detector. The advantage of this technique is that every data point of the interferogram possess information about every infrared frequency considered in the measurement.

For the analysis and characterization of a-SiO_xN_y layers deposited by PECVD, we used a Bruker Vertex 80v FTIR (Figure 3.18) with a spectral resolution of 2 cm^{-1}

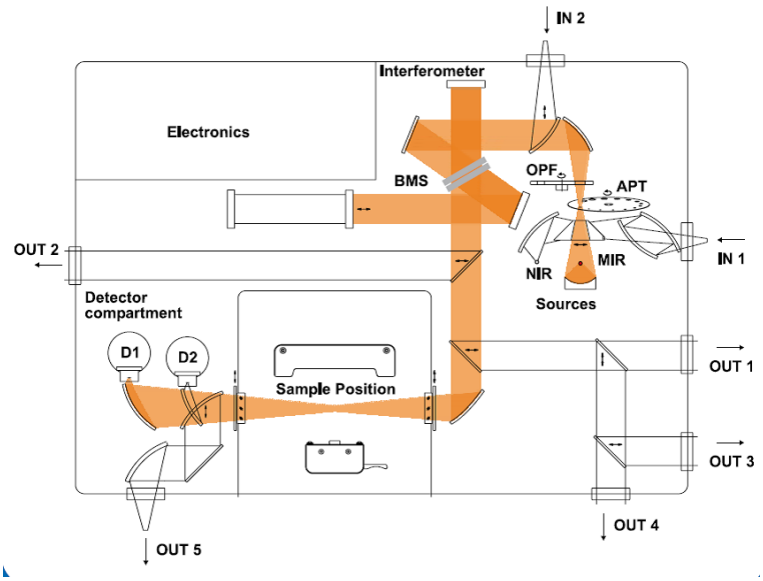

Figure 3.18: *Schematic and beam path of the Bruker 80v FTIR. The beam is produced from any of the two available sources (near- and mid-infrared) and passes through an aperture (APT) which can vary between 1 and 8 mm and has the possibility of couple an optical polariser filter (OPF). The beam travels then through a Michelson interferometer where the signal is process into an interferogram. Afterwards, the beam is reflected and focus into the sample, located in vacuum at the sample chamber. The transmitted signal is the focus into any of the two available detectors (DTGS or LN-MCT).*

in the mid-infrared region in vacuum, to prevent any contribution from moisture. The mid-infrared source is a Globar source that emits wavelengths between 4 to 15 μm. The beam is diverted to a Michaelson interferometer configuration that holds a standard KBr beam splitter capable of covering a spectral range from 350 - 8000 cm^{-1}. The beam is then focused into the sample chamber, before reaching the detector area.

Two detectors were employed during this study, a standard room temperature pyroelectric DLaTGS with a KBr window, which covers a spectral range from 250 to 12000 cm^{-1} and a liquid N_2 cooled MCT narrow band with a BaF_2 window, with a spectral range from 600 to 12000 cm^{-1}. The first detector provides a full spectrum of the fingerprint region while the second is well-known for exhibiting a better spectral resolution in the region between 2500 and 4000 cm^{-1}, improving the resolution of the bands associated with H in the a-SiO_xN_y structure. Measurements were carried out with an aperture of 6 mm and an average of over 200 spectra was performed to improve data quality.

Infrared analysis

When the infrared beam impinges on a sample, photons of certain frequencies will be absorbed while for other frequencies they do not interact with the sample, i.e. they are transmitted. To be absorbed, the photon must have a frequency corresponding to the characteristic vibrational frequency of a certain molecule, resulting in the attenuation with respect to the original signal of the infrared beam. For a given illuminated area A, the attenuation I with respect to the initial intensity I_o can be quantified in terms of the Beer-Lambert law for a sample with thickness L by considering that the concentration $\alpha(\omega)N$ of infrared active molecules is distributed homogeneously across the sample, hence:

$$-\frac{dI(\omega)}{dx} = \alpha(\omega)I_0(\omega). \tag{3.25}$$

Which leads to the expression for the absorption coefficient $\alpha(\omega)$:

$$\alpha(\omega) = \frac{1}{L} ln \left[\frac{I(\omega)}{I_o(\omega)} \right] \approx 2.3 \frac{A(\omega)}{L}, \tag{3.26}$$

where the absorbance $A(\omega)$ is defined as:

$$A(\omega) = logI_o - logI = log \left[\frac{I_o}{I} \right]. \tag{3.27}$$

The absorption of a photon of a specific frequency will lead to an absorbance band, which translates into a bond density N as follows: [203]

$$N = \frac{1}{\Gamma} \int \frac{\alpha(\omega)}{\omega} d\omega = \frac{1}{\Gamma L} \int 2.3 \frac{A(\omega)}{\omega} d\omega \approx \frac{1}{\Gamma L} \left(\frac{2.3}{\omega} \right) A_{abs}, \tag{3.28}$$

where γ is the strength of the absorption bands, A_{abs} corresponds to the area of the absorbance band of interest. The relationship allows quantitative estimation of the density of oscillators (or bond density) with frequency ω.

Bond	Mode	Wavenumber [cm^{-1}]	Γ ($\times 10^{19}$) [cm^{-2}]
SiN	N-Si_3 symmetric stretching	490	-
Si-H	Si-H wag-rocking	640	-
Si-N	Si-N distorted stretching	790	2
Si-N	N-Si_3 asymmetric stretching	850	2
Si-N	Si-N stretching of H-SiN_3	950	2
Si-O	Si-O symmetric stretching	1040	-
N-H	Wag-rocking	1150	2
Si-O	Si-O asymmetric stretching	1180	-
Si-H	Si-H deconvoluted in seven modes	2000 - 2300	several values
N-H	N-H stretching	3400	9
O-H	H-O-H stretching	3500	32
O-H	SiO-H stretching	3600	32

Table 3.2: *Infrared vibrations and bond strengths of a-SiO_xN_y materials [16, 17].*

The absorbance signal is measured by normal incidence of an infrared beam on the selected sample layer which has been deposited on a c-Si wafer (100) of 500

μm thickness, exhibiting a variable content of dopants (depending on the electrical characteristics) which are infrared active as well. Therefore, the determination of the absorbance is done by acquiring the transmitted signal from the a-SiO_xN_y sample compared against the transmitted signal from a pristine c-Si (100) substrate. After the corresponding background subtraction, the resulting absorbance spectra typically exhibit a broad background in the absorption signal that is not related to the vibrational modes, which can be corrected using the OPUS software by fitting a baseline using a polynomial approximation. The signal processing is exemplified in Figure 3.19 where the transmitted spectrum from the Si substrate is subtracted from the actual measurement leading to the final absorbance spectrum. It is possible to distinguish four weak and one main absorbance band as part of the characteristic FTIR spectra of a-SiN_y. From the data in table 3.2 we can relate each band with its corresponding vibrational mode. In particular, the main absorbance band is not formed by a single or a two-band contribution but rather contains several contributions from symmetrical and asymmetrical vibrational modes from the Si-N bonding configuration and due to the presence of H bonds in the Si-N network.

The main absorbance bands of the samples analyzed by FTIR are formed by absorption bands between 790 to 1150 cm^{-1} represented by a composition of Gaussian and Lorentzian bands. A spectral analysis was carried out by deconvolution of the different contributions to the main absorbance band, where each vibrational mode involved contributes with a Gaussian absorbance band as shown in Figure 3.20. The selection of solely Gaussian contributions has been corroborated by different authors as the best fit to several spectral features [204, 205]. Figure3.20 shows the deconvolution of the main absorbance band for a-SiN_y. We can observe the good agreement between the four band contribution with the cumulative signal.

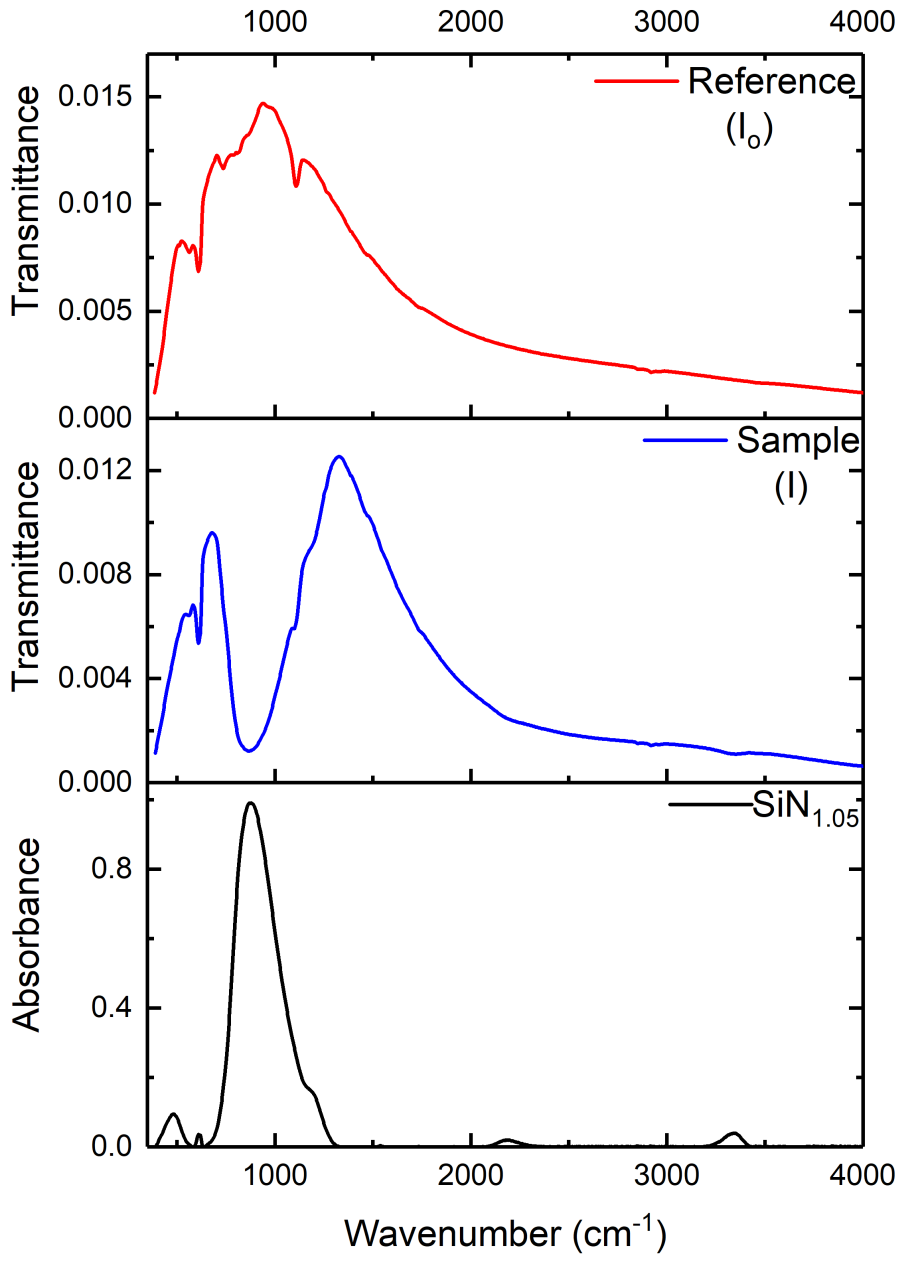

Figure 3.19: *FTIR transmittance spectra of a c-Si substrate (top), c-Si substrate with a deposited a-SiN$_y$ thin layer (middle), and corresponding absorbance spectra after background subtraction and baseline correction (bottom).*

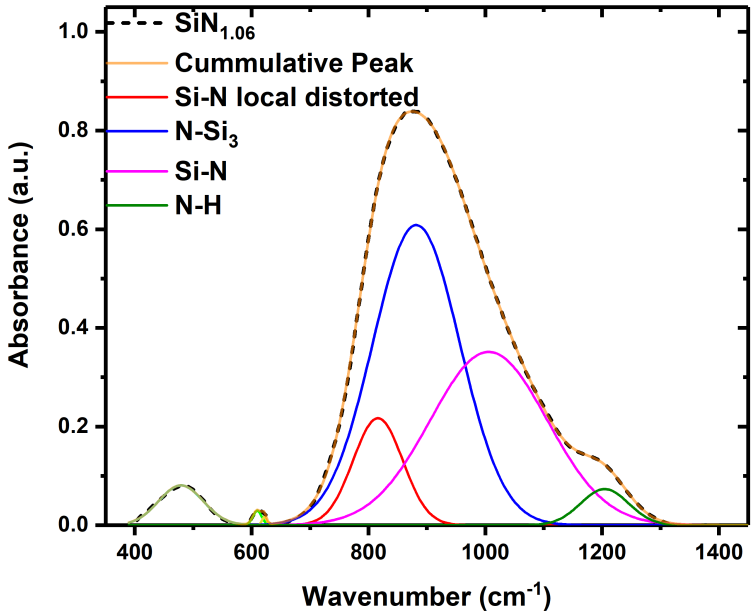

Figure 3.20: *Deconvolution of the main absorbance band for PECVD a-SiN$_y$.*

3.6 Thermal annealing

Selected samples were annealed to promote the formation of metallic nanoparticles after ion implantation or thermal deposition. We use two different annealing methods: furnace and rapid thermal annealing. Samples of a-SiN$_y$ implanted with Au followed a standard thermal annealing process in a conventional resistively heated quartz tube furnace (LINDBERG/MPH 1500 ° Heavy Duty tube furnace) [206]. The tube is enclosed by two metallic lides connected to an inlet and outlet tube. The inlet tube allows the usage of different annealing gases, such as N_2, Air, O_2, Ar or forming gas (95% N_2 + 5% H_2) and is limited to a flow of 100 sccm to create a laminar flow. The outlet tube is connected to a system composed by a beaker partially filled with oil to guarantee the continuous gas flux during annealing while preventing air contamination. The samples were placed on top of a c-Si substrate inside a quartz boat and positioned in the center of the furnace tube following temperature stabilization. Annealing was generally performed for 60 minutes at temperatures ranging between 1000 and 1100 C in N_2 and Air atmospheres.

Layered samples involving very thin Au layers were annealed using an RTA (AET thermal Rapid Thermal Processor RX) system [207]. The RTA equipment is composed of a water cooled, internally gold plated, aluminium enclosed chamber containing a quartz window and tray. The sample lies on top of a 4-inch c-Si wafer in contact with a thermocouple to monitor the c-Si wafer temperature. The heating system consists of an array of quartz lamps capable of providing a homogeneous infrared irradiation of the quartz chamber and heating rates up to 300 °C/sec. The system allows the use of N_2, O_2 and Ar annealing gasses. In contrast to the conventional annealing, where the sample reaches a thermal equilibrium with the environment inside the furnace, RTA is a non-equilibrium process where the increase of temperature depends on the light absorption of the sample. The annealing process was done at the AET Rapid Thermal Processor RX under a N_2 atmosphere at 1000 °C for two minutes. The RTA system and procedure was used based on the results observed for Ge thin layers deposited in-between a stack of a-SiO_2 layers [162], where the RTA process took place for two minutes at temperatures close to the melting point of Ge.

3.7 Thermal evaporator

Thermal evaporation was used for the deposition of very thin ($\leq$ 5 nm) Au layers on top of the a-SiO_x or a-SiN_y layers. A Lesker Nano 36 thermal evaporator with an FTC-2800 controller was used [208]. Thermal evaporation is a so-called physical vapour deposition (PVD) technique.

The desired metal to be deposited is generally in a highly pure form, placed in a tungsten boat, and resistively heated in a high vacuum chamber to a temperature which produces some vapour pressure, commonly close to the melting point (Fig.3.21). The evaporated material produces a vapour stream, which traverses the chamber and hits the substrate forming a coating or a thin film. The process is monitored in real time by a quartz crystal monitor, providing information on the

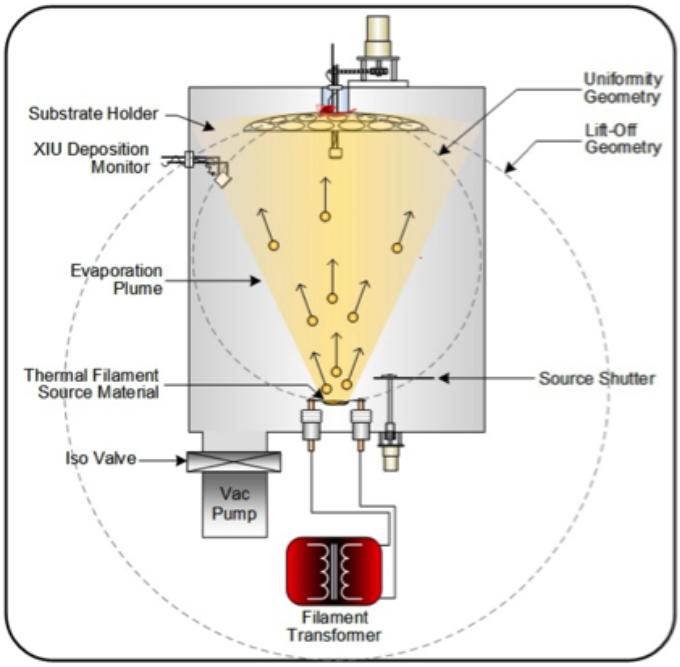

Figure 3.21: *Diagram of the thermal evaporation process.*

deposition rate. The equipment allows to run a heat profile to pre-condition Au before opening the source shutter and carry out the deposition. The deposition process commonly consists of two separated sequential power ramps. The first is a slower heating process that takes the material to a temperature slightly below vaporization aimed to reach an equilibrium before a second heating ramp, where vaporization takes place. The latter corresponds to the power required to reach the desired deposited rate. At this point, the substrate shutter, which prevents the material deposition until ideal conditions are met, is open and the deposition takes place. Once the desired film thickness is reached, the shutter closes and the material is cooled down.

3.8 Electron microscopy

Electron microscopy is a very powerful tool that allows to image objects with dimensions in the nanometre and sub-nanometre range. Such resolution is possible

because the wavelength associated with the electrons used in electron microscopy is about five orders of magnitude lower than in an optical microscope where the resolution is restricted to about half the wavelength of the light source, known as the Abbe diffraction limit [12]. As the electron's wavelength λ is inversely proportional to its kinetic energy E ($\lambda = \frac{hc}{E}$) an energetic electron can exhibit a rather short wavelength, for example, a 200 keV electron has a wavelength of 0.025 nm. It is worth to mention that very recently new optical microscopy techniques have been developed with resolution beyond the diffraction limit, such as far-field fluorescence or plasmonics microscopy [209]. While the wavelength of the electron beam λ is within a few pm, in a typical electron microscope the spatial resolution is commonly about 0.2 nm, which is a consequence of the spherical aberration of the objective lenses [210] [4]. Thus, the resolution can be improved by increasing the microscope voltage or by correcting for spherical and chromatic aberrations. Increasing of the microscope voltage is not always desirable as it can lead to radiation damage to the sample. For many materials the threshold for knock-on atom displacement is between 100 and 400 keV. Instead, aberration correction can lead to significant enhanced resolution while preventing radiation damage. Aberration corrected electron microscopes have become more widely used nowadays and can achieve sub-Angstrom resolution [211]. Chromatic aberrations can be corrected by using a monochromator, which can reduce the energy spread to 0.1 eV, and with the use of an imaging energy filter, reducing the inelastically scattered electrons. Spherical aberration is unavoidable for rotationally symmetric focusing systems, such as solenoid focus, and is commonly compensated by adopting a different symmetry for electron optics like a paraxial electron optics arrangement, which involves either sextupoles or octopoles in combination with quadrupoles [212].

[4] The resolution limit is given by Scherzer formula $\leq C_s^{1/4}\lambda^{3/4}$ where C_s is the aberration coefficient.

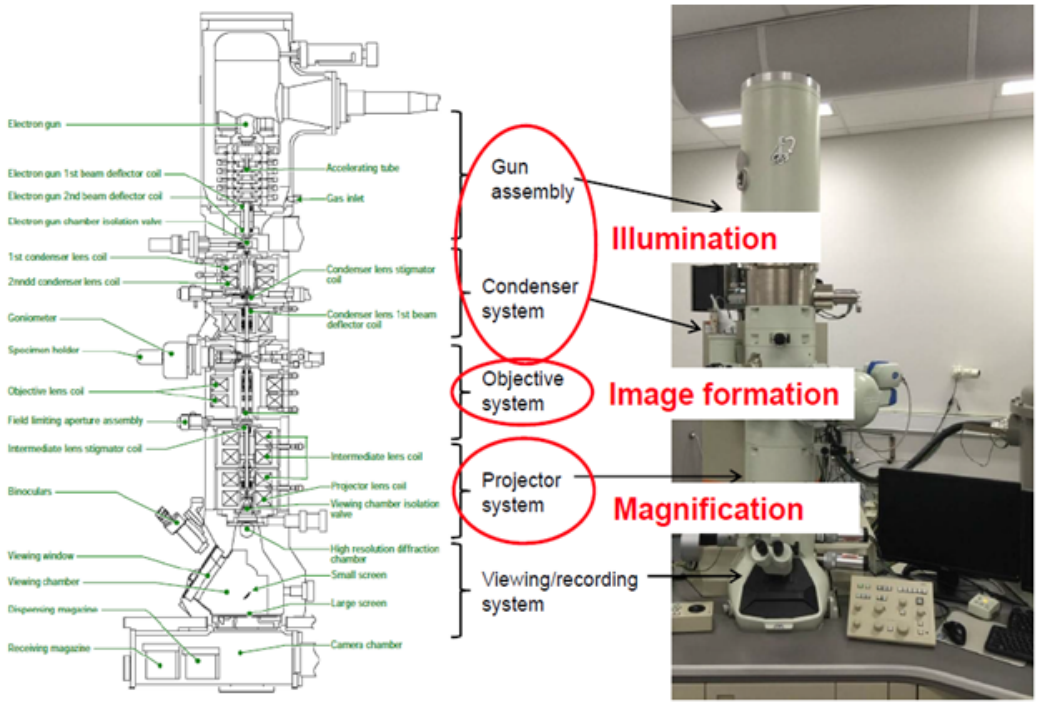

Figure 3.22: *TEM set-up of the JEOL 2100F.*

3.8.1 Transmission electron microscope

For this thesis, a JEOL-2100F was employed for transmission electron microscopy, which is a 200 kV FE (field emission) analytical microscope with a resolution of 0.23 nm in high resolution mode located at the Centre for Advance Microscopy at ANU.

A schematic and image of the JEOL 2100F is presented in Figure 3.22 where the elemental components of the electron microscope are highlighted: the illumination, image formation and magnification system. At the top of the microscope, electrons are emitted from a field emission gun (FEG) composed of a Schotky (ZrO_x/W) pointed cathode tip of 0.1 μm in diameter and two anodes, where the ZrO_x reservoir further reduces the work function of W. A positive voltage of few kV is applied at the first anode for extraction which is capable of producing a field-emission current of 1 - 10 μA, followed by a post-acceleration configuration between the cathode tip and a second grounded anode, where the electron beam reaches its final energy, producing a

focused electron probe of several nm in diameter, crucial to obtained a probe beam of widths between 0.2 and 1.5 nm for scanning transmission electron microscopy (STEM) mode. In particular, FEG are sources of high brightness, coherent and low energy spread electron beams [12, 213, 214].

The generation of the electron probe is followed by a two condenser-lens system, for focusing the beam to provide sufficient uniform illumination of the specimen and intensity for high magnification, and to reduce specimen drift and radiation damage. The condenser-lens system also allows to control the illumination aperture, for medium and high-resolution and the generation of a small electron probe to work in STEM mode. The condenser system is equipped with a stigmator to compensate for astigmatism and decrease the crossover image diameter (Fig.3.22). The size of the aperture of the second condenser determines the maximum semi-angular aperture of the illumination and the convergence of the beam at the specimen.

Behind the specimen, the objective lens is responsible for the formation of the first image. It has an asymmetric design capable of tilting the beam for diffraction experiments. Although it has a low magnification, the quality of the image generated determines the resolution of the final image. Together with the objective lens, an objective aperture can be selected in order to select the electrons that will contribute to the image. Aberration does not only affect the resolution but also the phase of the electron waves after passing through the specimen, which is relevant for high resolution TEM (HR-TEM).

While the image is formed by the objective lenses (objective system), the intermediate and the projector lenses are responsible for the magnification (projector system). The intermediate lens can be focused on the image formed by the objective lens or in the back of the focal plane of the objective lens to show the real space image of the specimen or the corresponding diffraction pattern, respectively. The final magnification can be varied by controlling the strength of the intermediate and projector lenses. The resulting image is then projected onto a fluorescent screen or a

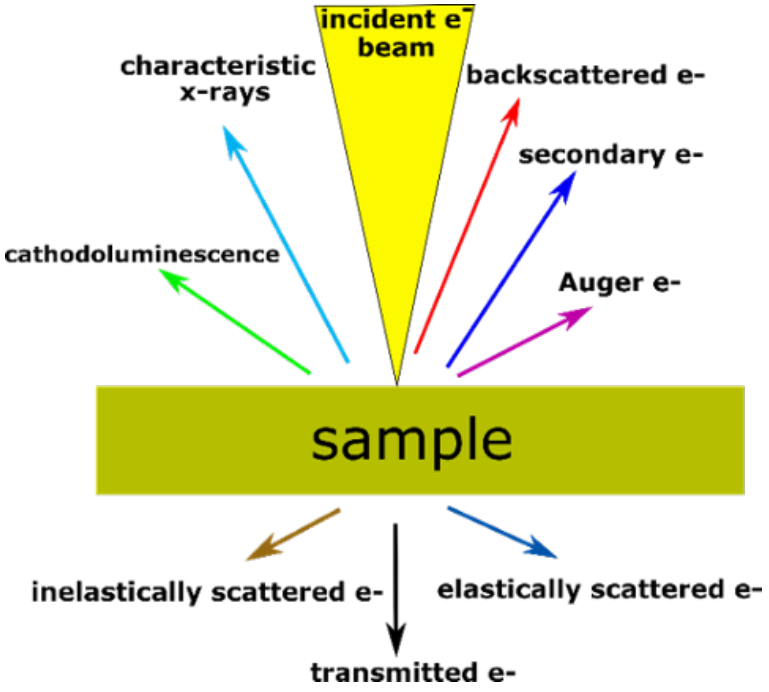

Figure 3.23: *Schematic of the electron-matter interactions, adapted from [12].*

CCD (charge-coupled device) camera by the projector lens where the formed image is recorded.

3.8.2 Transmission electron microscopy

When energetic electrons penetrate the sample, they will lose kinetic energy via elastic and inelastic collisions. Elastic collisions can occur with the target nuclei, i.e. Rutherford scattering, or with their electrons via screened Coulomb potentials that result in small deviations from their original path. On the other hand, inelastic collisions lead to the ionization of the sample, producing X-rays or the emission of secondary electrons characteristic of the sample's composition. Figure 3.23 summarizes the electron-matter interactions.

In this thesis, the samples were imaged predominantly via bright- and dark-field imaging, and to lesser extend by using high-resolution imaging. Bright-field (BF)

imaging uses a small objective aperture to block the diffracted beam. Hence, everything that diffracts will look dark (diffraction contrast). In this configuration, two mechanisms of diffraction contrast can be distinguished according to the mass and thickness of the sample. Mass contrast results from Rutherford scattering, where heavy elements exhibit a larger Rutherford cross-section and result in darker objects. This is exemplified in Figure 3.24 (a) for elongated Au NPs when located at the interface of a-$SiO_{1.9}$/a-$SiN_{1.06}$. Also, when the thickness of the sample increases, or of a region in the sample, the probability of an electron being scattered to high angles and blocked by the aperture increases too. This produces a thickness contrast and can be seen in Figure 3.24 (a) on the top right section as it corresponds to the region further from the surface of the sample. On the other hand, dark-field (DF) imaging uses a small objective aperture too, but, in this case the electrons that formed the image in BF are blocked allowing the detection of those scattered at higher angles at a particular diffraction spot. This contrast principle is also used in HAADF imaging and it is shown in Figure 3.24 (b). Electrons are weakly scattered by the substrate (which looks dark in the micrograph) but stronger by the Au NPs. A further capability is the formation of nanometre-sized electron probes, 0.2 - 10 nm in diameter, by means of the four-stage condenser-lens system which enables the microscope to operate in scanning transmission electron microscopy (STEM) mode with a resolution defined by the electron-probe diameter.

High-resolution TEM (HRTEM) images are formed by the interference produced between the forward-scattered beam, which provides a reference phase of the electron wave-front, and at least the first diffracted beam (phase-contrast) by selecting an objective aperture large enough to avoid truncation in k-space. Another source of phase contrast is produced when two crystalline structures of nearly identical periodicity are superimposed, parallel to each other or slightly rotated, producing an interference pattern known as Moiré patterns, which is commonly observed for Au NPs when two or more grain boundaries are present in the same NP (Figure 3.24 (c)).

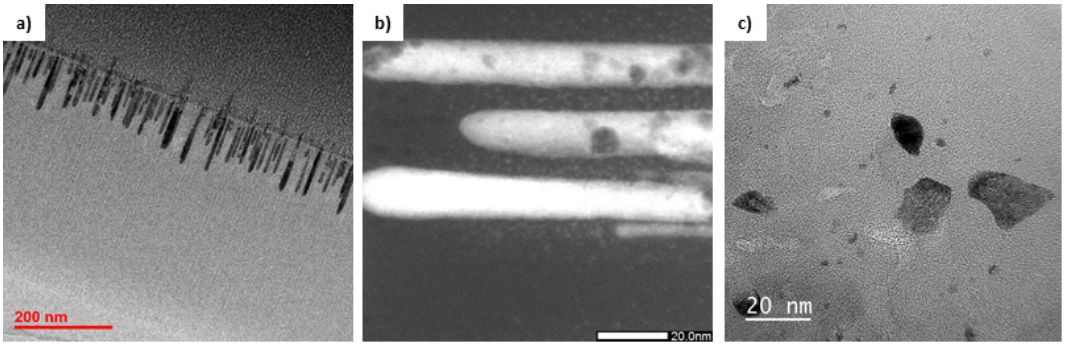

Figure 3.24: *BF-TEM image of elongated Au NPs (a). HAADF in STEM mode image of elongated Au NPs (b). HR-TEM image of Au NPs in polycrystalline Si_3N_4 (c).*

3.8.3 High angle annular dark field (HAADF) in STEM mode

Scanning transmission electron microscopy is different from TEM as the specimen is scanned point-by-point with a very small probe perpendicular to the surface rather than illuminating the whole area simultaneously. In STEM mode, two pairs of magnetic coils are used to scan the beam around the first focal point. The third condenser lens then ensures the electron beam probe is parallel to the optical axis, avoiding chromatic aberration. In STEM mode, magnification is controlled by the dimensions of the scanned area rather than through lenses, as in TEM. However, they are still affected by aberration originated at the source. Typically, for HAADF the resolution is estimated in terms of the FWHM of the probe beam profile.

In HAADF, images are formed from incoherently elastically scattered electrons, where heavier elements are stronger scatterers, leading to a mass contrast termed 'Z-contrast imaging'. Because incoherent scattering is involved, phase differences and interference effects between electrons are not relevant and only the scattering intensities from individual atoms are considered. The image is formed by collecting the electrons that are elastically scattered to high-angles using an annular detector (DF), as shown schematically in Figure 3.25. As the scattering angle is about one order of magnitude larger than Bragg scattering, within this configuration contributions due to Bragg scattering are avoided [12].

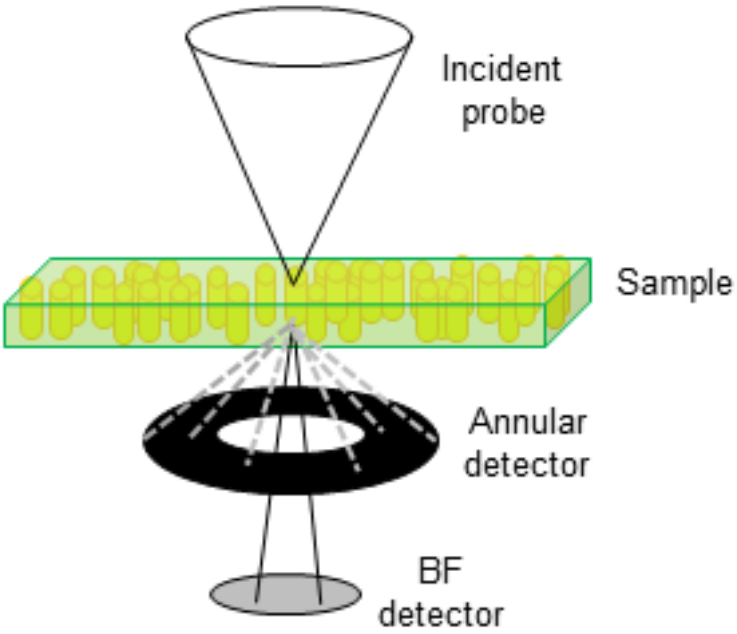

Figure 3.25: *Schematic of the HAADF-imaging set-up in STEM mode. HAADF was carried out with a conventional ADF detector by varying the position of the detector to reach higher scattering angles. The position of the BF detector was added for clarification.*

Elastic high angle scattering is the result of Rutherford scattering of energetic electrons travelling close to the atomic nucleus and where the scattering cross-section scales with atomic number, leading to composition information. Thus, similar to RBS analysis, HAADF exhibits small scattering cross-sections for light elements, such as N or Si in the present case. By taking this into account, HAADF was employed mainly to analyse Au nanostructures embedded in a-SiO_x and a-SiN_y, where the high Z contrast permits better resolution of nanostructures with dimensions below 2 nm. Finally, in the JEOL-2100F there is only one ADF detector available thus the high-angle ADF condition is achieved by increasing the camera length using the objective lens. It is important to mention that the requirement of a high-intensity electron probe during the scanning process can lead to detrimental effects such as contamination and beam damage, effects that were observed to lesser extent in this work.

3.8.4 Sample preparation

The specimen preparation varies from cross-sectional to plan view, the former allows a depth resolution while the latter a lateral view of the specimen. In this work cross-sectional transmission electron microscopy (X-TEM) was employed to study the ion irradiation-induced structural modification of the samples as a function of depth.

The selected specimen preparation was carried out by cutting rectangular sections of the selected samples of 3 mm in length and 1 to 2 mm in width using a slow speed diamond saw with a widh of 0.05 mm (Fig. 3.26 (a)). The specimen is then prepared by gluing two samples with the area of interest facing each other together with an epoxy glue, and by adding two Si pieces with a similar width on both sides for support (Fig. 3.26 (b)). Afterwards, a cross-sectional cut is carried out with an ultrasonic cutter and a circular cutting tip of 3 mm in diameter (Fig. 3.26 (c)). Then, the specimen is thinned down by mechanical polishing (down to ≤ 100 μm), followed by dimple grinding (down to ≤ 10 μm around the area of interest) (Fig. 3.26 (d)). To reach the ideal thickness, a subsequent ion milling process took place with a precision

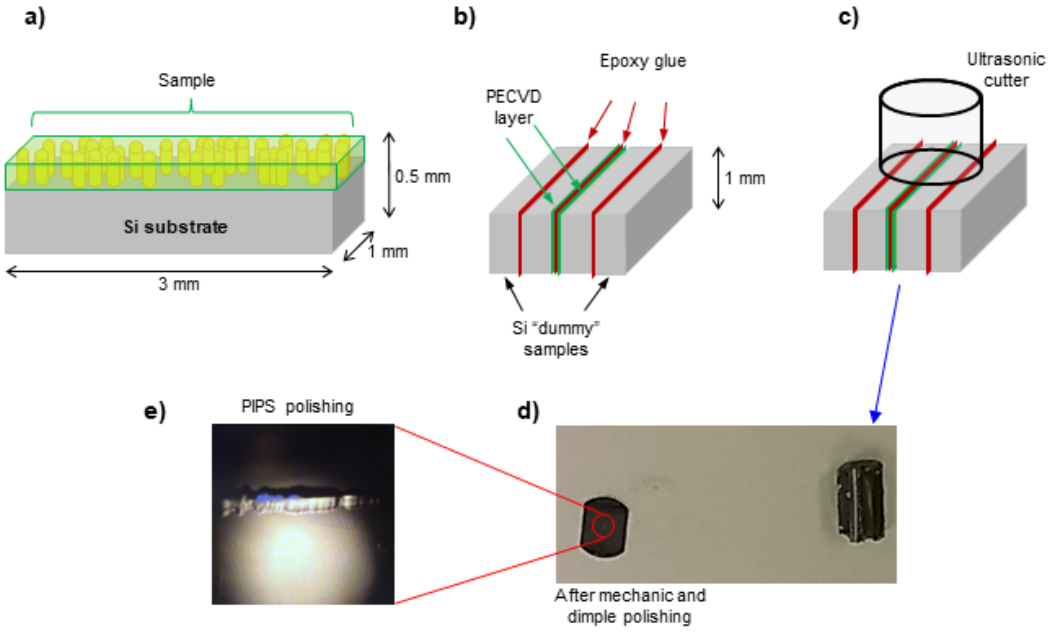

Figure 3.26: *TEM sample preparation process.*

ion polisher system (PIPS), using two Ar beam guns with an angle incidence of ± 4 and energies between 4 and 0.4 keV until observing an aperture of the sample(Fig. 3.26 (e)). Around the aperture, the thickness of the sample is about few nm near the surface and extends typically for around 1 mm. For the case of ion implantation or ion beam shaping of Au NPs, the ion milling process was carried out at room temperature while in the case of Ag NPs, the process took place at LN temperature (- 169 °C) to prevent heating and diffusion effects. Due to the preparation process, the samples presents a thickness gradient with depth, allowing the imaging of the sample at different depths.

Chapter 4

Synchrotron-based small angle X-ray scattering

SAXS possesses high sensitivity to changes in the electron density at the nanometre scale. Such changes can be correlated to the atomic density and the morphology of the scattering objects can be obtained. In many cases the technique allows the determination of the dimensions and the fine structure of ion tracks formed in amorphous materials, a very challenging task with other techniques. At the same time, the simultaneous measurement of a large number of scattering objects provides good statistics, making it a powerful standalone or complementary technique. In the present chapter the physical principles, experimental details and data analysis of the SAXS technique related to this thesis are presented.

4.1 Introduction

X-rays are part of the electromagnetic spectrum with energies between hundreds of eV and a few hundred keV corresponding to wavelengths between 10^{-6} to 10^{-10} cm (Figure 4.1). They were first discovered and named by W. C. Röntgen in 1885, for which he was awarded the first Nobel prize in physics, after observing the fluorescence of a barium platinocyanide plate while studying cathode rays from Hittorf's, Crookes' and Lenard's tubes [215,216]. Furthermore, he reported two very significant properties of X-rays: (i) they can be absorbed by solids at different rates depending on their density, and (ii) they did not show evidence of refraction or reflection.

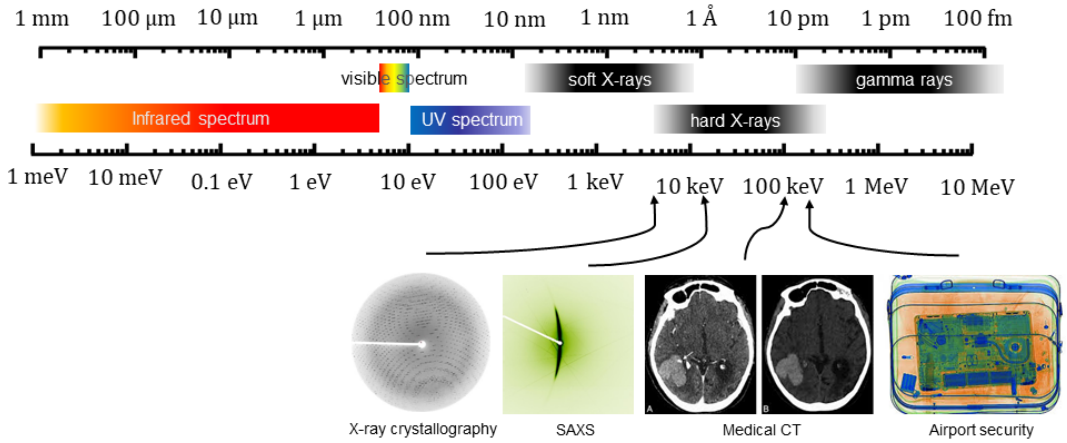

Figure 4.1: *Spectrum of electromagnetic radiation.*

Upon incidence of an X-ray beam on a solid or liquid medium, photons can be either absorbed or scattered. For the energies used for our experiments (10 - 12 keV), the absorbed X-ray photons can excite electrons or interact via the photoelectric effect, resulting in ionized target atoms. It is noteworthy that at this energy range, pair production has negligible effects.

The absorption of an incident X-ray beam of Intensity I_0 by a material of thickness x, can be correlated to the transmitted intensity $I(x)$ by the following equation:

$$I(x) = I_0 e^{-\mu x}, \tag{4.1}$$

where the term $\mu = \mu(E)$ is the attenuation coefficient and is dependent on the energy of the X-rays. It is of great importance to determine the penetration and energy deposition of the incident X-rays, relevant in biological and medical applications, radiation shielding and material science. The difference in attenuation rates is the basis for medical X-ray imaging, for example. Because the reflection is negligible for X-rays, the attenuation coefficient can be determined directly from transmission experiments.

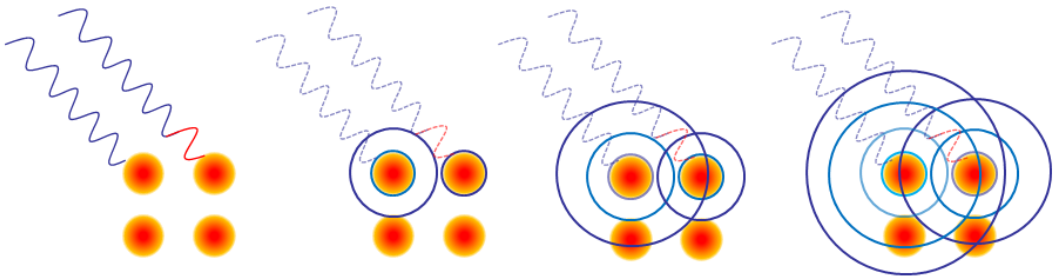

Figure 4.2: *X-rays are primarily scattered by atomic electrons. During the scattering process the electron starts oscillating with the same frequency as the incident X-ray photon. The electron becomes a dipole leading to the emission of a spherical wave. The secondary wave possess the same amplitude and wavelength as the incident signal (elastic scattering).*

On their passage through a material, X-ray photons can be scattered either by the target nuclei or electrons. However, at the energy range used for SAXS, X-rays are primarily scattered by electrons. According to the nature of the interaction between X-rays and electrons, scattering can be elastic or inelastic. The former is characterised by exhibiting neither loss nor gain in energy between the incident and the scattered X-ray photon, while for the latter energy is exchanged as well as momentum. Inelastic scattering, such as Compton scattering is expected to occur, however, it is weak at small angles, its contribution can be neglected. The elastic scattering process is the result of X-rays being absorbed by the target electrons which causes them to resonate at the frequency of the incident beam, leading to the emission of coherent secondary waves, which can interfere with each other (Figure 4.2). The scattering intensity can be described by the Thomson scattering relation:

$$I(\theta) = I_0 \cdot \frac{r_e^2}{L^2} \left(\frac{1 + \cos^2(2\theta)}{2} \right), \tag{4.2}$$

where I_0 corresponds to the beam intensity, r_e is the classical electron radius $\left(\frac{e^2}{mc^2}\right)$, L is the distance between the target and the detector for a given scattering angle 2θ [217].

Diffraction is the result of the interference of secondary waves scattered by a target. In the case of X-ray diffraction (XRD), it can be used to study the periodic atomic arrangement by the relation:

$$n\lambda = 2d \sin\theta, \tag{4.3}$$

for which constructive interference can be expected when the relationship between the angle of diffraction θ and the spearation of the lattice planes d is equal to a multiple integer n of half the wavelength of the incident X-ray beam λ. Equation 4.3 is known as Bragg's law [218]. When the lattice spacing is comparable to the wavelength of the incident beam (few Å), as in the case of inorganic crystals, the angles of diffraction are rather large, typically between 10° and 180° [219]. When the lattice spacing increases to tens or hundreds of interatomic distances, such as in macromolecular crystals or polymers, the diffraction angles are confined within 2° [219]. Such limitation can be overcome by increasing the wavelength of the incoming X-ray beam by decreasing its energy, however, because the X-ray attenuation increases significantly at lower energies, X-ray scattering at lower energies is not the best alternative, instead it is necessary to resolve the scattering at small angles to determine large features. Krishnamurti [220] and Warren [221] observed intense and continuous scattering formed in this angular range for different carbon samples, similar to that found at larger angles. This was later related to the presence of heterogeneities in the material in the form of particles with dimensions of tens to several hundred times the wavelength of the incoming X-rays [219]. Therefore, small angle X-ray scattering can be described, analogous to X-ray diffraction, as a general scattering problem of small particles with sizes between few nm up to few μm [217].

Small angle X-ray scattering (SAXS) has evolved into a powerful technique for determining the size distribution, shape, internal structure, and orientation of particles embedded of dimensions several times larger than the wavelength of the incident X-ray

beam. The motivation of this chapter is to present an overall theoretical background of SAXS, with focus on the scattering produced by particles of specific geometries (spheres and cylinders), the production of highly monochromatic and brilliant X-ray beams, an overview of the experimental set-up used, and scattering pattern acquisition and analysis.

4.2 Experimental details

This section aims to give a brief introduction into synchrotron radiation, the technical information regarding the production of X-rays at the Australian Synchrotron and the SAXS experiments carried out in this thesis.

A bright and monochromatic primary beam is produced by an X-ray source which is collimated into a fine beam before reaching the sample. When the primary beam reaches the sample, a small fraction of the beam is scattered and collected by a 2D detector separated from the sample by a distance dependent on the size of the scattering objects to resolve small angles (the distance from the sample to the detector is called the camera length). The resulting scattering pattern is then analysed to obtain information of the morphology of the scattering objects.

The ideal X-ray source possesses a high spatial and spectral brightness [222]. The former allows the incidence of 10^{15} to 10^{20} X-ray photons per second to a small sample while the latter is essential for high spatial resolution. The production of X-rays can be carried out with conventional X-ray tubes, typically by the conversion of kinetic energy of electrons into X-ray emissions [15]. This is done by accelerating thermal electrons from a hot filament towards a metallic target by the application of a potential difference V. When the electrons penetrate the metallic target, X-rays are produced by two mechanisms: by rapid deceleration of the electrons yielding a continuum photon spectrum, such that $\lambda = \frac{\hbar c}{eV}$. This mechanism is known as Bremsstrahlung. The second mechanism arises from the knocking out of an electron from the inner shells of

the atom followed by the relaxation of an electron located at a higher shell to occupy the available position. This relaxation process is accompanied by the emission of a photon whose wavelength is characteristic of the transition and metal, thus, leading to a characteristic discrete emission [15]. This is the working principle of classical X-ray sources. They can produce a large X-ray flux with a narrow bandwidth (the most widespread corresponds to the electronic transition from the L-shell towards the ground state in copper, known as the Cu-K_α-line). However, it is delivered over a large solid angle at a fixed wavelength. Unfortunately, the continuum radiation from Bremsstrahlung is typically of few orders of magnitude less intense than the discrete peaks [222].

An alternative to conventional X-ray sources originated from the discovery of X-ray synchrotron radiation in 1947 [223–225]. Their origin lies in the fact that electrons moving in a circular trajectory with relativistic velocities emit continuum electromagnetic radiation in a narrow cone, tangential to their trajectory. This radiation has a broad spectral range with spatial and spectral brightness several orders of magnitude higher than conventional laboratory sources. Their properties of self-collimation, high polarization and brightness resulted in a boost in research capability [222]. In the following section the principal characteristics of synchrotron radiation as well as a brief description of the design of the Australian Synchrotron it is presented. Special emphasis is put on the beamline optics of the SAXS/WAXS beamline, where the SAXS measurement for this thesis were carried out.

4.3 Synchrotron radiation

Several decades before the discovery of synchrotron radiation, the electromagnetic radiation generated by a relativistic charged particle moving in a circular trajectory had already been studied. The expression for the instantaneous power emitted in the tangential direction was determined for the first time by Lienard in 1898 [226], which lead to the expression regarding its corresponding angular distribution by

Schott [227]. The construction of the first particle accelerators motivated further studies of this phenomena, resulting in the development of the classical radiation theory for charged particles moving in an arbitrary trajectory in the 1940's by different groups [228, 229], and the consideration of quantum mechanical corrections when the momentum of the radiated photon is similar to that of the charged particle, typically an electron [229–231]. The new theory suggested two main significant effects: the radiation emitted is sharply peaked along the tangent to the orbit, and the power radiated increases with with the electron energy by a power of four. While these results were known to the high energy and nuclear physics community, several groups remained reluctant to accept the radiation emission theory of the electron.

Synchrotron radiation was first observed at the General Electric Research Labs, in N.Y. while searching for radiation losses in cyclic particle accelerators (Betatron and cyclotrons), that were mainly used for collision of high-energy particles. The first attempts to find the proposed radiation were carried out in a 100 MeV Betatron, which was a silver-coated doughnut with complete radiation shielding, but these were unsuccessful. A couple of years later, in 1947 and at the same laboratory, a second attempt was carried out after the construction of a 70 MeV electron synchrotron with the difference that it was not completely enclosed by a radiation shield and had a transparent coating. During the experiments, one of the assistants followed the experiment with the aid of a mirror located next to the radiation shield looking for sparking. The assistant reported the presence of an intense arc inside the chamber coming from the electron beam, confirming the existence of synchrotron radiation [223, 224, 232]. Following the characterization of the newly discovered radiation, it was first applied in spectroscopy analysis in the UV-range using beam ports connected to the main facility. In this configuration, the beam undergoes a repeated sequence of injection, acceleration and extraction at different rates. However, the main use of these facilities remained for high-energy or nuclear science. Therefore, the first-generation of synchrotron-radiation facilities are also referred to as parasitic facilities in storage ring colliders.

The first results using synchrotron light helped to elucidate the potential of the new light source for future applications, resulting in an increasing demand for dedicated sources. With the rapid increasing demand, dedicated sources were designed. For the second- generation of synchrotrons, electron storage rings were built. In the new storage rings, electrons were injected, and accelerated around the ring using a configuration of dipole bending magnets. The bending magnets were energized with an alternate current, which allowed the increase of the field strength with increasing electron energy while the circular trajectory is kept constant.

In the third-generation of synchrotron facilities, such as the Australian Synchrotron (a schematic is presented in Figure 4.4), the working principles are similar to its predecessors with the addition of the so-called insertion devices. Electrons are produced by an electron source and accelerated to relativistic velocities by a linear accelerator (a few hundred MeV) before being injected into a booster synchrotron ring where they are accelerated to velocities closer to the speed of light (a few GeV). The booster ring is formed by two straight sections connected by two semicircular curves composed of several dipole bending magnets. A set of magnetic lenses keep the electrons focused and travelling along the desired trajectory. The straight sections are formed by a series of RF cavities, where the electrons are further accelerated. The electron beam then reaches the adequate energy, or velocity, before being injected into the storage ring. The storage ring consists of a sequence of alternating straight and arc sections. The arc sections comprise of bending and focussing magnets, with the function of bending the beam keeping it tightly packed at the entry of the straight sections. The straight sections are used for different purposes, one is the injection site from the booster ring, a second straight section consists of RF cavities (similar to those described in Chapter 2) to compensate for the energy lost to X-ray production. The remaining sections are designed to incorporate the so-called insertion devices (Fig 4.3 (a) and (b)), which generate X-rays much brighter than the bending magnets. The brightness is defined as the flux per unit area of the radiation source per unit of solid angle of the radiation cone per unit spectral bandwidth: $\frac{Numberofphotons/second}{(mrad)^2(mm^2 sourcearea)(0.1\%bandwidth)}$.

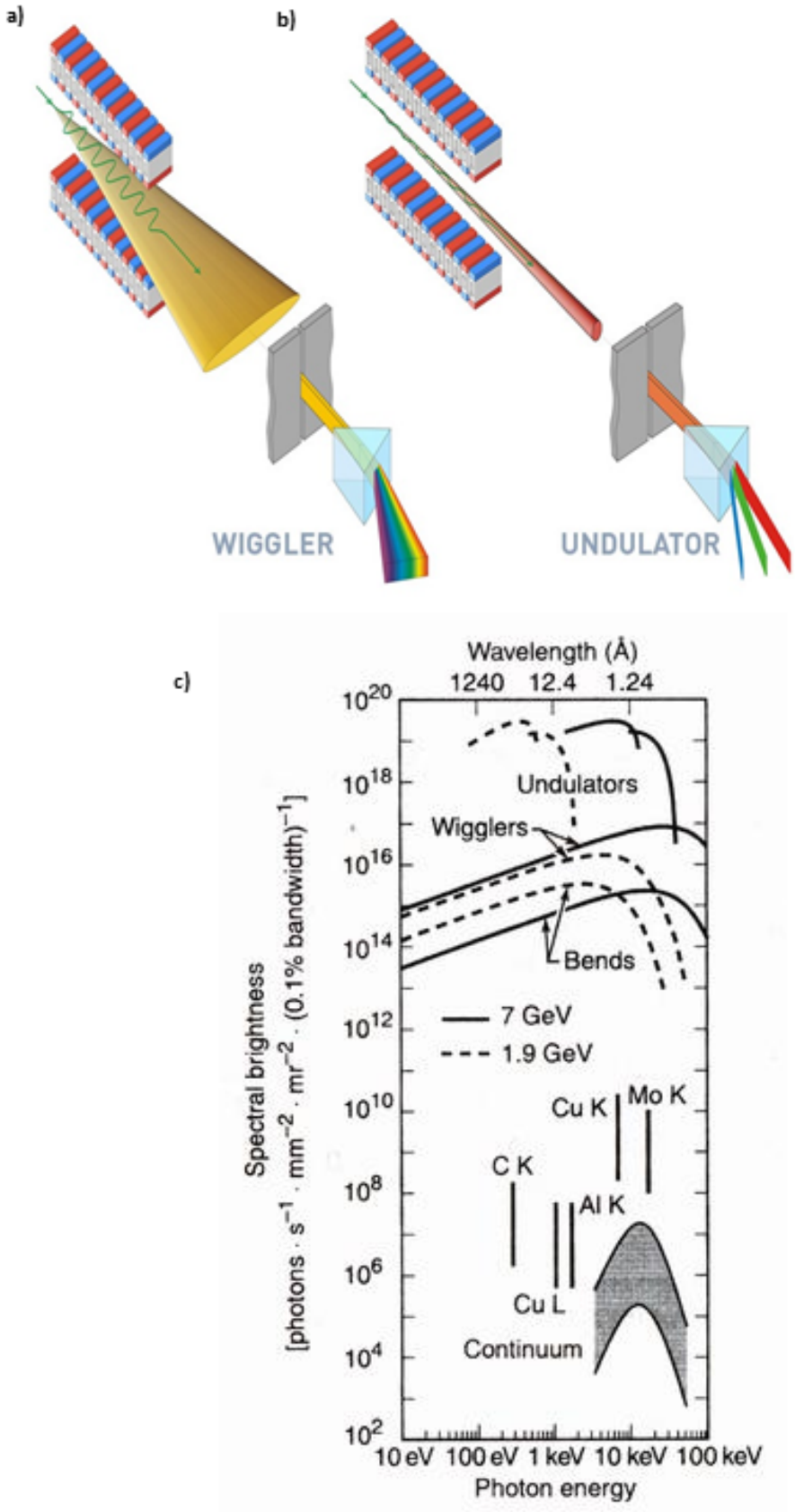

Figure 4.3: *Width, radiation cone and spectrum of synchrotron radiation produced by a wigler (a), undulator (b), and spectral brightness for several synchrotron and conventional X-ray sources [13] (c).*

The insertion devices are arrays of north and south magnetic dipoles that deflect the electron beam in alternate directions and do not produce a net change in the direction of the beam [233]. Two kind of insertion devices are used: wigglers and undulators [222]. Different to the case of the bending magnets, wigglers and undulators are located in the straight sections of the storage ring and they emit light during each oscillation period by the electron beam. In the case of a wiggler, electrons move in a straight line except for small 'wiggles' where radiation is emitted. The produced emission cones overlap and intensity builds up from the sum of each emission cone resulting in an intense radiation emission over a wide spectral range (Figure 4.3 (a)). On the other hand, the periodic arrangement of magnetic dipoles in undulators makes electrons to follow a sinusoidal path. The small oscillation amplitudes result in narrower radiation emission cones which overlap and interfere, producing a brighter, coherent and collimated beam compared to a wiggler (Figure 4.3 (b)). A summary of their spatial and spectral brightness is plotted and summarized in Figure 4.3 (c).

While the fourth generation of synchrotron radiation facilities known as free-electron lasers (FEL)[1] are under development, capable of producing orders of magnitude brighter beams than the current third generation, they are not relevant for the experiments described, and will not be further discussed in this section.

4.3.1 The Australian Synchrotron

The Australian Synchrotron (AS) is a third-generation facility whose design is presented in Figure 4.4. Electrons are produced by an electron gun (by thermal emission from a Tungsten cathode) operating at 500 MHz (labelled (1) in Fig. 4.4). The electron source is connected to a linear accelerator (LINAC) where electrons are accelerated to 100 MeV (labelled (2)), which has a length of 10 meters. The LINAC is connected to a booster ring, 130 meters in circumference (labelled (3)) that consists of a series of RF cavities where electrons are accelerated to an energy of 3 GeV, corresponding

[1] their working principle is based on a very long undulator coupled to a high-energy linear accelerator

to a velocity of 99.99996% the speed of light. After reaching the final energy, the electron beam is transferred to the storage ring (labelled (4)), with a circumference of 216 meters, which consists of 28 bending magnets and currently 9 insertion devices. At the storage ring, the electron beam current is kept at 200 mA with a lifetime over 20 hours with a brightness of 10^{16} or 1 million times brighter than the sun.

The AS currently possess nine beamlines, Imaging and medical, IR spectroscopy, far IR, macromolecular crystallography, powder diffraction, SAXS/WAXS, soft X-ray spectroscopy, X-ray absorption spectroscopy and X-ray fluorescence, with another 6 already commissioned and expected to be available by 2022. As mentioned in the previous subsection, synchrotron radiation is produced by the travel of the electron beam at the storage ring through any of the three devices: bending magnets, undulators or wigglers. The selection of any of these insertion devices depends on the application and performance required at each beamline. For the SAXS/WAXS beamline, the X-rays are produced from an undulator (labelled (5)). The synchrotron X-rays produced at the undulator are afterwards monochromatised and collimated in the experimental hutch (labelled (6)), located at the end section of the beamline.

The SAXS/WAXS beamline at the Australian Synchrotron

The SAXS/WAXS beamline has been designed as a highly flexible undulator beamline for transmission and grazing incidence SAXS with the option of simultaneously performing wide-angle X-ray scattering (WAXS) measurements. A bounce-down vertical focusing mirror allows grazing incidence (GISAXS) experiments. The design of the optics, end station and sample stage make it a flexible facility for scattering experiments [14]. An overview of the beamline optical layout is shown in Figure 4.5.

The in-vacuum undulator delivers an X-ray beam with an energy range between 5.5 and 21 keV and a flux of 10^{11} - 10^{13} photons per second, optimised for 8.15 and 12 keV. From the undulator front end, the beam enters the optics hutch and passes through a set of white beam slits before being collimated and monochomatised by a cryo-cooled Si (111) double-crystal monochromators (DCM) with a peak width

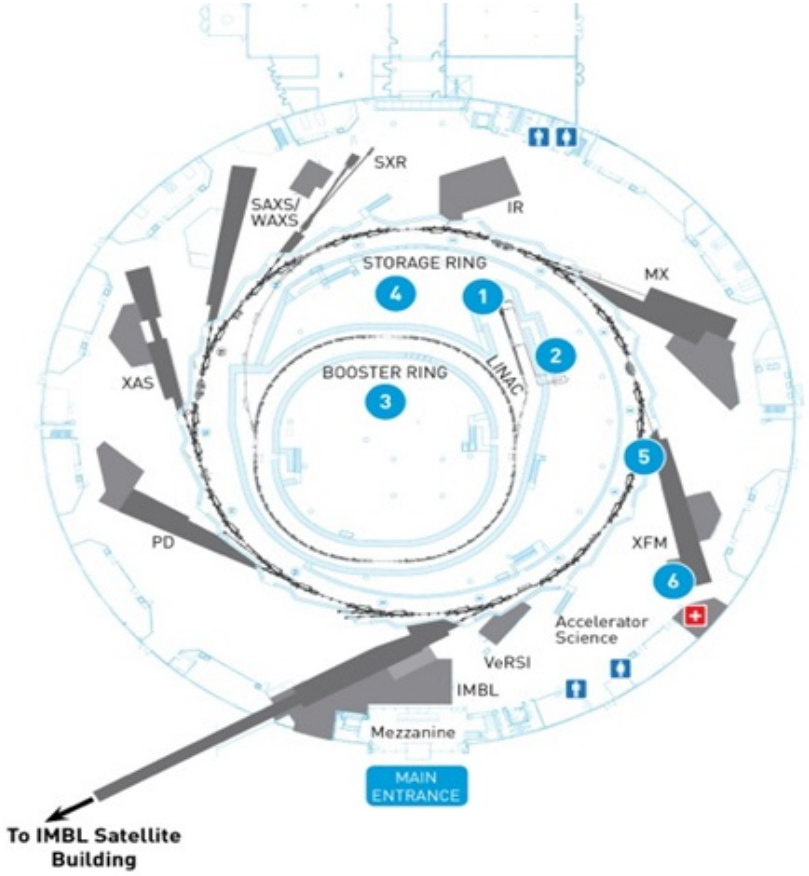

Figure 4.4: *Design of the Australian Synchrotron. The electron beam is produced by an electron gun (1) and then accelerated by the LINAC (2) before entering the booster ring (3). At the booster ring the electron beam reaches velocities closer to the speed of light and then is injected into the storage ring (4). In the storage ring the electron beam passes through different undulators and wigglers (5), where X-rays are produced according to the specifications and then collimated and monochromated before reaching the experimental hutch (6).*

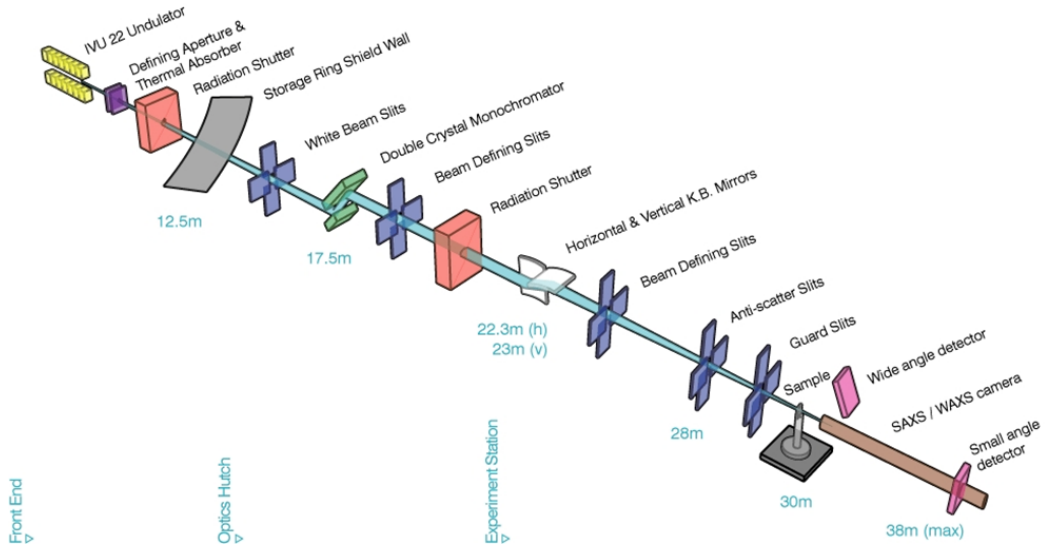

Figure 4.5: *X-ray optical layout of the SAXS/WAXS beamline at the Australian Synchrotron [14].*

resolution of 0.1 eV, sufficient for performing anomalous scattering measurements. The beamline optical design is tailored to a q-range between 0.0015 - 3 $\mathring{A}^{-1}$. The design enables the measurement of weakly scattering samples, high-throughput and time-resolved analysis. At the entrance of the experimental hutch, the monochromatic beam passes through a set of Kirkpatrick-Baex (KB) mirrors for achromatic and versatile focusing. The slits before and after the KB mirrors are used to define the incident beam flux and shape and are made of hybrid Ge single crystals. The beam size is typically $\sim$ 220 μm $\times$ 100 μm (horizontal and vertical dimensions, respectively) and can be narrow down to 50 μm $\times$ 50 μm. At the end of the beamline the end station is located, where the detector and specific experimental set-up are located. Here, the X-rays pass through two a-Si_3N_4 windows which define a gap in the evacuated beam path where the sample is located in air. The beamline contains two beam monitors to measure the incident flux and provide feedback for the beamline alignment [14].

Experimental set-up

The end station supports a diverse range of experimental configurations and consists of five subsystems: the sample stage, optical table, SAXS camera, and the SAXS and WAXS detectors (Figure 4.6) [14]. The sample stage consists of an XYZ translation stage with a load capacity of 500 kg. The top surface is 30 × 45 cm breadboard for sample mounting. For the experiments carried out in this thesis, the samples were mounted on a sample holder for lateral and vertical fine adjustment coupled to a three axis goniometer that allows to tilt the mounted sample in all directions. The sample is located between the two a-Si_3N_4 windows at the centre of the ∼ 6 cm gap. The transmitted and scattered X-rays then pass through the nose cone that forms the front module of the evacuated SAXS camera.

The SAXS camera and detector are located on a 1.2 × 8.4 m optical table that possess an XYZ motion support. The table is aligned with the beam axis such that the lateral error is minimized, simplifying the coupling of the SAXS camera and detector.

The SAXS camera provides an in-vacuum flight tube between the sample and the detector. It is formed by interchangeable extension tubes that enable different camera lengths between 600 and 7200 mm. The rear module hosts the beamstop (an obstacle to protect the detector from the primary transmitted X-ray beam at the centre of the beampath) on an in-vacuum translation stage for rapid alignment and an exit window of 320 mm in diameter. At the end of the SAXS camera, a 2-D Dectris Pilatus-1M hybrid photon counting detector is located to record the scattered X-rays from the sample. It provides single photon per pixel sensitivity, low noise and rapid acquisition (up to 30 frames per second). Ten detector modules are organized in a 2 × 5 array conform the detection area of 169 × 179 mm, providing 981 × 1043 pixels. Due to the configuration, a 7 × 17 pixel gap exists between each module, where scattered X-rays cannot be detected. The detector is mounted on a motorized vertical and horizontal stage for positioning across the exit window. The motorized stage allows the formation of images free of gaps between the detector modules. This is done by

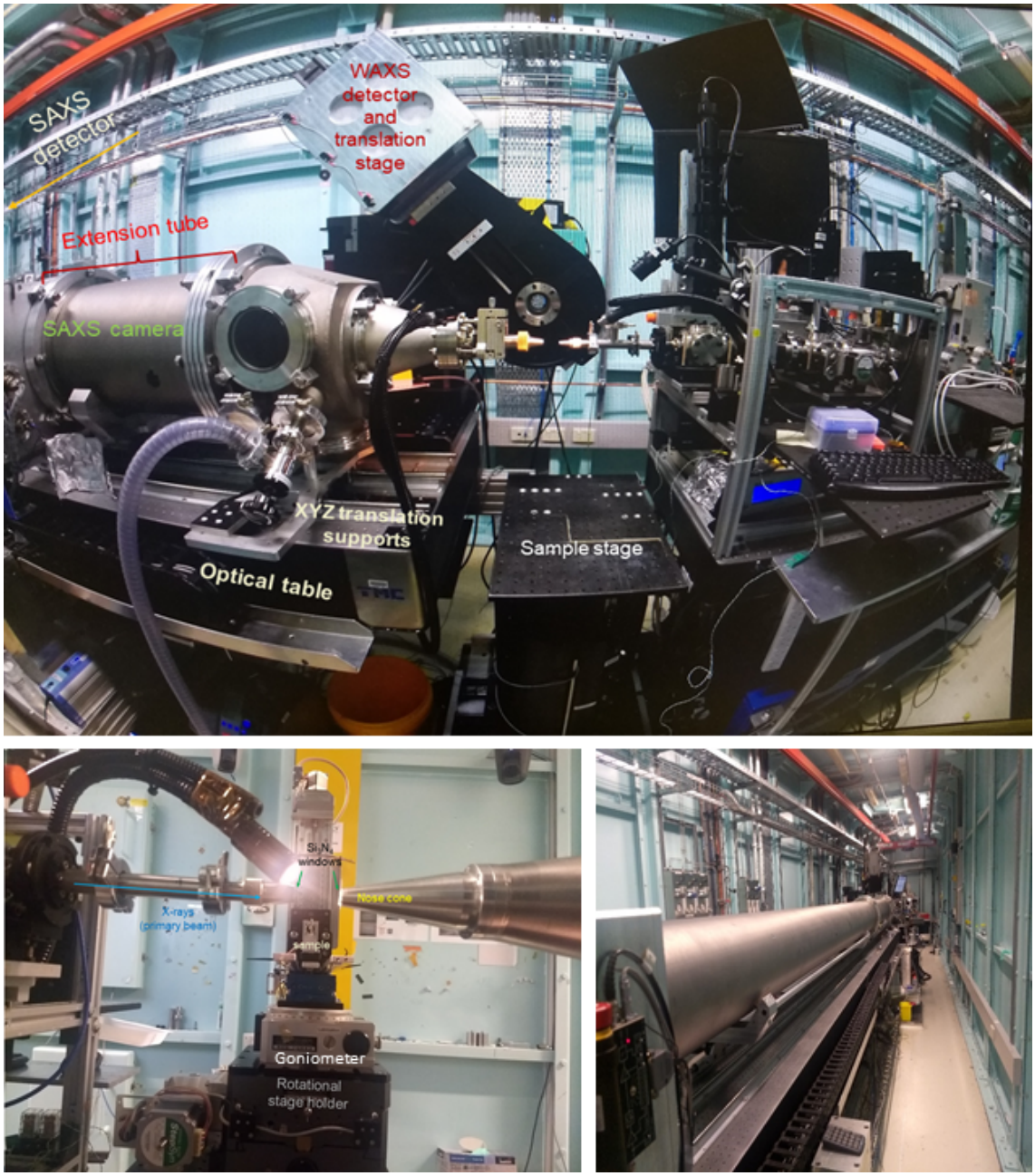

Figure 4.6: *End-station layout wide angle image of the sample stage (top), the sample stage set-up (bottom/left) and the view of the long camera length (bottom/right).*

acquisition of three images at different detector positions to compose a composite image with the help of the data acquisition software. The WAXS stage consists of a Dectris Pilatus 200k in the vertical plane. It is mounted on a goniometer on a vertical translation stage on the optical table. The WAXS detector is rotated above the nose cone of the SAXS camera for simultaneous measurements. In this thesis, experiments were carried out with an X-ray energy of 11 keV and a camera length of 960 mm.

4.4 Small angle X-ray scattering

The previous section was aimed as an introduction to the interaction of X-rays with matter, synchrotron radiation and technical details on the working principles of the AS and the SAXS/WAXS beamline. The following section is devoted to introduce the theoretical framework regarding the SAXS technique and the description of the experiments and analysis of the samples containing ion tracks or NPs carried out for this thesis.

4.4.1 Theoretical background

The monochromatic X-rays hitting the sample are collimated and can be described by an incident plane wave. After incidence on the sample, most of the X-ray photons will keep travelling in a straight trajectory without deflection however, a fraction of them are scattered due to the elastic interaction with the target electrons. Because the energy of the X-rays are above the binding energy of atoms the target electrons behave as if they were free [217]. Thus, we will first consider the scattering from a single electron, then the scattering of an atom as the superposition of the scattering from the electrons of the atom and finally, the scattering of an object as the superposition of a group of atoms.

The scattered wave ψ_f of a single electron can be expressed as a spherical wave front, such that:

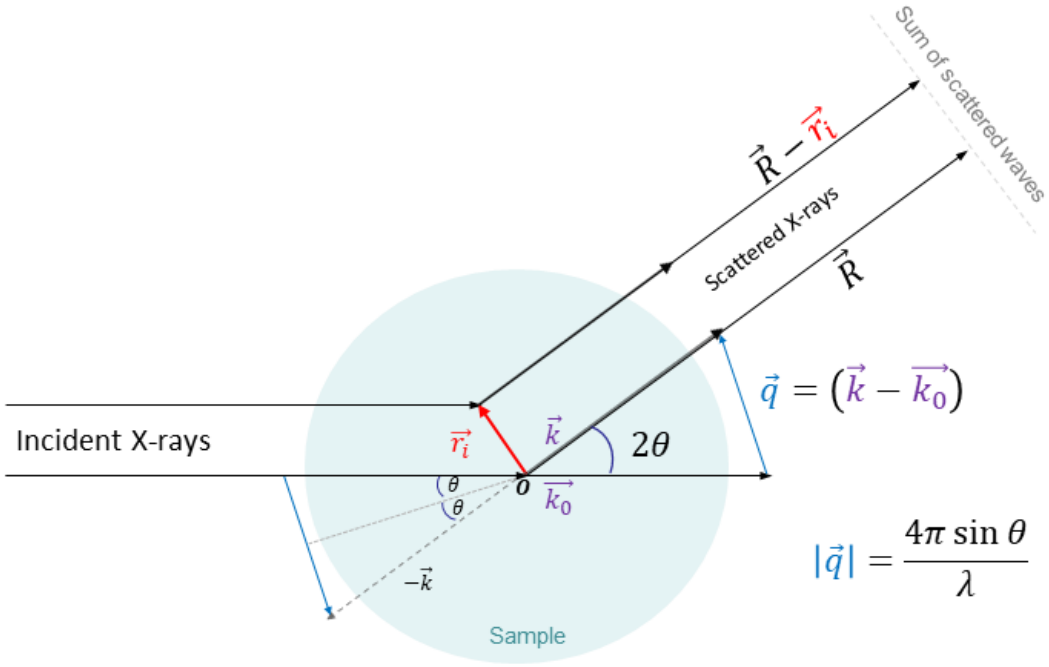

Figure 4.7: *Diffraction by two point centres, based on [15].*

$$\psi_f = \psi_0 \cdot f_e(\theta) \frac{e^{i\vec{k}\cdot\vec{r}}}{r} \tag{4.4}$$

with a scattered wave vector $\vec{k}$, where the condition of elastic scattering requires that: $|\vec{k}| = |\vec{k_0}| = 2\pi/\lambda$, with the wave vector of the incident plane wave $\vec{k_0}$ with amplitude ψ_0, the radial distance r = $|\vec{r}|$ and the scattering length $f_e(\theta)$. This term represents the probability of the incident wave to be scattered into a certain direction from the incident beam.

As mentioned before, the intensity of elastic X-ray scattering can be described by Thomson scattering, and can be related to the scattered wave function by:

$$I_T(\theta) = |\psi_f|^2 = \psi_f \cdot \psi_f^* = \frac{|\psi_0|^2}{r^2} \cdot |f_e(\theta)|^2 \tag{4.5}$$

where ψ_f^* is the complex conjugate of the scattering amplitude ψ_f. By comparing the left hand side of equation 4.5 with equation 4.2, it is possible to calculate the scattering length of a single electron with the resulting relationship:

$$f_e^2(\theta) = r_e^2 \cdot \frac{1 + \cos^2(2\theta)}{2}. \tag{4.6}$$

For small angles, the angular dependency can be approximated to unity, and the scattering length of a single electron corresponds to the electron radius r_e, also known as the Thomson scattering length.

With the scattering length of a single electron, it is possible to calculate the scattering length of a single atom f_a which is proportional to its atomic number:

$$f_a = Z r_e. \tag{4.7}$$

SAXS is a technique for studying particles or features in the range of few to hundreds of nanometres which can be considered as an ensemble of N atoms, each of them contributing to the net scattering. Thus, the total scattering can be expressed as the superposition of scattering from each i-th atom as: [15]

$$\vec{\psi_f} = \sum_{i=1}^{N} f_{a,i}(\theta) \cdot e^{i(\vec{k_0} - \vec{k_f}) \cdot \vec{r_i}}, \tag{4.8}$$

where the vector $\vec{k_0} - \vec{k_f} = \vec{q}$ represents the scattering vector of an atom located at the position $\vec{r_i}$ relative to the arbitrary origin at the centre of the particle (Fig. 4.7). It is meaningful to remember that in this interpretation the scattered wavelets interact weakly with the incident beam, which is known as the *Born* approximation [15]. Multiple scattering effects are neglected too.

Because the number of atoms in the ensemble is very large and electron density

fluctuations on an atomic scale are not of relevance, the total scattering (Equation 4.8) can be expressed by the scattering length density function in continuous form by replacing the sum with a volume integral:

$$\psi_f(\vec{q}) = \int \beta(\vec{r}) \cdot e^{i\vec{q}\cdot\vec{r}} d^3\vec{r}, \tag{4.9}$$

where $f_a(\theta) = \beta(\vec{r})d^3r$.

Meaningful SAXS signal is result from electron density inhomogeneities exist in the sample [217]. The SLD term $\beta(\vec{r})$ in equation 4.9 is best expressed as the contrast of the scattering density inhomogeneities to the bulk or substrate density β_0, *i.e.* the difference in electron density of the scattering object and its surrounding medium. The SLD can then be expressed as $\Delta\beta(\vec{r}) = \beta(\vec{r}) - \beta_0$, for clarity. Equation 4.9 can be rewritten as:

$$\psi_f(\vec{q}) = \int \Delta\beta(\vec{r}) \cdot e^{i\vec{q}\cdot\vec{r}} d^3\vec{r} \tag{4.10}$$

where the SLD contains information regarding the geometry of the scattering object.

The SLD distribution is proportional to its mass density $\rho(\vec{r})$, and for a single elementary scattering object it becomes the product of the scattering length of a single atom and the number of atoms n enclosed in the volume density of the object:

$$\beta(\vec{r}) = nf_a. \tag{4.11}$$

The number of scattering sources n enclosed in the volume density can be calculated using the material atomic density ρ as:

$$n = \frac{\rho(\vec{r})N_A}{m}, \tag{4.12}$$

N_A the Avogadro constant and m the atomic mass. In the case of an scattering object containing N different types of atoms, the SLD distribution can be re-written as:

$$\beta(\vec{r}) = \frac{\rho(\vec{r})N_A}{m_N}\sum_{i=1}^{N} n_i f_{a,i}, \tag{4.13}$$

where $m_N = \sum_{i=1}^{N} n_i m_i$ corresponds to the total atomic mass.

Thus, we can correlate the SLD with the material density change of the scattering object by the following relation:

$$\frac{\Delta\beta}{\beta} = \frac{\Delta\rho}{\rho}. \tag{4.14}$$

The latter relationship is commonly used to express equation 4.10 in terms of the density distribution of the inhomogeneities, such that:

$$\psi_f(\vec{q}) = \int \Delta\rho(\vec{r}) \cdot e^{i\vec{q}\cdot\vec{r}} d^3\vec{r}. \tag{4.15}$$

Thus, a small angle scattering process is related to the Fourier transform of the real space object, which results in an inverse relationship of the particle's dimensions and scattering angle [217].

For the general case, when considering an ensemble of scattering objects, the scattering intensity is dependent of two factors: (i) the scattering pattern arising from the geometrical shape, also known as the form factor $F(\vec{q})$; and (ii) scattering occurring due to the ordered arrangement of the scattering objects or from the correlation between near neighbours, known as the structure factor $S(\vec{q})$. Both factors

are non-dimensional functions. The scattering intensity of an ensemble of scattering objects then, can be expressed as: [234]

$$\langle I(\vec{q})\rangle = C \cdot (\langle F(\vec{q})\rangle^2 S(\vec{q}) + \langle F(\vec{q})^2\rangle - \langle F(\vec{q})\rangle^2), \tag{4.16}$$

the brackets $\langle\rangle$ indicate time-average functions with respect to the scattering volume. The last term on the right-hand side is known as the 'Laue scattering' and cancels out the first term if there is no structural correlation between near neighbour particles, as in this case the structure factor becomes unity. In the cases considered in this thesis it is assumed that the structure factor equals unity as the density of scattering objects for either ion tracks or MNPs is low enough to neglect inter-particle interaction. This allows to express equation 4.16 in a simplified way:

$$\langle I(\vec{q})\rangle = C \cdot \langle F(\vec{q})^2\rangle. \tag{4.17}$$

The accompanying factor C contains the information regarding the volume V, density N of scattering objectives, and the electron density contrast $\Delta\rho_e$, such that: $C = (\Delta\rho_e \cdot V)^2 \cdot N$. In this thesis, all systems under investigation are considered to be independent of time as they consist of scattering objects embedded in solid materials, therefore, expression 4.17 can be re-written as:

$$I(\vec{q}) = C \cdot F(\vec{q})^2, \tag{4.18}$$

where the form factor $F(\vec{q})$ has the form:

$$F(\vec{q}) = |\int \Delta\rho(\vec{q}) \cdot e^{i\vec{q}\cdot\vec{r}} d^3\vec{r}|^2. \tag{4.19}$$

Expression 4.18 refers to an ensemble of identical particles yet, in practice this is not the case. Thus, it is necessary to account for the presence of scattering objects

with the same geometry but different volume or size. This is known as polydispersity.

In practice, the analysis of scattering patterns translates into finding adequate models according to prior knowledge about the geometry of the particles (form factor), any potential inter-particle scattering (structure factor) and the size distribution of the scattering objects. Also, for the case of non-spherical particles, it is important to include orientation effects, only if they are randomly oriented.

In this thesis, the scattering objects under study are metallic NPs or ion tracks. For the former, TEM images have confirm the presence of a spherical geometry. The ion tracks are considered as cylindrical inclusions of different morphology, where we observe a linear increase of the scattering intensity with fluence, for low fluences, supporting the lack of inter-particle scattering effects, nearly monodisperse and well-aligned. In the following section, the the calibration of the q-space was carried out and the data reduction of the measured scattering patterns. Then, calculation of the form factors for scattering objects with spherical and cylindrical geometries relevant for our study is presented.

4.5 Scattering range and intensity calibration

The scattering patterns collected by the detector possess information regarding geometry, orientation and density difference of the scattering objects. As the scattering intensity is dependent on the q-vector (*i.e.* the scattering angle and wavelength) it is important to accurately determine the distance between sample and detector, known as camera length, to calculate the corresponding scattering angle. The wavelength of the X-rays is known (energy is known and fixed), thus, with the help of a standard the camera length can be determined. The camera length calibration was carried out using the scattering pattern of silver behenate (AgBeh), which displays multiple concentric rings at well-knwon q_r positions [235]. Figure 4.8 (a) shows the scattering pattern of AgBeh where the appearance of the concentric scattering ring is apparent. The first

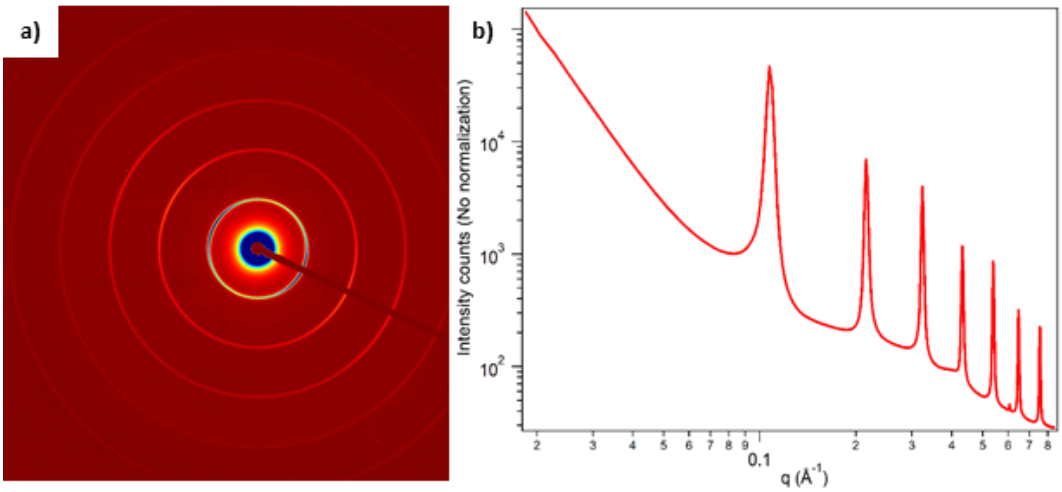

Figure 4.8: *AgBeh scattering pattern in gapless mode from Pilatus 1M detector for X-rays of 11 keV and a calculated camera length of 962 mm (a). Plot of $I(q_r)$ vs q_r of AgBeh showing the lower scattering rings (b).*

two scattering rings for AgBeh are located at $q_{001} = 0.1077\ \mathring{A}^{-1}$ and $q_{002} = 0.2153\ \mathring{A}^{-1}$ (Fig. 4.8 (b)). The q-range is then calibrated using the elastic scattering relationship $|\vec{q}| = \frac{4\pi \sin\theta}{\lambda}$ (Fig. 4.7). The trigonometric term is determined as the ratio between the distance from the beamstop to the any of the two scattering rings and the camera length, where the corresponding wavelength is defined by the beam energy ($q = \frac{4\pi}{\lambda} \cdot \frac{d}{L}$).

The expression derived in equation 4.18 shows the existing correlation between the scattering intensity and the density difference and scattering volume exhibited by the scattering objects, encoded in the accompanying factor C. The measured intensity is proportional to the number of scattering objects and the square of the volume thus, if known, it is possible to calculate the density change from the scattering intensity. This information is accessible in the case of ion tracks formed in a-SiO_xN_y thin layers, where the number of scattering objects is equivalent to the irradiation fluence while the volume can be extracted from the analysis of the scattering patterns. To quantify this information, it requires an absolute calibration of the scattering intensity.

The scattering intensity is commonly expressed in terms of the scattering coefficient

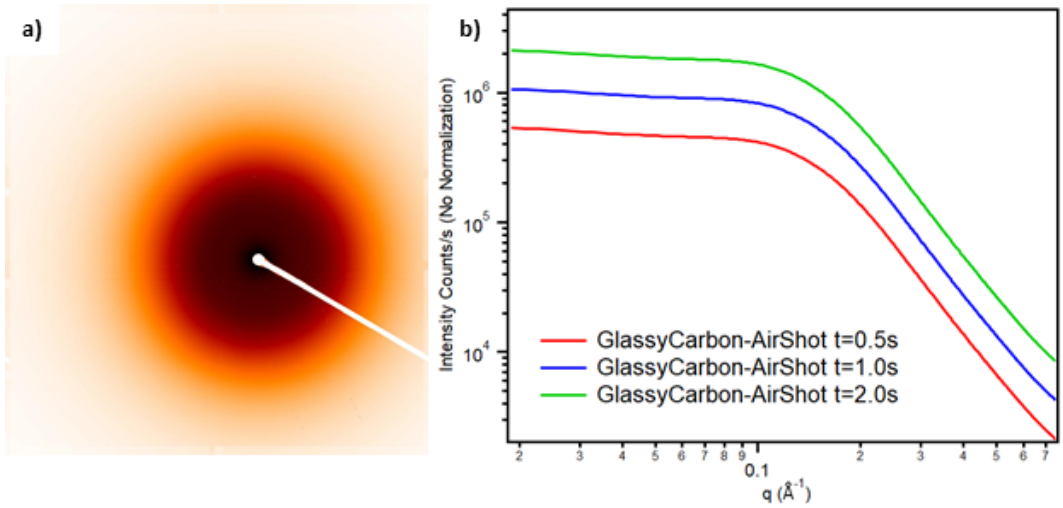

Figure 4.9: *Scattering pattern of glassy carbon reference of 1 mm thickness after exposure of t = 2s (a) and I(q) vs q plot of glassy carbon reference of 1 mm thickness after subtraction of air scattering at three exposure times: t = 0.5, 1 and 2 s..*

μ_s, defined as the scattering cross-sectional area per unit volume thus, given in units of cm^{-1}. The scattering intensity calibration was carried out using glassy carbon of 1 mm thickness as a reference. The latter is relevant as the scattering intensity is proportional to the interacting volume. Glassy carbon has been widely used as a calibration standard as it presents an almost continuous scattering plateau over a wide q-range with a known scattering intensity [236]. Because the samples were located at the middle of a 6 cm air gap between the two a-Si_3N_4 windows (see Experimental set-up section), it is necessary to account for the contribution from air scattering to the measured pattern. To do so, the scattering intensity without a sample along the beam path was recorded and used as a baseline for normalization. The absolute calibration of the scattering cross-section was then carried out by performing measurements of air and glassy carbon at three different exposure times (0.5, 1 and 2 seconds), confirming the linear dependency of the photon-count with exposure. This can be seen in Fig. 4.9 (b) where the scattering intensity of glassy carbon for the three exposure times after the corresponding subtraction of the air scattering is plotted.

Determination of the density difference from the absolute scattering intensity can

be carried out using equation 4.18:

$$\Delta\rho_e^2 = \frac{I(\vec{q})/10}{N \cdot V^2 \cdot F(\vec{q}^2)}. \tag{4.20}$$

The intensity $I(\vec{q})$ is divided by 10 to account for the thickness of the normalization standard (1 mm) to the unit of cm^{-1}.

The term $\Delta\rho_e$ can be substituted with the density change with respect to the bulk material using the relationship from expression 4.14:

$$\Delta\rho^2 = \left(\frac{\rho}{\beta}\right)^2 \cdot \frac{I(\vec{q})/10}{N \cdot V^2 \cdot F(\vec{q})^2}, \tag{4.21}$$

where it can be more practical to express the density variation relative to the bulk density $\left(\frac{\Delta\rho}{\rho}\right)$.

4.5.1 Data acquisition and reduction

All scattering data was collected and processed using the scatterbrain software package developed at the SAXS/WAXS beamline.

Because of the reciprocal law that characterizes scattering processes such as SAXS [217], the image produced by the detector corresponds to a 2D cut of the scattering object in reciprocal space [214]. Figure 4.10 (a) shows the scattering resulting from a sample of a-$SiN_{1.06}$ after irradiation with 5×10^{11} cm^{-2} when aligned to the X-ray beam. In this configuration, the axis of the ion tracks are aligned with the direction of the X-ray beam. The scattering pattern corresponds to their Fourier transform, which comprises thin disks with a radial oscillating pattern that contains all information about the radial density distribution. When tilted by 5° or 10° (Figure 4.10 (b)) an anisotropic scattering pattern is observed, characterized by narrow streaks due to the high aspect ratio of the ion tracks. Both aligned and tilted images possess

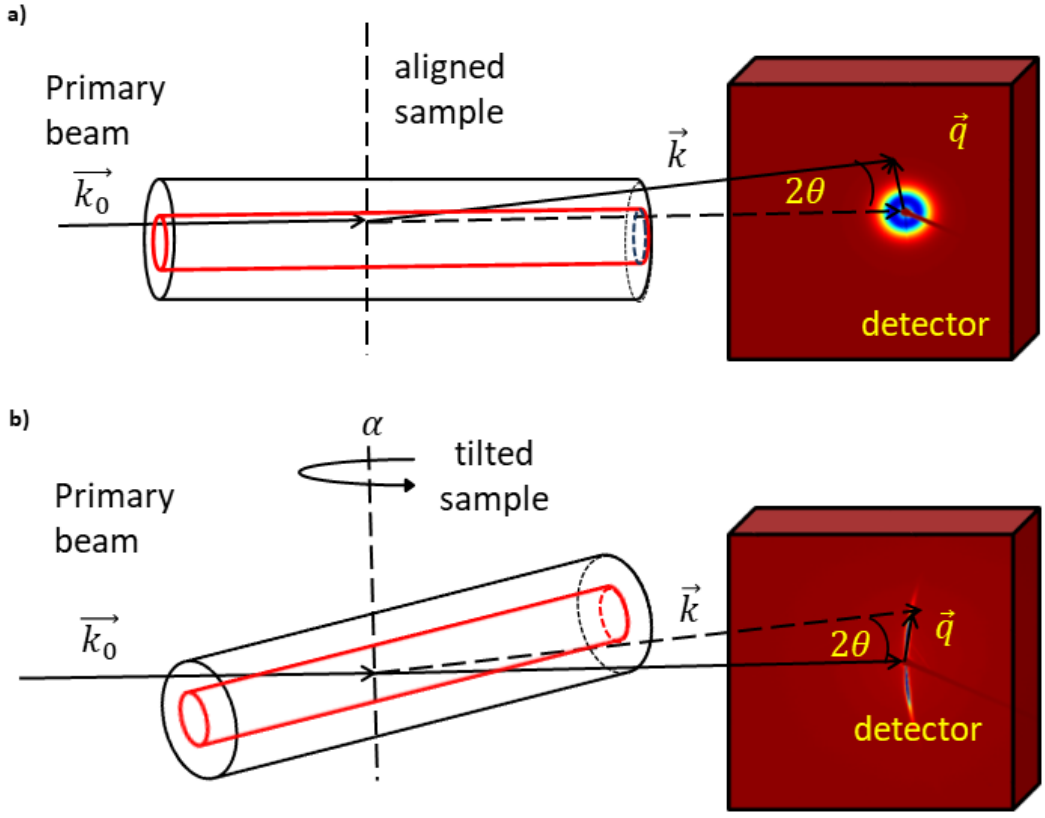

Figure 4.10: *Schematic of the scattering from an ion track in a-$SiN_{1.06}$ when sample is aligned to the X-ray beam (a) and tilted (b).*

the information regarding the radial density distribution. However, accurate alignment of ion tracks with the beam axis is a difficult task where slight misalignments have a major impact on the scattering pattern. Also, the narrow streaks present in the scattering pattern of tilted samples are characteristic of the high aspect ratio present in the ion tracks, which is not available in the aligned case. For these reasons, tilted samples by 5° or 10° were considered for the analysis of the morphology of ion tracks. This consideration is not necessary in the case of spherical NPs due to the spherical symmetry present.

The quantitative analysis of the scattering intensity requires the subtraction of any other contributions, such as scattering from a substrate and from the embedding matrix material. In the case of swift heavy-ion irradiated samples, the studied scattering intensities were extracted by a selective mask of the streaks shown in the scattering pattern followed by a background subtraction defined by a mask outlined in an angular sector perpendicular to the streaks. This is exemplified in Figure 4.11. From the typical scattering pattern of a sample containing ion tracks, intense and narrow streaks can be seen (Figure 4.11 (a)). In figure 4.11 (b) the same scattering pattern is shown with the selective masking on the streak (signal) and in a semi-perpendicular direction (background). While ideally the background subtraction would be carried out using the scattering pattern from an unirradiated sample, the scattering intensity along the perpendicular direction of the visible streak does not carry any information on the ion tracks[2], as long as they are long and continuous (otherwise it could present inter-particle scattering). Furthermore, the background is dependent, to certain degree, on the particular sample, and the use of another sample would imply a slight difference in thickness due to mechanical polishing of the Si substrate , inhomogeneities in the sample and surface roughness, effects that can be reduced using the perpendicular sections. In each mask, the intensity is integrated angularly for constant q-values and is normalized to the mask width. The corresponding integrated intensities are plotted in Figure 4.11 (c) where the scattering

[2]This method has been compared with the subtraction from unirradiated standards as background, yielding the same scattering intensity

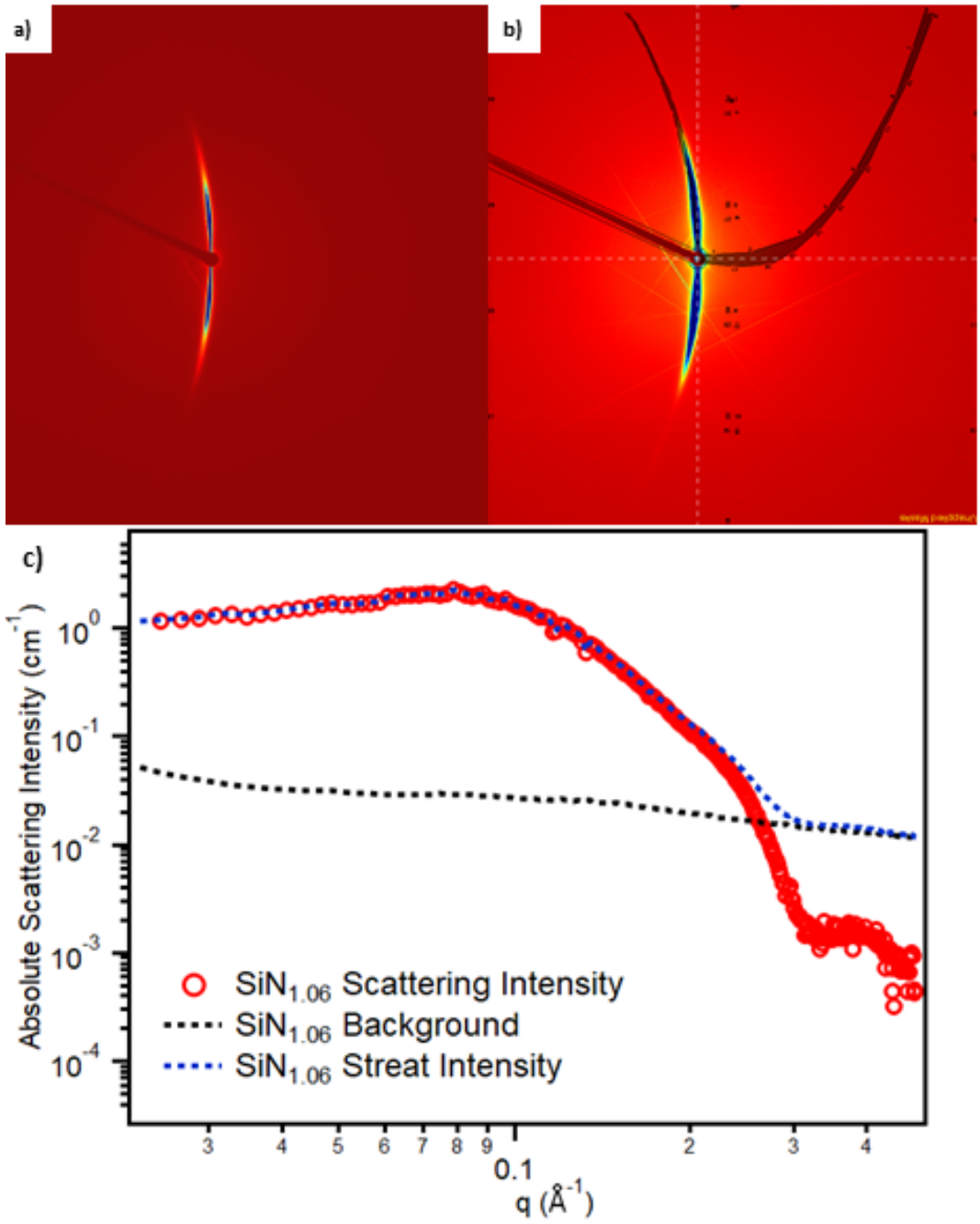

Figure 4.11: *Scattering pattern of a-$SiN_{1.06}$ irradiated with 185 MeV Au ions at a fluence of 5 × 10^{11} cm^{-2} (a). Selective masking of the scattering streak and background (b). Scattering intensity corresponding to the selective masking of the streak, background and background corrected (c).*

intensity is shown before and after background subtraction.

During each measurement $\sim 10^7$ ion tracks are measured simultaneously such that the analysis reveals statistical information about the mean ion track structure. As the tracks are parallel and almost identical (because of the well-defined ion energy and direction), the results are representative of the individual track structure, averaging out fluctuations on atomic scales. Due to their alignment, averaging over different orientations is not required [237]. The data manipulation and analysis of the extracted scattering and background intensities was carried out with the SAXS analysis tool Irena [238] and in-house numerical fitting routines, both developed for the Igor Pro software.

4.6 Modelling of the scattering patterns from particles of specific shape

4.6.1 Spherical nanoparticles

We can express the general small angle X-ray scattering expression (Eq. 4.15), in spherical coordinates as [234]:

$$\psi_{sph}(\vec{q}) = \int_0^{\infty} \int_0^{2\pi} \int_0^{\pi} \rho(\vec{r}) \cdot r \cdot e^{i\vec{q}\cdot\vec{r}} \cdot r \sin\theta d\theta d\phi dr, \tag{4.22}$$

where $\rho(\vec{r})$ for a particle with a centrosymmetric density profile only exhibits a dependency on the radial distance $r = |\vec{r}|$. By using the inner product identity: $\vec{q}\cdot\vec{r} = qr\cos\theta$, due to azimuthal symmetry, the scattering amplitude can be expressed as [239]:

$$\begin{aligned}\psi_{sph}(\vec{q}) &= \int_0^{\infty}\int_0^{2\pi}\int_0^{\pi}\rho(\vec{r})\cdot r\cdot e^{i\vec{q}\cdot\vec{r}}\cdot r\sin\theta d\theta d\phi dr,\\ &= \int_0^{\infty} r^2\rho(r)\int_0^{\pi}\int_0^{2\pi} e^{iqr\cos\theta}\cdot\sin\theta d\theta d\phi dr,\\ &= 4\pi\int_0^{\infty} r^2\rho(r)\frac{\sin(qr)}{qr}dr.\end{aligned} \tag{4.23}$$

The expression for the radial density distribution of a particle with a constant density is given by:

$$\rho(r) = \begin{cases}\rho, & for\ r \le R\\ 0 & for\ R < r\end{cases}. \tag{4.24}$$

After integration by parts the scattering amplitude then reduces to the expression:

$$\begin{aligned}\psi_f(\vec{q}) &= 4\pi\rho\int_0^{R} r\frac{\sin(qr)}{q}dr\\ &= \frac{4\pi}{q}\rho\left[\frac{\sin(qr) - Rq\cos(qR)}{q^2}\right]\\ &= \frac{4\pi}{3}R^3\rho\left[\frac{3(\sin(qR) - Rq\cos(qR))}{(qR)^3}\right],\end{aligned} \tag{4.25}$$

where the last expression can be simplified in terms of the volume of the spherical particle $V = \frac{4}{3}\pi R^3$, to:

$$\psi_{sph}(\vec{q}) = V\cdot\rho\cdot\left[\frac{3(\sin(qR) - Rq\cos(qR))}{(qR)^3}\right]. \tag{4.26}$$

The term in brackets corresponds to the form factor $F(q)$ of a single spherical particle, thus:

$$\psi_{sph}(\vec{q}) = V\cdot\rho\cdot F(q). \tag{4.27}$$

In the case of spherical NPs formed by Au implantation, the scattering contrast results from the difference in electronic density between Au and the substrate, mainly

a-$SiN_{1.06}$, thus $\rho = \rho_{Au} - \rho_{a-SiN_{1.06}}$.

4.6.2 Cylindrical objects

As ion tracks are nanoscale density fluctuations of few nm width and up to several micrometres long, they can be succesfully approximated as cylindrical structures, with a density profile that is only dependent on the distance from the cylinder (track) axis $\rho(\vec{r}) = \rho(r)$. In cylindrical coordinates, centred at the middle of the ion track, the scattering vector is expressed as: $\vec{q} = (q_x, q_y, q_z) = (q_r \cdot \cos\nu, q_r \cdot \sin\nu, q_z)$, such that $q_r = \sqrt{q_x^2 + q_y^2}$, the radial distance $\vec{r} = (r \cdot \cos\phi, r\sin\phi, z)$ and the volume element is $d^3\vec{r} = rdrd\phi dz$. The general X-ray scattering expression (Eq. 4.15) transforms into: [234]

$$\begin{aligned}\psi_{cyl}(\vec{q}) &= \int_{\frac{-L}{2}}^{\frac{L}{2}} \int_0^{2\pi} \int_0^{\infty} \rho(\vec{r}) \cdot e^{i\vec{q}\cdot\vec{r}} \cdot r dr d\phi dz \\ &= \int_{\frac{-L}{2}}^{\frac{L}{2}} \int_0^{2\pi} \int_0^{\infty} \rho(\vec{r}) \cdot e^{i(q_r r\cos\nu\cos\phi + q_r r\sin\nu\cos\phi + q_z z)} \cdot r dr d\phi dz \\ &= \int_{\frac{-L}{2}}^{\frac{L}{2}} e^{i(z\cdot q_z)} dz \int_0^{\infty} \rho(\vec{q}) \cdot r \cdot e^{i(rq_r\cos(\nu-\phi))} dr d\phi,\end{aligned} \tag{4.28}$$

where the identity $\cos\nu\cos\phi + \sin\nu\sin\phi = \cos(\nu - \phi)$ has been used. By substituting $\theta = (\nu - \phi)$ equation 4.28 simplifies into:

$$\psi_{cyl}(\vec{q}) = \int_{\frac{-L}{q}}^{\frac{L}{2}} e^{i(zq_z)} dz \int_0^{2\pi} \int_0^{\infty} \rho(r) \cdot r \cdot e^{i(rq_r\cos\theta)} dr d\theta. \tag{4.29}$$

The first integral in 4.29 is related to the height of the cylinder corresponding to the length of the ion track L, and the following dependent on the radial and angular components. The integral of the length component yields:

$$\int_{\frac{-L}{2}}^{\frac{L}{2}} e^{i(zq_z)}dz = L \cdot \frac{\sin\left(\frac{L}{2}q_z\right)}{\left(\frac{L}{2}q_z\right)}. \tag{4.30}$$

The value of the first integral can be computed using the small angle approach, for which $\lim_{q_z \to 0} \frac{\sin\left(\frac{L}{2}q_z\right)}{\frac{L}{2}q_z} = 1$. On the other hand, we can use the Bessel function $J_n(r) = \frac{1}{2\pi i^n} \int_0^{2\pi} e^{ir\cos\theta} e^{in\theta} d\theta$ [240] to simplify the radial and angular integrals $\psi_{f,r,\theta}$, such that:

$$\begin{aligned} \psi_{cyl,r,\theta}(q_r) =& \int_0^{\infty} \rho(r) \cdot r dr \int_0^{2\pi} e^{i(r \cdot q_r \cos\theta)} d\theta \\ =& 2\pi \int_0^{\infty} \rho(r) \cdot r \cdot J_0(q_r \cdot r) dr, \end{aligned} \tag{4.31}$$

where J_0 is the zeroth order Bessel function. Thus, it is possible to re-write equation 4.29 in a simplified form as:

$$\psi_{cyl}(r) = 2\pi L \int_0^{\infty} \rho(r) \cdot r \cdot J_0(q_r \cdot r) dr. \tag{4.32}$$

In the most common case of randomly oriented anisotropic particles, it is necessary to consider every orientation and average the results that contribute to the total scattering intensity [217]. An advantage of swift heavy-ion irradiation lies in the near perfect alignment of the formed ion tracks, where the amorphous nature of the substrate supports the idea of an underlying radial symmetry. Assuming only small changes of the energy-loss when the ions penetrate the layer and the formation of continuous tracks, the modelling of the data concerns mainly the radial density profile. Hence, the modelling is now reduced to find adequate radial density distributions for the cylindrical tracks. Possible radial density changes are shown in Figure 4.12, and consist of cylinders with a constant density (a), a core-shell structure (b) and a core-shell structure with a smooth transition connecting the two regions (c). In the following, the derivations of the corresponding form factors for the proposed radial distributions are presented.

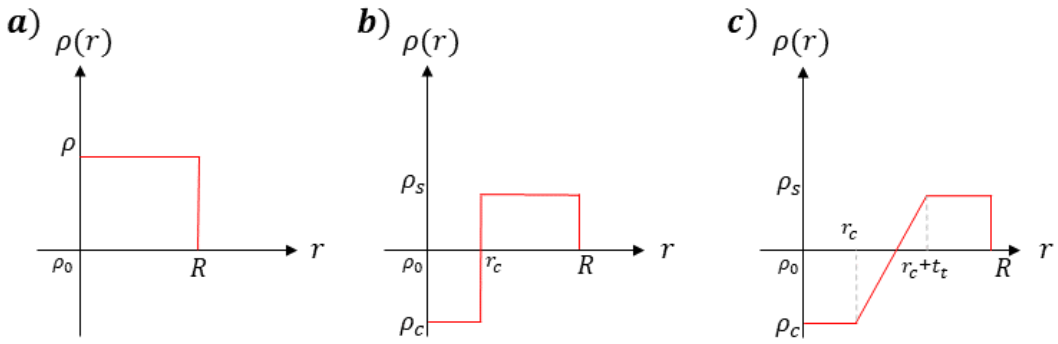

Figure 4.12: *Radial density profile $\rho(r)$ for spherical and cylindrical NPs (a), and the special cylindrical particles exhibiting a core-shell cylindrical (b) and with a transition region t_t (c).*

Cylinder with constant density

The simple cylinder with constant density shown in Figure 4.8 (a):

$$\rho(r) = \begin{cases} \rho_c, & for\ 0 \leq r \leq R \\ 0, & for\ R < r \end{cases}, \tag{4.33}$$

can be calculated using the derivative identity for the Bessel functions $\frac{d}{dx}\left[x^m J_m(x)\right] = x^m J_{m-1}$ [240], and the radial distribution given by equation 4.24:

$$\begin{aligned} \psi_{cyl,r,\theta}(q_r) =& 2\pi\rho \int_0^R r \cdot J_0(q_r \cdot r) dr, \\ =& 2\pi \frac{\rho}{q_r} \left[r \cdot J_1(q_r \cdot r)\right]_0^R, \\ =& 2\pi R^2 \cdot \rho \cdot \frac{J_1(q_r \cdot R)}{q_r \cdot R}, \end{aligned} \tag{4.34}$$

and J_1 the Bessel function of first order. Therefore, the scattering amplitude of a simple cylinder results from combining equations 4.30 and 4.34:

$$\begin{aligned}\psi_{cyl}(q_r) =& 2\pi R^2 L \cdot \rho \cdot \left(\frac{J_1(q_r \cdot R)}{q_r \cdot R}\right), \\ =& 2 \cdot V \cdot \rho \cdot \left(\frac{J_1(q_r \cdot R)}{q_r \cdot R}\right).\end{aligned} \tag{4.35}$$

The term $\pi R^2 L$ is equal to the volume V of the ion track. Analogously to the case of a spherical particle, the term in parenthesis can be correlated to the form factor for simple cylindrical particles, leading to the expression:

$$\psi_{cyl}(q_r) = 2 \cdot V \cdot \rho \cdot F(q_r). \tag{4.36}$$

Cylindrical particles with a core-shell radial density

As indicated in section 2.2.1, ion tracks formed in amorphous insulating materials exhibit a radial density profile comprised of an under-dense core surrounded by an over-dense shell. The determination of the scattering amplitude of a cylindrical particle with a core-shell radial density follows the same path as for a cylindrical particle but where the radial density profile is defined as (Figure 4.12 (b)):

$$\rho(r) = \begin{cases} \rho_c, & for\ 0 \leq r \leq r_c \\ \rho_s, & for\ r_c \leq r \leq R. \cdot \\ 0, & for\ R < r \end{cases} \tag{4.37}$$

In this case, the scattering amplitude transforms into:

$$
\begin{aligned}
\psi_{c-s}(q_r) =& \pi L \left[\int_0^{r_c} \rho_c \cdot r \cdot J_0(q_r \cdot r) dr + \int_{r_c}^{R} \rho_s \cdot r \cdot J_0(q_r \cdot r) dr \right] \\
=& \pi L \left[\rho_c r_c^2 \frac{J_1(q_r \cdot r_c)}{q_r \cdot r_c} + \rho_s \left(R^2 \frac{J_1(q_r \cdot R)}{q_r \cdot R} - r_c^2 \frac{J_1(q_r \cdot r_c)}{q_r \cdot r_c} \right) \right] \\
=& \pi L \left[\rho_s \cdot R^2 \frac{J_1(q_r \cdot R)}{q_r \cdot R} + \rho_s r_c^2 \frac{J_1(q_r \cdot R)}{q_r \cdot R} \left[\frac{\rho_c}{\rho_s} - 1 \right] \right] \\
=& 2\pi R^2 L \cdot \rho_s \left[\frac{J_1(q_r \cdot R)}{q_r \cdot R} + \left[\frac{\rho_c}{\rho_s} - 1 \right] \left(\frac{r_c}{R} \right)^2 \cdot \frac{J_1(q_r \cdot r_c)}{q_r \cdot r_c} \right] \\
=& 2 \cdot V \rho_s \cdot F(q_r).
\end{aligned}
\tag{4.38}
$$

Because the scattering intensity is proportional to the square of the form factor (equation 4.18), it is not possible to determine if the core or shell regions are under- or over-dense.

Cylindrical particles with a core-shell radial density connected by a smooth transition

While the use of the form factor of core-shell cylindrical particles has shown good agreement with the extracted scattering intensity of ion tracks in a-SiO_2, for a-SiO_xN_y they have failed to reproduce the scattering intensities at higher q-values. This suggests that the core-shell cylindrical form factor requires a refinement to better describe the experimental scattering intensities. In this subsection the extension for a cylindrical particle with a radial density resembling an under-dense core surrounded by an over-dense region connected by a smooth transition is presented. For simplicity, the transition is defined in terms of the straight line such that $\rho(r) = b + mr$ with slope $m = \frac{\rho_c - \rho_s}{t_t}$ and $b = \rho_c \left(1 + \frac{r_c}{t_t}\right) - \rho_s \left(\frac{r_c}{t_t}\right)$ as plotted in Figure 4.12 (c). In the same fashion, the scattering amplitude can be determined following the corresponding radial density:

$$\rho(r) = \begin{cases} \rho_c, & for 0 \leq r \leq r_c \\ b + mr, & for r_c \leq r \leq r_c + t_t. \\ \rho_s, & r_c + t_t < r \leq R \\ 0, & for R < r \end{cases} . \tag{4.39}$$

The scattering amplitude turns then into the following expression:

$$\begin{aligned} \psi_f(q_r) =& 2\pi L \Big[\int_0^{r_c} \rho_c \cdot r \cdot J_0(q_r \cdot r) dr \\ &+ \int_{r_c}^{r_c+t_t} (b + mr) \cdot r \cdot J_0(q_r \cdot r) dr + \int_{r_c+t_t}^{R} \rho_s \cdot r \cdot J_0(q_r \cdot r) dr \Big] \\ =& 2\pi r^2 L \Big[(r_c - b) \frac{r_c^2}{R^2} \frac{J_1(q_r \cdot r_c)}{q_r \cdot r_c} + (b - \rho_s) \frac{(r_c + t_t)^2}{R^2} \frac{J_1(q_r \cdot (r_c + t_t))}{q_r \cdot (r_c + t_t)} + \rho_s \frac{J_1(q_r \cdot R)}{q_r \cdot R} \\ &+ \frac{1}{R^2} \int_{r_c}^{r_c+t_t} m \cdot r^2 \cdot J_0(q_r \cdot r) dr \Big], \\ =& 2 \cdot V \rho_s \cdot \Big[\frac{(\rho_c - b)}{\rho_s} \frac{r_c^2}{R^2} \frac{J_1(q_r \cdot r_c)}{q_r \cdot r_c} + \frac{(b - \rho_s)}{\rho_s} \frac{(r_c + t_t)^2}{R^2} \frac{J_1(q_r \cdot (r_c + t_t))}{q_r \cdot (r_c + t_t)} + \frac{J_1(q_r \cdot R)}{q_r \cdot R} \\ &+ \frac{1}{\rho_s} \cdot \frac{1}{R^2} \int_{r_c}^{r_c+t_t} m \cdot r^2 \cdot J_0(q_r \cdot r) dr \Big], \\ =& 2 \cdot V \cdot \rho_s \cdot F(q_r). \end{aligned} \tag{4.40}$$

where the integral term in equation 4.40 can be approximated by an infinite series based on the Struve polynomials [241–243] however, in this thesis, the contribution to the scattering amplitude was determined numerically.

An example of scattering intensities extracted from the narrow streaks for a-$SiO_{1.9}$ is shown in Figure 4.13, together with the numerical fit to the cylindrical core-shell and core-shell with a smooth transition models. In comparison to previous work using the form factor of a cylindrical object with a core-shell morphology [237], the use of a core-shell model with a smooth transition shows an improvement in fitting the scattering pattern at high q-values and yields a more realistic density distribution.

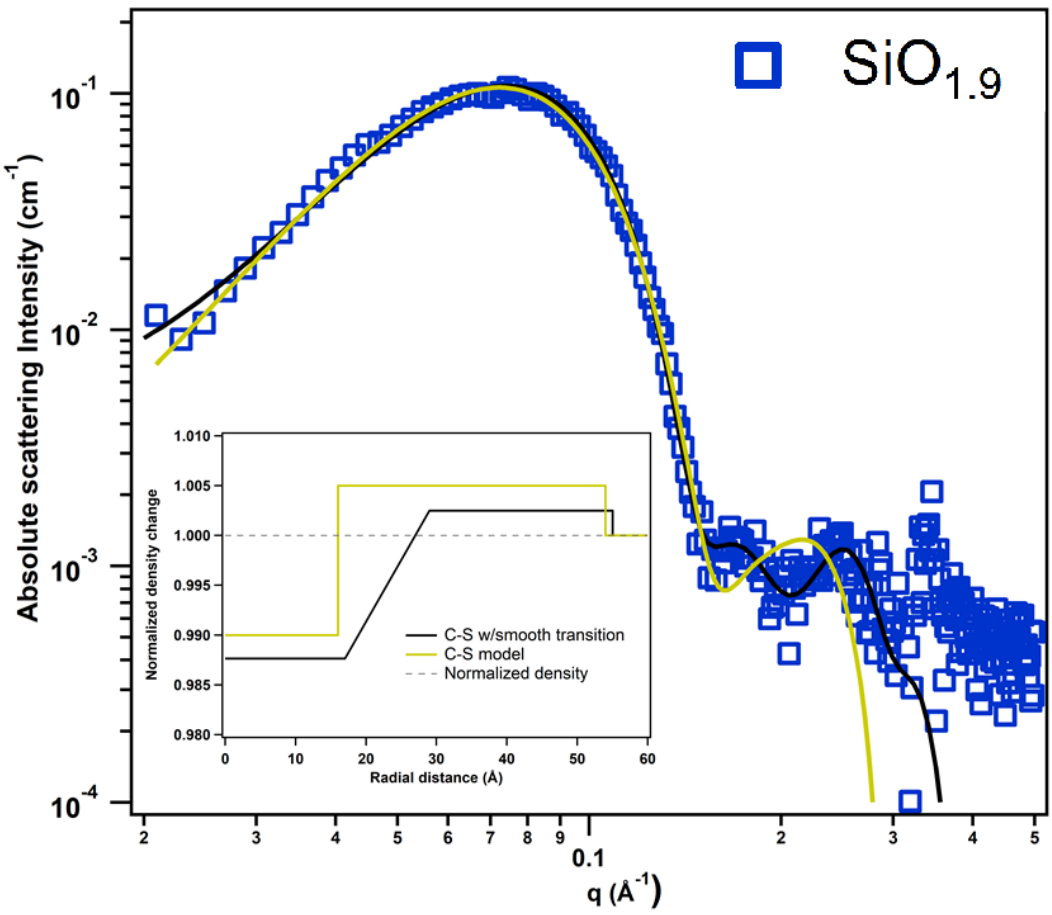

Figure 4.13: *SAXS scattering intensity and its corresponding numerical fit for a-$SiO_{1.9}$ considering two cylindrical models: a core-shell structure (yellow) and a core-shell with a smooth transition (black).*

4.7 Particle polydispersity

The systems studied in this thesis correspond to either spherical NPs or structures exhibiting a cylindrical geometry. In the former, the symmetry present does not require to account for a preferential orientation of the system. For the latter, as they are produced by the impingement of a parallel beam where the electronic interactions lead to negligible deviations from the initial trajectory, a consideration of multiple orientations inside the sample are not required. Thus, in this thesis the term polydispersity refers uniquely to variations in the radial dimensions of the two systems.

In the previous section the scattering amplitude of single particles with different geometries and density distributions were presented. However, systems studied in SAXS experiments are generally formed by more than one particle. For example, in this thesis ion fluences between 0.5 and 50 $\times$ 10^{11} cm^{-2} are considered for the characterisation of the ion track morphology, where each ion produces a single ion track thus, a large amount of ion tracks contribute to the scattering amplitude and hence, to the scattering intensity. For ion-beam synthesised Au NPs, the polydispersity or size distribution of the NPs population plays a central role in our study. The method used to account for the NPs size distribution was the maximum entropy method. It describes the NPs size distribution as a histogram from which the scattering intensity of each contribution is determined and is explained in more detail in section 6.2. On the other hand, ion tracks are extremely monodisperse systems due to the well-defined energy of the beam. The polydispersity accounts to some extent for stochastic variations but also for the fact that the energy loss varies slightly over the depth of the ion track and the model is an approximation to the real density distribution. In the absence of inter-particle interactions, the scattering intensity is the sum of the scattering intensities corresponding to each particle, such that:

$$I(q) = \sum_{i=1}^{N} I_{f,i}(q) = N \cdot V^2 \cdot \rho^2 \cdot \Big(F(q)\Big)^2, \tag{4.41}$$

where N corresponds to the ion fluence, V represents the particle's volume, ρ the density change with respect to the bulk material and $F(q)$ the form factor for each particle. To consider the particle's radial polydispersity of nearly identical particles, the term 4.41 transforms into

$$I(q) = \sum_{i=1}^{N} I_{f,i}(q) \cdot D(r_i), \tag{4.42}$$

where $D(r_i)$ is a normalized distribution function. In the following sections and corresponding analysis the polydispersity of the system is accounted for by using the normalized Schulz-Zimm distribution $SZ(R, \sigma_R, \bar{R})$ [234]

$$SZ(R, \sigma_R, \bar{R}) = exp\Big[z_q \log(z_1 \bar{R}) + z \log(R) - \log \Gamma(z_1) - z_1 \frac{R}{\bar{R}}\Big], \tag{4.43}$$

where $z = \left(\frac{\bar{R}}{R}\right)^2 - 1$, $z_1 = z + 1$, Γ is the gamma function and σ_R the width of the distribution. The Schulz-Zimm distribution was adopted to account for the polydispersity of the ion track core dimensions, which in some cases was comparable to the core size and leading to negative radial dimensions when considering a Gaussian distribution. The Schulz-Zimm distribution offers the advantage of avoiding negative radial values. Thus, equation 4.42 can be expressed as:

$$I(q) = N \cdot V^2 \int_0^{\infty} |f_f(q)|^2 SZ(R, \sigma_R, \bar{R}) dR. \tag{4.44}$$

4.8 Determination of the density change

The number of objects and volume can be determined from the irradiation fluence and thickness of the irradiated layer. The determination of the morphology and dimensions

of the ion tracks was carried out by fitting the appropriate models to the scattering amplitudes of cylindrical scattering objects, described earlier in this chapter. The scattering intensities available through SAXS measurements can be correlated with the scattering amplitudes by:

$$I(q) = N \cdot V^2 \cdot (\rho_s)^2 \cdot |F(q)|^2. \tag{4.45}$$

As mentioned before, the new form factor possess an integral term which can be numerically solved by the fitting routine implemented in Igor Pro. To determine the absolute density difference we considered the $\lim_{q\to 0}$ as the form factor exhibits a nearly constant behaviour where information regarding the number and volume of the scattering particles, and the absolute density change is stored [217, 219]. As can be seen from equation 4.45, only the form factor possesses a dependency on the scattering vector q. The calculation of $\lim_{q\to 0} f_f(q)$ was carried out using the identity $\lim_{q\to 0} \frac{J_1(qr)}{qr} = \frac{1}{2}$, leading to:

$$\begin{aligned}\lim_{q\to 0} f_f(q) = \lim_{q\to 0} \Big[& (\rho_c - b)\frac{r_c^2}{R^2}\frac{J_1(q_r \cdot r_c)}{q_r \cdot r_c} + (b - \rho_s)\frac{(r_c + t_t)^2}{R^2}\frac{J_1(q_r \cdot (r_c + t_t))}{q_r \cdot (r_c + t_t)} \\ & + \rho_s \frac{J_1(q_r \cdot R)}{q_r \cdot R} + \frac{1}{R^2}\int_{r_c}^{r_c + t_t} m \cdot r^2 J_0(q_r \cdot r) dr \Big] \\ = \Big[& \frac{1}{2}(\rho_c - b)\frac{r_c^2}{R^2} + \frac{1}{2}(b - \rho_s)\frac{(r_c + t_t)^2}{R^2} + \frac{1}{2}\rho_s + \frac{1}{R^2} m \cdot \lim_{q\to 0} \int_{r_c}^{r_c + t_t} r^2 \cdot J_0(q_r \cdot r) dr \Big].\end{aligned} \tag{4.46}$$

The last term of equation 4.46 can be simplified easily following two paths: (i) by applying the Lebesgue dominated convergence and monotone convergence theorems [244] it is possible to exchange the order and carry out the limit first and then the integration with respect to the radial variable; or (ii) expanding the Bessel function of zeroth order using its polynomial expression ($J_0 = \sum_{i=0}^{\infty} \frac{(-1)^i (x/2)^{2i}}{i!i!}$), for the first three terms it can be approximated as $J_0(x) \sim 1 - \left(\frac{x}{2}\right)^2 + \frac{1}{4} \cdot \left(\frac{x}{2}\right)^4$ thus, the integral term in equation 4.46 can be re-written as:

$$\begin{aligned}\lim_{q\to 0}\int_{r_c}^{r_c+t_t} r^2\cdot J_0(q_r\cdot r)dr &\sim \lim_{q\to 0}\int_{r_c}^{r_c+t_t} r^2\cdot\Big[1-\Big(\frac{q_r\dot{r}}{2}\Big)+\frac{1}{4}\cdot\Big(\frac{q_r\cdot r}{2}\Big)^4\Big]dr\\ &=\lim_{q\to 0}\int_{r_c}^{r_c+t_t}\Big[r^2-r^4\Big(\frac{q_r}{2}\Big)^2+\frac{1}{4}\cdot r^6\Big(\frac{q_r\cdot r}{2}\Big)^4\Big]dr\\ &=\lim_{q\to 0}\Big[\frac{r^3}{3}-\frac{r^5}{20}q_r^2+\frac{r^7}{448}q_r^4\Big]_{r_c}^{r_c+t_t}\\ &=\Big[\frac{r^3}{3}\Big]_{r_c}^{r_c+t_t}.\end{aligned} \tag{4.47}$$

It is noteworthy that both approximations lead to the same result and the presentation of the latter path is motivated by the simplification of the argument instead of providing the monotonically convergence of the Bessel function of zeroth order (which was demonstrated independently). Substitution of equation 4.47 into equation 4.46 leads to:

$$F(q)=(\rho-1)\Big(\frac{R_c+T_t}{R}\Big)+1-\frac{2}{3}(\rho-1)\Big[\Big(\frac{R_c+T_t}{R}\Big)^2+\Big(\frac{R_c}{R}\Big)^2+\Big(\frac{R_c(R_c+T_t)}{R^2}\Big)\Big] \tag{4.48}$$

To carry out the quantitative analysis, a fitting routine implemented in Igor Pro considering the form factor as described in equations (Fig. 4.13). The fitting routine is capable of fitting the ratio ρ_s/ρ_s, the radius of the core region r_c, the transition width t_t, and the thickness of the shell such that the total radius $R = r_c + t_t + t_s$. Because the ratio ρ_s/ρ_s is the only available quantity related to the density change from the numerical fitting, in the case of ion tracks it presents a negative sign which is characteristic of an under-/over-dense morphology. From SAXS, however, it is not possible to distinguish which one is under-/over-dense. The length of the ion track L is equal to the layer thickness and q is the radial component of the scattering vector. We considered a normalized Schulz-Zimm distribution for the core dimensions to account for deviations from the proposed model while scaling the distribution of the shell region following the method from Kluth *et al.* [56]. A narrow distribution of

the core region is assumed with a mean alue of R_c, while the distribution of the shell thickness, $t_s = R - r_c - t_t$, is fixed by scaling to the distribution of r_c to $\frac{t_s}{r_c}$.

Finally, the corresponding absolute SAXS intensity can be re-written as:

$$I(q=0) = NV^2\rho_s^2\Big[(\rho-1)\Big(\frac{r_c+t_t}{F}\Big)+1-\frac{2}{3}(\rho-1)\Big[\Big(\frac{r_c+t_t}{R}\Big)^2+\Big(\frac{r_c}{R}\Big)^2+\Big(\frac{r_c(r_c+t_tT)}{R^2}\Big)\Big]\Big]^2. \tag{4.49}$$

The absolute density change is calculated following the existing relation between the X-ray scattering length density (SLD) β and the local density variations: $\rho/\rho_{bulk} = \beta/\beta_{bulk}$. The term $I(q = 0)$ is determined from the extrapolation to lower q-values of the numerically fitted integrated scattering intensity extracted from the normalized scattering patterns measured.

Chapter 5

Swift heavy-ion irradiation of amorphous silicon dioxide, silicon nitride and silicon oxynitride thin layers

In this chapter, the characterization of the fine structure of ion tracks formed in amorphous silicon dioxide (a-SiO_x), silicon nitride (a-SiN_y) and silicon oxynitrides (a-SiO_xN_y) deposited by PECVD is presented. The physical properties of the thin layers such as thickness, density, composition and bond configuration were determined using spectral ellipsometry, RBS, ERDA and IR spectroscopy. The dimension and fine structure of ion tracks was measured by SAXS. The ion track morphology resembles an under-dense core surrounded by an over-dense shell with a smooth transition between the two regions for all materials, in agreement with MD simulations for a-SiO_2 and a-Si_3N_4. The absolute density variation in the ion tracks was determined for all materials. A larger density variation was found for tracks in a-SiN_y, in comparison to a-SiO_x, attributed partially to a larger thermal conductivity leading to a short-lived thermal spike, confirmed by i-TS model calculations. Results corresponding to high ion velocities in comparison to lower velocities are presented to quantify the velocity effect in these materials. For a-SiO_xN_y samples, the ion track radii exhibited two trends with composition: first, a constant increasing ion track radius is observed when the O/Si ratio is below one ($0 \leq x \leq 1$). This is followed by the saturation of the ion track

dimensions above this value with an ion track radius slightly above that of a-SiO_x. Examination of the IR spectra allowed to quantify the bond configuration and its evolution with fluence. The bond configuration was demonstrated to be governed by the random bonding model. Furthermore, the energy deposited by the SHI irradiation leads to a trade-off between the formation of Si-O bonds and preferential damage of Si-N bonds. At the same time, in the single ion track regime, H is not released but rather bonded preferentially to Si instead. The behaviour observed from the IR measurements supports the hypothesis of an ion-induced structural modification of the amorphous network where the ion-induced coordination defects are not directly related to the ion track dimensions.

5.1 Introduction

The lack of contrast in amorphous materials has limited the study of the ion track formation process by SHI irradiation in these materials to techniques such as FTIR spectroscopy and synchrotron-based small angle X-ray scattering (SAXS). FTIR is sensible to change in the infrared active bond configuration, relating any change in the spectra to the cross-sectional dimension of the ion track formed by SHI irradiation. SAXS on the other hand, is sensitive to small variations in the electronic density, where the scattering can be ascribed to the fine structure of the resulting ion track. In order to assess the potential of ion irradiation to modify the bond configuration of a-SiO_xN_y materials, it is meaningful to study the material response of their binary components (a-SiO_x and a-SiN_y) before looking into ternary compositions.

The competition between heat and mass transport, together with the rapid quenching of the thermal spike have a major impact on the ion track morphology [104]. The temperature profile in the thermal spike leads to non-uniform thermal stresses and internal mass transfer [119,120]. In amorphous materials, such as metallic glasses, if the temperature in the ion track region surpasses a critical value, the material experiences a local abrupt decrease in the viscosity [245]. The compressive strains

are redistributed causing a purely hydrostatic stress. During the cooling period, the track relaxation kinetics depends strongly on the viscosity value of the material. As the process occurs from the ion track boundary towards the center progressively, it is possible for the generated strains to undergo a reversal process. If the ion track cooling down process is quicker than the density oscillation time, the density fluctuations are only partially restored and a spatial density profile with an under-dense core surrounded by an over-dense shell is expected [245].

In this chapter, the radial dimensions as well as the fine structure and quantification of the absolute density variation profiles determined by SAXS are presented for ion tracks in one micron thick a-SiO_x, a-SiN_y and a-SiO_xN_y layers deposited by PECVD. Furthermore, MD simulations and FTIR spectroscopy analysis were performed for comparison and better understanding of the structural changes amorphous insulators undergo after SHI irradiation, where no consistent picture exists on the nature of the ion track morphology [58, 59], as well as an adequate interpretation of the FTIR spectroscopy currently in the literature [27, 53, 54, 86, 89]. Hence, a new model for the ion track formation process is proposed, as well as a new framework for a better interpretation of the FTIR spectra based on the methodology proposed originally by Brodsky *et al.* [201], and Langford *et al.* [246].

5.2 Thin film deposition and characterisation

Thin a-SiO_x, a-SiN_y and a-SiO_xN_y layers were deposited on c-Si substrates with an Oxford Plasma Technology 100 PECVD system at 600 C. The relative concentration of Si, O and N was varied by controlling the SiH_4:NH_3:N_2:N_2O chemistry (see chapter 3.1 for details). The SiH_4 flow rate was kept constant while the gas ratio R was varied within the range $0 \leq R \leq 1$, where R is defined as: [247, 248]

$$R = \frac{N_2O}{N_2) + NH_3}. \tag{5.1}$$

The gas ratio is related to the Oxygen content and thus to the stoichiometry of the thin film. For example, when $R = 0$, the stoichiometry corresponds to a-$SiN_{1.06}$ while for $R = 1$ to a-$SiO_{1.9}$[1].

The refractive index and thickness of the films were measured by spectral reflectometry, with a spectral range of 440 to 1660 nm using the Tauc-Lorentz dispersion function [171, 172]. Figure 5.1 shows the refractive index n at 632 nm as a function of R, starting at $n = 1.94$ for $R = 0$ and monotonically decreasing to 1.48 when $R = 1$. The former corresponds to the typical value found in hydrogenated a-SiN_y [43], while the latter is very close to that of a-SiO_2 (~ 1.5) [249].

The decrease of the refractive index is associated with compositional and bond configurational changes. In the case of a-SiO_xN_y materials, two models have been proposed to describe their structure. The first is known as the random mixture (RM) model, which assumes that the structure is formed by a linear combination of two tetrahedra SiO_4 and SiN_4. Thus, it can be considered a linear combination of Si_3N_4 and a-SiO_2. The second corresponds to the random bonding (RB) model where the local arrangement consists of a statistically distributed mixture of five tetrahedra (SiO_nN_{4-n} for n = 0, 1, 2, 3, 4) [42, 43].

Following the RM model, some of the physical properties of a-SiO_xN_y materials have been proposed to be described as a linear combination of those corresponding to a-SiO_x and a-SiN_y in terms of their relative molar concentration, for example the refractive index. Under this approximation the composition of a-SiO_xN_y thin layers can be determined using the following relationship: [41]

$$n_{SiO_xN_y} = x_{SiO_x} \cdot n_{SiO_x} + x_{SiN_y} \cdot n_{SiN_y}, \tag{5.2}$$

[1]The stoichiometric values correspond to those determined by RBS, as it will be explained in the subsequent paragraphs.

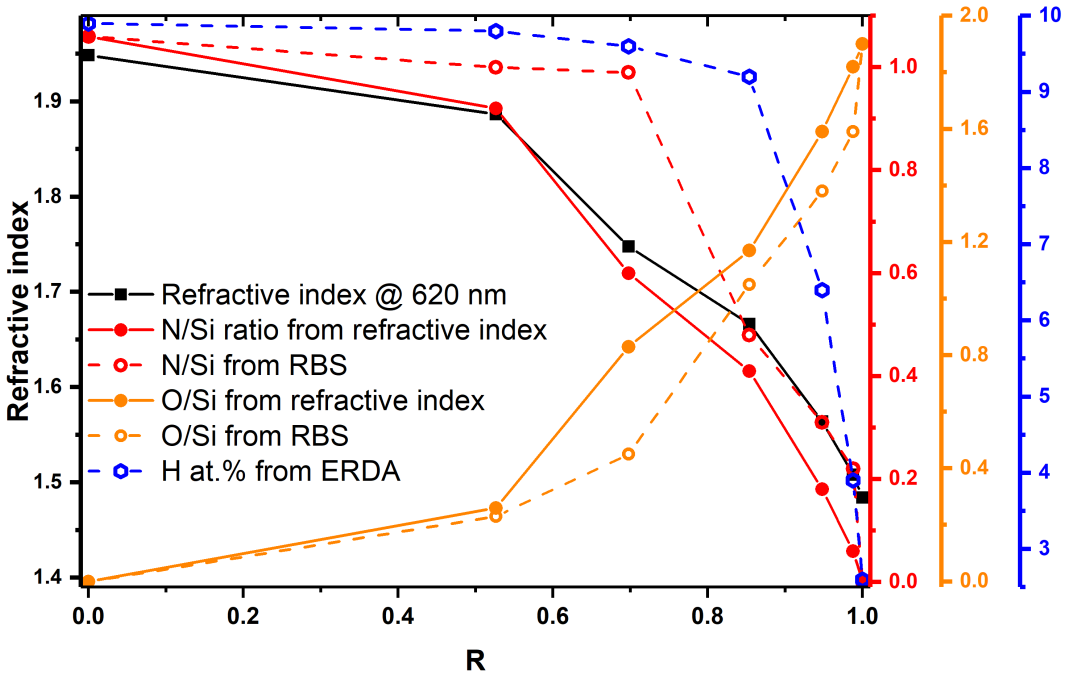

Figure 5.1: *Refractive index measured at 620 nm (full black squares joined by continuous lines), N/Si compositional ratio determined from the refractive index (full circles connected by a continuous line in red) and measured from RBS analysis (open circles conneted by a dotted line in red); O/Si compositional ratio determined from the refractive index and RBS analysis (full/open circles connected by a continuous/dotted line in orange, respectively), and H content in atomic percent deducted from ERDA measurements as a function of the R ratio (open blue circles).*

with the condition: $x_{SiO_x} + x_{SiN_y} = 1$.

The Si, N and O content were determined by RBS measurements, with the O/Si and N/Si ratios for a-SiO_x and a-SiN_y determined to be 1.90 ± 0.03 and 1.06 ± 0.04, respectively. With these base values, the relative molar concentration and the respective estimation of the composition based on the RM model for the a-SiO_xN_y layers were determined. The results are shown in Figure 5.1 as full circles connected by continuous lines in red for the N/Si ration and in orange for the O/Si ratio, and are summarized in Table 5.1. For the values determined by Eq. 5.2, we observed two different regimes for the behaviour of the ratios as a function of the gas ratio. When $R < 0.5$, a small O increase and N decrease from a-$SiN_{1.06}$ is observed. Above $R = 0.5$, a steep increase/decrease above that value of O/Si and N/Si content was determined, respectively.

Sample	Refractive index	Thickness	Density	Ellipsometry		RBS		ERDA	FTIR
	[632 nm]	[nm]	[g · cm^{-3}]	x	y	x	y	H	
SiN_y	1.946 ± 0.002	1180.0 ± 1.2	2.72 ± 0.02	0.00 ± 0.01	1.06 ± 0.02	0.00 ± 0.01	1.06 ± 0.02	9.90 ± 0.20	14.80 ± 1.20
	1.884 ± 0.002	1124.2 ± 0.8	2.64 ± 0.2	0.26 ± 0.04	0.92 ± 0.05	0.23 ± 0.07	1.00 ± 0.07	9.76 ± 0.56	
	1.746 ± 0.002	1539.3 ± 0.9	2.47 ± 0.2	0.83 ± 0.05	0.60 ± 0.05	0.45 ± 0.07	0.99 ± 0.06	9.62 ± 0.45	
SiO_xN_y	1.665 ± 0.002	1012.0 ± 0.8	2.37 ± 0.2	1.17 ± 0.05	0.41 ± 0.04	1.05 ± 0.06	0.48 ± 0.06	9.16 ± 0.50	
	1.563 ± 0.002	968.0 ± 0.4	2.25 ± 0.3	1.59 ± 0. 5	0.18 ± 0.04	1.38 ± 0. 5	0.31 ± 0.08	6.36 ± 0.36	
	1.507 ± 0.002	990.0 ± 0.6	2.18 ± 0.3	1.82 ± 0.04	0.06 ± 0.04	1.59 ± 0.03	0.22 ± 0.07	3.92 ± 0.28	
SiO_x	1.484 ± 0.002	944.2 ± 0.9	2.15 ± 0.02	1.90 ± 0.03	0.00 ± 0.02	1.90 ± 0.03	0.00 ± 0.06	2.58 ± 0.32	2.62 ± 0.24

Table 5.1: *Physical parameters for the a-SiO_xN_y thin films: refractive index measured by spectral reflectometry at 632 nm, thickness, density and composition determined in combination with RBS, and H content determined from ERDA measurements and calculated from FTIR parameters.*

Independently, the stoichiometry of the different a-SiO_xN_y layers was determined by RBS. A similar behaviour to that expected from the RM model was determined, however with the change in behaviour at $R < 0.7$ (Fig. 5.1, full circles connected by dashed lines). Hence, Fig. 5.1 allows to relate the values of the gas ratios used during the thin layer depositions to the determined layer stoichiometries. The difference in stoichiometry between the RM model, based on the refractive index values, and RBS measurements have been previously related to the relative content of NH_3 in the gas mixture during the film growth [16], where the steep slope is indicative of the dissociation-controlled equilibrium between polyaminosilanes ($Si[NH_2]_2$, for $n = 3$, 4)

and Si and N atoms [202], as polyaminosilanes are precursors for Si-N bonding [250]. Thus, the change from gradual towards a steep slope can be related to the threshold of polyaminosilane formation [16].

Because the bond configurations of a-$SiO_{1.9}$, a-$SiN_{1.06}$ and a-SiO_xN_y are infrared active, FTIR spectroscopy in absorbance mode was used to obtain information on the short-range order for all materials. Figure 5.2 shows the corresponding absorbance spectra as a function of R. In the region between 380 and 1450 cm^{-1}, the absorbance bands correspond to the principal Si-O and Si-N vibrational modes. A smoot transition is observed when the composition of the thin a-SiO_xN_y layers varies from a-$SiO_{1.9}$ to a-$SiN_{1.06}$. During this transition, the presence of a single main absorbance band is indicative of the bonding configuration being better described by the RB model. On the contrary, the RM model suggests that the main absorbance signal should be formed by two main contributions corresponding to a-$SiO_{1.9}$ and a-$SiN_{1.6}$, where the relative intensity would depend on the molar concentration of each of the two components [43].

The 2050 - 3750 cm^{-1} region is comprised of three absorbance bands that correspond to Si-H, N-H and Si-OH vibrational modes. The first band, located in the region 2000 - 2300 cm^{-1}, corresponds to the Si-H stretching mode and can be deconvoluted into up to seven Gaussian contributions [16]. The contributions are located at frequencies above 2150 cm^{-1} and correspond to Si-H bonded to a N atom in the H-Si-N_xSi_{3-x} configuration and can be determined by the relationship $2080 + 33 \cdot x$ cm^{-1} according to their band position [251]. From the corresponding deconvoloution of the Si-H absorbance band in Figure 5.2, we observe the contribution of two bands belonging to H-SiN_2Si at 2170 cm^{-1} and to H-Si_3 at 2200 cm^{-1} for lower O/Si ratios, followed by a shift towards higher frequencies when the O content increases, up to 2250 and 2270 cm^{-1}. It is still unclear if this corresponds to the same configuration when N atoms are being replaced by O. A similar shift in position occurs for the absorbance bands located around 3200 and 3500 cm^{-1}. When $O/Si \geq 0.7$, the presence of the O-H and Si-OH vibrational modes located around 3500 and 3600 cm^{-1}, respectively, becomes apparent.

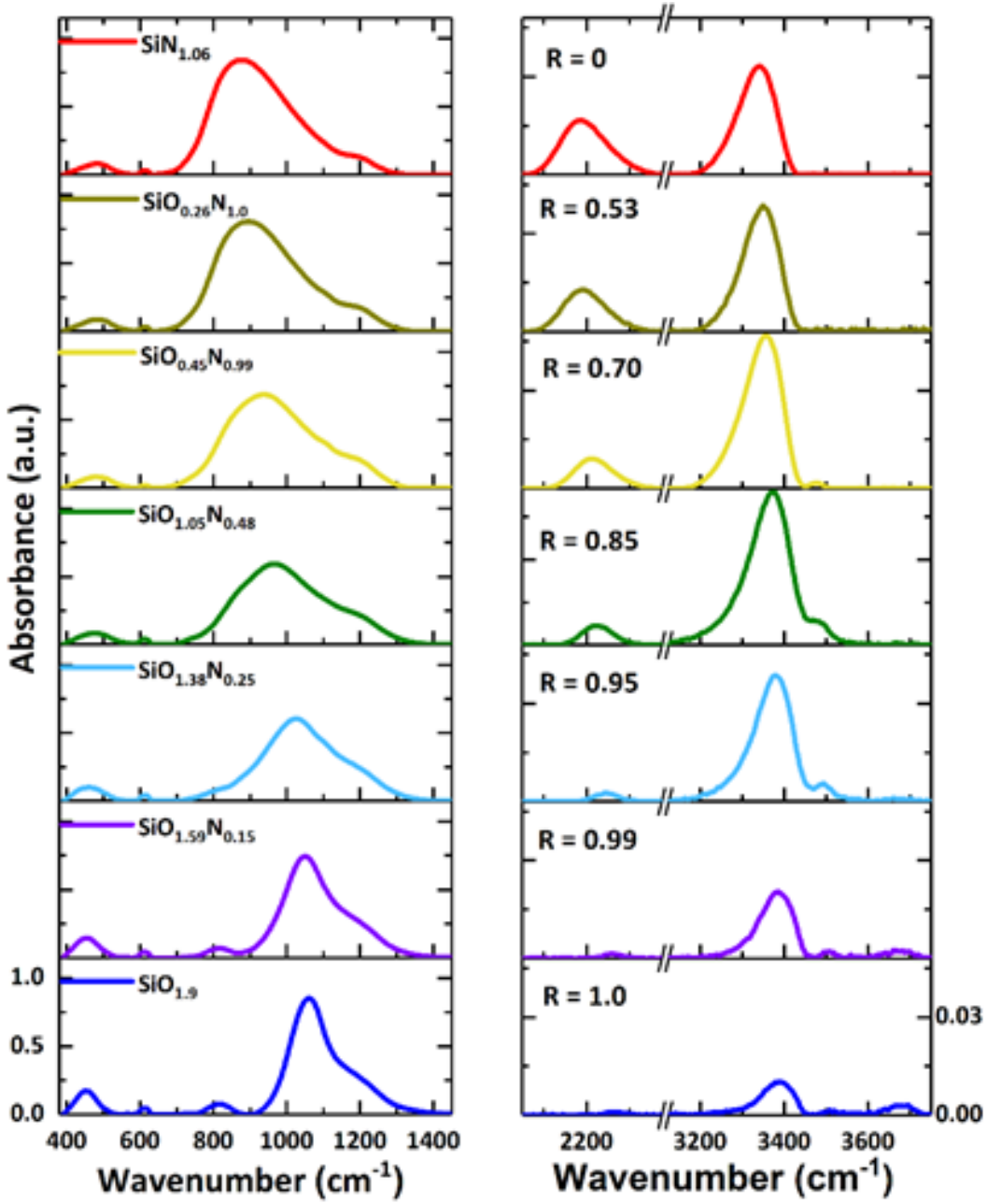

Figure 5.2: *FTIR spectra in the region between 380 - 1450 cm^{-1} and 2050 - 3750 cm^{-1} for a-$SiN_{1.06}$, a-$SiO_{1.9}$ and a-SiO_xN_y with different configurations. The first region corresponds to the typical region where the Si-N and Si-O vibrational modes are located while the second corresponds to the position of Si-H, N-H and Si-OH modes.*

All layer depositions were carried out at 600 °C to promote the formation of dense layers while reducing the H content in the network, as previously reported elsewhere [252]. However, as observed from FTIR spectra, residual H remains present in the network at this temperature. To quantify the content of residual H, ERD analysis (see section 3.5.1) was carried out and the results are plotted in blue in Figure 5.1 and summarized in Table 5.1. A nearly constant H content for $R < 0.8$ was observed, followed by a steep decrease in H content above this value. Quantification of the H content for a-$SiO_{1.9}$ led to a value of 2.6 ± 0.4 at. %, while for a-$SiN_{1.06}$ the content corresponds to 9.9 ± 0.6 at. %. For these materials, a quantification of the H content was also carried out based on FTIR spectroscopy, as first suggested in [201] and under considerations drawn in [253–255] (see section 3.5.1). The observed IR bands were deconvoluted into Gaussian contributions, followed by the corresponding identification of the Si-N, Si-H, N-H, O-H and Si-OH vibrational modes present (Figs. 5.3 (a) to (d)). Using their corresponding area, position and signal width, it is possible to calculate the corresponding bond intensity using the proportional coefficients, summarized in [254] and [17], following the framework from Langford *et al.* [246] (see section 3.5.1):

$$[A-B] = C \int_{-\infty}^{\infty} \frac{A_{A-B}(\omega)}{\omega}, \tag{5.3}$$

where $A-B$ represent any of the vibrational modes present (Si-N, Si-O, Si-H, N-H, O-H and Si-OH) and thus, $[A-B]$ represents their corresponding bond density for a given peak area from the FTIR spectra. $A_{A-B}(\omega)$ is the abosrbance as a function of frequency ω and is described by a Gaussian contribution and C the calibration constant, within the order of $\times\ 10^{22}$ cm^{-2}.

Equation 5.3 is used to determine the H content as follows: [17]

$$H_{cont} = \frac{[Si-H] + [N-H]}{[Si-N] + [Si-H] + [N-H]} \times 100\%, \tag{5.4}$$

for a-$SiN_{1.06}$, while for a-$SiO_{1.9}$ the term $[Si-N]$ needs to be replaced by $[Si-O]$

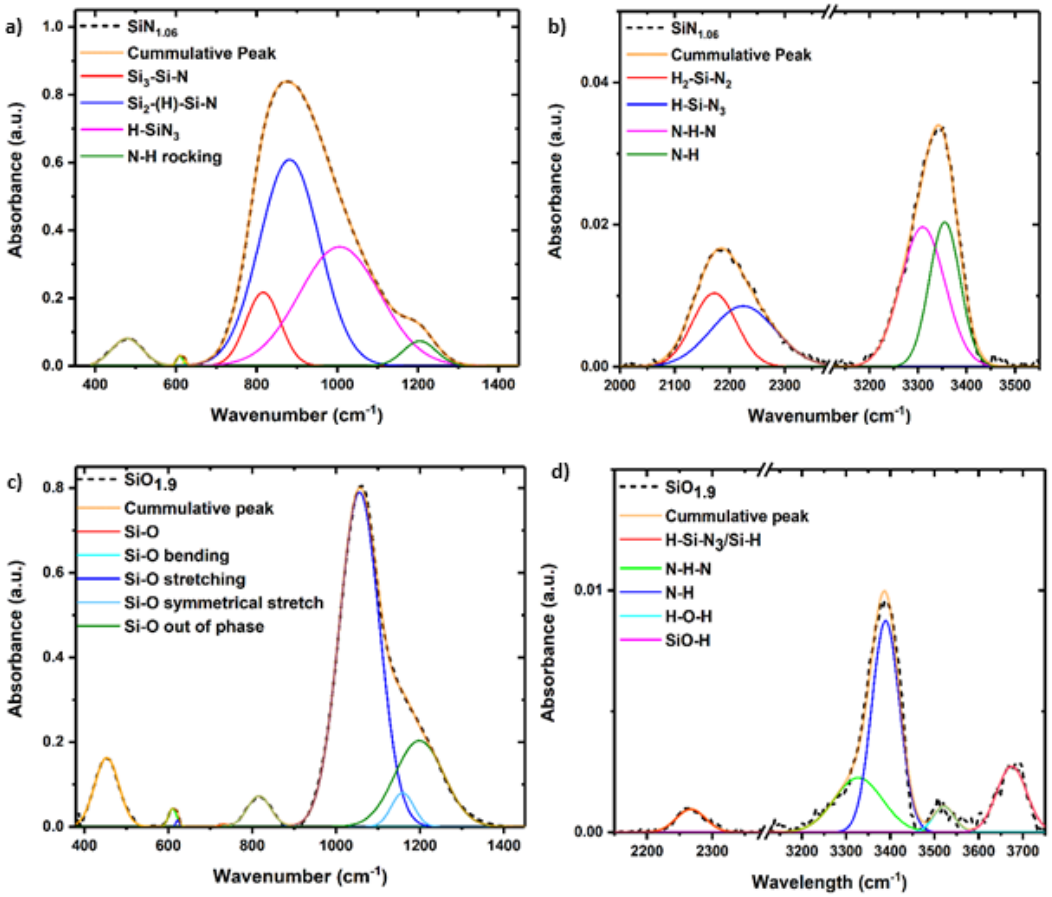

Figure 5.3: *FTIR absorbance spectra of pristine a-$SiN_{1.06}$ ((a) and (b)), and a-$SiO_{1.9}$ ((c) and (d)), and their deconvolution in Gaussian contributions after identification of their corresponding vibrational configuration at low and higher frequencies.*

and the contribution from hydroxide bonds $[O-H]$, thus:

$$H_{cont} = \frac{[Si-H]+[O-H]}{[Si-O]+[Si-H]+[O-H]} \times 100\%. \tag{5.5}$$

The H content estimated by FTIR measurements result in $\sim$ 15 at. % for a-$SiN_{1.06}$ and below 3 at. % in the case of a-$SiO_{1.9}$. This represents a good agreement of the H content for a-$SiO_{1.9}$ layers with previous reports [252], while showing a considerable deviation for a-$SiN_{1.06}$. This behaviour is a result of the stoichiometric deviation from the ideal composition of the two materials. The deviation in the case of a-$SiN_{1.06}$, can

be ascribed to the proportional coefficients used to estimate the bond density as it has been shown that they exhibit a dependency on the stoichiometry [253–255], where they are proportional to the N/Si or O/Si ratios. Hence, the large overestimation of 50 % of the H content for a-$SiN_{1.06}$ can be the result of considering the coefficient values known for a-Si_3N_4.

Up to date no study has been carried out to determine the proportional coefficients for a-SiO_xN_y materials, where the use of coefficients determined for a-Si_3N_4 and a-SiO_2 can potentially lead to erroneous estimation of the H content [17]. For this reason the FTIR determination of the H content was not pursued further, aiming to avoid misleading conclusions.

In the same fashion, an analysis was carried out to determine the O/Si and N/Si compositional ratios for a-$SiN_{1.06}$ and a-$SiO_{1.9}$, respectively. An agreement within 3 % of the values from RBS measurements was determined for the composition of a-SiO_x and a-SiN_y, amounting to $x = 1.89 \pm 0.03$ and $y = 1.06 \pm 0.04$, respectively. The results are summarized in Table 5.1. Based on our observations, the local structure of a-SiN_xN_y materials is better described by the RB model and hence, the calibration constants known for a-SiO_x and a-SiN_y cannot be used to determine their elemental composition using FTIR spectroscopy. In particular, no investigation has been carried out that allows to estimate how the calibration constants should be amended with O or N content. Because of the good agreement between the RBS and FTIR analyses for a-SiO_x and a-SiN_y, together with the lack of a dependence on the bond configuration of the backscattering cross-section, for the rest of this thesis the values presented for the O/Si and N/Si ratios correspond to those determined by RBS.

Many studies of the a-SiO_x, a-SiN_y and a-SiO_xN_y structures have been carried out using FTIR spectroscopy, X-ray absorption spectroscopy (XAS) and X-ray photoemission spectroscopy (XPS), supporting the validity of the RB model to describe the local structure, and thus the vibrational configuration, of these materials [43] and therefore, the Mott rule [42]. However, with larger incorporation of H and excess of Si

into the network, both the RM and the RB models exhibit significant disagreements with experimental measurements [43].

In this section the determination of the physical properties and the O and N content for a-SiO_x, a-SiN_y and a-SiO_xN_y thin layers was presented. From the experimental measurements of the refractive index the stoichiometric composition based on the RM model was estimated. The results were compared to the Si, O, and N content determined by Rutherford backscattering spectrometry. Significant differences were observed between the two methodologies, which, together with the analysis of the FTIR spectra of the a-SiO_xN_y layers, suggests that the local structure is better described by the RB model. Furthermore, a relation between the stoichiometry and the precursor gas mixture in terms of the gas ratio R, as well as the H content was confirmed. This relation is very relevant as it facilitates the deposition of single a-SiO_xN_y layer with a specific property.

5.3 Swift heavy-ion irradiation of amorphous silicon nitride and silicon dioxide

5.3.1 Small angle X-ray scattering

The ion track morphology and fine structure was studied predominantly using synchrotron-based transmission SAXS. SAXS shows a high sensitivity to small changes in the electron density such as those occurring in ion tracks which which can be correlated to their morphology [56, 96, 256]. When the ion tracks are perfectly aligned with respect to the X-ray beam, it is possible to observe the azimuthal symmetry present (Figs 5.4 (a) and (c)). When tilted by 10° an anisotropic scattering pattern is observed due to the high aspect-ratio of the aligned ion tracks (Figs. 5.4 (b) and (d)). Following irradiation, samples were prepared for the SAXS measurements by thinning the Si substrate down to 100 μm thickness by mechanical polishing to reduce parasitic scattering from the substrate yet provide enough support for the layers. The

scattering intensities for further analysis were extracted by selectively masking the streaks shown in the scattering pattern followed by a background subtraction defined by a mask outlined in an angular sector perpendicular to the streaks (see section 4.5.1). At fluences below 5×10^{11} cm^{-2}, ion track overlap is negligible as discussed in previous results and confirmed by a stochastic overlap model [257]. The amorphous nature of our samples supports the assumption of an azimuthally symmetry present. While we measure $\sim 10^7$ ion tracks, the resulting analysis reveals information about the 'individual' ion track structure averaging out fluctuations on atomic scales, as the tracks are parallel and almost identical (because of the well-defined ion energy and direction) [237].

The scattering intensities extracted from the narrow streaks are shown in Figs 5.5 (a) and (b) for different fluences. The best fit to the data was obtained with a cylindrical core-shell model with a smooth transition between core and shell densities (see section 4.6). The corresponding scattering amplitude $f(q)$ for the radial density distribution can be expressed as:

$$\begin{aligned} f(q) =& \frac{2\pi L \rho_s}{q} \Big[(\rho - 1) \Big((R_c + T_t) \frac{J_1(q \cdot (R_c + T_t))}{q} \\ &+ R \frac{J_1(q \cdot R)}{q} \Big) - \int_{R_c}^{R_c + T_c} \frac{(\rho - 1)}{T_t} r^2 J_0(q \cdot r) dr \Big]. \end{aligned} \tag{5.6}$$

The length of the ion tracks L is equal to the layer thickness and q is the radial component of the scattering vector. The factor ρ describes the density change ratio between the core and the shell regions, ρ_s is the maximum absolute density change of the shell. J_0 and J_1 are the Bessel function of zeroth and first order respectively, R_c is the core radius considered to have a constant density change value ρ_c, T_t corresponds to the width of the transition region and S_t is the shell width. The total track radius corresponds to $R = R_c + T_t + S_t$. We are considering a smooth transition between the core and shell region approximated by a linear function. We used a narrow normalized Schulz-Zimm distribution for the core dimensions to account for deviations from the proposed model while scaling the distribution of the shell region following the method

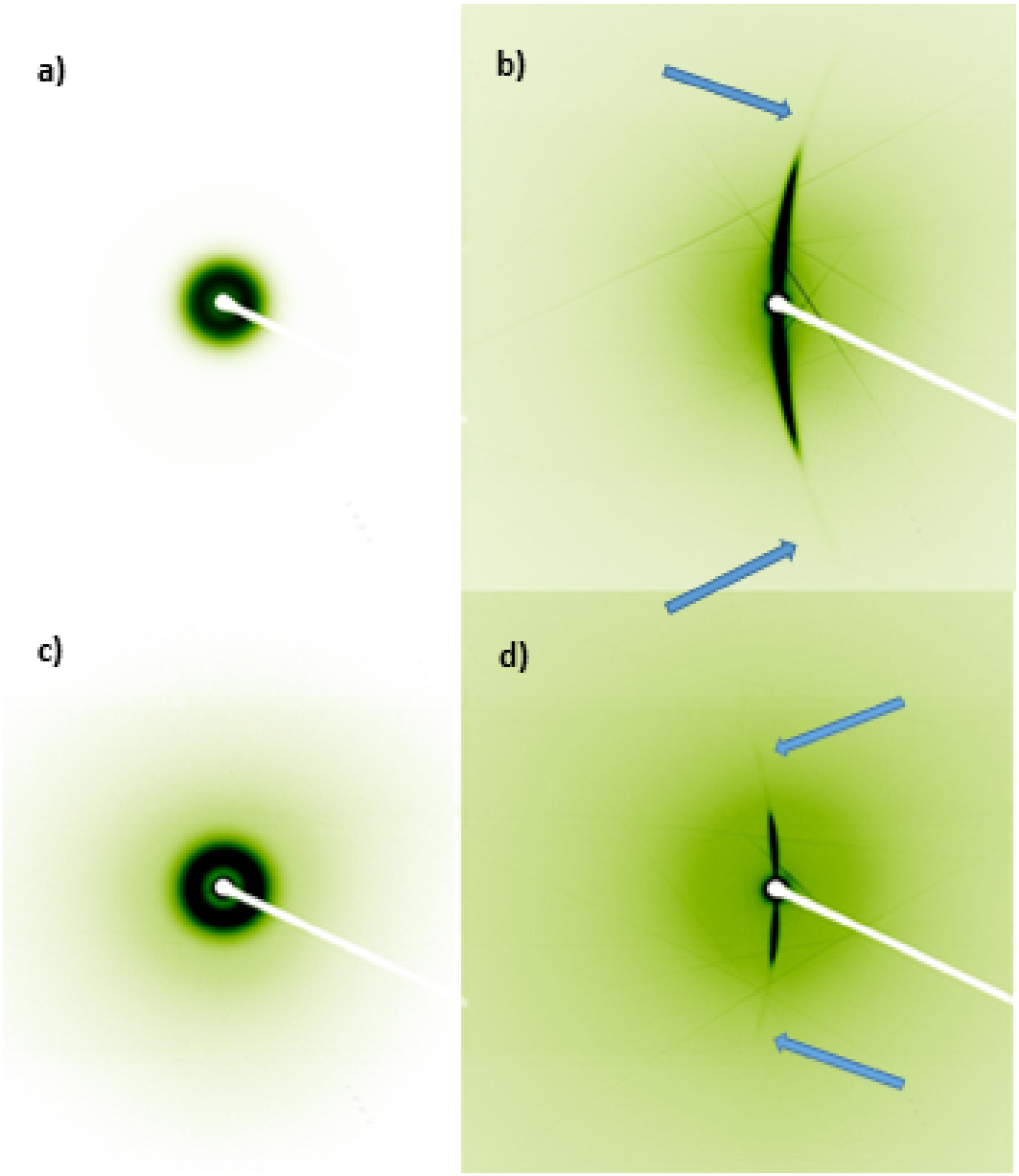

Figure 5.4: *Scattering patterns of ion tracks formed after irradiation with* 1×10^{11} cm^{-2} *185 MeV Au ions in a-*$SiN_{1.06}$ *(a) and a-*$SiO_{1.9}$ *(c) aligned, and tilted with respect to the X-ray beam by 10° (b) and (d), respectively. The arrows point to the curved anisotropic secondary oscillations in the streaks resulting from ion track scattering.*

from Kluth *et al.* [56].

The numerical fits with the proposed model are in Figs. 5.5 (a) and (b), agree very well with the observed measurements with high accuracy for all fluences considered, in particular in the extended q-range. This is a clear improvement compared to previous models where a sharp transition between the two regions was considered [56]. We assigned the nature of the weak secondary oscillations to the scattering originated in the transition region. The total track radius R for 185 MeV Au ions extracted from the theoretical fits amounts to 4.2 ± 0.1 nm for a-$SiN_{1.06}$, and 5.5 ± 0.1 nm for a-$SiO_{1.9}$. The value for the total ion track radius determined for a-$SiO_{1.9}$ agrees with previous experiments carried out for thermally grown a-SiO_2 (R = 5.4 ± 0.1 nm) [56]. Despite the higher energy deposition during the ion irradiation (20.9 keV/nm for a-$SiN_{1.06}$ and 16.3 for a-$SiO_{1.9}$), a-$SiN_{1.06}$ exhibit a significantly smaller track radius than a-$SiO_{1.9}$. This behaviour can be the result of the higher melting point (∼1900 °C for a-$SiN_{1.33}$ and ∼ 1700 °C for a-SiO_2, respectively) but we attribute it mainly to the lower value of the optical band gap, which can be as low as 3 eV for nearly stoichiometric silicon nitride [251] and around 5 eV for silicon dioxide [258]. This results in a higher electron-phonon mean-free path leading to a comparatively lower value for the electron-phonon coupling (see section 2.3) [108]. Information on the ion track morphologies is summarized in Table 5.3.1.

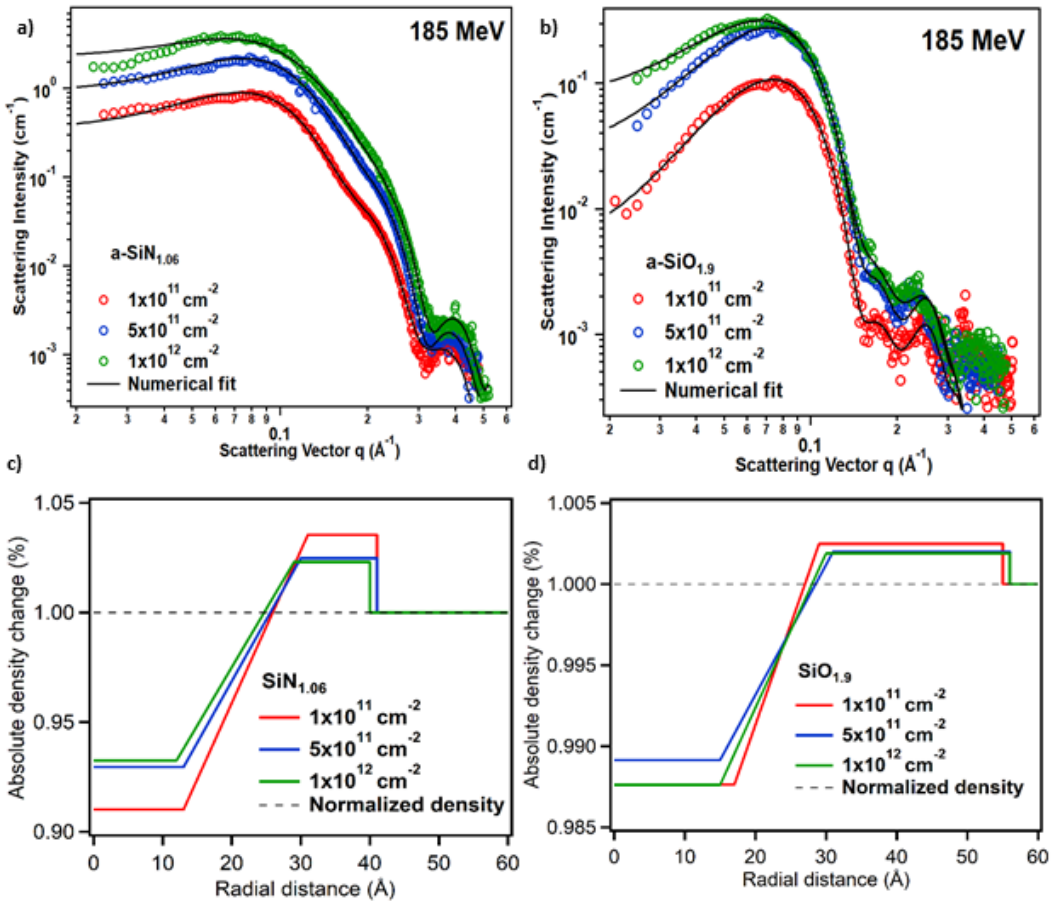

Figure 5.5: *Integrated SAXS scattering intensities for samples irradiated with 185 MeV Au ions with different fluences and their corresponding numerical fits using the core-shell model with a smooth transition for a-$SiN_{1.06}$ (a) and a-$SiO_{1.9}$ (b). Normalized absolute density change profiles extracted from the numerical calculations (c) and (d), respectively.*

Sample	Physical properties		Irradiation conditions		Morphology						
	x	Density [g/cm^3]	Energy [MeV]	S_e [keV/nm]	R_c [nm]	T_t [nm]	R [nm]	σ_c [nm]	$\frac{\rho_c}{\rho_s}$	ρ_c (%)	ρ_s (%)
SiN_x	1.06 ± 0.03	2.72 ± 0.02	185	20.7	1.5 ± 0.1	1.2 ± 0.1	4.2 ± 0.1	0.5 ± 0.1	-4.0 ± 0.1	-8.5 ± 0.4	2.1 ± 0.3
			2300	23.9	1.3 ± 0.1	1.1 ± 0.1	4.1 ± 0.1	0.4 ± 0.1	-4.5 ± 0.1	-4.4 ± 0.2	1.0 ± 0.2
	1.10 ± 0.03	3.10 ± 0.05	185	23.8	1.2 ± 0.1	0.3 ± 0.2	4.9 ± 0.3	0.4 ± 0.1	-11.9 ± 0.3	-1.5 ± 0.2	0.1 ± 0.2
SiO_x	1.90 ± 0.02	2.15 ± 0.02	185	16.3	1.7 ± 0.1	1.2 ± 0.1	5.5 ± 0.1	0.3 ± 0.1	-4.9 ± 0.1	-1.5 ± 0.1	0.3 ± 0.1
			2300	19.5	1.8 ± 0.1	0.9 ± 0.1	5.3 ± 0.1	0.2 ± 0.1	-5.0 ± 0.1	-1.5 ± 0.2	0.3 ± 0.1
	2.00 ± 0.02	2.20 ± 0.02	185	16.6	0.6 ± 0.1	3.0 ± 0.1	5.3 ± 0.1	0.5 ± 0.1	-1.6 ± 0.1	-3.2 ± 0.2	2.0 ± 0.2

Table 5.2: *Physical parameters as determined from RBS and spectral reflectometry, irradiation parameters including electronic energy-loss S_e as calculated by SRIM2013 considering 1 μm thick layers and fitted parameters from SAXS measurements after irradiation with a fluence of 1 × 10^{11} cm^{-2}. The values R_c, T_s, R, σ_c and $\frac{\rho_c}{\rho_s}$ corresponding to: the inner core radius, the width of the transition region, the total ion track radius, the polydispersity of the inner core radius and the ratio between the density change of the inner core and shell regions, respectively.*

Figures 5.5 (a) and (b) show the absolute scattering intensities for both materials irradiated with 185 MeV Au ions. It is clearly apparent that the scattering intensity from tracks in a-$SiN_{1.06}$ is significantly higher than that from tracks in a-$SiO_{1.9}$. Given the same fluence (number of tracks) and layer thickness, this difference is related to a higher density change in the tracks in a-$SiN_{1.06}$. The absolute density change can be obtained from the absolute scattering intensity by considering $\lim_{q\to\ 0} I(q)$ after normalization.

The corresponding absolute SAXS intensity can be re-written as:

$$\begin{aligned} I(q=0) =& NV^2\rho_s^2\Big((\rho-1)\left(\frac{R_c+T_t}{R}\right)+1-\frac{1}{6}(\rho-1)\Big[\Big(\frac{R_c+T_t}{R}\Big)^2 \\ &+\Big(\frac{R_c}{R}\Big)^2+\Big(\frac{R_c(R_c+T_t)}{R^2}\Big)\Big]\Big)^2. \end{aligned} \tag{5.7}$$

The absolute density change is calculated following the existing relation between the X-ray scattering length density (SLD) β and the local density variations: $\frac{\rho}{\rho_{bulk}} = \frac{\beta}{\beta_{bulk}}$. The term $I(q = 0)$ is determined from the extrapolation to lower q values of the numerically fitted integrated scattering intensity extracted from the normalized scattering patterns measured. The calculated absolute density change for a-$SiN_{1.06}$ was determined to be - 8.5 ± 0.3 %/2.1 ± 0.3 % for the core/shell configuration, and - 1.2 ± 0.1 %/0.25 ± 0.1 % in the case of a-$SiO_{1.9}$. The density profiles calculated from equation 5.7 are shown in Figures 5.5 (c) and (d). The ion track morphology corresponds to a constant under-dense region surrounded by a thin transition region and an over dense shell. The determination of the configuration is supported by the negative values fitted for ρ, the minus sign implies and over/under or under/over dense configuration. From the analysis by SAXS, the latter two possible configurations can be determined yet, it is not possible to distinguished between them. To resolve the most-likely configuration, MD simulations are carried out, where it is possible to simulate the atomistic behaviour of the two materials as well as retrieve the final density profile, a procedure that will be discussed in the next subsection.

5.3.2 Molecular dynamics simulations

The two-temperature molecular dynamics model (2T-MD) [128] was used to simulate ion tracks produced in a-SiO_2 and a-Si_3N_4 after irradiation with 185 MeV Au ions. For a-SiO_2 we considered the electron-phonon coupling to be $g = 1.25 \times 10^{13}$ W/cm^3 K [117], while for a-Si_3N_4 it was estimated using the expression $g = k_e/\lambda^2$ in terms of the electron-phonon mean-free path λ. Two values of λ were considered in this study: $\lambda = 4.3$ nm (estimated from the empirical relation with the optical band gap according to Toulemonde *et al.* [1]) and $\lambda = 3$ nm (the same value as a-SiO_2).

The a-SiO_2 cell was created using the Wooten-Winer-Weaire (WWW) method, and the a-Si_3N_4 by heating a random stoichiometric mixture of atoms and then cooling it slowly such that the atoms relax towards their local minima. For both methods we followed the procedure described in detail in [259]. The a-SiO_2 structure produced with the WWW method shows small amount of initial defects (< 1 %). The a-Si_3N_4 structure produced with the heat and cool method contained even in the initial state (before irradiation) a rather significant amount of coordination defects, which is a known problem of Tersoff-type potentials [260], and it is necessary to be taken into account. The dimensions of the cells employed were 263 Å $\times$ 227 Å $\times$ 46 Å for a-SiO_2. To account for statistical uncertainties, the presented simulations were averaged over 5 routines for each material.

Figures 5.6 (a) and (b) show the relative radial density change distribution calculated by MD simulations across the ion track 100 ps after the passage of a single Au ion with an energy of 185 MeV in amorphous SiO_2 and Si_3N_4, respectively. The simulations illustrate the formation of ion tracks with an under-dense core surrounded by an over-dense shell in both cases. For a-SiO_2, we explored the density change profile using the Watanabe-Samela many body interatomic potential, which shows good agreement with the experimentally observed value for the under-dense core (3.0 nm) and the total ion track radius (5.9 nm) but exhibits larger density change values (Figure 5.6 (a)). Such behaviour can be the result of the frozen-in

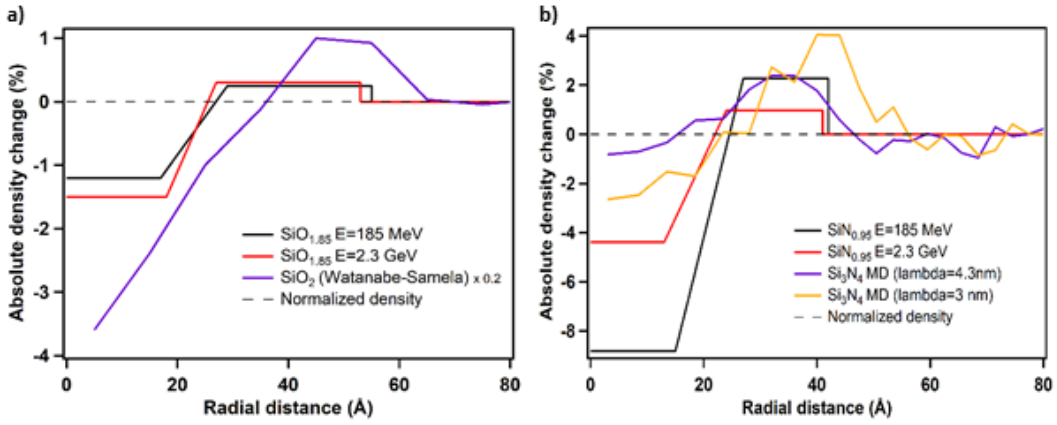

Figure 5.6: *Normalized radial density change calculated by molecular dynamics simulations after 100 ps and the corresponding normalized density profile determined from SAXS for: (a) a-Si_3N_4 (MD) and a-$SiN_{1.06}$ (SAXS), (b) a-SiO_2 (MD) and a-$SiO_{1.9}$ (SAXS).*

shock waves obtained after 100 ps, however, the material relaxation may in reality proceed for much longer periods. On the other hand, for a-Si_3N_4, the experimental and calculated density profiles are shown in Figure 5.6 (b). A good agreement of the ion track radius with the MD simulations for a value $\lambda = 4.3$ nm is observed. The latter suggests that a lower electron-phonon coupling value for a-Si_3N_4 yields a better agreement than the value adopted by Kitayama *et al.* [58] ($\lambda = 3$ nm), leading to the decrease of the energy transferred to the lattice subsystem limiting the melted volume during the ion track formation process. Similar to the argument used for a-SiO_2, the lower density change values determined for a-Si_3N_4 can be the result of a reduced relaxation process occurring in a-$SiN_{1.06}$ with respect to a-Si_3N_4.

From the 2T-MD modelling, we also extracted the change in the content of coordination defects in Si after the passage of an energetic ion for both systems. The numerical model predicts several atoms being displaced outwards, changing environment and ending up trapped in their corresponding new position, because of the density waves propagating through both materials. By analysing the Si environment at different radial distances, before and after the passage of the swift heavy-ion, we

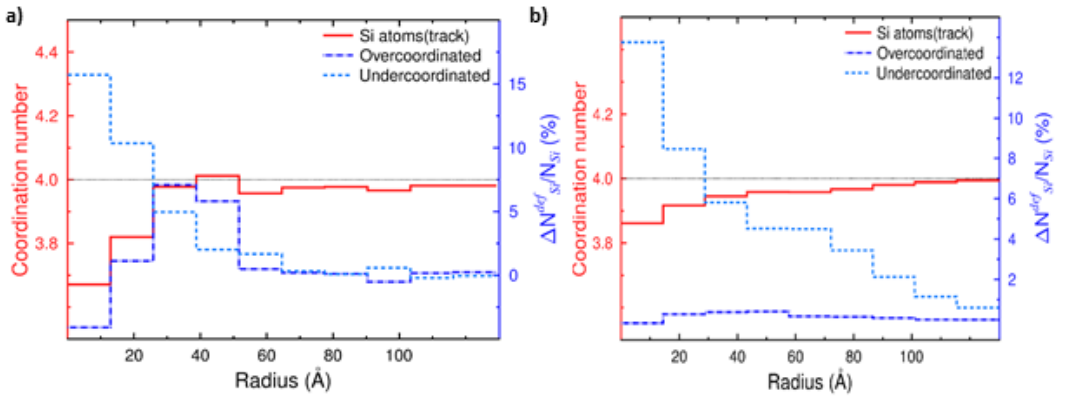

Figure 5.7: *The left axis (in red) corresponds to the coordination number of Si (solid lines) for a-Si_3N_4 (a) and a-SiO_2 (b), while the right axis (in blue) represents the relative increase of under- and over-coordination defects (dashed lines) after the passage of an 185 MeV Au ion, both as a function of the distance from the ion track centre.*

determined the production of under- and over-coordination defects after the irradiation with respect to the unirradiated structure are shown are shown in Figure 5.7 (a) and (b). The ΔN(def)/N axis denotes the relative increase of over- and under-coordination defects after the ion passage with respect to the initial condition, which is a more appropriate value than the absolute increase N(def)/N, since some coordination defects are already present in the cell, a common feature in Tersoff-like potentials [260], and were not created by the swift heavy-ion irradiation. For a-Si_3N_4, we observe a decrease in the coordination number of Si within 3 nm from the ion track axis (Figure 5.7 (a)). Additionally, the distributions of under- and over-coordinated defects are in good agreement with the under-dense and over-dense region within the ion track. In the case of a-SiO_2, the main change in the coordination number for Si is also encompassed within the first 3 nm of the ion track (Fig. 5.7 (b)), and remains under-coordinated at distances further than the total track radius. The Watanabe-Samela potential does not favour the formation of over-coordinated defects, which is the reason why the amount of these defects remains low, although in the over-dense shell region it is somewhat higher.

5.3.3 Ion energy dependence of the track structure

As mentioned in section 2.3, the initial spatial distribution of the δ-electrons produced during the passage of an energetic ion has an impact on the dimensions of the ion track formed [103]. In the case of Au ions with kinetic energy closer to or above 4 MeV/u, their resulting relativistic velocity leads to a larger radial δ-electron distribution and a lower energy density. Hence, the formation of an ion track of smaller dimensions, compared to Au ions of lower kinetic energy but comparable electronic stopping power, is expected. This is known as the velocity effect [1,99].

This effect was studied by irradiation of a-$SiO_{1.9}$ and a-$SiN_{1.06}$ thin layers with 2.3 GeV Au ions at fluences between 5 - 50 $\times$ 10^{10} cm^{-2} at the UNILAC accelerator at GSI in Darmstadt, Germany. The experimental conditions yield an energy-loss rate of 16.7 and 23.9 keV/nm, respectively, which in the case of a-$SiO_{1.9}$ is approximately 20 % above the corresponding value for irradiation carried out at 185 MeV and about 15 % for a-$SiN_{1.06}$.

The corresponding SAXS scattering patterns are similar to those shown in Figure 5.4. The corresponding integrated scattering intensities, after appropriate background removal, are compared with those irradiated at lower energies in Fig. 5.8 (a). An almost identical integrated scattering intensity is apparent for a-$SiO_{1.9}$ samples irradiated at both energies. A similar trend was observed for a-$SiN_{1.06}$ samples with a slight difference in the shape of the shoulder at higher values of the scattering vector (q$\sim$ 0.2 $Å^{-1}$). Numerical fitting the corresponding integrated scattering intensities using a cylindrical core-shell model with a smooth transition yields a similar morphology and size for both materials at low and high irradiation energies, despite the difference in energy loss.

Following the same procedure as for samples irradiated with lower ion energies, the normalized radial density change profiles were determined from the numerical fits performed. The resulting profiles are plotted in Figure 5.8 (b). For a-$SiO_{1.9}$

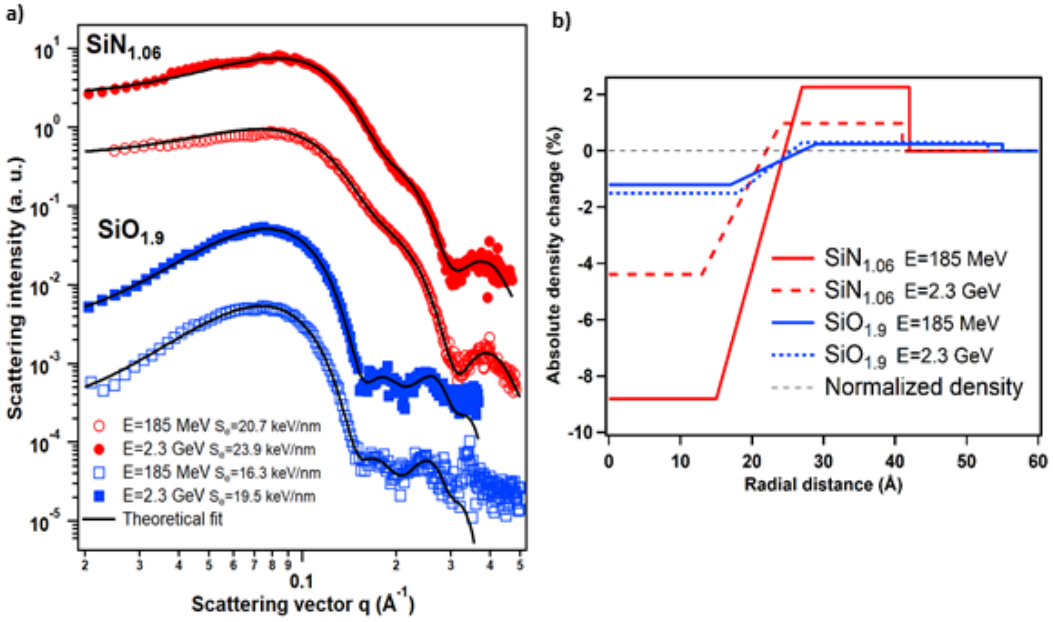

Figure 5.8: *Integrated SAXS scattering intensities and numerical fits for a-$SiN_{1.06}$ and a-$SiO_{1.9}$, after irradiation with 185 MeV and 2.3 GeV Au ions with a fluence of 1 × 10^{11} cm^{-2} (a). The corresponding normalized absolute density change profiles extracted from the numerical calculations (b).*

samples, an almost identical radial density change profile was found at both irradiation energies. For a-$SiN_{1.06}$, a stronger scattering was found for samples irradiated at low ion irradiation energies, while exhibiting a similar ion track radius. This suggests that the difference in the S_e value ($\sim$ 15% higher for irradiation with 2.2 GeV Au ions) does not lead to a larger ion track radius, presumable because the decrease in the radial energy density is approximately compensated by the increase in stopping power. The results are summarized in Table 5.3.1. Based on the i-TS model, for the same material irradiated at two different velocity regimes the difference lies in the radial distribution of the δ-electrons generated after the ion passage. In section 2.3 the corresponding distribution for a-SiO_2 and a-Si_3N_4 at both irradiation energies was presented, where it was possible to observe an almost identical energy deposition within radius around the track center of 2 nm followed by a slight increase at higher radii for lower ion velocities. This means that the variation of the absolute density change profile can be the result of a lower energy density, result of the velocity effect,

and a reduced amplitude of the density wave formed during the thermal spike lifetime.

5.3.4 Comparison of the ion track morphology with stoichiometric amorphous silicon dioxide and nearly stoichiometric silicon nitride layers

At the beginning of this chapter, the characterization of a-$SiO_{1.9}$ and a-$SiN_{1.06}$ was presented and included their Si-rich and hydrogenated composition. However, in our characterization of the two materials, we have considered the equilibrium thermodynamic parameters to be the same as those known for a-SiO_2 and a-Si_3N_4, except for the experimental determination of the density and the optical band gap. To extend the experimental results presented in this chapter it is important to compare them with near stoichiometric materials. Thus, a comparison was performed with thermally grown (stoichiometric) silicon dioxide (a-SiO_2), the most widespread material used to study the effect of SHI irradiation, and silicon nitride synthesized by low pressure chemical vapour deposition (LPCVD). The latter is known to be closer to the ideal stoichiometry with the absence of H (the N/Si ratio was determined by RBS to be 1.10 $\pm$ 0.05 while FTIR measurements demonstrate the absence of H hence, it is referred to as a-$SiN_{1.1}$).

The 2 μm thick a-SiO_2 and a-$SiN_{1.1}$ layers were irradiated with 185 MeV Au ions with the same fluence as a-$SiO_{1.9}$ and a-$SiN_{1.06}$. The corresponding scattering patterns obtained by SAXS of a-SiO_2 and a-$SiN_{1.1}$ are presented in Figure 5.9 (a) and (b), respectively. Both patterns show the anisotropic scattering characteristic produced by continuous, high aspect-ratio ion tracks [56, 96]. The extracted integrated scattering intensities of a-SiO_2 and a-$SiN_{1.1}$, and their corresponding numerical fits are presented in Figure 5.9 (c) and (d) together with those from a-$SiO_{1.9}$ and a-$SiN_{1.06}$.

By inspection of the integrated scattering intensities or amorphous silicon nitride with different stoichiometries, we can identity a very similar oscillatory pattern at lower q-values (q $\sim$ 0.15 $Å^{-1}$) for both compositions with a subtle but clear shift

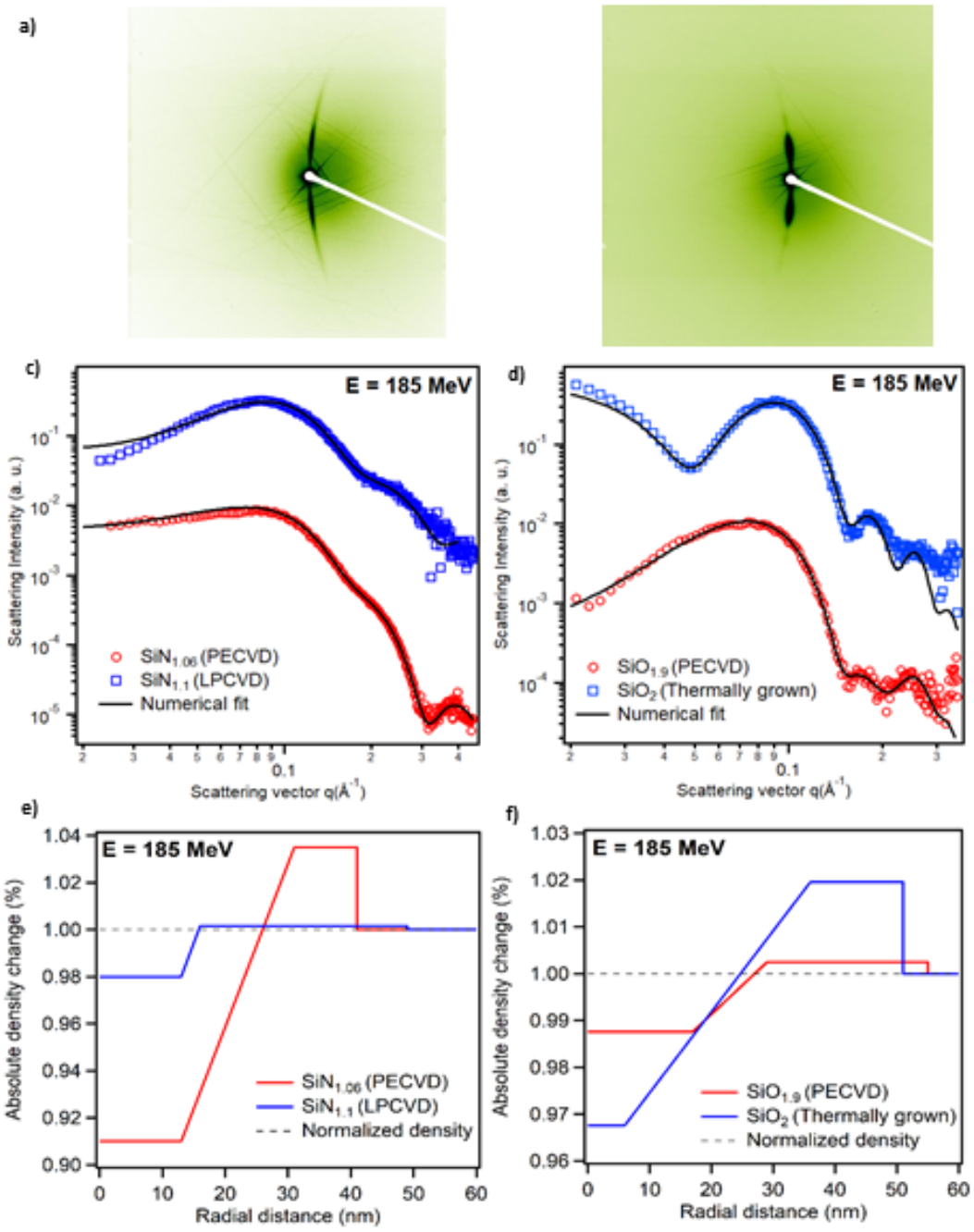

Figure 5.9: *Scattering patterns of ion tracks formed in a-$SiN_{1.1}$ (a) and a-SiO_2 (b). Integrated SAXS scattering intensities and numerical fits for amorphous silicon nitride (c) and amorphous silicon dioxide (d) of different stoichiometries. Comparison of the normalized absolute density change profiles extracted from the numerical calculations (e) and (f), respectively.*

toward lower values of the local maxima for a-$SiN_{1.1}$, indicative of a larger ion track radius. At higher q-values we observe the formation of a shoulder exhibiting different slopes between the two samples, an indication of the slope and thickness of the transition region. Direct comparison of the normalized integrated scattering intensities show a larger intensity at $\lim_{q\to\ 0} I(q)$ for a-$SiN_{1.06}$ (not shown). As shown in section 4.4, the intensity at $\lim_{q\to\ 0} I(q)$ is dependent on the volume of the scattering object (the cylindrical ion track), fluence and the density change of the object thus, the larger intensity observed for a-$SiN_{1.06}$ is indicative of a larger density change than for a-$SiN_{1.1}$. Figure 5.9 (e) presents a comparison of the absolute density change for the two stoichiometries considered, where we can observe a reduction in the magnitude of the density change of nearly four times when the N/Si ratio increases from 1.06 to 1.1. Also, we observe an increase in the total on track radius from 4.1 ± 0.1 to 4.9 ± 0.3, and a decrease in width of the transition region. The increase in the total ion track radius and the reduction of the density change for a-$SiN_{1.1}$ can be understood in terms of the i-TS model. The electronic energy-loss rate calculated for a-$SiN_{1.1}$ of S_e = 23.8 keV/nm is 15 % higher than the value for a-$SiN_{1.06}$ (S_e = 20.7 keV/nm), because of the difference in density. The higher S_e value leads to an increase in the molten volume and a larger ion track radius, while the difference in stoichiometry and lack of H for a-$SiN_{1.1}$ might result in a different thermal conductivity which affects the duration of the thermal spike. Such difference can allow the compensation of the density wave formed during the inhomogeneous increase in temperature linked to the ion track formation process.

In the case of a-SiO_2, the corresponding extracted scattering intensity shows a different pattern exhibiting the presence of a local minimum (q ∼ 0.05 $Å^{-1}$) that is not present in a-$SiO_{1.9}$. A good agreement was still observed when fitted by a core-shell model with a smooth transition (Fig. 5.9 (d)). The numerical fit of a-SiO_2 suggests that the observed behaviour is related to the reduced dimensions of the core radius (R_c = 0.6 ± 0.1 nm) while the total ion track radius of R = 5.3 ± 0.1 nm is similar for both stoichiometries. The results of the combined analysis of the extracted scattering intensity and numerical fits are shown in Figure 5.9 (f). The difference in

amplitude of the density change and the comparable total ion track radius suggests that the equilibrium thermo-physical parameters of the two materials are similar while they exhibit different flow properties due to differences in local order.

5.3.5 Fourier transformation infrared spectroscopy

Figures 5.10 (a) and (b) show FTIR spectra for a-$SiN_{1.06}$ and a-$SiO_{1.9}$ and their respective deconvolution into Gaussian contributions of their main absorbance peaks before irradiation in the 400 and 4000 cm^{-1} range. The deconvoluted absorption bands can be ascribed to the respective vibrational modes of Si-N and Si-O and those related to the presence of H. For a-$SiN_{1.06}$, the main infrared absorption peak is centred at 874 cm^{-1} and exhibits a shoulder around 1200 cm^{-1}, which can be deconvoluted into four contributions (Fig. 5.3 (a)): (i) the Si-N local distorted stretching at around 816 cm^{-1}, (ii) the main contribution located at 890 cm^{-1}, which is attributed to the *Restsrahlen* effect or TO mode, due to the forbidden photon propagation in the IR leading to a high reflectivity [17, 254], but also to the Si-N asymmetric stretching mode in the N-Si_3 configuration, (iii) the 1005 cm^{-1} band, originating from the asymmetric stretching mode in the N-Si_3 configuration [16], and (iv) near 1200 cm^{-1}, the contribution of the N-H wag-rocking mode [261–263]. At 2180 cm^{-1} different Si-H vibrational modes are present [251], while around 3340 cm^{-1} the absorption peaks from N-H_2 asymmetric stretching modes are observed due to the H content of around 10 at % [252, 261–263]. These were already described earlier in this chapter.

The infrared spectrum of a-$SiO_{1.9}$ shows two absorption peaks in the region between 750 and 1400 cm^{-1}. The first, centred at 815 cm^{-1}, corresponds to the Si-O-Si bending mode [255, 258, 264]. In the region between 900 - 1400 cm^{-1} the main absorbance signal centred at 1050 cm^{-1} encompasses the Si-O-Si stretching and the Si-O symmetrical modes, while exhibiting a shoulder at 1200 cm^{-1} due to the Si-O out-of-phase stretching modes associated to the Si(O_4) configuration (Fig. 5.3 (d)). Very weak absorption peaks are located around 2300 cm^{-1} and 3500 cm^{-1} corresponding to Si-H and SiO-H. The stronger bands in this region were recorded

around 3400 cm^{-1} which have been commonly related to N-H, thus their origin is still unclear due to the absence of N during the layer deposition. The overall absorbtion intensities confirm a very low concentration of H, below 3 % (Fig. 5.3 (d)).

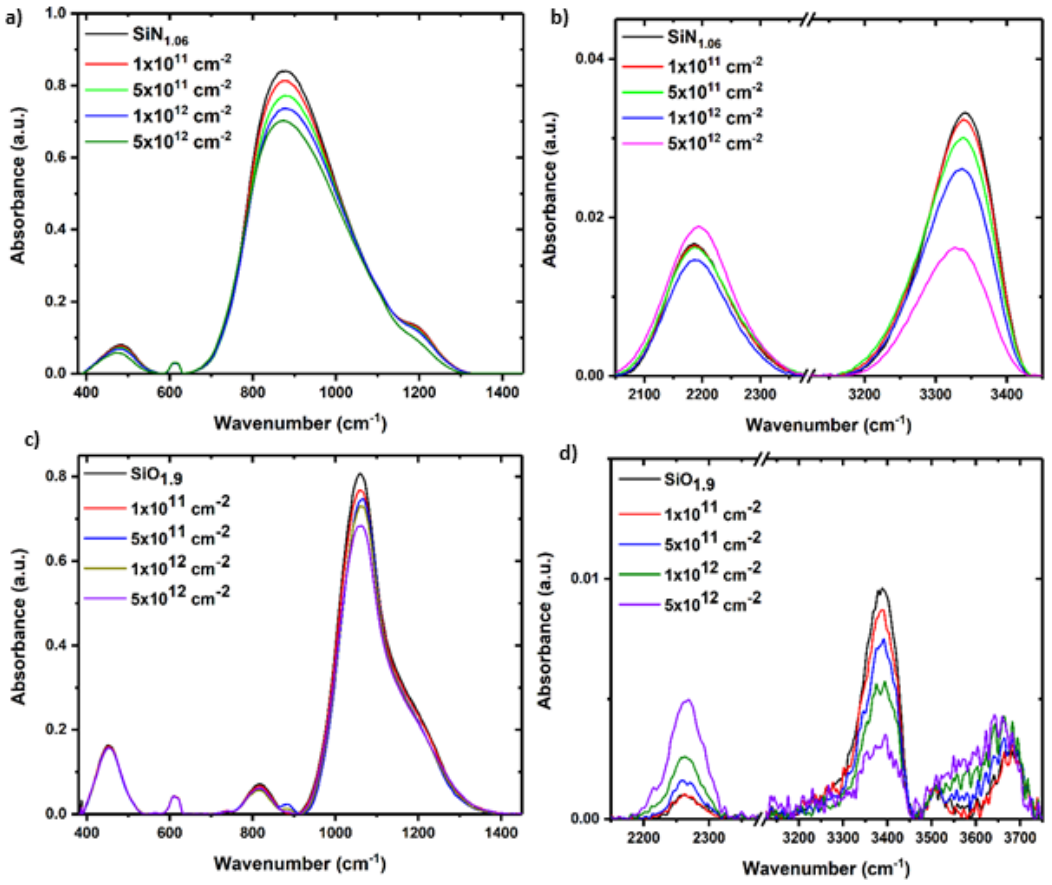

Figure 5.10: *FTIR absorbance spectra of a-$SiN_{1.06}$ ((a) and (b)) and a-$SiO_{1.9}$ ((c) and (d)) prior to and after irradiation with 185 MeV Au ions at different fluences.*

After irradiation, we observe a decrease in the absorbance for all our samples, which is correlated to the radiation damage due to SHI irradiation (Figures 5.10 (a) to (d)) [53, 54, 86, 89, 111]. In contrast to previous studies [27, 53, 89], no significant shift towards higher wavenumbers is observed below a fluence of 5×10^{12} cm^{-2}, where overlapping effects become relevant. A non-uniform decrease of the main absorbance band is observed as a function of the irradiation fluence in both materials. The

combined behaviour corresponding to Si-H and N-H bands shows no obvious trend (Figs 5.10 (c) and (d)). Furthermore, the band located at 620 cm^{-1} has been ascribed to the Si-H wagging mode for both materials [251, 263], yet, no change in intensity is observed with increasing irradiation fluence contrary to the behaviour of the Si-H bands present around the 2200 cm^{-1}. Hence, the nature of this band agrees with being the phonon absorption in the substrate instead of the Si-H wagging mode, as suggested by [251]. Furthermore, at 2280 and 2250 cm^{-1} the Si-H bending modes of a-$SiN_{1.06}$ and a-$SiO_{1.9}$ show no decrease in absorbance with increasing fluence; instead, a clear increase occurs up to 5 $\times$ 10^{12} cm^{-2}. This is probably a result of the complex behaviour of H and its corresponding interaction with the Si dangling bonds and a product of the Si-N and Si-O, N-H and O-H bond-breaking in the irradiation process [251, 264].

As the densities of Si-N or Si-O bonds are related to the stretching modes [2, 263, 263], the change in the corresponding integrated absorbance signal has been considered a direct result of radiation damage being created by the ion track formation process [27, 53, 89, 111]. For Si-N, the TO mode is proportional to the Si-N bond density [261]. While at higher fluences, such as 5 $\times$ 10^{12} cm^{-2}, swelling is expected to occur, the change in thickness is within 2 % and within our experimental error hence, compaction or swelling effects are not considered in this analysis.

To quantify the radiation-induced damage as a function of fluence, the changes in the 400 - 3800 cm^{-1} range were determined and modelled by a Poisson distribution considering the relative change in (i) the bond density and (ii) the absorbance [54, 86], as follows:

$$[a-b](R,F) = [a-b] + (1-[a-b]) \cdot exp(-\pi R^2 F), \tag{5.8}$$

$$A_{(a-b)}(R,F) = A_{(a-b)} + (1-A_{(a-b)}) \cdot exp(-\pi R^2 F), \tag{5.9}$$

where $[a-b]$ is the term that represents the bond density and $A_{(a-b)}$ the total integrated absorbance area of the vibrational mode $a-b$ under consideration (Si-N, Si-O, Si-H, N-H and O-H, respectively) after normalization with respect to the unirradiated values. The terms $[a-b](R,F)$ and $A_{(a-b)}(R,F)$ correspond to the change in bond density or absorbance, respectively, of the radiation-induced damage considering a circular damage cross-section with radius R at a given irradiation fluence F (see section 3.5.1). It is worth to mention that in this approach, the radiation-induced damage is considered to be evenly distributed within the modified region. As it has been shown by SAXS, ion tracks in a-$SiN_{1.06}$ and a-$SiO_{1.9}$ exhibit an under-/over-dense core/shell morphology. In the following analysis it is attempted to correlate the data obtained from SAXS with that from FTIR.

At 480 and 455 cm^{-1}, the absorbance bands have been related to the breathing modes for N-Si_3 [251] and O-Si_3 [254], respectively. For a-$SiN_{1.06}$, this band shows a small decrease in intensity only at the highest fluence, while remaining unchanged for a-$SiO_{1.9}$. These bands have never been taken into account when FTIR has been used to determine the effective ion track dimensions for a-Si_3N_4 [54] and a-SiO_2 [27, 53], however, in the present case it is proposed that the change observed with ion fluence is the result of the same ion-induced bond-breaking mechanism commonly applied to the analysis of the main absorbance band. Hence, for a-$SiN_{1.06}$, we considered the bands centred at 480, 816, 880, and cm^{-1} to quantify the corresponding radius of the damage cross-section, leading to a value of 8.5 $\pm$ 1.2 nm. Figures 5.11 (a) and (c) show the fitted curves using equation 5.9 for a-$SiN_{1.06}$ and a-$SiO_{1.9}$, respectively. As shown in Figure 5.11, the variation of the N-H, Si-H and the combination of both was also studied, where we observe a steep decrease of the N-H bond density with fluence, leading to a damage cross-section radius of 5.7 $\pm$ 0.8 nm. For Si-H a slight decrease at lower fluences was observed followed by an abrupt increase at higher values, probably result of the preferential H bonding released by the breaking of N-H bonds with existing Si dangling bonds. The amount of H bonded to the material network can be studied by combining the Si-H and N-H bands [17]. Following a decrease of 20 %, after irradiation with $5\times\ 10^{11}$ cm^{-2} the H content seems to remain constant at higher

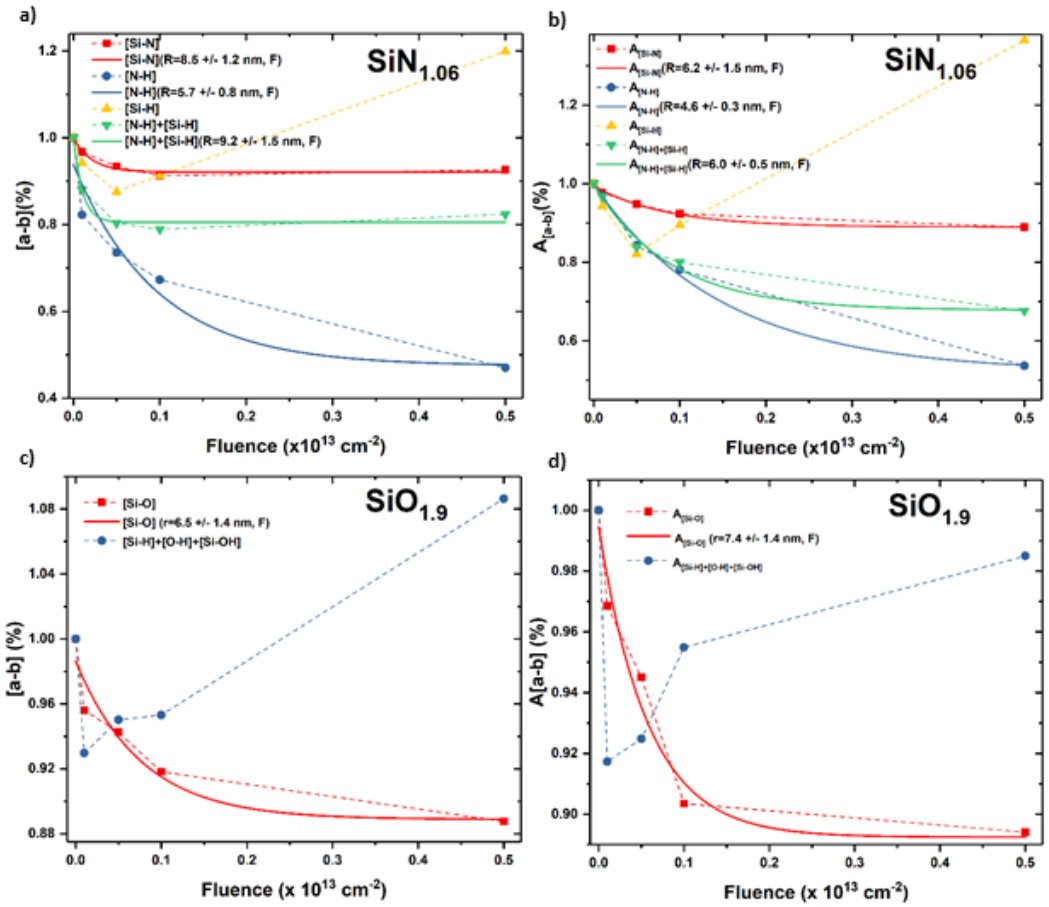

Figure 5.11: *Evolution of the bond density of Si-N, N-H, Si-H and H content as a function of fluence for a-$SiN_{1.06}$ (a), and of Si-O and H content of a-$SiO_{1.9}$ (c). Evolution of the aborbance area associated with the Si-N, N-H, Si-H contribution to the IR absorbance spectra as a function of fluence for a-$SiN_{1.06}$ (b) and a-$SiO_{1.9}$ (d). Dashed lines were added to show the trend exhibited while continuous lines represent the numerical fit to the evolution with fluence following equations 5.9 ((a) and (c)), and 5.9 ((b) and (d)).*

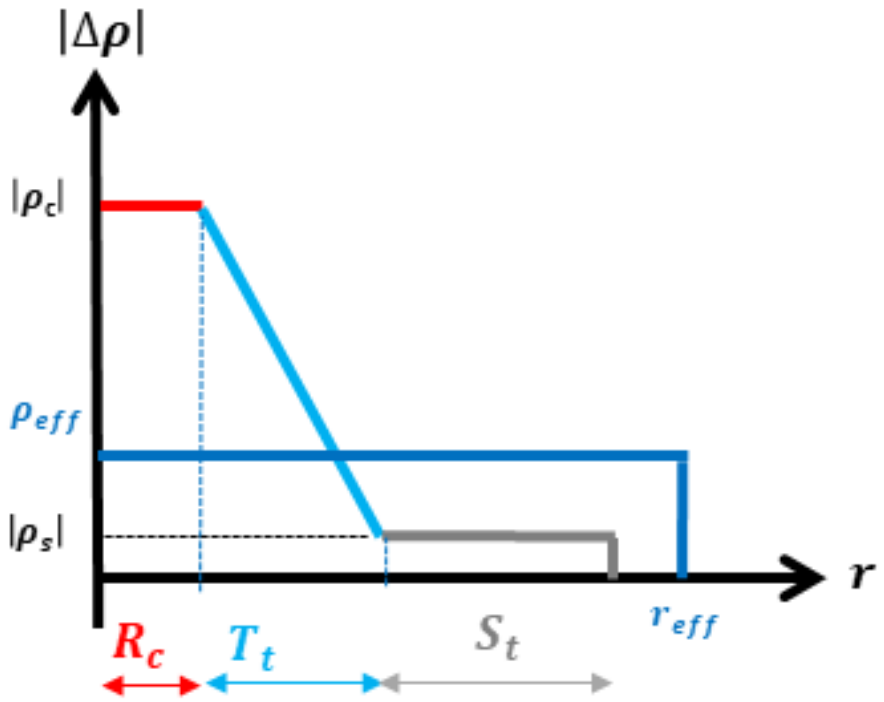

Figure 5.12: *Overlay of the absolute density change of the determined profile by SAXS and the corresponding modified area considered by the single Poisson statistical model.*

fluences, leading to a cross-section radius of 9.2 ± 1.5 nm.

In the case of a-$SiO_{1.9}$, a similar analysis of the Si-O bond density was carried out while considering the contributions from the 455, 730, 815, 1055, and 1160 cm^{-1} bands. This leads to a damage radius of 6.5 ± 1.4 nm. Due to the difficulty to relate the absorbance bands located between 3200 and 3400 cm^{-1}, related to H it was not possible to analyse the H evolution with fluence. In Fig. 5.11 (c) the evolution of the bond densities of Si-H, O-H and Si-OH with fluence is plotted, where from inspection of Fig. 5.10 (d) their increase with fluence is evident in a similar fashion to the Si-H bond in a-$SiN_{1.06}$. Figures 5.11 (b) and (d) show the analysis carried out in the same fashion but in terms of equation 5.9. While similar trends were observed for the two frameworks, it is important to clarify that the absorbance area is not a direct measure of the bond density as it is weighted by frequency (see section 3.5.1). Thus, an increase

in the band area accompanied by the broadening of the peak can lead to the same or even to a lower bond density. For a-$SiN_{1.06}$, the damage cross-section for Si-N, N-H and H was determined to be 6.2 ± 1.5, 4.6 ± 0.3 and 6.0 ± 0.5 nm, respectively. On the other hand, the corresponding radius calculated for Si-O turned out to be 7.4 ± 1.4 nm.

While the effective radial dimensions of the modified region exceed that determined from SAXS, it is necessary to consider the fine structure of the ion tracks in a-$SiN_{1.06}$ and a-$SiO_{1.9}$. In Figure 5.9, the density change radial profile of an ion track determined for a-$SiN_{1.06}$ or a-$SiO_{1.9}$ were presented. The results contrasts with the adopted interpretation of the FTIR spectrum of amorphous insulating materials where a single Poisson statistical model is used which considers that the radiation damage is homogeneously distributed inside the ion track. Thus, due to the demonstrated fine structure present in the ion tracks formed in a-$SiN_{1.06}$ and a-$SiO_{1.9}$ a pathways is proposed aiming to correlate the information obtained from FTIR with the presented SAXS data in terms of the absolute density change profile (Figure 5.12). The effective cross-sectional ion-induced radiation damaged A_{eff} can be expressed as:

$$A_{eff} = \pi R_{eff}^2 = A_{core} + A_{trans} + A_{shell}, \tag{5.10}$$

where $A_{core} = C_c \pi R_c^2$ corresponds to the contribution of the core region to the effective area, C_c is the proportionality coefficient of the core region and corresponds to $C_c = \left| \frac{\rho_c - \rho}{\rho} \right|$. In a similar fashion, $A_{trans} = C_t \pi (R_t^2 - R_c^2)$ represents the contribution from the transition region with $C_t = \bar{\rho}$ defined as an intermediate value of the density change ratio or the mean value of the absolute density change between the core and shell region. Finally, $A_{shell} = C_s \pi (R^2 - R_t^2)$ where $C_s = \left| \frac{\rho_s - \rho}{\rho} \right|$. The radial dimensions and density change ratios and values are taken from Table 5.3.1.

For a-$SiN_{1.06}$, an effective area with a corresponding R_{eff} = 8.1 ± 0.5 nm is determined, while for a-$SiO_{1.9}$ R_{eff} is equal to 4.3 $/pm$ 1.0 nm. The estimation of the effective radii show good agreement with the ion track morphology deduced from SAXS,

supporting the idea of a high damage concentration in the inner region of the ion track such as that presented in the MD simulation results where the coordination defects are concentrated in the inner region of the ion track.

5.4 Mechanisms of ion track formation in amorphous silicon nitride and silicon dioxide

The complex interaction of an energetic ion with a solid target involves different electronic and atomic processes and occurs on different timescales. The duration of the ion passage is 10^{-18} - 10^{-17} s, followed by an electron cascade known as δ-electrons moving radially outwards between 10^{-15} - 10^{-13} s. The excited electrons interact with the target atoms transferring energy from the electronic to the atomic subsystem via electron-phonon coupling causing local heating often referred to as a thermal spike, which commonly occurs in insulators between 10^{-13} and 10^{-11} s, leading to local melting and finally to the plastic flow of the molten region in the last stage. A key part of the ion track formation process is the thermal spike that results in local melting of the material. The corresponding i-TS model has been widely used to estimate the dimensions of the modified region. Figure 5.13 (a) shows two fundamental differences in the calculated time-evolution of the thermal spike based on the i-TS model between a-$SiN_{1.06}$ and a-$SiO_{1.9}$: (i) the difference in the optical band gap is mainly responsible for the variation in the ion track dimensions between the two materials as it leads to an electron-phonon coupling value in a-$SiN_{1.06}$ of less than half the value of a-$SiO_{1.9}$, and (ii) the higher thermal conductivity of a-$SiN_{1.06}$ (nearly one order of magnitude higher than a-SiO_2) reduces the duration of the occurrence of the molten phase in a-$SiN_{1.06}$ by one order of magnitude compared to a-$SiO_{1.9}$.

The density variation profiles determined by SAXS support the time evolution numerically calculated an the impact of the bulk material properties in the target response. Previous studies, based on MD simulations, on the density evolution within the ion track core region in insulators have shown that in the case of a-SiO_2, an abrupt decrease in density occurs around 4 ps followed by a recovery of the density

change for up to 150 ps without a full recovery of the initial density [104]. Hence, when the duration of the thermal spike is reduced, it leads to a more efficient energy dissipation and faster freeze-in of the density wave induced by the incident ion. As a consequence, the time for recovery is much chorter in a-$SiN_{1.06}$, freezing in a higher density deficit in the core region (close to 10 %) compared to a-SiO_2, where a density change of 2 % is observed, in agreement with previous [104] and the present MD simulations. A similar ion track morphology with high density fluctuations in the core region has been observed in very thin layers of low-pressure CVD deposited silicon nitride (thicknesses between 5 - 100 nm) where the variation in density within the ion track region was estimated by HAADF-STEM [59]. While the results are in good agreement with our measurements, it is important to highlight that the track length in our experiments is far greater than that ($\sim$ 1 μm) and the measurement technique is non-invasive such that we can rule out surface effects and artefacts due to sample preparation and measurements. Our results clearly demonstrate: (i) the track radius in a-$SiN_{1.06}$ is smaller than in a-$SiO_{1.9}$ possibly resulting from the difference in the optical band gap; (ii) the density change is comparably larger in a-$SiN_{1.06}$ compared to a-$SiO_{1.9}$ due to a larger thermal conductivity, which leads to shorter relaxation times, i.e. time for the density change to recover (Figure 5.13 (b)); (iii) the ion tracks are continuous with a morphology exhibiting a core-shell density change distribution with a smooth boundary between the under-dense and the over-dense region that can be estimated by a linear function satisfactorily rather than an abrupt transition [56].

The 2T-MD density calculations of the radial density distribution also exhibit a morphology of an under-dense core surrounded by an over-dense shell with a smooth transition region in between. The over-densification arises from the movement of toms radially outwards from the centre of the ion track, increasing the number of coordination defects in the inner region of the ion track. Thus, the under-dense core/over-dense shell track in a-SiO_2 is not a result of the density anomaly above 1800 K as was previously noted as an open question [56, 57, 104].

For a-Si_3N_4 the track morphology has previously been ascribed to the high

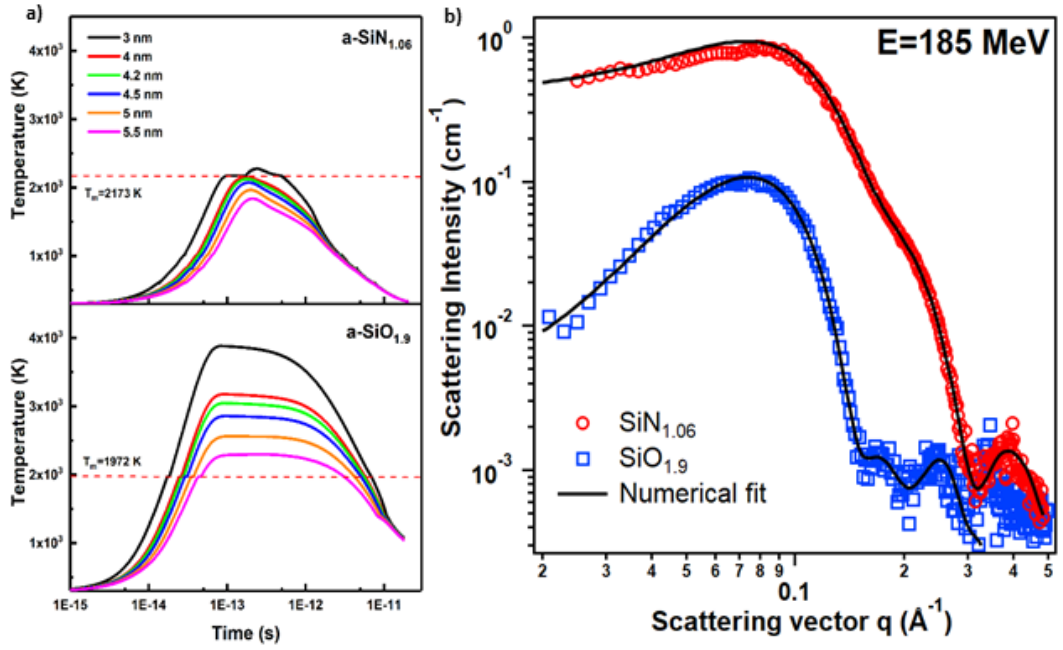

Figure 5.13: *Comparison of the lattice temperature time-evolution between a-Si_3N_4 and a-SiO_2 calculated using the i-TS model (a). Direct comparison of the normalized integrated SAXS scattering intensities for a-$SiN_{1.06}$ and a-$SiO_{1.9}$ after irradiation with 185 MeV Au ions to a fluence of 1 × 10^{11} cm^{-2} (b).*

temperature reached in the inner region, surpassing the vaporization point, however no experimental support was provided for this argument [58]. It is in fact questionable if the equilibrium vaporization point is relevant in a spatially enclosed area such as the track centre. In contrast, the 2T-MD simulations suggested that the results above can be explained by the plastic viscous flow without the necessity of consider the reach and surpass of the boiling point, as proposed by Kitayama *et al.* [58]. They adopted the formalism originally proposed for the formation of ion tracks with a core-shell morphology in CaF_2 [59], where the core dimensions correspond to the volume that reaches boiling. Instead, in the present results the idea proposed by Borodin *et al.* [245] is adopted regarding the formation of a damped density wave, combined with the role played by the spatiotemporal evolution of the temperature profile. Thus, the temperature profile as described by the 2T-MD simulations, leads to a non-uniform thermal expansion in the molten track restricted by a cold boundary imposed by the matrix. The generated internal stresses lead to redistribution of matter due to defect diffusion. Although different to amorphous metals, where above a critical temperature T_c a glass transition takes place exhibiting a viscosity drop [245], a-SiO_2 undergoes a transition towards a critical flow state and a drastic decrease in viscosity [265] while a-Si_3N_4 experiences a transition from ceramics towards a ductile state [266, 267]. Borodin suggested that the density variation, described as a damped density wave, is dependent on the relation between the cooling down period and the oscillation period [245]. In our case, viscosity cannot be disregarded hence, the damping constant can exceed the oscillation frequency quenching in a steady-state that partially compensates the thermal strain gradients. Thus, the ion track does not fully return to the original state, leaving a trace of redistributed matter, similar to the observations from MD simulations [104].

The information extracted from our 2T-MD results showing the change in coordination number for Si (Fig.5.7) demonstrate that the increment in coordination defects inside the ion track region is smoothly decreasing with increasing radial distance from the track centre for both materials. This suggests that the radius of the damage cross-section obtained by our FTIR analysis can be understood as an effective cross-section

area where most of the coordination defects are located. Because typically the analysis by FTIR of irradiated samples considers a single Poisson statistical model, it considers that the defects produced inside the ion track are homogeneously distributed. From the 2T-MD plot of the change in the coordination number of Si, it is clear that the core concentrates the majority of the radiation-induced damaged, and thus, it should have a different impact on the measured FTIR spectra than the shell region of the track. Thus, a relation between the dimension of the damage region defined by FTIR and the total ion track radius as determined by SAXS can be constructed. This is done by considering the density change ratio ρ as a proportionality term between the core and shell region which results in a larger modified area, different to what is often observed for the case of amorphisable insulators [59]. This is not surprising as in the latter a phase change of the material from crystalline to amorphous often defines the track region.

The accurate determination of the morphology of ion tracks in amorphous materials is of crucial relevance in order to understand the corresponding effects on the modification of the material properties. Previous results based on indirect techniques such as electrical conductivity or infrared spectroscopy have been applied to estimate the ion track dimensions in a-Si_3N_4 and a-SiO_2, where concepts developed for crystalline materials were applied. In a-SiO_2, the evolution of the absorbance band located around 1080 cm^{-1} has been used to study the radiation damage in the local structure induced by SHI [53, 86, 89, 111]. The decrease of the absorbance peak area was considered as a direct indication of bond-breaking after the ion passage and therefore, a direct measurement of the ion track dimensions. However, a study of the Si-O bond density evolution as a function of fluence has shown that the modification of the FTIR spectrum cannot uniquely be attributed to bond breaking but also to structural deformation and irradiation-induced strain, responsible for the observed red shift and increase in peak width [86]. The red shift of the absorbance band position is indicative of the variation of the Si-O-Si angle, suggesting a decrease in the bond angle as a consequence of the irradiation-induced strain. It is noteworthy that the observed changes in bond-angles are mostly reported for fluences above 5×10^{12}

cm^{-2}, where multiple track impacts and material compaction becomes relevant [257] and it becomes difficult to correlate the overall irradiation-induced strain to the single ion track morphology.

For a-Si_3N_4, only few experiments have been carried out and mainly in very thin layers where the ion track dimensions are estimated solely by the decrease of the absorbance peak and the appearance of a shoulder around 900 and 1200 cm^{-1} [54]. The decrease of the absorbance signal was fitted with a single Poisson statistical model to determine the ion-induced damage cross-section for fluences below 5×10^{12} cm^{-2} while at higher fluences a second damage cross-section was added to account for nuclear interactions, without considering any further aspects in the evolution of the FTIR spectra. No observation regarding a red shift of the asymmetric Si-N stretching modes were reported. Our experiments presented in Figs. 5.10 (a) and (c), show no apparent shift in the FTIR spectra below 5×10^{12} cm^{-2}, as consequence of the small extent of the radiation damage. This suggests that the coordination defects, following the radial distribution calculated by the 2T-MD simulations, do not lead to an observable effect at low fluences as they are below the detection limit. They only become important as a collective effect at high fluences where sufficient radiation-induced damage is present.

5.5 Swift heavy-ion irradiation of silicon oxynitride thin layers

In the previous section a study of the mechanism for ion track formation in a-$SiN_{1.06}$ and a-$SiO_{1.9}$ was presented. The track structure was studied in view of the difference in the equilibrium thermodynamic parameters between the two materials and their role in the final density change profile. MD and i-TS calculations used to study these binary materials showed good agreement with the experimental observations presented. So far, very little is known about the structural modification of the ternary a-SiO_xN_y materials under SHI irradiation. The following section presents a first

approach based on the methodology used for their binary counterparts.

5.5.1 Small angle X-ray scattering

Thin a-SiO_xN_y layers were irradiated with 185 MeV Au ions with fluences between 1 - 50 $\times$ 10^{11} cm^{-2}. At this energy, the electronic energy-loss rate varies from $\sim$ 21 keV/nm, in the case of a-$SiN_{1.06}$, down to $S_e \sim$ 16 keV/nm for a-$SiO_{1.9}$, as calculated using the SRIM2008 code. Because of the thickness of the layers (around 1 μm), the energy-loss rate can be considered constant over the depth of the layer.

In Figure 5.14, the integrated SAXS scattering intensities after removal of the corresponding background are shown for the different compositions (described in terms of the gas ratio R, Fig. 5.1) after irradiation with 5 $\times$ 10^{11} cm^{-2}. The patterns can be numerically well fitted using a core-shell cylinder model with a smooth transition (black lines), *i.e.* the same model used for the binary compositions. From the figure, a clear similarity of the scattering patterns to the a-$SiN_{1.06}$ pattern is apparent when $R \leq 0.7$, with a smooth shift of the main scattering oscillation towards lower q-values and a separation of the shoulder towards higher q-values when R increases. Above this value, the scattering patterns are more similar to that of a-$SiO_{1.9}$ with a slight variation in the oscillation slope at low q-values.

The extracted total ion track radii from the numerical fits are plotted in Figure 5.15 (a) as a function of the R ratio. As mentioned before, a-SiO_xN_y layers with compositions similar to a-$SiN_{1.06}$ exhibit a secondary weak oscillation at higher q-values, relevant to determine the dimension of the transition region between the under-dense core and the over-dense shell. For this reason, the SAXS patterns correspond to a fluence of 5 $\times$ 10^{11} cm^{-2} were analysed, at which overlap effects weakly influence the scattering patterns but exhibit a higher scattering intensity where the oscillation present at higher q-values are well-defined. Below $R < 0.7$, a gradual increase of the ion track radius from 4.1 $\pm$ 0.1 up to 4.6 $\pm$ 0.1 nm is observed. For $0.7 < R < 1$, the ion track radius exhibits a more abrupt increase to a steady value of 5.7 $\pm$ 0.1

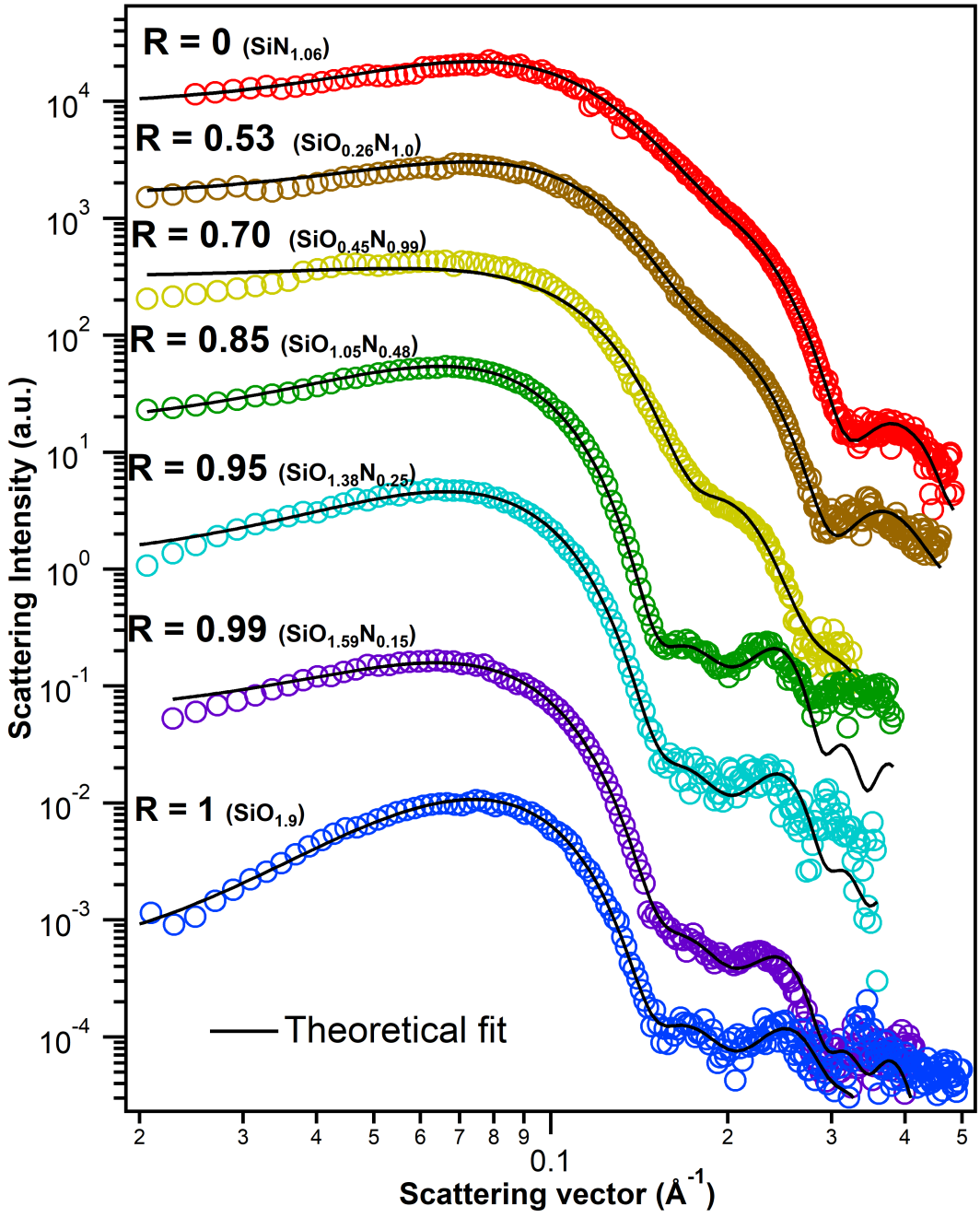

Figure 5.14: *Integrated SAXS scattering intensities for a-SiO_xN_y samples of different stoichiometries after irradiation with 185 MeV Au ions at a fluence of 5×10^{11} cm^{-2}. The black lines correspond to the numerical fit considering a core-shell with a smooth transition.*

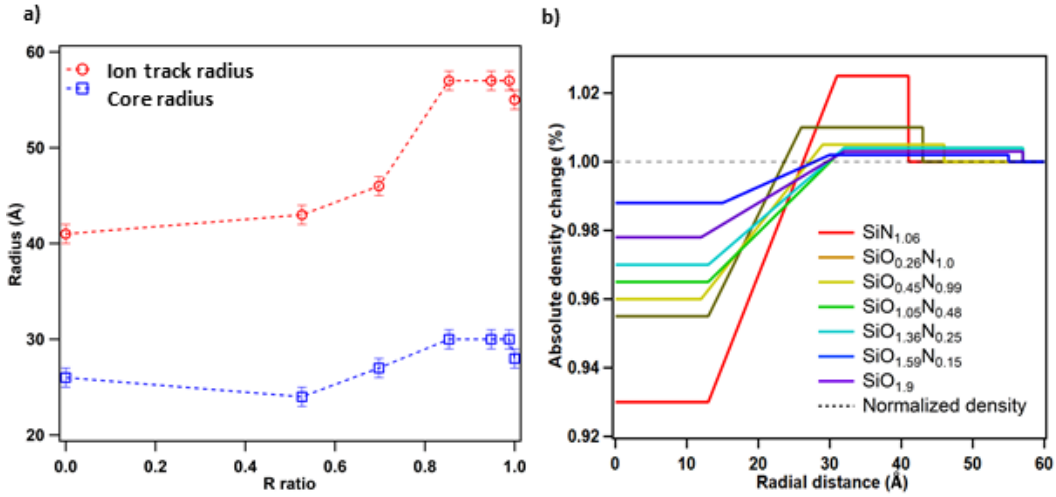

Figure 5.15: *Total ion track radius (red) and core radius R_c (blue) as a function of the R ratio (a). Dashed lines are added for clarity. Comparison of the absolute density change profiles for a-SiO_xN_y layers with different compositions (b).*

nm. The dimensions of the under-dense core region are also plotted in Fig. 5.15 (a), where a similar trend is followed as that of the total ion track radius. Fig. 5.15 (b) shows the radial density profiles of the a-SiO_xN_y layers for all compositions extracted from the numerical fits. The radial density change decreases gradually with increasing O content. As soon as O is incorporated in the layer, the absolute density change is reduced by about one third of the value for a-$SiN_{1.06}$. Afterwards, the density change appears to decrease at an almost constant rate with further O addition, until N is no longer present. From the SAXS scattering intensities, two characteristic patterns were observed: one resembling that of a-$SiN_{1.06}$ (for $R < 0.7$), and the other resembling a-$SiO_{1.9}$ at higher R values. This might be related to the reduction of coordination defects with higher O content that enhances the relaxation process of the lattice and thus, the reduction of the density change.

To improve the understanding of the ion track formation process in ternary materials, such as a-SiO_xN_y it is necessary to combine SAXS measurements with other techniques for a better description of the SHI irradiation effects on the local atomic arrangement. From the presented results it is clear that the materials response

is strongly linked to the O and N content, and seems to be determined by the element of highest content.

5.5.2 Fourier transform infrared spectroscopy of amorphous silicon oxynitride layers

In the case of the binary materials, it was shown how the characteristic FTIR absorbance spectra smoothly decreases after irradiation with increasing fluences. The decrease in absorbance can be used to estimate the damage cross-section left by the ion track. In the following subsection two a-SiO_xN_y layers of a specific stoichiometry were selected to exemplify the different response of ternary materials to SHI irradiation. The FTIR spectra of a-$SiO_{0.45}N_{0.99}$ ($R = 0.7$) and a-$SiO_{1.05}N_{0.48}$ ($R = 0.85$) at low and high frequencies are plotted in Figure 5.16 ((a) and (b), and (c) and (d), respectively). The presented materials have the particularity of exhibiting N/Si or O/Si ratios of nearly one, respectively, while exhibiting sufficient content of O/N so the response is not dominated by the element of highest concentration. Different to Fig. 5.10, where a single dominant absorbance peak is observed, for the selected materials the initial single main absorbance band splits into two contributions with increasing fluence. The FTIR spectra of a-$SiN_{1.06}$ and a-$SiO_{1.9}$ were plotted as dashed lines for clarity, as the signal splitting appears to occur towards the frequency of the main signal of the binary materials.

In the case of $R = 0.7$ the band located at 480 cm^{-1}, which is commonly associated with the Si-N symmetric stretching in the N-Si_3 configuration, shows a slight decrease in intensity with increasing fluence with an almost undistinguishable shift towards lower frequencies for fluences higher than 1×10^{12} cm^{-2}. Similar to a-$SiN_{1.06}$ and a-$SiO_{1.9}$, no change in the position nor in the absorbance intensity for the two peaks located at 610 and 621 cm^{-1} was observed for any of the compositions, suggesting these peaks result from phonon absorption in the substrate rather than from the Si-H wag-rocking vibrational mode. By considering the main absorbance band as composed by Gaussian contributions of different bond configurations, it was possible

to distinguish six contributions: four strong peaks centred at 835, 930, 1075 and 1025 cm^{-1}, and two weak signals at 742 and 1110 cm^{-1} (not shown). Some authors have assigned the four main peaks to the Si-N asymmetric stretch in a N-Si_3 configuration, the Si-N stretch in a H-SiN_3 configuration, the Si-O asymmetric stretch of the Si-O_3 configuration, respectively [17]. On the other hand, the weak absorbance bands are difficult to assign where it is not clear if their nature is linked to the low content of O [254] and N [253]. The difficulty to assign the weak contributions arises from the assignment of the IR contributions, which in the literature is commonly carried out following the RM model, where the nature of the deconvoluted peaks are assigned by comparison with the peak positions of those known for a-Si_3N_4 and a-SiO_2 [16, 17]. This approach agrees well only when the a-SiO_xN_y stoichiometry is similar to a-$SiN_{1.06}$ and a-$SiO_{1.9}$. When the stoichiometry exhibits a comparable O and N content (as in the case of the plotted samples), the positions of the deconvoluted contributions do not match the expected positions described by the RM model. This observation supports the previous notion that the RB model describes the local order of the a-SiO_xN_y layers better, and their local structure consists of a combination of SiN_4, $SiON_3$, SiO_2N_2, SiO_3N and SiO_4 tetrahedra instead, as shown by X-ray photoelectron spectroscopy [42, 248].

For $R = 0.7$, a significant decrease of the band centred at 1075 cm^{-1} is observed after irradiation, exhibiting a shift from 1075 towards 1100 cm^{-1} at high fluences. At the same time, the bands centred at 835 and 930 cm^{-1} do not show a decrease in intensity with increasing fluence as expected, instead, the former exhibits a 50 % increase in the bond density and no redshift larger than 3 cm^{-1}, and the latter shows a decrease in bond density below 3 % and a shift towards 950 cm^{-1}.

By inspection and analysis of the higher frequency region (Figure 5.16 (b)), a similar trend as for a-$SiN_{1.06}$ regarding the contribution to the absorbance bands was found with the difference of a weak band located around 3480 cm^{-1} possibly related to the H-O-H stretching mode. As mentioned before, a decrease in the bond density of the N-H and O-H contributions is apparent while an increase in the signal ascribed

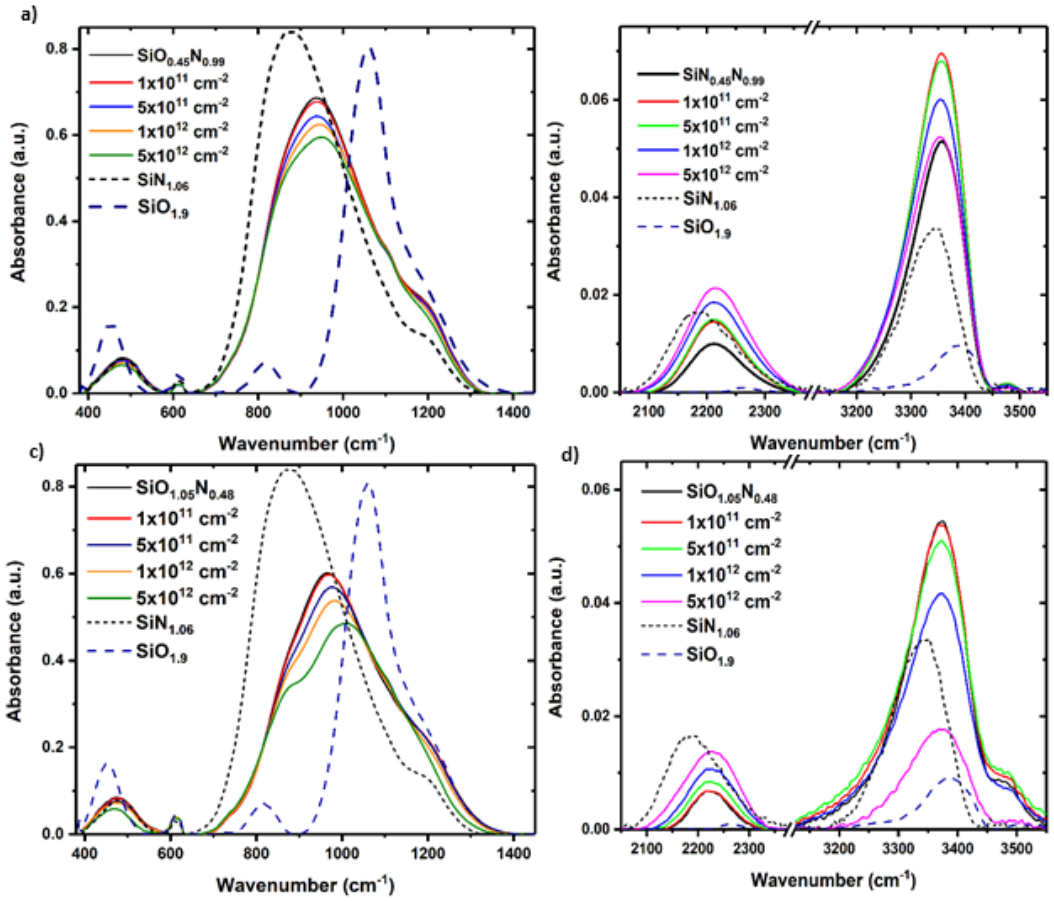

Figure 5.16: *FTIR spectra of a-$SiO_{0.45}N_{0.99}$ ((a) and (b)), and a-$SiO_{1.05}N_{0.48}$ ((c) and (d)). The FTIR spectra of a-$SiN_{1.06}$ (dotted lines) and a-$SiO_{1.9}$ (dashed lines) were added for comparison.*

to two Si-H vibrational modes was observed. As mentioned early in this Chapter, the proportionality coefficients to determine the bond concentration are dependent on the composition and have not been determined for a-SiO_xN_y. Thus, it is not possible to quantify the bond concentration.

In Figure 5.16 (c) the evolution of the FTIR peaks with fluence is plotted for $R = 0.85$. The main absorbance band follows a smooth transition towards higher frequencies leading to the separation in two distinguishable bands after irradiation with 5×10^{12} cm^{-2}. Analogous to the preceding case, we observe a band centred at 475 cm^{-1} that corresponds to the symmetric stretch of the Si-N bond in an N-Si_3 configuration. It is important to mention that no shift or change in shape and position of this band was detected below irradiation with the highest fluence, where a transition towards a weaker band with a lower frequency ($\sim$ 467 cm^{-1}) appears. The comparison of the FTIR spectra with a-$SiO_{1.9}$ (dashed lines) is also plotted in Fig. 5.16 (c), which indicates the shift occurs towards the position of the Si-O rocking mode which has been previously located at 465 cm^{-1} [268]. This suggests the band might be a superposition of both contributions and the change in position and the measured shape is the result of two different damage rates for Si-N and Si-O, and not attributed to the Si-Si breathing mode as some authors have argued [269]. The main absorance band was deconvoluted into six Gaussian contributions: four strong bands centred at 880, 955, 1020 and 1170 cm^{-1} and two weak bands at 750 and 1100 cm^{-1} (not shown). The nature of the 880 cm^{-1} band was assigned to the Si-O stretching mode in a Si-O-Si configuration in a $(SiO)_n$ linked to H, remaining unaltered at all fluences considered. The band at 955 cm^{-1} corresponds to the Si-N stretching mode in a H-SiN_3 configuration, exhibiting a shift towards 965 cm^{-1} with fluence and a great reduction in intensity and width with increasing fluences. The modification of this band appears to be responsible for the shape of the main infrared band at higher fluences, nearly disappearing at 5×10^{12} cm^{-2}. The band centred at 1020 cm^{-1} was related to the asymmetric Si-O stretching mode where we observed constant increase in the bond density up to 1×10^{12} cm^{-2} followed by an abrupt decrease at 5×10^{12} cm^{-2}. At 1170 cm^{-1} we have a similar behaviour to the and at 465 cm^{-1} as this band

can be ascribed to the Si-O out-of-phase stretching mode and to the N-H wag-rocking mode. This is clear in Fig. 5.16 (c) where we can observe a very smooth change in the slope of the shoulder located around 1200 cm^{-1}, most evident at the highest fluence. As the H content is greatly reduced in this sample, it becomes difficult to deconvolute this band into the two contributions known in this range. The two weak bands are very difficult to identify but in this work it is believed to be due to Si-O symmetrical stretching mode in the SiO_3 configuration and Si-O, respectively. No change of theses bands is observed until reaching the highest fluence applied in this study.

At higher frequencies, it is possible to detect the contributions commonly assigned to the stretching modes of Si-H, N-H and O-H (Fig. 5.16 (d)). Around 2200 cm^{-1} we can observe a single band that can be deconvoluted into two Gaussian contributions centred at 2200 and 2235 cm^{-1}. In the literature, the first is related to the Si-H stretching in a H-Si-HN_2 configuration, while the last to the Si-H mode in a H-Si-N_3 structure [16]. As these positions are shifted to higher frequencies in comparison with a-$SiN_{1.06}$, it is believed this is because of the substitution of O into the known configurations. At higher frequencies we found the overlap of the contributions from N-H when another N atom is nearby (N-H-N), the typical N-H stretching mode and the O-H stretching mode at 3320, 3378 and 3490 cm^{-1}, respectively. In the same fashion as for samples with high N concentration, but opposite to those with low N concentrations, we observe a monotonically decreasing IR intensity with increasing fluence of the bands in this region while the intensities of the bands associated with Si-H increase. This might suggest a recombination of H with the Si dangling bonds associated with the deposition method.

5.5.3 Discussion of ion track formation process in amorphous silicon oxynitride layers

In the past section, the morphology and absolute density profiles determined for a-$SiN_{1.06}$ and a-$SiO_{1.9}$ were consistent with frozen-in density waves. Their formation results from the inhomogeneous temperature profile and corresponding thermal

expansion, where the absolute density change is related to the timescale of the thermal spike and thus the quenching process. Furthermore, the densification of the outer (shell) region was shown to be the result of the matter redistribution mediated by the diffusion of coordination defects towards the inner (core) region, in agreement with MD simulations and the effective modified region estimated by FTIR.

In the case of a-SiO_xN_y thin layers, two distinctive responses in terms of the N (or O) relative content were observed by SAXS and FTIR. The analysis of the scattering patterns for samples with a ratio N/Si > 1, showed a clear similarity to a-$SiN_{1.06}$. The slight increase in the ion track radius and decrease of the absolute density change can be explained by a likely increase in their optical band gap with increasing O incorporation. This parameter has been demonstrated to influence the efficiency of the energy deposited by the incident ion and thus, the dimensions of the ion track. When the O content increases, and the N content decreases to a ratio O/Si > 1 similar scattering patterns to a-$SiO_{1.9}$ were observed, where the only clear difference was the decrease in the absolute density change with increasing O content while the morphology and dimensions remained almost unchanged.

To understand the previous observations, the FTIR absorbance spectra of a-SiO_xN_y thin layers were studied, following the same principles as for a-$SiN_{1.06}$ and a-$SiO_{1.9}$. From the corresponding deconvolution of the different absorbance bands two different evolutions with fluence were observed. When the ratio N/Si > 1, it was observed that the bands potentially ascribed to the N-Si_3 and Si-N asymmetrical vibrational mode, show a very weak reduction with fluence while the Si-O stretching mode is significantly reduced. Interestingly, the trend changes when the O content is significantly increased to O/Si > 1. In this case, the amplitude of the absorbance band related to the Si-N stretching mode in the H-SiN_3 configuration decreased around 70 % with increasing fluence while the Si-O stretching mode shows a greated resistance to radiation damage.

It has been shown that the random bonding (RB) model describes the structure of the tetrahedral a-SiO_xN_y more adequately and is characterised by a statistically

controlled mixture of five kind of tetrahedra, $SiO_\nu N_{4-\nu}$ with $0 \leq \nu \leq 4$ [42,43,248,270]. However, for a-SiO_x [253] and a-SiN_y [254] it is known that the relative O or N content significantly modifies the statistical mixture of the corresponding tetrahedra. When the value of x surpasses unity, the formation of the SiO_3 or SiN_3 tetrahedra is favoured while below unity, Si_3O and Si_3N are favoured instead. If the previous findings can be extended to a-SiO_xN_y materials, it can help explaining the two characteristic SAXS intensity patterns plotted in Figure 5.14 and the related ion track dimensions determined. However, it is noteworthy to highlight that it has been shown that the local structure of a-Si_3N_4 materials shows a strong dependence on the deposition method while for a-SiO_2, this does not seem to be the case [43]. This was shown in the previous section where a comparison with near-stoichiometric materials was presented. Thus, such differences might explain the saturation of the ion track dimensions with high O content while in the case of N, clear deviations are observed.

Furthermore, it is worth highlighting the fact that the evolution of the FTIR absorbance bands related to the presence of H is similar to the binary materials. With increasing fluence, a reduction of the absorbance bands corresponding to N-H followed by the increase of the bands related to the Si-H bonds are apparent. This is accompanied by the formation of new O-H bonds with increasing O content. While a quantitative analysis of the evolution of the H content with fluence was not performed, qualitatively we can expect a similar behaviour as seen for a-$SiO_{1.9}$ and a-$SiN_{1.06}$. It has been demonstrated that H bonded to the a-SiO_xN_y structure is not only released at a lower rate than the breaking of Si-N or Si-O bonds, but it can link to pre-existing or newly formed Si dangling bonds. This demonstrates that an improved atomistic analysis of the ion track formation process is still needed to fully understand the materia response under SHI irradiation and that the energy deposited not only induces structural damage, but it can transform the local structure in amorphous materials too.

5.6 Summary

In conclusion, SAXS measurements in combination with 2T-MD simulations and FTIR spectroscopy provide not only an accurate picture of the morphology of ion tracks in amorphous silicon dioxide, silicon nitride and silicon oxynitrides but also explain the nature of the under-dense core surrounded by an over-dense shell morphology with a smooth transition. The morphology is a result of the viscous flow present in the molten region driven by thermal stresses arising from the non-uniform temperature profile. As the decrease of the viscosity in the inner region is not as abrupt as in the case of amorphous metals, the quenching process is faster than the oscillation frequency or relaxation period, leading to large density fluctuations. Furthermore, the larger value of the lattice thermal conductivity of amorphous silicon nitride appears to have a major role in the larger values for the density variations remaining compared to a-SiO_2. The core-shell structure with a smooth transition is then the result of the quenched density wave.

For a-SiO_xN_y materials, it was shown that the composition played a major role in the material response under SHI irradiation. When their stoichiometry is closer to a-$SiN_{1.06}$, the structure appears to be controlled by the SiN_4 tetrahedra, where quantitative analysis of FTIR shows higher Si-O bond breaking in comparison to Si-N, explaining the observed behaviour with fluence. On the other hand, when the stoichiometry is closer to a-$SiO_{1.9}$, the structure is dominated by the Si-O bond configurations clearly following a similar behaviour. These trends agrees with the random bonding RB model but disagrees with the proposed mixture of five kind of tetrahedra due to the presence of H. The qualitative analysis of the deconvoluted FTIR spectra allowed to identify two different trends in the material response when the content of N (or O) is significantly increased. Such trends agree with those observed by SAXS, demonstrating the effect of the local order on the dimensions and morphology of the formed tracks.

Chapter 6

Synthesis of Au nanoparticles in amorphous silicon nitride, silicon dioxide and at the interface of silicon dioxide and silicon nitride

The present chapter reports on the synthesis of Au NPs in a-$SiN_{1.06}$, a-$SiO_{1.9}$ and at the interface of the two dielectric materials, aiming to gain control of their size distribution. First, the synthesis of Au NPs in a-$SiN_{1.06}$ by implantation with 2 MeV Au ions followed by thermal annealing is investigated. The corresponding characterisation by TEM and SAXS showed the synthesis of NPs of mean radii smaller than 3 nm for all conditions while the matrix remained amorphous but reveals the formation of voids near the implanted region. To understand if this behaviour is correlated to the deposition technique (PECVD), a-$SiN_{1.1}$ deposited by LPCVD was implanted and annealed under similar conditions as a-$SiN_{1.06}$, for comparison. At all annealing temperatures, a-$SiN_{1.1}$ exhibited a phase transformation towards crystalline (trigonal (α-) and hexagonal (β-)) phases as confirmed by XRD. FTIR measurements of a-$SiN_{1.06}$ annealed at 1100 °C showed the disappearance of the absorbance bands associated with the N-H vibrational modes while those associated to Si-H were still present. The latter suggests that the synthesis of Au NPs is influenced by the deposition technique in nitrides. The synthesised Au NPs in a-$SiO_{1.9}$ by ion implantation was studied under similar conditions as for a-$SiN_{1.06}$. TEM and SAXS

show the presence of NPs of larger diameters while no indication of void formation was observed. Similar to the previous case, thermally grown a-SiO_2 implanted with Au ions was annealed under the same conditions as a-$SiO_{1.9}$ where similar size distributions were observed for the two materials, demonstrating little dependence on the deposition or growth technique of the oxide. Finally, the synthesis of Au NPs using RTA of dielectric/metal/dielectric multilayers is presented. In this method, a thin Au layer ($\sim$ 5 nm thick) is located between two a-$SiO_{1.9}$ (or a-$SiN_{1.06}$) thin layers deposited by PECVD. The corresponding characterisation by TEM showed the formation of NPs with dimensions larger than those observed by ion implantation, but with a much narrower size distribution.

6.1 Introduction

Composite materials consisting of noble metal NPs (MNPs), such as Cu, Au Ag, embedded in a dielectric medium have been widely studied in the last decade due to their interesting linear and nonlinear optical properties [26, 271]. Such properties are strongly dependent on the collective oscillation of the conduction electrons of the MNPs, known as surface plasmon resonance (SPR). Its spectral response is determined by the metal species, volume, shape and the dielectric properties of the surrounding medium [50] and can be tuned by controlling these parameters.

Nowadays, physical and chemical techniques are available for the fabrication of such composite materials. Among the physical methods, ion implantation has been used to tailor the size and spatial distribution of MNPs in solid materials as it allows the addition of foreign species in solid materials above their equilibrium solubility [3,272–274].

Another method used is electron beam lithography (EBL), where a focused electron beam is used to pattern an electron-sensitive film (resist) with sub 10-nm resolution followed by the deposition of the desired metal species [275]. Finally, the resist is removed leaving behind the desired metallic structures, which in several cases were subsequently

covered by a capping layer [275,276]. While this method allows the design of NP arrays with a narrow size distribution, for some substrate/metal combinations the deposition of a very thin sub-layer is necessary to guarantee the adhesion of the metallic layer to the substrate [277]. It has been shown that the sub-layer can modify the response of the MNPs resulting in an undesired response [278, 279]. Furthermore, patterning of areas larger than few μm^2 is very time consuming in comparison with other techniques.

Many methods are available to achieve mono disperse MNPs based on chemically synthesis methods [280]. After the NP synthesis, a substrate is immersed in a diluted NP solution, where the density of the deposited NPs is controlled by the immersion time. To do so, the substrate surface is first functionalized with an amino silane as a coupling agent in the case of Au NPs in a-SiO_2 [123, 281, 282]. Finally, a capping layer to protect the NPs from the environment is deposited. While this method permits the preparation of monodisperse size distributions, the MNPs are typically coated with chemical agents to inhibit further growth and particle aggregation which alter the optical response.

These techniques allow to control the volume of the NPs as well as their relative position within the solid matrix. Nevertheless, ion implantation offers an easy path to influence the synthesis of MNPs by modifying its parameters, such as ion energy, flux, fluence, implantation temperature and sequential implantation at different energies [3, 283]. The final NP dimensions can be commonly controlled by two methods: (i) post-implantation thermal annealing in different atmospheres [144, 272, 284], or (ii) by ion irradiation [62, 285]. For both methods, several studies have been performed for Au in a-SiO_2 [3, 283], where the mobility of Au as well as the effect of the annealing atmosphere and time on the size distribution are known [61, 144]. For the second method (ii), it has been shown that ion irradiation can lead to MNPs of smaller dimensions with narrower size distributions [62, 285]. Besides the broad applications, ion implantation possesses several limitations such as the addition of ion irradiation induced defects and generally broad NP size distributions, not relevant for specific photonic or plasmonic applications [3].

In addition, swift heavy-ion irradiation can be used to tailor the optical response of the composite system as it allows the formation of highly anisotropic and well-aligned MNPs [3, 283, 286]. Such systems are very difficult to produce by other methods. This process has been first reported more than a decade ago and predominantly studied for MNPs embedded in a-SiO_2, where it is possible to transform spherical NPs to rod-like shapes aligned with the beam direction. The first report in ion-shaping was carried out for ion beam synthesized Co NPs in a-SiO_2. The shape transformation was induced by irradiation with 200 MeV I ions at different fluences [4]. In this first work, the relevance of the initial NP size was outlined. Therefore, to tailor the geometry it is important to achieve a good control over the initial size of the MNPs. Following experiments were carried out by Dawi *et al.* [68, 149], to study the dependence of the process on NP size to better understand the proposed mechanism followed by the corresponding rationalization of their observations by Rizza and collaborators [123]. As a result, the relationship between initial size and the ion-shaping process proposed by D'Orleans *et al.* [4] was extended and showed that the size needs to be about twice that of the ion track for efficient elongation.

This chapter presents a study of the synthesis of embedded Au NPs by two methods: (i) ion beam synthesis, and (ii) rapid thermal annealing of a sequentially deposited dielectric/Au/dielectric layer stack. In (i) it is aimed to study the viability of ion beam synthesis in a-$SiN_{1.06}$ to achieve good control over the NPs size distribution. In (ii) it was the aim to develop a simple procedure to achieve a high areal density of Au NPs and control over their size distribution which provides the size range needed to study the ion shaping process for swift heavy-ion irradiation with 185 MeV Au ions. The proposed methodology is of particular interest as it allows the synthesis of a single layer of Au NPs at the interface of two dielectric materials.

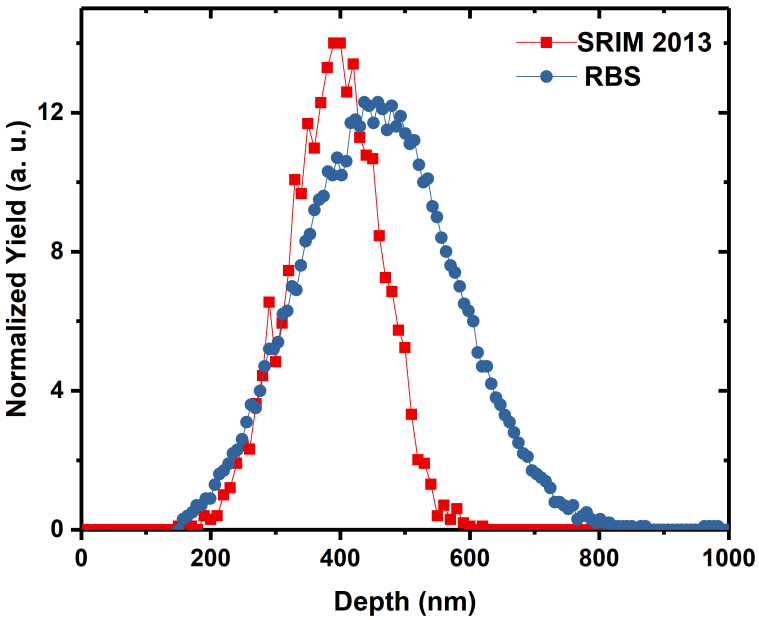

Figure 6.1: *Depth distribution of implanted Au ions as calculated by the SRIM2013 code and measured by RBS.*

6.2 Ion beam synthesis of Au NPs in amorphous silicon nitride

The synthesis of Au NPs was carried out by implantation of Au ions into ∼1 μm thick a-$SiN_{1.06}$ layers with an energy of 2 MeV and a fluence of 5.5 × 10^{16} cm^{-2} at room temperature. The ion implantation process was followed by thermal annealing for 60 minutes in air and N_2 atmospheres at temperatures of 1000, 1050 and 1100 °C, respectively, to promote the formation and growth of Au NPs.

The projected range and straggling of the implanted ions were calculated using the SRIM code [92] resulting in values of 390 and 70 nm, respectively. Prior to the thermal annealing of the implanted samples, RBS was carried out to characterise the depth profile of the implanted ions. The experimentally and numerically calculated depth profile of the implanted Au ions are plotted in Figure 6.1. The conversion from the RBS spectrum into a depth profile was carried out following equation 3.16 in section

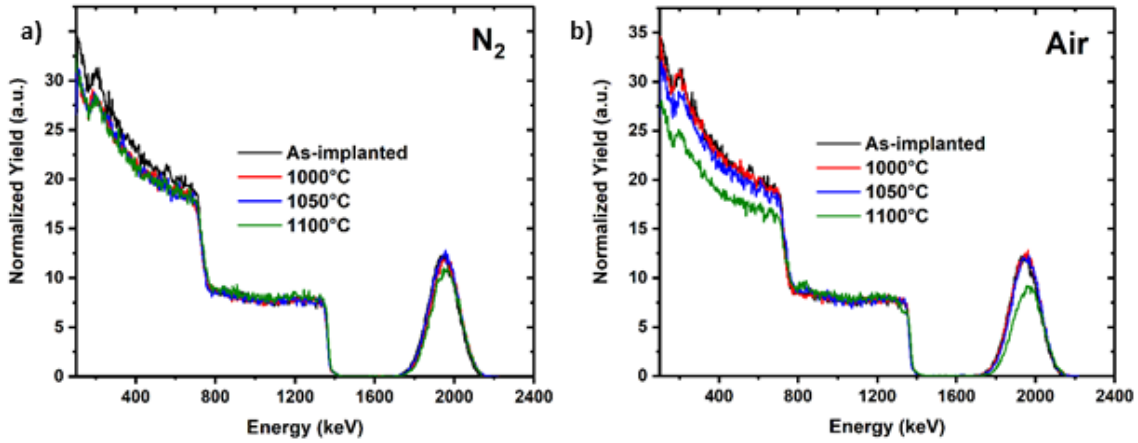

Figure 6.2: *RBS spectra of implanted a-$SiN_{1.06}$ thin layers with 2 MeV Au ions before and after thermal annealing for 60 minutes in N_2 (a) and air (b) atmosphere at different temperatures.*

3.4.1. In the plot a larger projected range and straggling are observed from the RBS measurements in comparison to the predicted values. Such discrepancies have been related to simplifications and inaccuracies in the simulation parameters [287], or due to the deviation from the ideal stoichiometry. Furthermore, it has been pointed out that the SRIM code commonly underestimate the projected range as in the case of Pt implantation in a-SiO_2 layers, where a discrepancy of 150 nm was observed between SRIM calculations and RBS measurements for Pt ions implanted with 4.5 MeV [287].

After thermal annealing, the samples were characterised by RBS to quantify the occurrence of Au redistribution. Figure 6.2 (a) shows the plots of the corresponding RBS spectra for samples annealed in a N_2 atmosphere at 1000, 1050 and 1100 °C. The RBS spectra were numerically fitted using the RUMP code [195, 196] (see section 3.4.1, fits not shown). For the samples annealed in N_2, no change in stoichiometry was observed above the detection level. The implanted region followed a Gaussian distribution for the three samples. In the Au distribution, no meaningful change was observed, except for the sample annealed at 1100 °C where a small shift towards the surface of the projected range (less than 50 nm) was observed. In the case of the samples annealed in Air (Figure 6.2 (b)) no change in the projected range or straggling

was recorded below 1100 °C. At 1100 °C, the projected range shifted almost 70 nm with respect to the un-annealed sample and a decrease of nearly 20 % of the Au peak concentration. Such decrease can be a consequence of the roughness in the samples, as a reduction in the yield is observed for backscattering energies below 700 keV. The signal from this region is formed by alpha particles backscattered from the c-Si substrate and from the N atoms at the a-$SiN_{1.06}$ layer. Around channel 200 we can observe the tail of the yield from N, which does not show a distinguishable change with respect to the annealed samples at lower temperatures. Thus, the reduction of the yield goes beyond the N contribution, suggesting a homogeneous decrease of the Si content of the substrate, which is not physically possible. Together with the lack of evidence of Au diffusion towards the surface, it is likely an effect of surface roughness due to the high annealing temperature, which explains the slight shift towards the surface of the overall deposition while preserving the Gaussian distribution. The results are summarized in Table6.1.

Annealing atmosphere			N_2			Air		
temperature (°C)	SRIM2013	as-implanted	1000	1050	1100	1000	1050	1100
Projected range (nm)	390	462 ± 12	441 ± 11	446 ± 4	394 ± 9	448 ± 8	442 ± 11	409 ± 9
Straggling (nm)	70	116 ± 3	113 ± 3	113 ± 3	116 ± 4	113 ± 4	109 ± 5	117 ± 5
Fluence ($\times 10^{16}$ cm^{-2})		5.6 ± 0.1	5.4 ± 0.1	5.6 ± 0.1	4.8 ± 0.1	5.6 ± 0.1	5.4 ± 0.1	4.3 ± 0.1

Table 6.1: *Depth distribution parameters determined by RBS for a-$SiN_{1.06}$ samples implanted with 2 MeV Au ions before and after annealing under different conditions. The error values correspond to the standard deviation associated with the normal size distribution.*

Figure 6.3, shows the TEM micrographs for samples annealed in N_2 ((a) and (b)) and in Air ((c) and (d)) for 60 minutes at 1000 and 1100 °C, respectively. From the micrographs the formation of spherical Au NPs is apparent, however, the NP dimensions show little dependence on the annealing temperature. In figure6.3, the corresponding size distributions are plotted. From the TEM images over 300 NPs were used to evaluate these samples. The size distributions resemble normal distributions for all annealing conditions.

Complementary SAXS measurements were carried out on the samples with Au NPs embedded in a-$SiN_{1.06}$. As discussed in section 4.4, from the scattering intensities it is possible to determine the size distributions of the Au NPs. The numerical fitting was done using the maximum entropy module available in the Irena package [288]. It describes the NP size distribution as a histogram with a fixed number of bins defined over a range of diameters. The fit to the scattering intensity is done by iteration, where a trial histogram is proposed followed by correction of the amplitudes of the trial histogram distribution constrained to the initial conditions. The histogram possesses the characteristic of not being forced to follow a particular form yet, all scattering objects are considered to have the same scattering contrast and morphology while inter-particle scattering effects are neglected. This approach has been adopted as it has shown good agreement with TEM results for MNPs synthesized by ion implantation in a-SiO_2 [274, 284, 289]. Figure 6.4 shows the scattering intensities and their corresponding numerical fits, considering spherical NPs, for the two annealing atmospheres (N_2 and Air, respectively) and different annealing times. The results of TEM and SAXS analysis are summarized in Table6.2. Comparison of the size distributions determined by the two techniques indicates that TEM analysis yields smaller NP sizes than those estimated by SAXS. From the ion beam synthesis theory discussed in section 2.4, the small sizes of the Au NPs observed by both, TEM and SAXS, suggests that the low mobility of dopants known for a-Si_3N_4 is also valid for a-$SiN_{1.06}$ thin layers deposited by PECVD.

Technique	TEM		SAXS	
Annealing atmosphere	N_2	Air	N_2	Air
Temperature				
1000 °C	1.7 ± 0.3	1.8 ± 0.3	2.6 ± 0.2	2.2 ± 0.2
1050 °C	1.8 ± 0.3	2.1 ± 0.4	2.6 ± 0.6	2.4 ± 0.2
1100 °C	2.0 ± 0.3	2.5 ± 0.4	3.0 ± 0.2	3.4 ± 0.2

Table 6.2: *Mean diameter of ion beam synthesised Au NPs in a-$SiN_{1.06}$ after annealing for 60 minutes at different conditions. The uncertainties correspond to the standard deviations of the observed normal size distributions.*

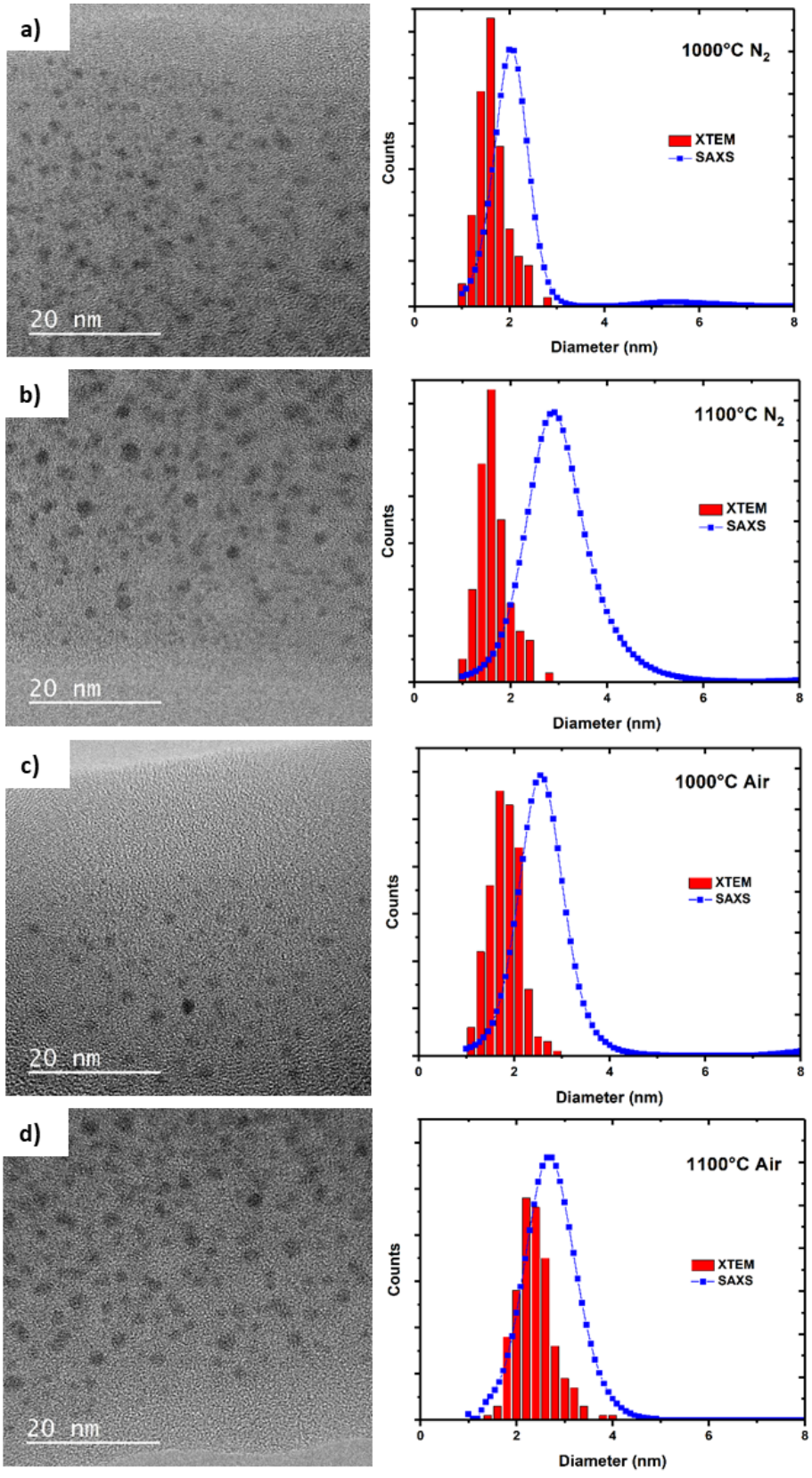

Figure 6.3: *TEM micrographs of Au NPs formed in a-$SiN_{1.06}$ after implantation with 5.5×10^{16} cm^{-2} and thermal annealing for 60 minutes in N_2 at 1000 °C (a) and 1100 °C (b), and Air at 1000 °C (c) and 1100 °C (d), and their corresponding size distributions determined from TEM and SAXS.*

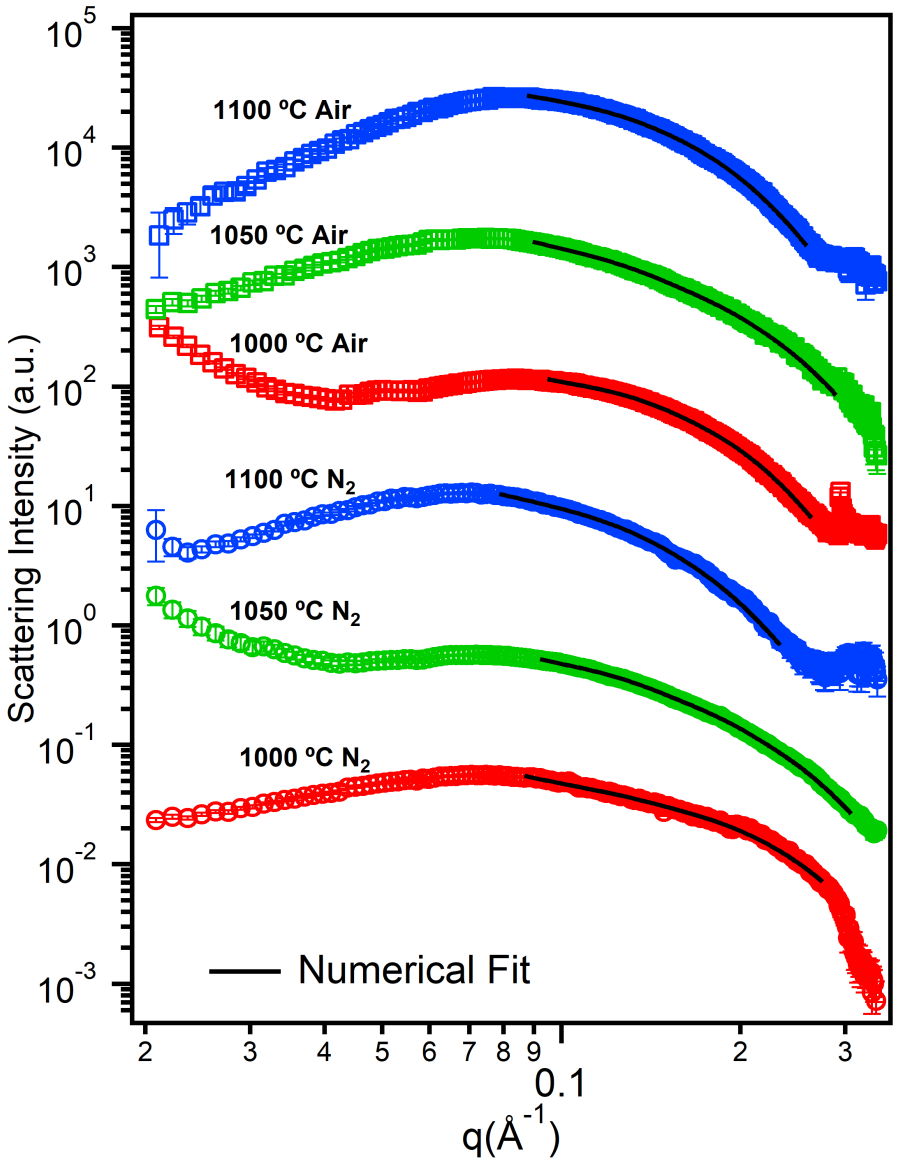

Figure 6.4: *SAXS scattering intensities for Au NPs synthesized in a-$SiN_{1.06}$ after thermal annealing in N_2 and air at different temperatures. The solid lines correspond to the numerical fits based on the maximum entropy module.*

As shown in table6.2, for both annealing atmospheres, with increasing annealing temperature NPs of larger dimensions were formed. This would suggest that it is possible to reach NPs with sizes above 10 nm by annealing a sample implanted with Au ions at 1100 °C or higher for longer times. However, it is also important to study the potential structural modification induced by ion implantation of a-$SiN_{1.06}$ thin layers. Figure6.5 shows the vacancies produced by the ion implantation in a-$SiN_{1.06}$ after implantation of 2 MeV Au ions calculated by the SRIM2013 code [92]. In the inset, an under-focussed TEM micrograph[1] of the region near the maximum of the vacancy profile is shown. In the image, the formation of voids, of sizes at least twice that of the formed Au NPs, after annealing with 1100 °C in a N_2 atmosphere can be observed. For ceramic materials exhibiting porosity, it is known that the effective thermal conductivity is decreased [290]. This can have a great impact on the ion shaping process[2] yet, the decrease in the local density might lead to a decrease in the electron-phonon coupling, too. While theory suggests that larger NPs would be formed by annealing for longer times, it is unclear what the effect of annealing at higher temperatures or for longer periods would have on the evolution of the voids. If the voids are the result of the aggregation and nucleation of coordination defects created during the ion implantation process or already present in the sample, annealing could lead to a significant increase in their size. It may the case that coordination defects have a larger mobility than Au ions in a-$SiN_{1.06}$, because after 60 min larger dimensions for the voids are observed than for the Au NPs. Furthermore, the presence of voids can distort the scattering pattern measured by SAXS and may lead to the difference in the size distributions with respect to the TEM values.

The ion beam synthesis of Au NPs was also carried out in a-$SiN_{1.1}$ deposited by LPCVD to study the difference in the synthesis process with stoichiometry. Figure6.6 (a) shows the RBS spectra before and after annealing for 60 minutes in N_2 between

[1] In under-focused TEM micrographs the formation of Fresnel fringes can be observed, in the form of subtle white rings on the side edge of the voids. Such features allow to distinguish the formation of voids, not visible in well-focused images

[2] the effect of the thermo-physical properties in the ion shaping process is discussed in the following chapter

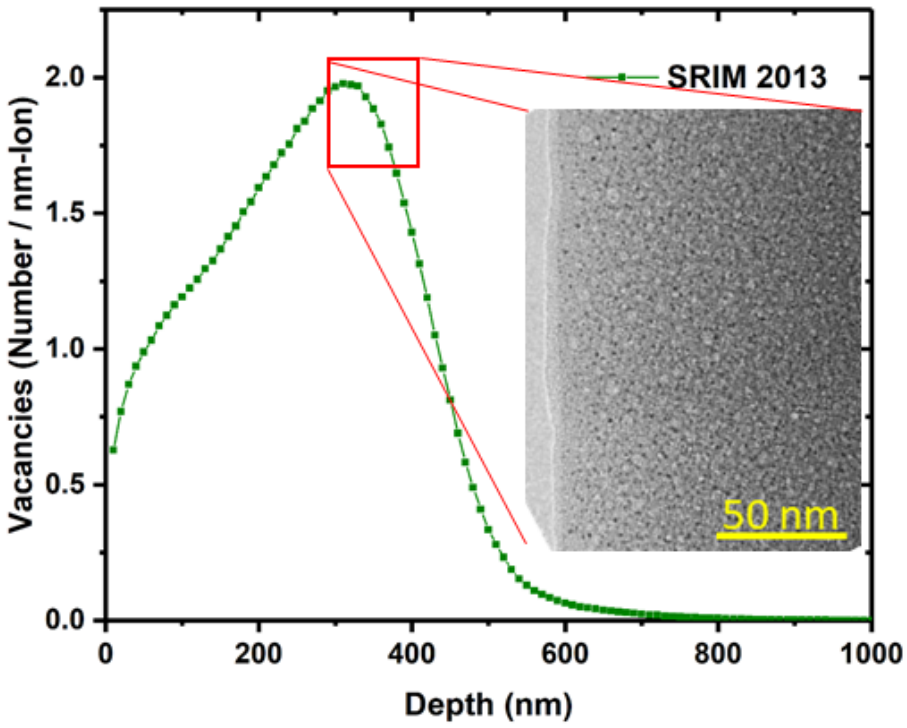

Figure 6.5: *Depth profile of the vacancies produced in a-$SiN_{1.06}$ after implantation of 2 MeV Au ions calculated by the SRIM2013 code. The inset shows a cross-sectional TEM image of the void formation after thermal annealing at 1100 C in N_2 near the region of maximum radiation damage.*

1000 and 1100 °C. For all annealing temperatures it is observed that the implanted Au diffuses nearly even through the entire layer, showing a slightly higher concentration around the region close to the surface. TEM micrographs indicate that the observed diffusion is accompanied by a phase transformation of the a-$SiN_{1.1}$ from amorphous to crystalline (Figure6.6 (b)). In the TEM micrograph, it is possible to identify the formation of large Au agglomerates near regions where large crystallites are observed. Figure6.6 (c) shows the corresponding XRD pattern for a-$SiN_{1.1}$ and a-$SiN_{1.06}$ after annealing in N_2 at 1100 °C. For a-$SiN_{1.06}$, the amorphous phase is retained while a-$SiN_{1.1}$ undergoes an amorphous-to-crystalline phases of a-Si_3N_4, trigonal (α-) and hexagonal (β-). HAADF in STEM mode image (Figure6.6 (d)) clearly shows that Au agglomerates at the grain boundaries of the Si_3N_4 crystallites.

A similar effect had been observed in LPCVD a-Si_3N_4 thin layers implanted with Ge and Ni at higher fluences [291], yet the nature of the amorphous-to-crystalline phase transformation was not explained. It is possible that this phase transformation can be explained by the excess of Si and absence of H in the local structure, which results in an excess of Si dangling bonds. This is exemplified in Figure 6.7, where the FTIR spectra of a-$SiN_{1.06}$ PECVD samples annealed at 1100 °C and unannealed are compared. In the figure, the remnants of absorbance bands associated with the Si-H bonds can be observed while those related to N-H were absent in the annealed sample. Thus, a possible scenario is the release of H from the N-H bonds initially formed allowing the formation of new Si-N networks while the remaining H bonded to Si, preventing the formation of Si_4 structures. In the case of a-$SiN_{1.1}$ layers, the thermal annealing can lead to the formation of Si-rich regions, which in contact with Au can induce a phase transformation into crystalline Si_3N_4 regions. This can occur as Au is a eutectic forming metal [292]. In contact with Au, the Si bonds are weakened due to screening of the covalent bonding facilitating the inter-diffusion of Au and Si. Thus, the formed crystalline regions can reduce the energy required for the phase transformation into α-Si_3N_4 resulting in the observed formation of polycrystalline samples.

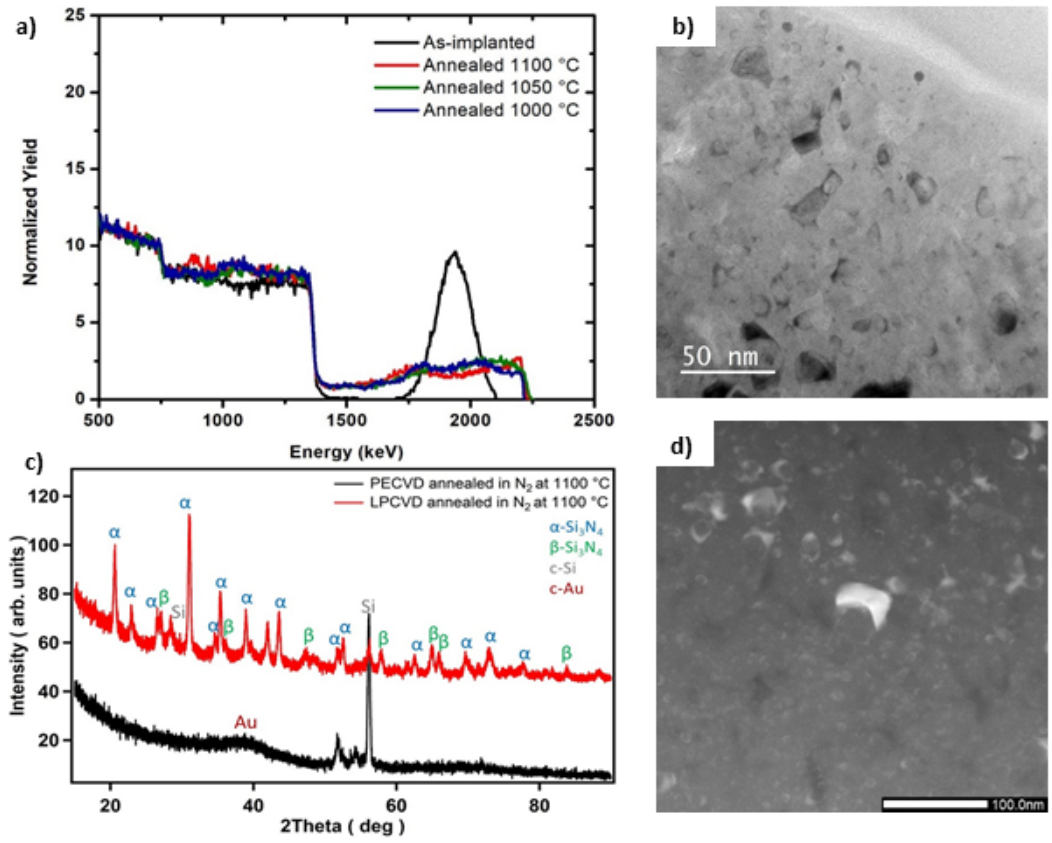

Figure 6.6: *RBS spectra of a-$SiN_{1.1}$ thin layer implanted with 2 MeV Au ions before and after annealing in N_2 at different temperatures (a). TEM micrographs of Au NPs implanted in a-$SiN_{1.1}$ layer after annealing for 60 minutes in N_2 at 1100 °C (b), its corresponding XRD pattern (a-$SiN_{1.06}$ was added for comparison) (c) and HAADF in STEM mode image where the bright region represents the Au near the grain boundaries (d).*

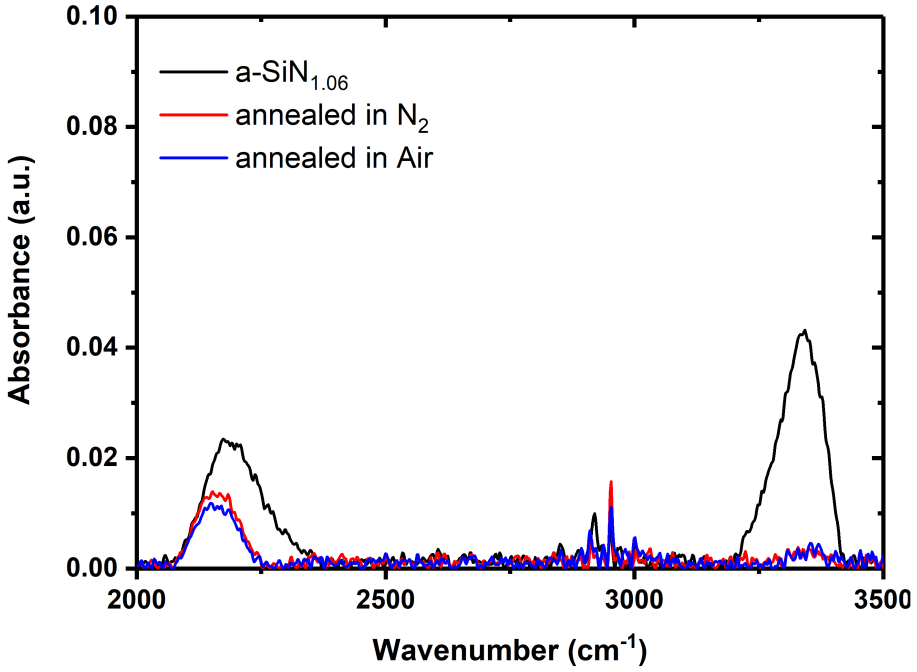

Figure 6.7: *FTIR spectra of a-$SiN_{1.06}$ implanted with 5×10^{16} cm^{-2} Au ions showing the Si-H (2200 cm^{-1}) and the N-H (3350 cm^{-1}) vibrational modes before and after annealing at 1100 °C for 60 minutes at different atmospheres.*

In conclusion, the limited control over the NPs dimensions in combination with the void formation and the amorphous-to-crystalline transformation can potentially limit the use of this method for the study of the ion-shaping process. For completeness, in the next section a summary of our results on the ion beam synthesis process studied in a-$SiO_{1.9}$ and a-SiO_2 is presented. However, as the ion beam synthesis technique was not used for the study of the ion-shaping process, no further discussion is provided.

6.3 Ion beam synthesis of Au NPs in amorphous silicon dioxide

In the previous section, the characterization of the ion beam synthesised Au NPs in a-$SiN_{1.06}$ using SAXS, TEM and RBS was presented. Due to the limited information on ion implantation of metallic species in a-Si_3N_4, together with their well-known diffusivity in a-Si_3N_4, it was difficult to determine the conditions necessary to synthesize metallic NPs with the dimensions needed to study the ion-shaping process. This is in contrast to a-SiO_2, where the process has been studied under several conditions and the diffusion coefficient of Au is known [61]. In this section, a brief summary of the characterisation carried out for the ion beam synthesis of Au NPs in a-$SiO_{1.9}$, and its comparison to a-SiO_2, under the same ion implantation and annealing conditions considered in the previous section is presented.

Thin PECVD a-$SiO_{1.9}$ ($\sim$ 1 μm thick) and thermally grown a-SiO_2 ($\sim$ 2 μm thick) layers were implanted with 2 MeV Au ions with a fluence of 5.5 $\times$ 10^{16} cm^{-2}. Numerical calculations carried out with the SRIM2013 code [92] yield a projected range of $\sim$500 nm and straggling of $\sim$90 nm. Characterization by RBS of the Au implanted depth profile before and after thermal annealing shows a projected range of 650 $\pm$ 5 nm and a straggling of 137 $\pm$ 2 nm, where no significant redistribution was observed due to the thermal annealing. Figure 6.8 shows the depth profile of Au implanted in a-$SiO_{1.9}$ and a-SiO_2 and similar to the previous section, the SRIM calculations underestimate the expected values of the projected range and straggling by $\sim$ 150, respectively.

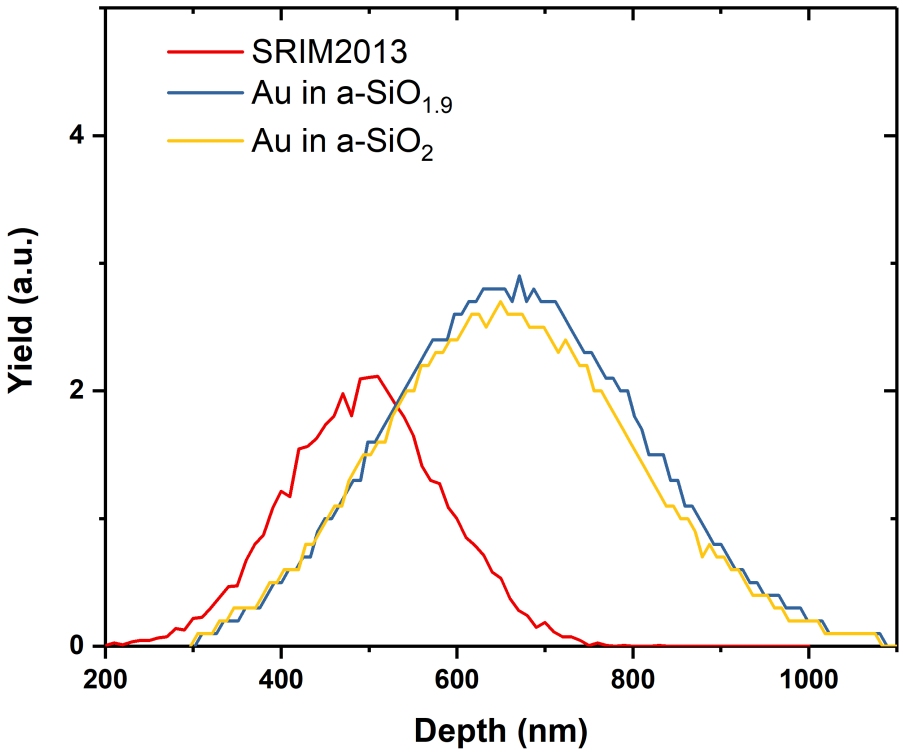

Figure 6.8: *Depth profile of 2 MeV Au implanted as calculated by SRIM2013 and as determined by RBS for a-$SiO_{1.9}$ and a-SiO_2.*

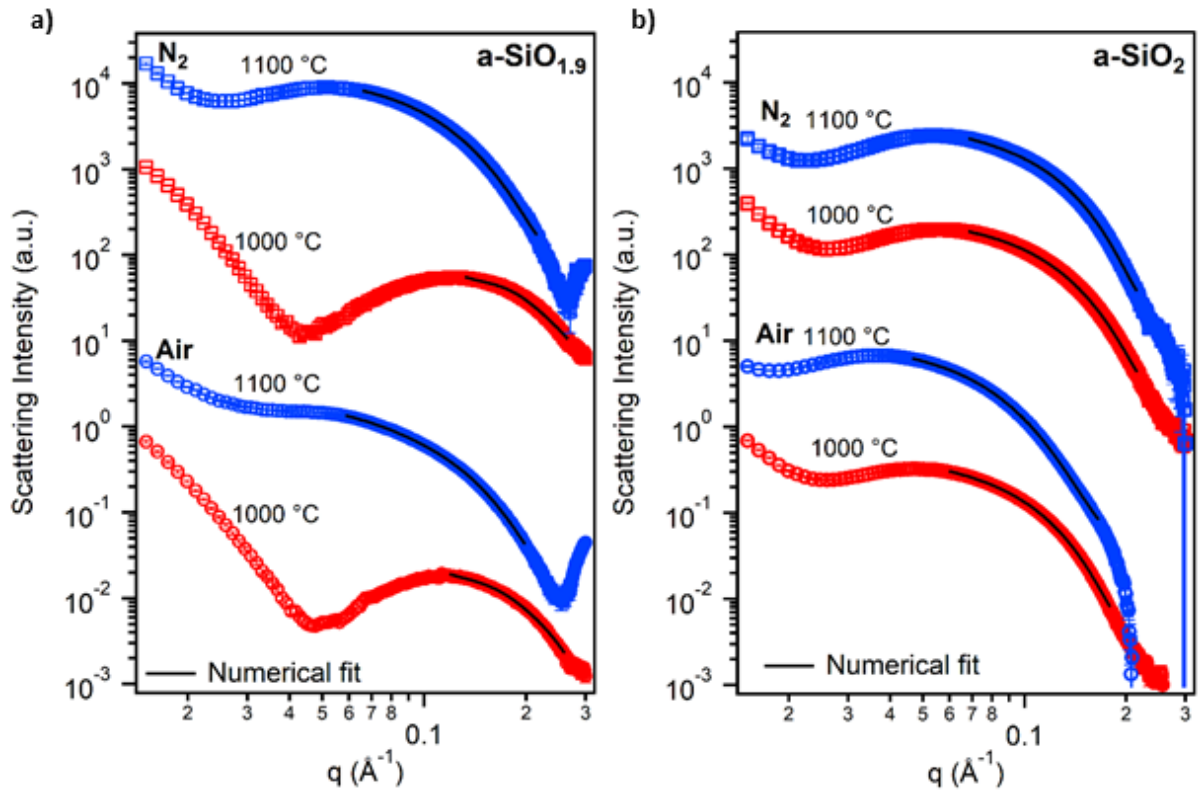

Figure 6.9: *SAXS scattering intensity and numerical fits (black lines) corresponding to Au NPs in a-$SiO_{1.9}$ (a) and a-SiO_2 (b) for different annealing conditions.*

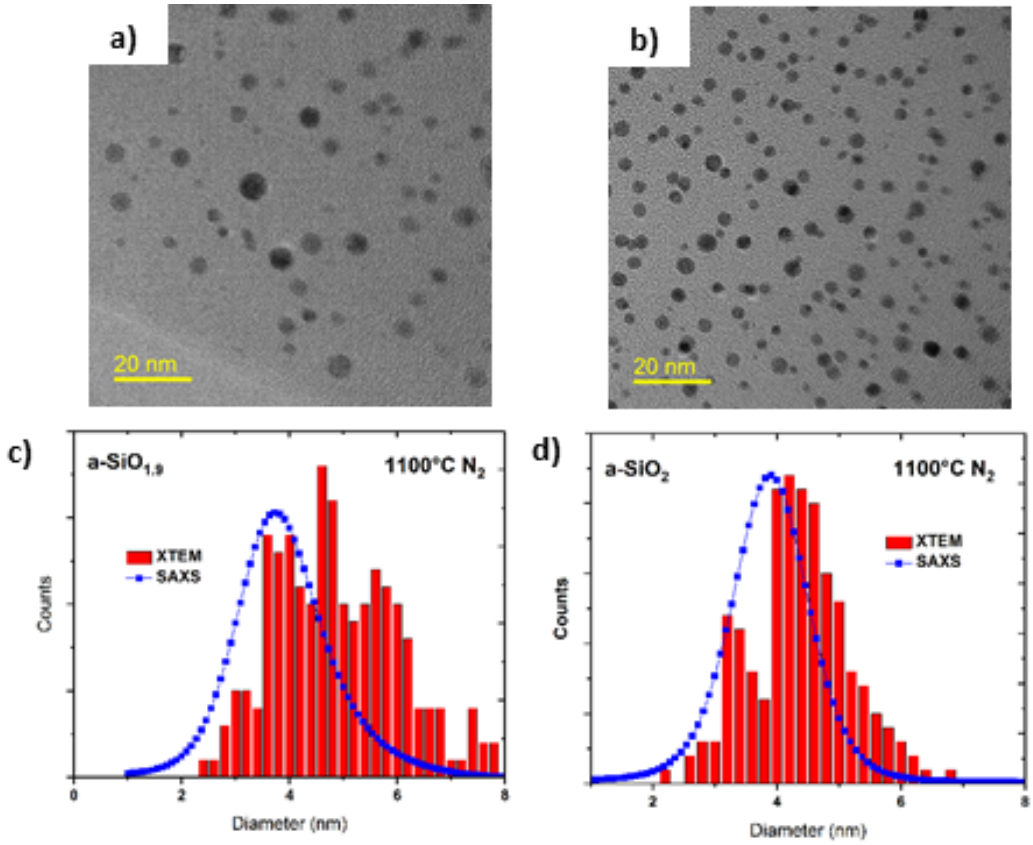

Figure 6.10: *TEM micrographs of Au NPs in a-$SiO_{1.9}$ (a) and a-SiO_2 (b) after annealing for 60 minutes in a N_2 atmosphere at 1100 °C and their corresponding histograms compared with the size distributions determined by SAXS (c) and (d).*

The size distributions of the synthesised Au NPs at different annealing times and atmospheres were determined by SAXS. Figure 6.9 shows the scattering intensities for the implanted samples after annealing for 60 minutes in N_2 at 1000 and 1100 °C for a-$SiO_{1.9}$ (a) and a-SiO_2 (b). Similar to a-$SiN_{1.06}$, the scattering intensities were fitted considering spherical objects (back lines) where good agreement was achieved with the experimental scattering intensities. Complementary TEM was carried out for samples annealed in N_2 at 1100 °C (Figure 6.10). As can be observed, spherical Au NPs were synthesized with diameters larger than their counterparts in a-$SiN_{1.06}$. Furthermore, for a-$SiO_{1.9}$ and a-SiO_2 the size distributions determined by TEM show

good agreement with those calculated by SAXS, supporting the claim that voids may distort the SAXS signal in the case of a-$SiN_{1.06}$. Also, very little differences in size were observed between the two studied materials, especially at 1100 °C. It is worth to mention that TEM can be misleading as the preparation method does not allow to trace the relative position with respect to the original sample's surface. This is an important feature since the NP size is dependent on the depth location and it is possible that influenced the TEM analysis. The size distributions are summarized in Table 6.3. The results suggest that Au in a-$SiO_{1.9}$ exhibits a similar behaviour as in a-SiO_2, besides the different deposition or growth conditions.

Technique	SAXS				TEM
Atmosphere	N_2		Air		N_2
Material/Temperature	1000 C	1100 C	1000 C	1100 C	1100 C
a-$SiO_{1.9}$	2.2 ± 0.6	4.0 ± 0.8	3.6 ± 0.6	4.0 ± 0.6	5.0 ± 1.2
a-SiO_2	2.4 ± 0.4	4.2 ± 0.8	4.4 ± 0.6	5.4 ± 1.0	4.4 ± 0.8

Table 6.3: *Mean diameter values of the size distribution of Au NPs in a-$SiO_{1.9}$ and a-SiO_2 after thermal annealing for 60 minutes at different conditions. The uncertainties correspond to the standard deviations considering a normal size distribution.*

6.4 Synthesis of single layer Au NPs in amorphous silicon nitride, silicon dioxide and at their interface

As shown in the previous sections, ion beam synthesis appears not to be an adequate technique to study the ion-shaping process of Au NPs in a-$SiN_{1.06}$. The difficulty to control the size distribution without introducing undesired effects in the matrix material such as voids or an amorphous-to-crystalline phase transformation represents a challenge. To comprehend the differences between the ion-shaping process between a-$SiN_{1.06}$ and a-$SiO_{1.9}$, it is desirable to deal with similar NP size distributions. For these reasons, a new approach to create single layers of Au NPs with a larger control over their size is presented in this section as an alternative to ion beam synthesis. The proposed methodology is motivated by that described by Schmidt *et al.* [162, 293] using simultaneous depositions of a-SiO_2 and Ge by DC magnetron sputtering.

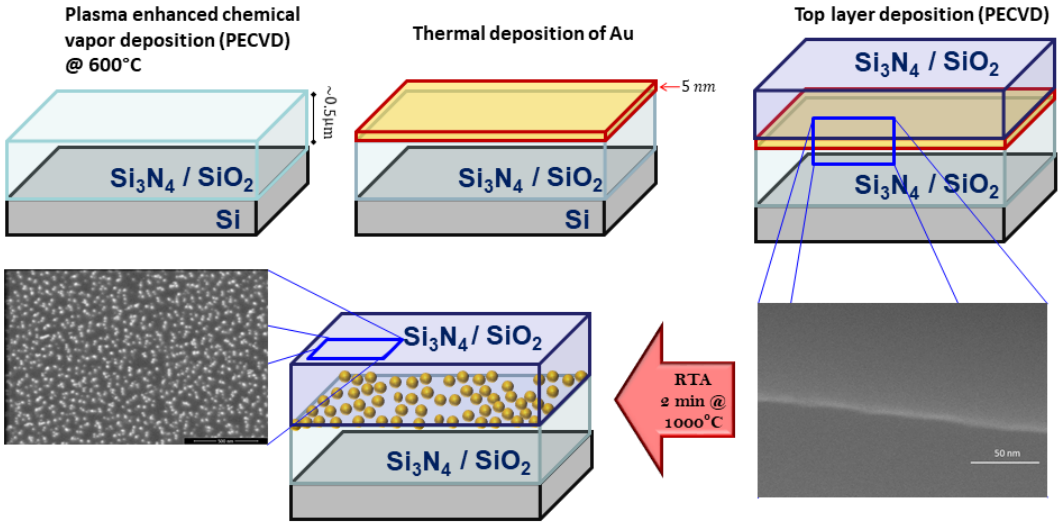

Figure 6.11: *Schematic of the sequential depositions using PECVD a-$SiN_{1.06}$ and a-$SiO_{1.9}$ and thermal deposition of a very thin Au layer. After thermal annealing, a high-density single layer of Au NPs is formed. Cross-sectional and plan view SEM micrographs have been added to exemplify the continuous Au layer formed after deposition of the top layer and the NP density after RTA, respectively.*

Te procedure is summarized in Figure 6.11 and consists of a deposition of an initial thin layer of a-$SiN_{1.06}$ or a-$SiO_{1.9}$ by PECVD with a thickness of up to 500 nm. The characterisation of the physical properties and deposition conditions of the two layers have been reported elsewhere [95, 252] and in more detail in section 3.1. This is followed by the deposition of a very thin (5 nm) Au layer by thermal evaporation, as seen by SEM in Figure 6.11. The metallic thin layer is then covered by a second layer of a-$SiO_{1.9}$ or a-$SiN_{1.06}$ PECVD with a thickness of 500 nm. While the thin Au layer in Figure 6.11 appears to be continuous, the formation of islands or small clusters due to the temperatures involved during the deposition of the top layer cannot be ruled out. As shown in the schematic, the use of PECVD allows the deposition of four combinations of bottom and top layers: a-$SiN_{1.06}$/a-$SiN_{1.06}$, a-$SiO_{1.9}$/a-$SiO_{1.9}$, a-$SiO_{1.9}$/a-$SiN_{1.06}$ and a-$SiN_{1.06}$/a-$SiO_{1.9}$ (Figure 6.12). After deposition of the top layer, the samples are annealed in an AET RX rapid thermal processor at 1000 °C in a N_2 atmosphere for two minutes. At temperatures close to the melting point of

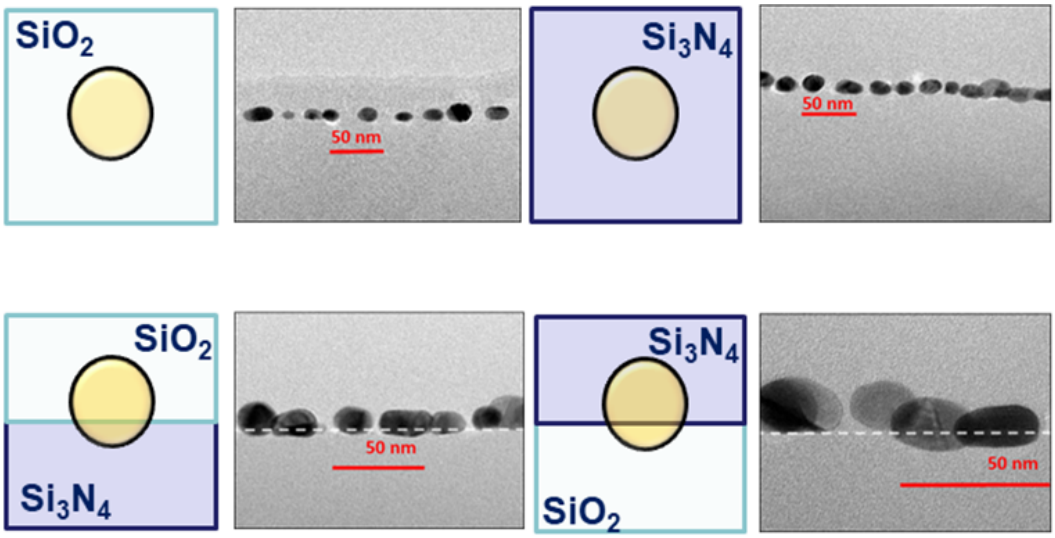

Figure 6.12: *Schematic and TEM micrographs of the cross-sectional cut of Au NPs formed in a-$SiO_{1.9}$, a-$SiN_{1.06}$ and at the two possible interface combinations. Dashed lines were added to highlight the relative position of the interface.*

Au, the thin Au layer transforms into Au droplets by spinodal dewetting, becoming polycrystalline after re-solidification (Figure 6.12). In figure 6.11, plan view by SEM in DF mode shows the high density of Au NPs formed. As can be seen in Figure 6.12, while the deposition of the top layer at 600 °C may induce the formation of small clusters it appears that it does not lead to major differences in the size distributions or the geometry of the Au NPs after the RTA step.

a-$SiN_{1.06}$/a-$SiN_{1.06}$		a-$SiO_{1.9}$/a-$SiO_{1.9}$		a-$SiO_{1.9}$/a-$SiN_{1.06}$		a-$SiN_{1.06}$/a-$SiO_{1.9}$	
L (nm)	W (nm)	L (nm)	W (nm)	L (nm)	W (nm)	L (nm)	W (nm)
20.2 ± 3.9	16.0 ± 2.5	19.9 ± 7.1	16.0 ± 4.5	18.8 ± 4.1	15.9 ± 2.9	19.0 ± 4.3	17.0 ± 3.6

Table 6.4: *Parallel and perpendicular axis dimensions of Au NPs formed for the arrangements presented in Figure 6.12. The uncertainties correspond to the standard deviation of a normal distribution.*

The formed Au NPs exhibit a spheroidal geometry, which can be described by two axes: the parallel (width) and the perpendicular (length) to the surface. Cross-sectional TEM was carried out to characterize the parallel and perpendicular dimensions of Au NPs formed in the four possible deposition combinations. The

values are summarized in Table 6.4. After annealing, only small differences between the parallel and perpendicular axis of the formed Au NPs are observed for the four different configurations, exhibiting a mean size of $\sim$ 20 and 16 nm for the parallel and perpendicular axis, respectively, while differences between the different configurations are below 10 %. Furthermore, the size distribution of Au NPs did not exhibit a strong dependence on the surrounding medium and thus, the elongation process can be directly compared between all configurations. When the NPs are located at the interface of a-$SiN_{1.06}$ and a-$SiO_{1.9}$, TEM micrographs show that the NPs are not located right at the interface of the two materials but exhibit a small shift into the top layer, creating an asymmetrical cover of the NP. As seen in Figure 6.12, the layer deposited on top is the predominant embedding medium, with an average shift of the NPs of 5 $\pm$ 1.5 nm upwards. This phenomenon still require further study, however, one possible pathway for the asymmetrical configuration can be the occurrence of dewetting during the deposition of the top layer, which occurs at 600 °C between 5 and 10 minutes, before the RTA step. The effect of the asymmetry on the ion-shaping process will be further discussed in the next chapter as it plays an important role in the final geometry of the irradiated Au NPs.

6.5 Summary

In conclusion, in this section a new methodology for the formation of Au NPs of the dimensions required for the study of the ion shaping process was presented, where detrimental effects from ion beam synthesis are avoided. The methodology can be used to produce large areas of NPs. Furthermore, the use of PECVD for the deposition of the insulating layers permits the study of different processes at the interface of a-$SiN_{1.06}$ and a-$SiO_{1.9}$ and can be extended to other a-SiO_xN_y compositions.

Chapter 7

Ion-shaping of Au nanoparticles in amorphous silicon dioxide, silicon nitride and at their interface

This chapter reports on the shape transformation of nearly spherical Au NPs when embedded in, and at the interface of a-$SiO_{1.9}$ and a-$SiN_{1.06}$ thin films upon irradiation with 185 MeV Au ions at fluences ranging from 0.3 to 30 $\times$ 10^{13} cm^{-2}. TEM and HAADF microscopy in scanning transmission electron microscopy (STEM) mode were used to study the ion shaping process. The former allows to follow the change in geometry, size and structure, while the latter reveals information about void and nanosatellite formation associated with the process. For Au NPs embedded in a single layer, a lower elongation rate for a-$SiN_{1.06}$ was found in comparison to a-$SiO_{1.9}$. When at the interface of the two materials, TEM micrographs show a preferential elongation towards a-$SiO_{1.9}$. The difference in elongation rates between a-$SiN_{1.06}$ and a-$SiO_{1.9}$, as well as the asymmetric behaviour when located at the interface were interpreted in terms of the three-dimensional version of the inelastic thermal spike (i-TS) model. Using the bulk thermo-physical properties, the calculations show good agreement with the experimental observations and reveal a correlation between the thermal profile and the resulting NP geometry.

7.1 Introduction

Much research on metallic nanostructures has been carried out in the past decades due to the advent of many promising applications using the coupling between photons and the conduction electrons at metal interfaces in the near ultraviolet, visible and near-infra red (NUV-Vis-NIR) range, a field known as plasmonics [294,295]. Plasmonic devices have attracted significant interest because of the possibility of sub wavelength confinement of light and the local intensity enhancement of electromagnetic fields. The former is important for the development of optical metamaterials [296–298], and light manipulation in on-chip nano-antennas [299], among others. The latter, on the other hand, has seen major applications in areas such as surface enhanced spectroscopy (SES) [300], bio-sensing [301, 302], near-field imaging [303], solar cells [304, 305], and nanolasers [306].

A special focus has been set on the design of metal-dielectric nanocomposites because their interesting optical response can be tuned by engineering the volume, geometry, orientation, metal species and the dielectric function of the surrounding medium [50]. Dielectric materials containing embedded metallic nanostructures with controlled anisotropy are of great interest for a broad range of applications. For example, anisotropic magnetic NPs embedded in a non-magnetic medium are used in storage technologies as they can overcome the superparamagnetic instability and allow high density recording with low exchange coupling of magnetic grains [4, 307, 308]. They have also been used to manipulate light-matter interactions arising from the coupling of oscillating external electromagnetic fields with the conduction electrons in metallic NPs, known as localized surface plasmon resonances (LSPRs). By controlling the NP anisotropy, it is possible to modify the linear and nonlinear optical response of the host material as their response is dependent on the size and geometry of the NPs. In particular, metallic NPs of different shapes have found applications as nano-antennas to couple near- and far-fields, to store energy in the free electron movement, and manipulate light at the nanoscale [26,65,156,272,309].

While many fabrication methods for metal-dielectric nanocomposites are available (among the most widespread are: chemical synthesis of metal colloids and core-shell particles, self-organization, electron beam lithography and nano imprinting) [300], ion irradiation of metallic NPs with swift heavy-ions has demonstrated the possibility to transform spherical NPs into well-aligned and high aspect-ratio nano-rods while embedded in a dielectric medium, a process often termed 'ion-shaping' [3, 4]. Ion-shaping offers certain advantages for plasmonic device fabrication, motivating the extension of our understanding of the physical processes underlying the shape transformation, the role of the different parameters involved and their behaviour in different dielectric materials.

Dielectric materials exhibit strong electron-phonon coupling which leads to the formation of so-called thermal spikes and the formation of ion-tracks when subjected to swift heavy-ion irradiation, as explained in section 2.5. On the other hand, metals exhibit a low energy transfer efficiency and a high electron diffusion and, as a result, the formation of a thermal spike is commonly inhibited [67].

In the case of the ion passing through a metallic NP while traversing the dielectric medium, an ion track is created around the NP, along or near its axis. Inside the NP, the energetic electronic cloud diffuses radially outwards from the ion's trajectory reaching the particle/dielectric boundary. At the interface, due to the stronger electron-phonon coupling of the surrounding dielectric matrix, the temperature increases, leading to an outer-boundary heating scenario followed by a partial or total melt of the NP [2, 52]. If the energy deposited by the ion surpasses a material-dependent threshold, elongation can be expected by preferential movement of the molten material into the ion track region [51].

The ion-induced shape transformation process of metal NPs has been studied predominantly with a-SiO_2 as the host matrix with various metallic species such as Au [117, 123, 146, 150–152], Ag [66, 153], Co [4], Ni [154, 155], Zn [156–158], V [159], and metal alloys [160, 161]. While the ion-shaping process is still not fully understood,

in a-SiO_2 it has been recently suggested that the elongation process of Au NPs takes place by diffusion into the under-dense core region formed in the ion track surrounding the NP [51]. Furthermore, the dimensions of the ion track region were associated with the upper limit of the saturation width observed in metallic NPs, where depending on the metal species it could be smaller [155]. Theses observations opened up a debate whether the formation of an under-dense ion track core region is a necessary requirement for elongation [51, 100, 123, 155]. Up to now, very little work has been done in dielectric materials other than a-SiO_2 [26]. As the plasmonic response of theses systems is dependent on the dielectric function of the host matrix [50], it is highly desirable to extend the approach developed for a-SiO_2 to other dielectric materials. Furthermore, the relationship between the NP and the track-core dimensions as well as the thermal spike lifetime have not yet been discussed in the context of the ion-shaping process. Experiments involving metallic NPs at the interface of two dielectrics can help to understand the effect of the ion track under-dense core region and the thermal spike lifetime, yielding a better fundamental understanding of the ion-shaping process, which can represent a step forward for the design of new plasmonic devices.

The present chapter reports on the ion-shaping process of Au NPs embedded in a-$SiO_{1.9}$, a-$SiN_{1.06}$ and at the interface of the two materials. Ion tracks in a-$SiO_{1.9}$ and a-$SiN_{1.06}$ present a very similar morphology (see section 5.3.1), with the difference that a-$SiN_{1.06}$ shows a higher density change compared to a-$SiO_{1.9}$, yet with smaller total ion track dimensions. The study has been divided in three subsections: the first and second subsections report on the ion-shaping of Au NPs while embedded in a-$SiO_{1.9}$ or a-$SiN_{1.06}$, and at the interface of the two dielectric materials. The NP shape and size evolution was characterized by TEM and HAADF in STEM mode prior to, and after irradiation with 0.3, 3 and 10 $\times$ 10^{13} cm^{-2}. The experimental observations are accompanied by calculations using the three dimensional version of the i-TS model. Differences in the thermal properties, as well as the strength of the electron-phonon coupling between the two materials are proposed as potential driving forces for the different shaping rates observed. Finally, experimental results on the confinement of the ion-shaping process of Au NPs in a thin a-$SiO_{1.9}$ layer sandwiched between two

a-$SiN_{1.06}$ layers are presented.

7.2 Ion-shaping of Au NPs in amorphous silicon dioxide and silicon nitride

Cross-section TEM micrographs of Au NPs embedded in a-$SiO_{1.9}$ and a-$SiN_{1.06}$ before and after irradiation with 185 MeV Au ions at different fluences are shown in figures 7.1 (a) and (b), respectively. The samples consist of Au NPs synthesized by depositing two layers of a-$SiO_{1.9}$ (or a-$SiN_{1.06}$ of 500 nm thickness, with a 5 nm thick Au layer in-between and subsequent rapid thermal annealing (RTA) (see section 6.4). At a total layer thickness of ~ 1 μm the electronic energy-loss rate does not change significantly and can be estimated by the surface values using the SRIM code [92], being 16.3, 50.0 and 20.9 keV/nm for a-$SiO_{1.9}$, Au and a-$SiN_{1.06}$, respectively (see section 5.3).

Prior to irradiation, the Au NPs exhibit a spheroidal geometry, which can be described by their axes parallel (width) and perpendicular (length) to the sample surface, as discussed in section 6.4. Furthermore, it was shown that the size distribution of both axis only showed a weak dependence on the layer composition. They are about 20 nm in width and 16 nm in length in a-$SiO_{1.9}$ with a difference within $\sim 5\%$ for a-$SiN_{1.06}$.

In the case of a-$SiO_{1.9}$ (Fig. 7.1 (a)), the transformation from spheroids to high aspect-ratio nano-rods with increasing fluence is similar to the elongation observed previously in thermally grown a-SiO_2 [123, 152, 155]. At lower fluences (3×10^{12} cm^{-2}) the NPs become spherical prior to exhibiting clear prolate shapes at higher fluences. After irradiation with a fluence of 3×10^{13} cm^{-2}, the NPs present aspect ratios between 2 and 6, where the average length and width corresponds to 40.6 ± 6.1 and $13.7 \pm 3{,}3$, respectively. At the highest fluence (1×10^{14} cm^{-2}) the prolate NPs become long nano-rods, with mean values of 64.0 ± 18.7 and 7.5 ± 1.6 for the length and width and aspect-ratios between 4 and 16, slightly above the trend observed in elongated Au NPs embedded in a-SiO_2 [152,155]. Accompanying the anisotropic NPs,

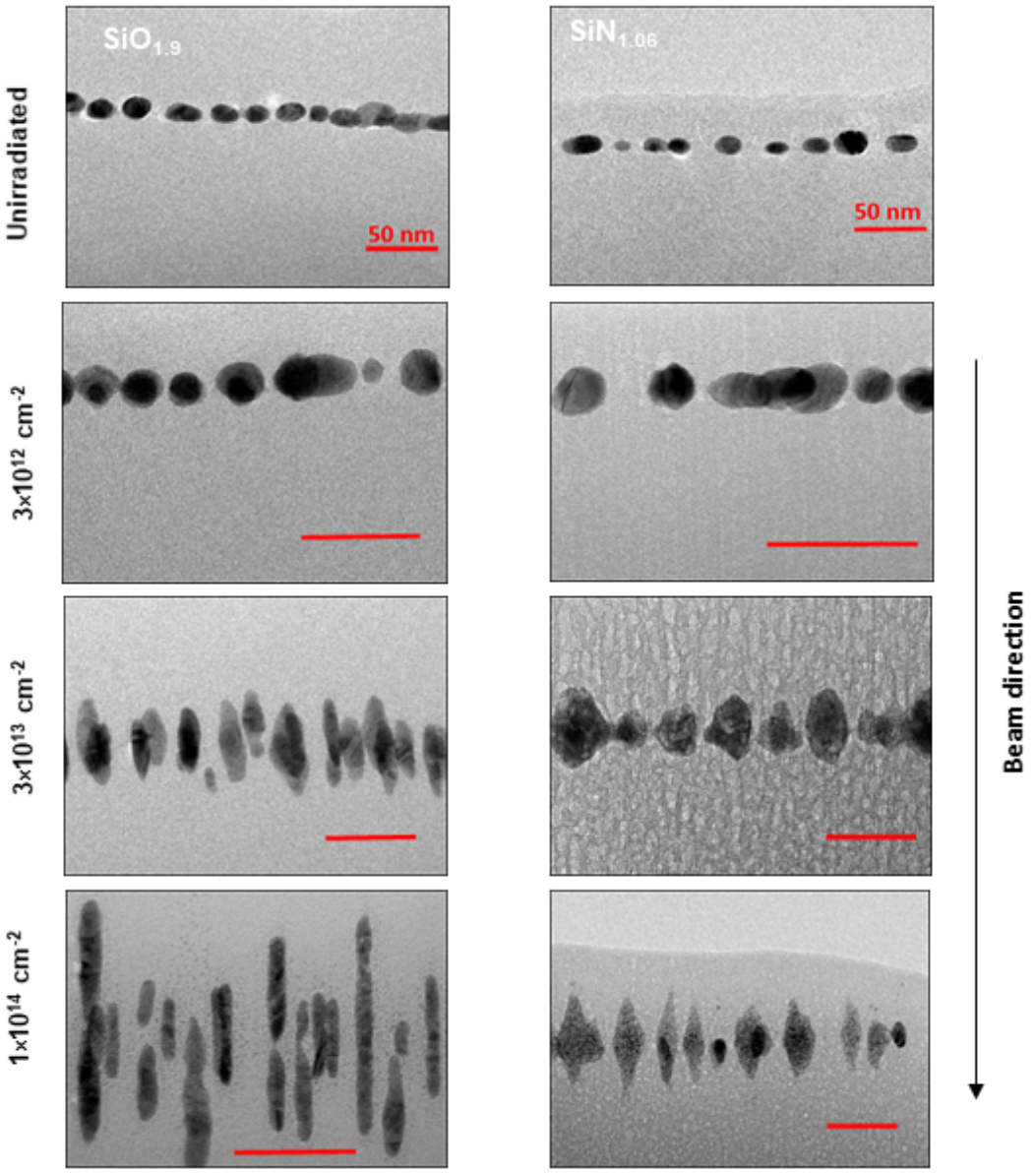

Figure 7.1: *Cross-section TEM (XTEM) images of Au NPs prior to and after irradiation with 185 MeV Au ions with different fluences (as indicated on the panel) for a-$SiO_{1.9}$ (a) and a-$SiN_{1.06}$ (b). The arrow indicates the beam direction for clarity.*

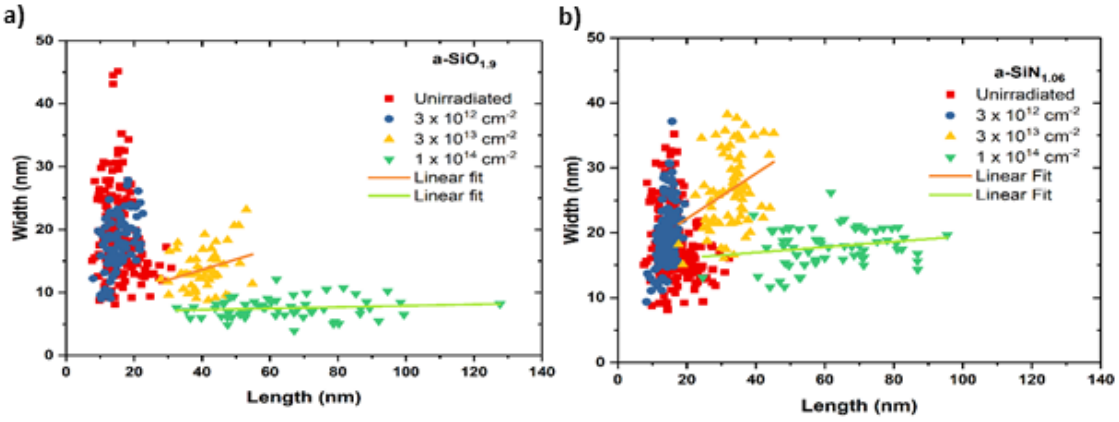

Figure 7.2: *Plot of the correlation between width and length dimensions of Au NPs as determined by XTEM, for different fluences for a-$SiO_{1.9}$ (a) and a-$SiN_{1.06}$ (b).*

the presence of small Au NPs with diameters below 2 nm is observed, also called nano-satellites [155], increasing in density with increasing fluence.

Figure 7.1 (b) shows the shape transformation of Au NPs embedded in a-$SiN_{1.06}$. Upon irradiation, the Au NPs first exhibit a transition from spheroidal shapes towards a spherical geometry at fluences around 3×10^{12} cm^{-2}, similar to the previous case. This is followed by the formation of prolate NPs for 3×10^{13} with aspect ratios between 1 and 2, and mean length and width of 32.6 $\pm$ 5.4 and 26.6 $\pm$ 5.6, respectively. At the highest fluence, the presence of elongated Au NPs with a high aspect ratio (between 2 and 6) can be observed with mean values 62 $\pm$ 14.4 and 17.9 $\pm$ 2.9 nm for length and width, respectively. However, the shape resembles a more rhombic-like geometry instead of a nano-rod. In addition, in the fluence series presented in figure 7.1 (b) it is possible to observe the formation of discontinuous defective, void-like regions accompanying the elongation process. For fluences as low as 3×10^{12} they exhibit a narrow width and are aligned parallel to the beam direction in the a-$SiN_{1.06}$ substrate. With increasing fluences, the width of the defective regions increases yet, retaining the directionality along the ion beam direction.

The relationship between width and length of the Au NPs before and after ion

irradiation for different fluences is plotted in Figures 7.2 (a) and (b) for a-$SiO_{1.9}$ and a-$SiN_{1.06}$, respectively. The continuous solid lines correspond to the mean width as a function of the length of the NP and were added to show the deformation process and the occurrence of the saturation of the width with increasing fluence. When Au NPs are embedded in a-$SiO_{1.9}$, after irradiation with 3×10^{13}, the NPs exhibited an aspect-ratio between 3 and 6 with a mean value of 4. For a-$SiN_{1.06}$ at the same irradiation fluence the aspect-ratio of the Au NPs was determined by comparing the length of the minor (width) and major (length) axes, where lower values, between 1 and 2 with a mean aspect-ratio of 1.4, were observed. At the maximum fluence, the aspect ratios of Au NPs in a-$SiO_{1.9}$ showed values between 4 and 16, and of 2 and 4.5 in the case of a-$SiN_{1.06}$. The former case presents an almost constant width of nearly 8.2 $\pm$ 0.5 nm, which is lower than the value of 10 nm previously reported for thermal SiO_2 [152] but similar to the saturation width observed in Au-Ag alloys [160]. Because the a-$SiO_{1.9}$ layers were deposited by PECVD, they commonly exhibit residual H content as well as stoichiometric and density differences compared to thermal SiO_2. Such differences might be correlated to the difference in the saturation width observed. In the case of a-$SiN_{1.06}$, the saturation of the width is not observed for all the fluences under consideration. Nevertheless, after irradiation with 1×10^{14} the mean relationship between width and length exhibits an almost constant slope, clearly above the saturation width in a-$SiO_{1.9}$.

7.3 Ion-shaping of Au NPs at the interface of amorphous silicon nitride/silicon dioxide

Figures 7.3 (a) and (b) show the cross-section TEM images of Au NPs at the interface of a-$SiO_{1.9}$ and a-$SiN_{1.06}$ layers (top/bottom and vice versa) prior to and after irradiation with 185 MeV Au ions at different fluences. The dashed lines were added to show the position of the interface with respect to the Au NP single layer. Because the total layer thickness corresponds to $\sim$1 μm, similar to the previous subsection, the electronic energy-loss rate is considered constant along the ion trajectory with the

values corresponding to those at the surface.

In the micrographs, the asymmetrical relative position of the NP plane with respect to the interface is evident. It is observed that the top layer forms the main medium surrounding the Au NPs, covering approximately 80% of the NPs surface. Such asymmetry is of great relevance, as briefly described in the introductory section, because the surrounding medium plays a key-role in the ion-shaping process.

Figure 7.3 (a) shows the shape transformation of the Au NPs upon irradiation with a-$SiN_{1.06}$ as the bottom layer and a-$SiO_{1.9}$ as the top layer. At a fluence of 3×10^{12}, we observe that Au NPs become spherical while it appears that the contact area with the bottom layer is reduced. Also, no observable irradiation damage is apparent in the a-$SiO_{1.9}$ region, while the a-$SiN_{1.06}$ layer shows narrow damage regions, similar to those described in the previous section. When the fluence increases to 3×10^{13}, the transformation of the NPs into nano-rods with an aspect ratio between 2 and 4 is observed where elongation mainly proceeds towards the a-$SiO_{1.9}$ layer while exhibiting a flat base at the interface, with very limited diffusion towards the a-$SiN_{1.06}$ layer (within 3-5 nm). Radiation damage formed at the a-$SiN_{1.06}$ layer is also evident, as well as the presence of very thin and long structures along the beam direction in the a-$SiO_{1.9}$ layer, which were not observed in the case Au NPs embedded in a-$SiO_{1.9}$ only. The observed nano-rods exhibit a high aspect-ratio with a mean length of 42.2 $\pm$ 18.1 nm and width of 11.2 $\pm$ 5.2, respectively. When the highest fluence is reached (1×10^{14} cm^{-2}), we observe the transformation of the Au NPs into high aspect ratio nano-rods, comparable to the previous case of a-$SiO_{1.9}$ single layers (with a mean length of 77.1 $\pm$ 24.8 nm and width of 8.6 $\pm$ 2.1, respectively), with some diffusion into the a-$SiN_{1.06}$ layer that shows very irregular shapes. The elongation process is also accompanied by the formation of porosity or voids inside the anisotropic Au NPs, with the majority observed in the NP region close to the a-$SiN_{1.06}$ interface.

In the other configuration (Figure 7.3 (b)), the corresponding XTEM images of Au NPs at the interface of a-$SiO_{1.9}$ and a-$SiN_{1.06}$ (bottom/top) layers prior to and after

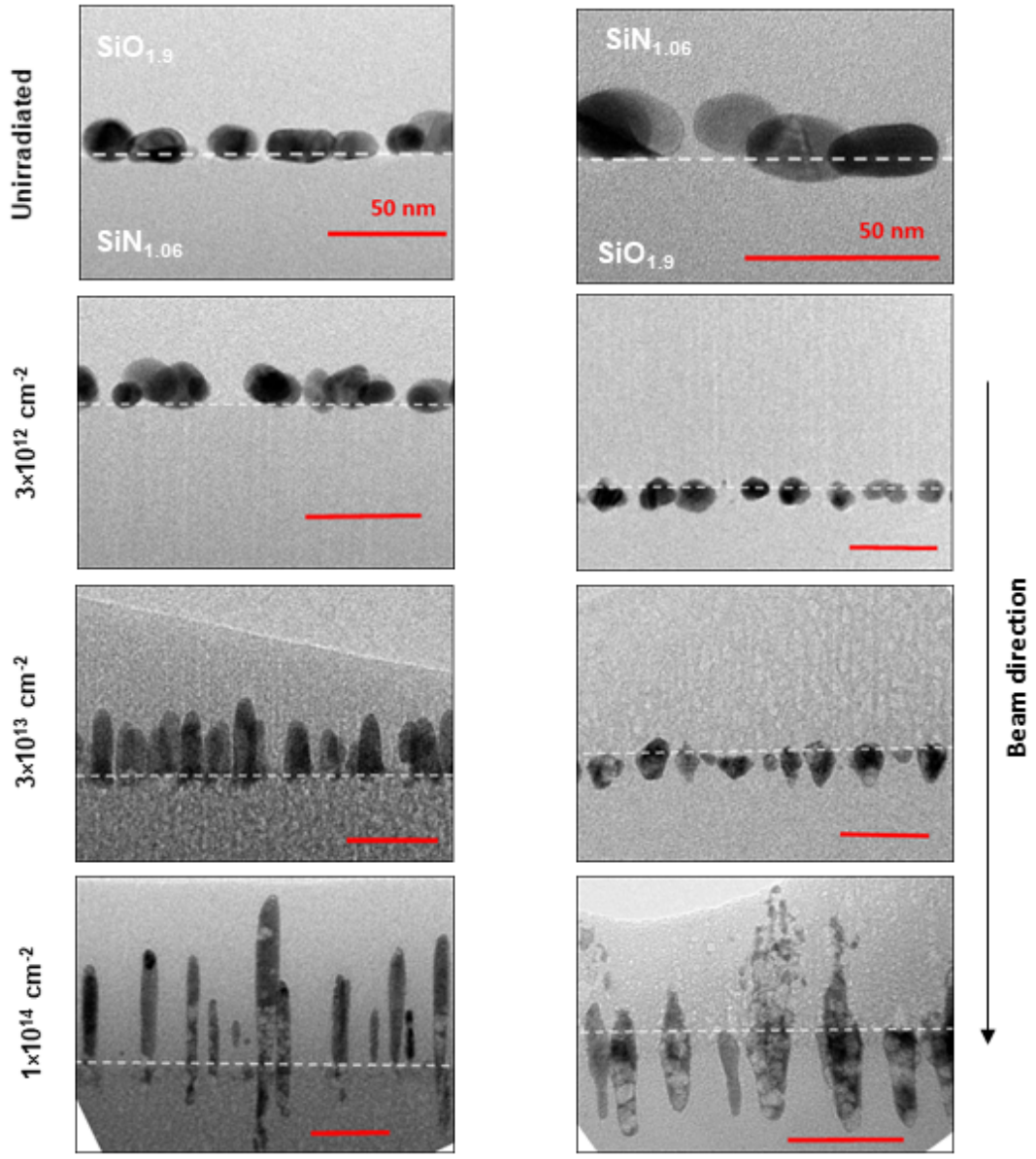

Figure 7.3: *Cross-section TEM (XTEM) images of Au NPs prior to and after irradiation with 185 MeV Au ions with different fluences (as indicated on the panel) located at the interface of a-$SiO_{1.9}$ and a-$SiN_{1.06}$, while being embedded predominantly in a-$SiO_{1.9}$ (a) or a-$SiN_{1.06}$ (b). The arrow indicates the beam direction for clarity.*

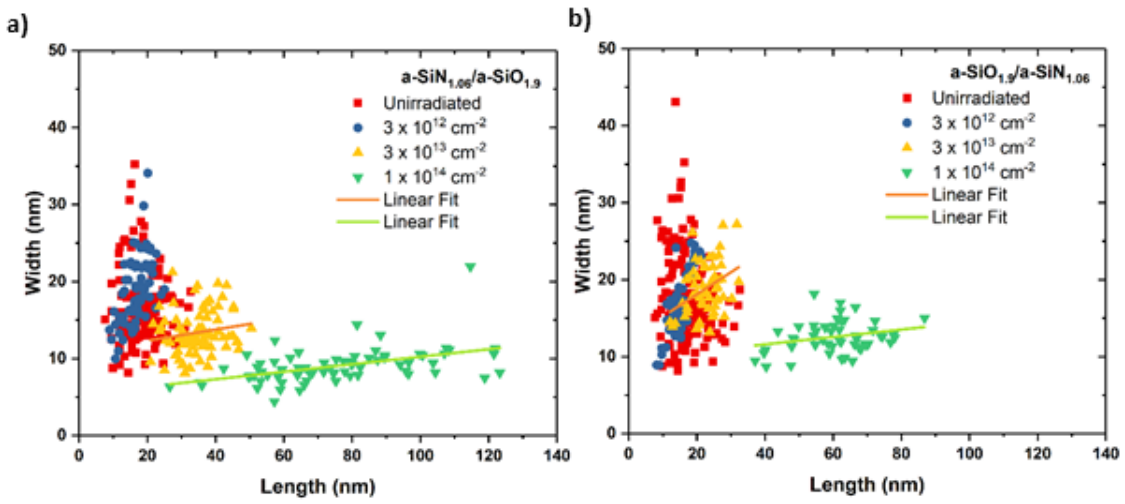

Figure 7.4: *Plot of the correlation between width and length dimensions, as determined by XTEM, while being embedded predominantly in a-$SiO_{1.9}$ (a) or a-$SiN_{1.06}$ (b).*

ion irradiation also exhibit a clear shape transformation with fluence. After irradiation with a fluence of 3×10^{12}, we observe the transformation from spheroids into spheres. This is accompanied by a clear shift into the a-$SiO_{1.9}$ layer. When the fluence increases to 3×10^{13}, the Au NPs are almost completely embedded in the a-$SiO_{1.9}$ layer. They show a transformation towards a prolate geometry with a mean length of 22.7 $\pm$ 4.4 nm and width of 18.9 $\pm$ 3.3 and , respectively while they are aligned with the beam direction, they exhibit rough and sharp edges and a nano-porous appearance. When reaching the maximum irradiation fluence of 1×10^{14}, highly nano-porous nano-rods with a mean aspect ratio of 5 and mean width and length of 12.6 $\pm$ 2.0 and 60.6 $\pm$ 10.7 nm, respectively, can be observed. Most of the NPs exhibit a flat and broad end at the interface with a-$SiN_{1.06}$, yet irregular elongation towards the top layer was observed in some cases. In those cases, the ion-induced damage in the a-$SiN_{1.06}$ layer may facilitate the Au diffusion towards this region noting that the elongation into this layer does not resemble the geometry observed in elongated NPs in a-$SiN_{1.06}$. For example, in figure 7.3 (b), fragmented and discontinuous Au structures in a-$SiN_{1.06}$ with irregular shapes can be observed that resemble the ion induced damage structure in the a-$SiN_{1.06}$.

Figure 7.4 (a) and (b) show the correlation between width and length of the Au NPs measured by XTEM for the two multi-layered systems after consideration of at least 250 NPs in each case, similar to the previous section. Due to the presence of irregular NP shapes, the width of each NP was measured at a distance of $\sim$ 5 nm from the interface (dashed lines) into the a-$SiO_{1.9}$ layer. On the other hand, the NP length was determined considering a straight line connecting both ends of the NP unless one end is not well defined, as for the NP at the centre of the TEM image in figure 7.3 (b) for the highest fluence. In this case the length was taken as the distance between the interface and the end of the NP in the a-$SiO_{1.9}$ layer. The solid lines represent the correlation trends for the fluences where clear elongation was observed. When a-$SiO_{1.9}$ is the main surrounding medium (Fig. 7.4 (a)), the Au NPs present a spherical geometry after irradiation with 3×10^{12} where an aspect-ratio of nearly 1 was determined. After irradiation with a fluence of 3×10^{13} cm^{-2}, a reduction in the width is observed accompanied by an increase in the length of the NPs, exhibiting an aspect-ratio between 2 and 3.5, below the values observed for Au NPs in a-$SiO_{1.9}$. For the highest fluence, the Au NPs become nano-rods with aspect-ratios between 4 and 14, similar to those of Au NPs in a-$SiO_{1.9}$ but the slope clearly differs from that in Figure 7.2 (a). Nevertheless, the values of the width measured are smaller or equal to 10 nm, suggesting a similar saturation of the width value to that of a-$SiO_{1.9}$. The difference in the slope might be a consequence of the NP elongation occurring in only one direction. In the other case, when a-$SiN_{1.06}$ is the main embedding medium (Fig. 7.4 (b)), nearly spherical NPs are observed after irradiation with 3×10^{12} cm^{-2}, similar to the previous case however, with increasing fluence (3×10^{13} cm^{-2}) Au NPs present anaspect-ratio between 1 and 1.5. At the highest fluence, the NPs show a clear increase in the aspect-ratio values between 4 and 8, lower than any of the previously presented cases nevertheless, the trend exhibits a similar slope as in Fig. 7.4 (a) but with higher width values ($\sim$ 12 nm). Such behaviour agrees well with the necessity of higher fluences to reach the saturation of the width due to the shift into the a-$SiO_{1.9}$ layer.

Based on the presented evidence on the ion-shape transformation of Au NPs

embedded in different media it has been found that: (i) Au NPs do elongate when embedded in a-$SiN_{1.06}$, (ii) the process is less efficient in a-$SiN_{1.06}$ and the geometry of the elongated Au NPs does not resemble high aspect-ratio nano-rods as in a-$SiO_{1.9}$, (iii) when the Au NPs are located at the interface of a-$SiO_{1.9}$ and a-$SiN_{1.06}$ they shift towards and preferentially elongates in the a-$SiO_{1.9}$ layer (iv) when Au NPs are embedded in or are in contact with the a-$SiN_{1.06}$ layer, the elongated NPs show nano-porosity, (v) defective void-like regions are formed in a-$SiN_{1.06}$ at higher fluences, and to a lesser extent in a-$SiO_{1.9}$ when in contact with a-$SiN_{1.06}$, while retaining the directionality along the ion beam direction. These structures are possibly empty regions or voids, yet can possibly be related to the formation of N_2 nano-bubbles. To better understand the ion-shaping process in the four systems presented, numerical 3D-iTS calculations were carried out. Such calculations provide an estimate of the time evolution of the temperature profile around the NP, which in a-SiO_2 it is known to have an influence on the ion-shaping process and thus, help to identify differences in the material response that can help explain the presented experimental observations.

7.4 Effect of the thermo-physical materials properties on the ion-shaping process

The time-evolution of the temperature profile around one Au NP while embedded in a-$SiO_{1.9}$, a-$SiN_{1.06}$ or at the interface of the two materials was calculated using the three-dimensional version of the i-TS model (3D-iTS) [2], to provide a further insight into the differences of the elongation process in the different dielectric media. The energy-loss rate was considered the same as those estimated by the SRIM code [92] for a-$SiO_{1.9}$, a-$SiN_{1.06}$ and Au at the surface, to match the experimental conditions. The calculations were performed considering a spherical Au NP with a diameter of 16 nm centred in a cubic cell of 60 $\times$ 60 $\times$ 60 nm^3 (see Fig. 7.5 (a) and (b)). The surrounding medium was approximated by the known bulk properties of a-SiO_2, and a-Si_3N_4 as expressed in [95] under the considerations outlined in [2] (see section 2.3). In the case of Au, bulk values are considered as in [2], in particular as thermo-physical

corrections for the dimensions of the NPs do not lead to relevant corrections [155]. The electron-phonon coupling values considered are the same as those presented in section 5.3.1.

Ion tracks in a-$SiN_{1.06}$ and a-$SiO_{1.9}$ present a very similar morphology, an under-dense core surrounded by an over-dense shell connected by a transition region (see section 5.3.1), with the difference that a-$SiN_{1.06}$ shows a higher density change (about four times larger) compared to a-$SiO_{1.9}$, yet with smaller total ion track radii, 4.2 ± 0.1 in comparison to 5.4 ± 0.1 nm in a-$SiO_{1.9}$ in the case of 185 MeV Au ion irradiation. From previous calculations using the one dimensional version of the iTS model to explain track formation in a-SiO_2 and a-Si_3N_4 we have observed two fundamental differences in the thermal spike evolution: (i) the difference in the optical band gap is responsible for the variation in the ion track dimensions between the two materials as it leads to an electron-phonon coupling value in a-Si_3N_4 of less than half the value of a-SiO_2, and (ii) the higher thermal conductivity of a-Si_3N_4 (nearly one order of magnitude higher than a-SiO_2) causes that the melting temperature is exceeded for less than half of the time compared to that in a-SiO_2. It can thus be expected that the thermal environment experienced by each Au NP depends on the embedding medium.

7.4.1 Amorphous silicon nitride and silicon dioxide

Figure 7.5 (a) and (b) show three cross-sectional snapshots of the 3D-iTS calculations at times t=0.1, 1 and 10 ps of the lattice temperature after the passage of an energetic ion through the centre of the Au NP while embedded in a-SiO_2 and a-Si_3N_4, respectively. At t=0.1 ps, the characteristic thermal profile of the thermal spike governing the ion track formation process can be observed in both dielectric media. Continuous lines have been added to indicate the boundary region for the melting temperature of a-SiO_2 (green), a-Si_3N_4 (blue) and Au (dark yellow). In a-SiO_2 (Fig. 7.5 (a)), a region above the melting temperature of Au can be observed around the NP boundary, displaying an early stage of the heating process that moves

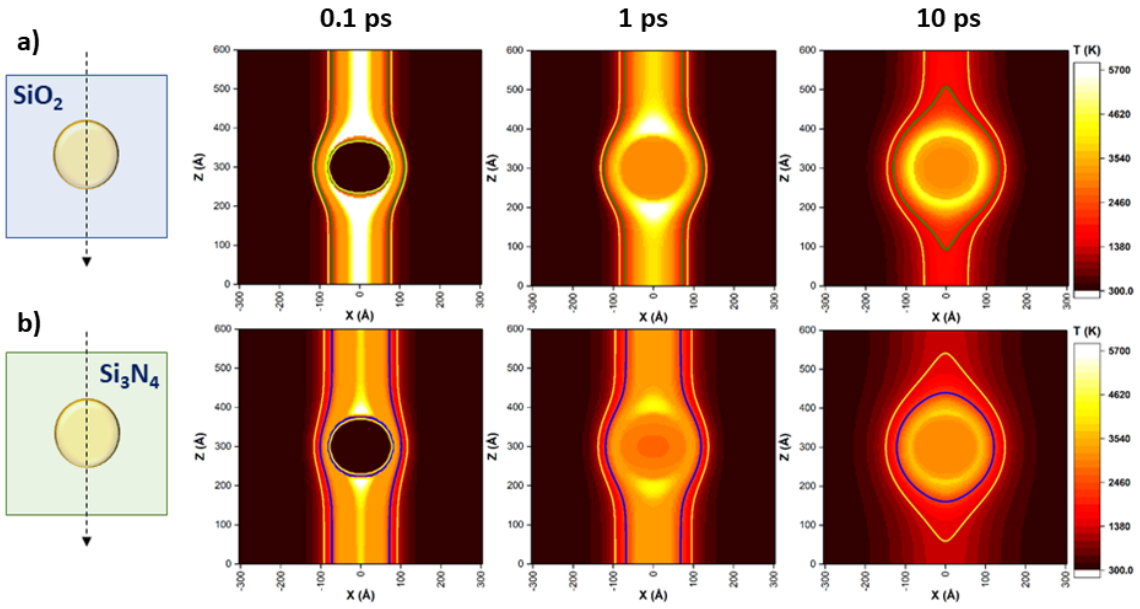

Figure 7.5: *Configuration of the 3D-iTS calculation cell and snapshots of the three-dimensional thermal evolution of a Au NP of 16 nm in diameter while embedded in a-$SiO_{1.9}$ (a) or a-$SiN_{1.06}$ (b). Solid lines were added to show the region surpassing the melting point of a-$SiN_{1.06}$ (dark blue), a-$SiO_{1.9}$ (green) and Au (dark yellow).*

from the boundary towards the centre of the NP. On the two sides of the NP in direct contact with the thermal spike, a molten region of the NP is observed. For a-Si_3N_4, the lower electron-phonon coupling strength leads to a lower temperature environment surrounding the Au NP, thus at this stage, the NP remains completely solid.

At t=1 ps, where both dielectric media are at the early stage of the cooling process, heating and melting of the NP is apparent. In the case of a-SiO_2, the Au NP is completely molten and the temperature is almost constant within the NP. Due to the low thermal conductivity of a-SiO_2 the formation of an extended region around the NP with a temperature significantly higher than the melting point of a-SiO_2 is apparent. This area extends nearly 10 nm beyond the NP boundary in the perpendicular direction to the ion path and nearly 20 nm at the zone in contact with the ion track. This region creates a thermal gradient towards the inner region of the ion track. The thermal profile formed around the Au NP in a-Si_3N_4 resembles a similar

shape to that for a-SiO_2, yet the maximum temperatures reached are significantly lower. While the NP is molten, too, the centre remains cooler with respect to the boundary and thus the energy is not homogeneously distributed within the NP volume.

At t=10 ps, the thermal spike is in the latest stage of the cooling period for the two dielectric materials. At this stage, it is observed that the temperature within the ion track region in a-SiO_2 has fallen below the mean melting point of a-SiO_2 but remains above that of Au. At the boundary of the NP, an anisotropic region remains above the mean melting point of a-SiO_2 exhibiting an 'eye' shape. For the other case, in a-Si_3N_4, the region that corresponds to the ion track has cooled down below the melting point of Au. Around the NP an anisotropic region is formed, too, with an 'eye' shape, but within this region the temperature remains above the melting point of Au while a nearly spherical region closer to the NP boundary (of about 5 nm in thickness) remains above the mean melting point of a-Si_3N_4.

In previous MD simulations (Leino *et al.* [51, 310]) it was proposed that the most relevant stage of the ion-shaping mechanism occurs between 5 and 20 ps, when the Au NP expands by a longitudinal flow into the under-dense core of the formed ion track. In their description, the Au NP melts during the first ps while an ion track is formed within the same timescale. Further MD simulations were carried out in the same study to provide insight into the saturation width and its dependence on the ion track radius in a-SiO_2. According to their findings, when the width of the track core is smaller than the diameter of the spherical NPs, or the width of the elongated NP (as with increasing fluence), the NP expands and diffuses more efficiently along the perpendicular than the parallel direction to the beam resulting in an increase in the aspect-ratio. This behaviour continuous until the width of the NP approaches the width of the under-dense track core, when the NP expands in all directions with the same efficiency. To identify the level of agreement between the MD simulations with the current experimental results and the differences with the ion-shaping process in a-Si_3N_4, the results of the 3D-iTS calculations are analysed in more detail.

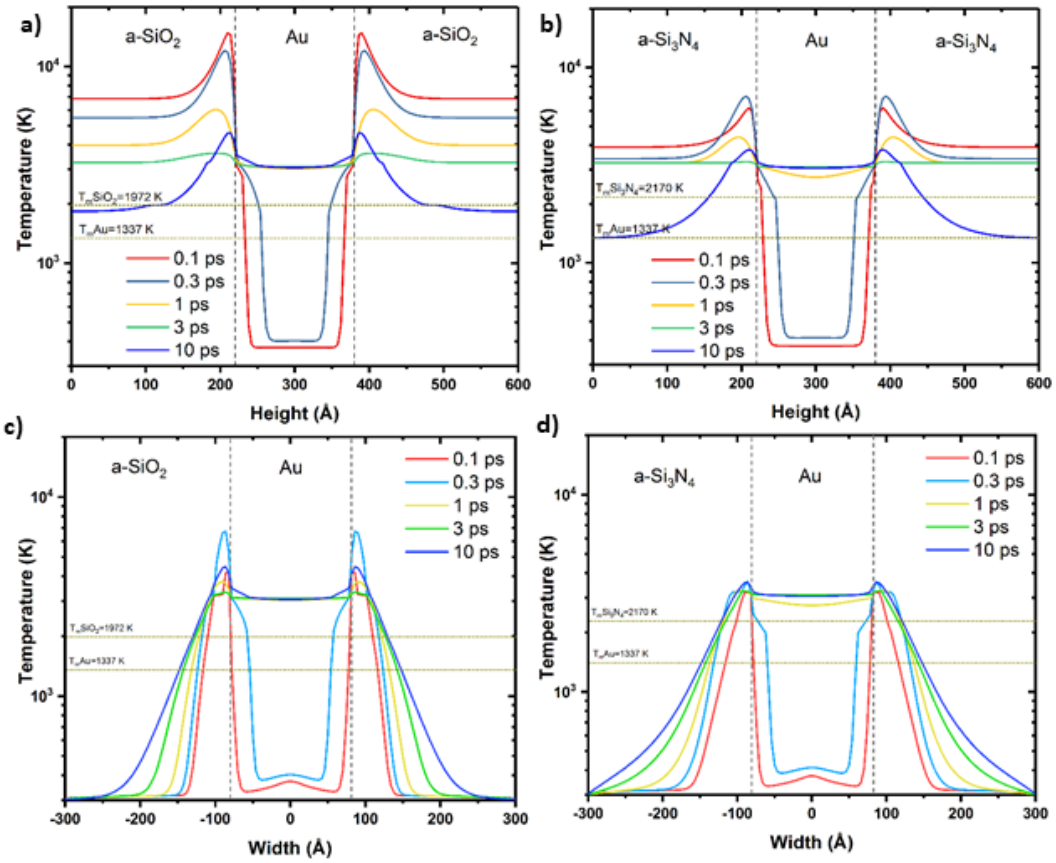

Figure 7.6: *Longitudinal (a) and (b) and transversal (c) and (d) temperature profile at different times for one Au NP embedded in a-SiO_2 (a) and (c), and a-Si_3N_4 (b) and (d), respectively. Dashed lines represent the position of the Au/dielectric boundary while dotted lines have been added to outline the melting point of Au and the mean melting point of a-SiO_2 and a-Si_3N_4.*

Figures 7.6 (a) and (b) shows the longitudinal temperatures, centred at the cell axis, for the Au NP embedded in a-SiO_2 and a-Si_3N_4, respectively, at relevant times based on the 3D-iTS calculations. Dashed lines represent the position of the metal/dielectric boundary while the dotted lines where added for reference with the known melting temperatures of Au, a-SiO_2 and a-Si_3N_4, respectively. From the plots it can be seen that the ion track is formed before the heating and melting of the Au NP in both a-SiO_2 and a-Si_3N_4. Also, an increase in the temperature in the dielectric layer at the metal/dielectric boundary above that of the metallic NP is observed. Such increase is related to what Dufour *et al.* [2] identified as the outer boundary heating scenario, where the energetic electrons generated during the ion passage in the Au NP axis spread out radially outwards transferring kinetic energy to the Au atoms before reaching the metal/dielectric boundary. While the energy transfer to the Au is inefficient, at the boundary, the electrons transfer their kinetic energy more efficiently due to a higher electron-phonon coupling in a-SiO_2 and a-Si_3N_4 with respect to Au, resulting in the increase of the dielectric lattice temperature at the boundary. This leads to increased heating of the NP at the interface due to the high thermal conductivity of Au, as seen in the plots, from the boundary to the centre of the NP. This is also evident when the corresponding equatorial temperature profiles are plotted for the two systems (Figs. 7.6 (c) and (d), for a-SiO_2 and a-Si_3N_4, respectively) where the increase in temperature of the dielectric boundary is due to the outer-boundary heating scenario. Furthermore, when comparing the perpendicular and parallel to the beam temperature profiles (Fig. 7.6 (a) and (c)) in a-SiO_2 and in a-Si_3N_4 (Fig. 7.6 (b) and (d)), respectively), it can be seen that for both systems the temperature along the meridional direction at the metal/dielectric boundary is several times higher than at the equatorial direction up to 10 ps.

The temperature profiles calculated using the 3D-iTS model agrees with MD simulations regarding the Au NP being molten for longer times than the ion track, longer than 20 ps according to MD simulations [51]. On the other hand, the 3D-iTS calculations show that for a-SiO_2 the ion track cools down below the glass transition temperature before 20 ps, closer to 10 ps, and it is the anisotropic region around the

boundary that remains above the mean melting point of the corresponding dielectric for longer times. In the 'eye' shaped region of the anisotropic thermal profile surrounding the Au NP, there is a narrow region at the meridional site of the NP which remains above the mean melting point of a-SiO_2 longer than 10 ps. As its position matches the location of the under-dense track core, the NP might remain expanding for timescales longer than 10 ps possibly at lower rates. Thermal diffusion along the thermal gradient cannot be ruled out as an additional cause for the anisotropic deformation of the Au NPs. As it is observed in Figures 7.3 (a) and (b), well-aligned voids are formed in both layers (a-$SiO_{1.9}$ and a-$SiN_{1.06}$) while such features were absent in Figure 7.1 (a). This suggests that the timescale at which the temperature inside the ion track remains near and above the melting point of a-SiO_2 is enough for defects formed in a-$SiN_{1.06}$ to diffuse along the thermal gradient into the a-$SiO_{1.9}$ layer, which does not discard the possibility of Au atom diffusion as well. Also, the saturation width observed is equal or similar to the total ion track radial dimensions, which has not been properly addressed by MD simulations. Thus, an under-dense core is not necessarily a requirement for elongations. Therefore, the origin of the elongation of Au NPs might not be solely the result of the thermal spike but a synergetic effect of the outer-boundary heating of the NP and the ion track formation process in a-SiO_2 near the NP.

On the other hand, it is observed that in a-SiO_2 higher temperatures are reached than in a-Si_3N_4, a result of the higher electron-phonon coupling in a-SiO_2. For a-Si_3N_4, within the first 10 ps the ion track cools down below the melting point of Au along the meridional direction. This rapid cooling results in the transformation of the 'eye' shaped anisotropic region surrounding the NP, which remains above the mean melting point of a-Si_3N_4, into an almost isotropic region with a thickness of about 5 nm within the first 10 ps. This is in contrast with the rational description presented by Rizza *et al.* [123] where the presence of a diamond or faceted geometry is linked to a partially molten NP after the passage of an energetic ion when the NP dimension become considerably larger than the total ion track diameter. In the current case, the reduction in the duration of the anisotropic thermal environment surrounding the Au NP in comparison to a-SiO_2 to almost half might be the reason behind the less ef-

ficient shape transformation leading to a rhombic-like geometry with increasing fluence.

The analysis of the elongation process was done by considering the temperature profile in time and space produced by a single ion passing through the center of a Au NP however, this is not fully consistent with the experimental situation. During irradiation, the SHI are homogeneously distributed through the sample and are equally likely to traverse the Au NP at different distances away from the centre. In consequence, the pathway followed by the SHI decreases when the impact occurs further away from the centre and decreases the energy transferred to the NP which can heat up the NP but not necessarily reaching melting [155]. The process has been studied in more detail by Dufour et. al. [2] for Au NPs embedded in a-SiO_2 using the 3D i-TS model, where they suggested that the maximum distance away from the centre at which the SHI can still lead to melting is three quarters of the NP radius. In our case, at that position from the centre the SHI path reduces to $\sim$ 66% of the maximum possible deposited energy. While the numerical calculations of the thermal profile for impacts at different off-centre impact positions are desirable, the relevance of studying the impacts though the NP centre is that it is possible to estimate the maximum deposited energy and thus, the highest temperature achievable by the NP and at the boundary region where it is easier to discover clear trends probably hard to distinguish if the energy deposited is decreased. Furthermore, if we consider an effective radius of 7.5 nm for all samples we can estimate about 5 impacts leading to melting after irradiation to a fluence of 3 $\times$ 10^{12} cm^{-2}, 53 for a fluence to 3 $\times$ 10^{13} cm^{-2} and 177 at 1 $\times$ 10^{14} cm^{-2}. This is without considering any further effect of the greater thermal conductivity of a-Si3N_4 compared to a-SiO_2. Due to the difference in electron-phonon coupling and thermal conductivity, it could be expected a reduced distance away from the centre to melt the Au NP, resulting in less events towards elongation. This is an argument that requires further study and surely will provide more light into the elongation process in different materials.

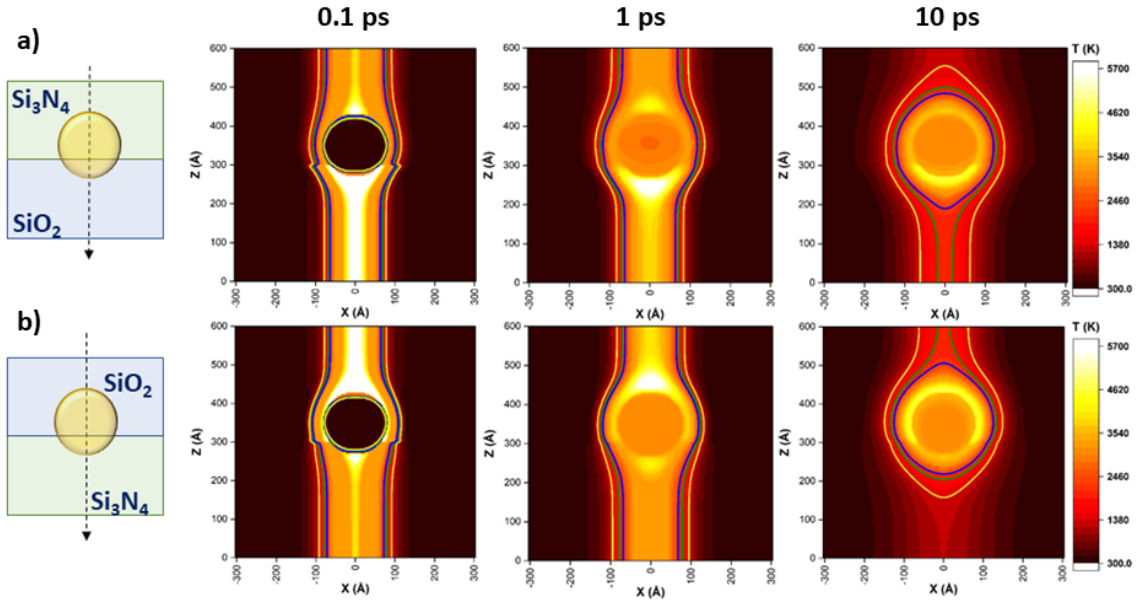

Figure 7.7: *Cross-sectional diagrams and snapshots of the three-dimensional calculations of the thermal evolution of a 20 nm in diameter Au NP while embedded predominantly of a-Si_3N_4 (a) and a-SiO_2 (b) based on the i-TS model, considering the passage of an ion through the axis of the NP. Solid lines were added to signal the region corresponding to the melting point of a-Si_3N_4 (dark blue), a-SiO_2 (light blue) and Au (dark yellow).*

7.4.2 Competing processes at the amorphous silicon dioxide/silicon nitride interface

The preferential shape transformation towards the a-$SiO_{1.9}$ layer observed when Au NPs are located at the interface of the latter and a-$SiN_{1.06}$ can also be rationalized in terms of the 3D-iTS model. Figures 7.7 (a) and (b) show snapshots of the calculated temperature profile at three representative times (0.1, 1 and 10 ps) for the two configurations studied. There is a similarity in the temperature profile along the parallel direction to the beam of the NP for both configurations and thus, a similar ion-shaping efficiency is expected for both configurations differentiated only by the material predominantly surrounding the perpendicular section to the beam of the NP.

In the first case, a-Si_3N_4 is the main surrounding medium and it can be observed that from the early stages (0.1 ps) the Au NP experiences two different temperature

gradients along the ion track. The temperature and the thermal gradient are larger at the Au/a-SiO_2 compared to the Au/a-Si_3N_4 boundary. This behaviour continues for at least t=10 ps. At this time, the temperature inside the ion track decreases below the melting point of a-Si_3N_4 while on the other end there is still a narrow region that extends into the a-SiO_2 layer above the melting point. For the case where a-SiO_2 is the predominant surrounding medium, along the parallel direction to the beam a very similar behaviour is observed as for the first case. As mentioned before, if the migration of Au atoms is governed by the thermal gradient formed at the metal/dielectric longitudinal boundary, the diffusion is favoured towards a-SiO_2 in both cases. The latter is supported by our TEM observations. The corresponding micrographs of samples after irradiation with 3×10^{13} cm^{-2} Au ions do not show an indication of elongation towards a-Si_3N_4. Instead, the deformation process seems to be characterised by the migration of the Au NP towards the a-SiO_2 layer accompanied by the formation of a slightly curved region at the Au/a-Si_3N_4 interface. The absence of nano-satellites supports the idea of a low mobility and diffusivity of Au in a-Si_3N_4 for the first case while for the second, the formation of small NPs around the elongated NP is observed as outlined above for a-SiO_2. As shown in Fig. 7.3 and quantified in Fig. 7.4, the ion-shaping process in this configuration is almost as efficient as when the Au NPs are embedded in a-SiO_2 only.

To better understand the preferential elongation, in Figure 7.8 (a) and (b) the temperature profile in the parallel direction to the beam is plotted for selected times. At around t=0.1 ps, after the passage of the energetic Au ion, an ion track is formed in each layer. Independently, we have characterised the ion track formation in a-$SiO_{1.9}$ and a-$SiN_{1.06}$ layers by SAXS, which under similar irradiation energies exhibit an ion track radius of 5.5 $\pm$ 0.1 nm for a-$SiO_{1.9}$ and 4.1 $\pm$ 0.1 nm for a-$SiN_{1.06}$ with similar morphology, comprised of an under-dense core surrounded by an over-dense shell connected by a smooth transition, where the core dimensions for both materials are very similar (Table 5.3.1). A detailed analysis is available in [56, 311]. As briefly outlined by Leino *et al.* [51], the ion-shaping process of Au NPs is limited by the lifetime of the ion track formation process. In the case of

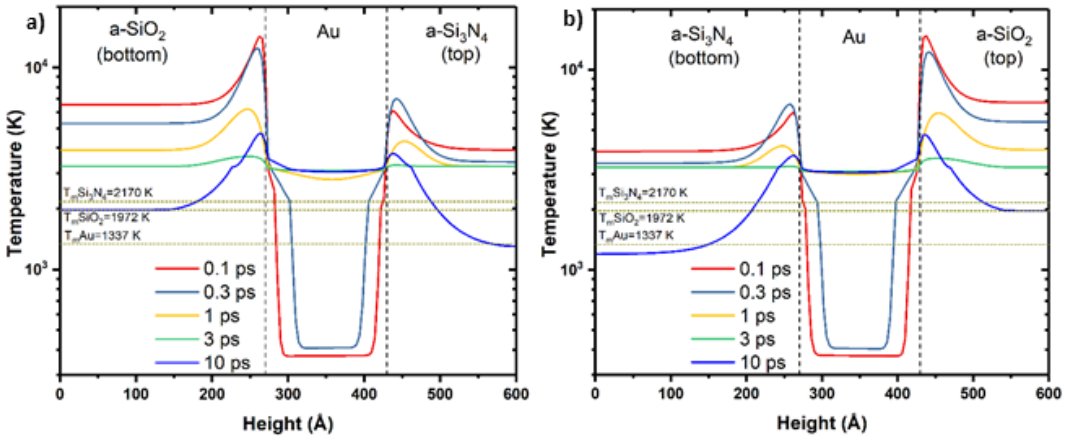

Figure 7.8: *Longitudinal temperature profile along the Au NP axis for the a-Si_3N_4/a-SiO_2 (top/bottom) (a) and a-SiO_2/a-Si_3N_4 (b) layer configuration. Dashed lines have been added to identify the Au/dielectric boundary position, while the horizontal dotted lines represent the melting point of Au, and the mean melting point of a-SiO_2 and a-Si_3N_4.*

a-SiO_2 this occurs within the first 20 ps after the ion passage. For a-Si_3N_4, on the other hand, this process can only occur up to 10 ps [286], thus, it is proposed that the difference in the lifetime should significantly influence the ion-shaping process.

Therefore, based on the numerical calculations of the 3D-iTS model it is possible to outline the following observations: (i) the ion track is formed before the Au NP increases its temperature for both configurations, (ii) the temperature reached and the thermal gradient along the parallel direction to the beam is higher at the Au/a-SiO_2 interface, (iii) at t=10 ps in a-Si_3N_4 the temperature along the ion track direction falls below the melting point while for a-SiO_2, the width of the region along the ion track direction exhibits a temperature above the melting point, which narrows down from about 12 to less than 5 nm. This suggests that in the presence of a NP, the formation of the thermal spike is followed by the outer-boundary heating process of the NP, a process that takes place between 10^{-12} - 10^{-10} s. However, the latter process leads to the formation of a local temperature spike at the metal/dielectric boundary where very high temperatures can be reached. This may explain the low energy threshold

observed for ion shaping of $\sim$ 4 keV/nm in a-SiO_2. As a consequence, the ion-shaping process can take place if the anisotropic thermal profile around the metal/dielectric boundary surpasses the melting temperature of the surrounding medium, and the efficiency is connected to the duration of this process, which is affected by the thermal conductivity of the surrounding medium.

7.4.3 Nano-satellite and void formation

A phenomenon observed in addition to the ion-shaping process is the formation of small nano-clusters surrounding the irradiated NPs when embedded in a-SiO_2 [155, 312]. As the NPs begin to elongate with increasing fluence the energy deposited by the ion increases too, likewise the energy per atom increases near the boundary and can surpass the energy required for vaporization. This can lead to the dissolution of Au atoms into the matrix which are likely to aggregate into small nano-clusters due to the low solubility and reactivity [155]. In Figure 7.9 (a) the TEM image of elongated Au NPs in a-$SiO_{1.9}$ after irradiation to a fluence of 1×10^{14} cm^{-2} is presented. In the image, the formation of the so-called nano-satellites of few nanometres between the elongated NPs is evident. On the other hand, Figure 7.9 (b) shows the micrographs of Au NPs embedded in a-$SiN_{1.06}$ under the same irradiation conditions where no evidence of their formation was found. Due to their small dimensions the nano-satellites can be difficult to distinguish with TEM thus, HAADF was used to complement the results obtained by TEM regarding the presence of nano-satellites [Figs. 7.9 (c) for a-$SiO_{1.9}$ and (d) for a-$SiN_{1.06}$] as contrast is based on the difference in atomic number between Au and the matrix. For the first case [Fig. 7.9 (c)] we can observe in more detail the distribution of the nano-satellites around the elongated NPs. It appears that each elongated NP posses a halo of nano-satellites which are within 10 nm from the surface. For the latter case [Fig. 7.9 (d)], a different behaviour is observed where no indication of the formation of nano-satellites can be distinguished while Au-deficient regions within the elongated NPs are revealed.

A possible pathway for the formation of nano-satellites in a-$SiO_{1.9}$ and not in

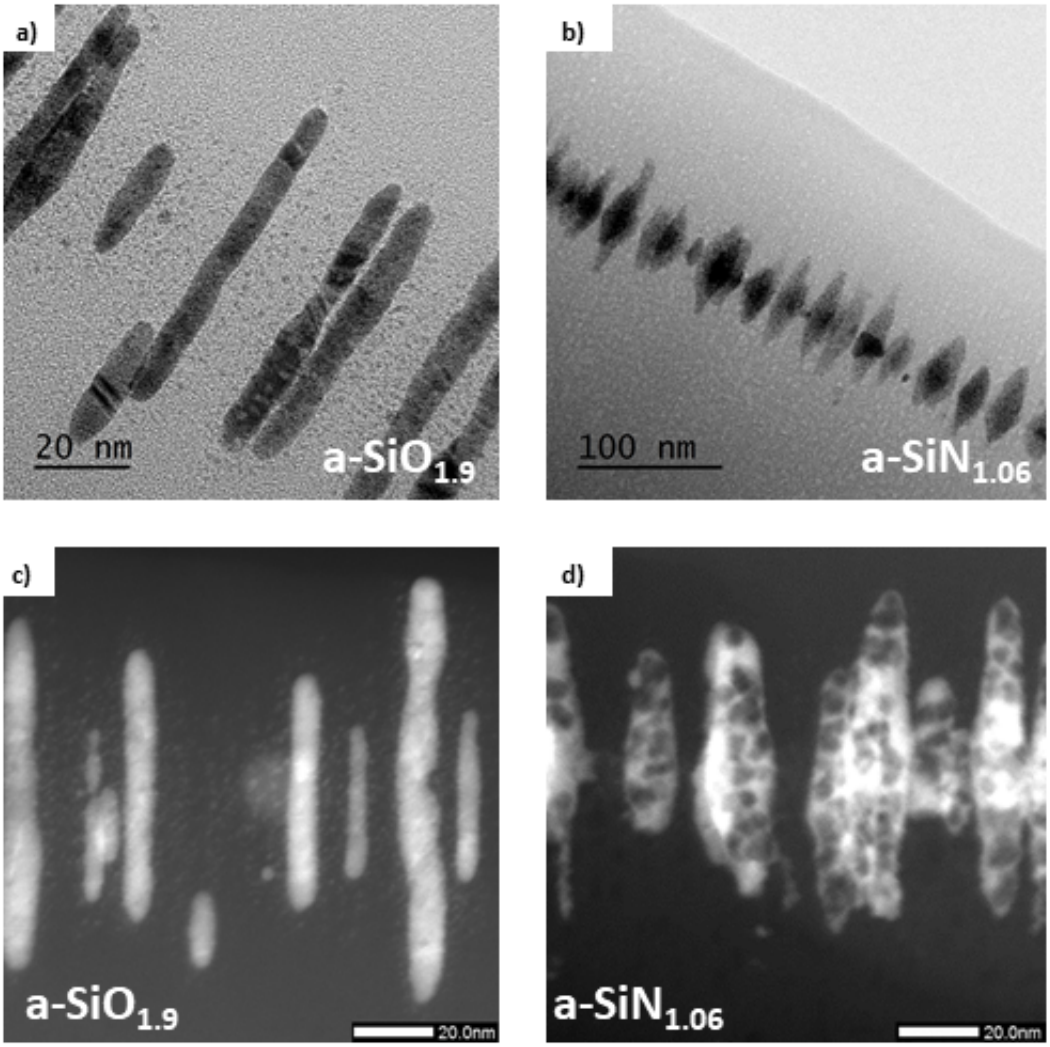

Figure 7.9: *TEM BF (a) and (b), and HAADF in STEM mode (c) (d) images of Au NPs embedded in a-$SiO_{1.9}$ ((a) and (c)), and a-$SiN_{1.06}$ ((b) and (d)) after irradiation with 1 × 10^{14} cm^{-2}.*

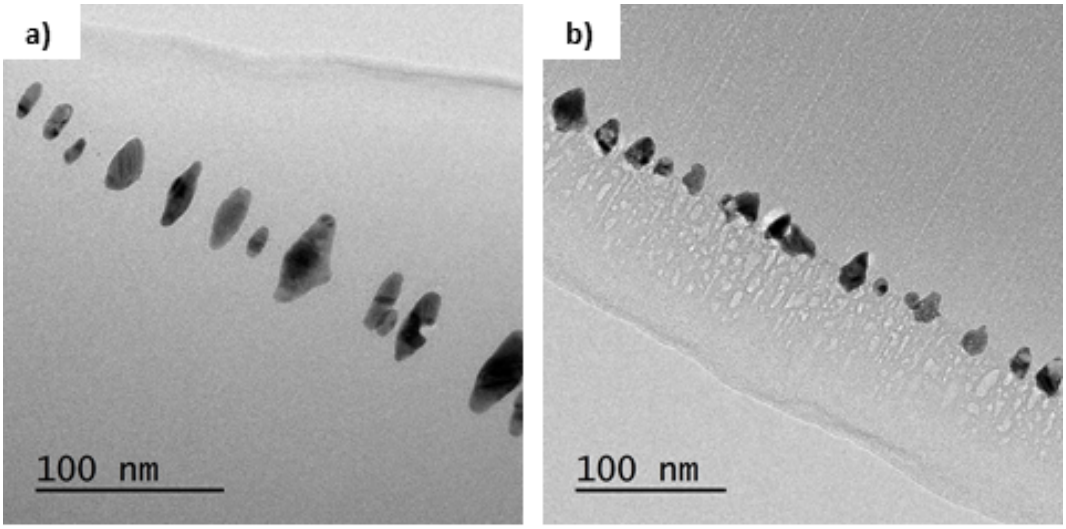

Figure 7.10: *Under-focused TEM micrographs of Au NPs embedded in a-$SiO_{1.9}$ (a), and at the a-$SiO_{1.9}$/a-$SiN_{1.06}$ interface (b) after irradiation with 3 × 10^{13} cm^{-2}*

a-$SiN_{1.06}$ can be explained based on the thermal profile during the ion shaping process. From the plots shown in Figs. 7.6 (c) and (d) the temperature profile inside the Au NP can be observed to follow a similar trend and appears to reach the same temperature (∼3100 K) when embedded in a-SiO_2 and a-Si_3N_4 yet, when embedded in a-SiO_2, the formation of a shell of nearly 2 nm thickness inside the NP is observed between 3 and 10 ps that reaches temperatures of nearly 3500 K. Such localised increment in temperature might be a consequence of the lower thermal conductivity of a-SiO_2 that prevents the heat flow to the matrix as efficiently as in a-Si_3N_4. Therefore, one possible condition is the necessity of surpassing the boiling temperature of Au (3129 K [2]) to form nano-satellites, a condition not reached when embedded in a-Si_3N_4 due to the high thermal conductivity of the substrate. This agrees with a decrease in the nano-satellite density formed around Au NPs when irradiated with Au ions at lower energies [152]. However, it cannot be ruled out that monomers are indeed formed near Au NPs in a-$SiN_{1.06}$, yet clustering might be inhibited or nano-satellites with diameters below 1 nm are formed that are difficult to observe by TEM because of the low mobility foreign atoms exhibit in a-Si_3N_4.

Besides reaching a high temperature at the metal/dielectric interface, the Au atoms require a medium where they can diffuse outwards from the NP. It is well-known from ion implantation experiments that Au atoms exhibit high mobility in a-SiO_2. Results, however, have not been reported for a-Si_3N_4, but it is known as a material exhibiting low diffusion coefficients for a broad range of impurities. Because the region surrounding the NP exceeds the melting point of a-SiO_2 (see Fig. 7.9 (a)) a high mobility of Au monomers is expected that can extend several nanometres from the surface of the NP. A different behaviour can be expected in a-Si_3N_4. Despite showing a region above the melting point of Au extending about 10 nm at t=10 ps, the combination of a low diffusion coefficient and lower temperature compared to a-SiO_2 can prevent the increase of Au monomer density around the elongated NP. For example, while the presence of very small clusters cannot be ruled out due to the resolution, of both TEM BF and HAADF in STEM mode micrographs show no cluster formation in a-$SiN_{1.06}$, whereas in a-$SiO_{1.09}$ they are clearly visible. On the other hand, the low solubility of Au in a-SiO_2 and the favorable conditions for the monomer production during the ion-shaping process, facilitate the formation of nano-satellites. This agrees with the observation of a higher nano-satellite density near the initial region occupied by the NPs, as seen by the corresponding HAADF images (Fig. 7.9 (c)) but not for a-$SiN_{1.06}$ (Fig. 7.9 (d)).

The fragmentation of elongated NPs, which has been previously explained as the result of a Rayleigh-like instability from the tension sustained by the Au NP of radius R and length L, is another phenomenon observed. Rayleigh instability occurs when the surface tension is larger than the yield strength. In the case of Au NPs, the minimum width for solidity can be estimated as in [123]: $D^{Au}_{Rayleigh} = \frac{2\sigma_s}{\sigma_Y}$, where σ_s corresponds to the surface tension and σ_Y to the yield strength. The value of the yield strength was adopted to be 150 MPa, as in [123]. For the value of the surface tension, it was compared the value used by Rizza *et al.* [313] of 1.3 $N \cdot m^{-1}$, which contrasts to the value determined by Kluth *et al.* [314] of 3.6 $N \cdot m^{-1}$. Thus, the corresponding widths are approximately 17 and 48 nm for the two values considered for the surface tension, respectively, clearly above the saturation width shown in Fig.

7.2 (a). While the reason for the difference between the minimum width for solidity and the saturation width observed is still unclear, in Figure 7.9 (a) we can observe an example of fragmented NPs, where the presence of continuous long nano-rods of aspect ratios higher than 6 next to shorter, discontinuous nano-rods is apparent. Rayleigh instability does not consider the creation of nanoclusters around the NP, thus it is possible that other factors related to radiation damage effects like point defects or crater formation (which are common at much lower energies) can facilitate the rupture of the long nano-rods too.

The micrographs shown in Figs. 7.9 (b) and (d) show that the elongated Au NPs in a-$SiN_{1.06}$ contain cavities leading to nano-porous metal structures. While this behaviour has not been observed when embedded in a-$SiO_{1.9}$ solely (Figure 7.10 (a)), it occurs when the NPs are totally or partially embedded in a-$SiN_{1.06}$ (Fig. 7.10 (b)). During annealing to temperatures near the melting point, a-Si_3N_4 is known to decompose into a-Si and N_2. In Figure 7.10 (b), the formation of void like nanostructures in a-$SiN_{1.06}$ is apparent. From narrow, long shapes at low fluences (visible from 3×10^{12} cm^{-2}), these increase to larger nano-bubbles or voids at higher values. While the nature of such voids or cavities has not been identified in a-$SiN_{1.06}$, *i.e.* if they are gas-filled or empty voids, it is possible they penetrate the Au NP at the Au/a-$SiN_{1.06}$ interface during the SHI irradiation process leading to the observed porous NPs. As such structures are not visible in a-$SiO_{1.9}$ their interpretation as ion tracks in the rest of the samples results inaccurate. Furthermore, the fluences involved correspond to the range where overlapping effects are important and can modify the morphology of single tracks [257] however, the width of such structures appear to be more stable with increasing fluence in a-$SiO_{1.9}$ than a-$SiN_{1.06}$ and may be linked to the radial dimension of a stable track-like structure formed at high fluences.

7.5 Amorphous silicon nitride as diffusion barrier

As demonstrated in the previous section, preferential elongation towards a-$SiO_{1.9}$ was observed when Au NPs are located at the interface of a-$SiN_{1.06}$/a-$SiO_{1.9}$. Thus,

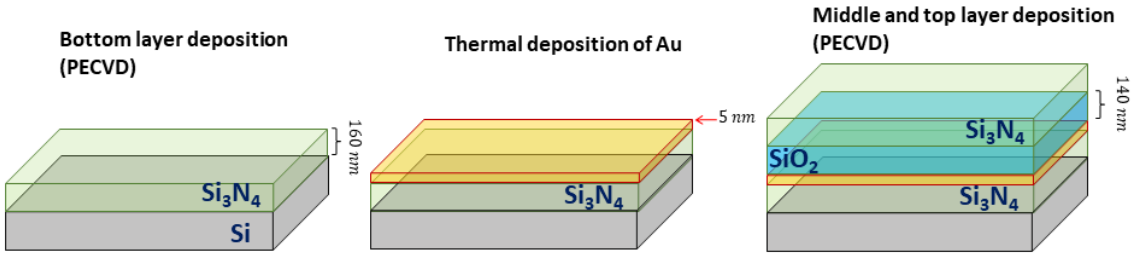

Figure 7.11: *Fabrication process of the multilayer system for the study of an a-SiN*$_{1.06}$ *layer as a diffusion barrier.*

a-SiN$_{1.06}$ can be used as a confining barrier for the elongation process. This is also interesting regarding existing applications of a-SiN$_{1.06}$, structural compatibility with Si-devices and the higher refractive index compared to a-SiO$_{1.9}$. For these reasons, we investigated the use of thin a-SiN$_{1.06}$ layers to confine the ion-shaping process to an intermediate a-SiO$_{1.9}$ layer.

In the previous section a trend in the saturation width for the ion-shaping process at the interface of a-SiN$_{1.06}$/a-SiO$_{1.9}$ was observed (Fig. 7.4 (a) and (b)). In particular, when a-SiO$_{1.9}$ is the main surrounding medium, the saturation of the width resembled that of Au NPs embedded in a-SiO$_{1.9}$ only (towards 8.5 $\pm$ 1.7 nm) after irradiation with 1 $\times$ 10^{14} cm^{-2}. At that fluence, a mean length of the nano-rods of 75.3 $\pm$ 21.9 nm was measured. As mentioned at the beginning of this chapter, the ion-shaping process in a-SiO$_{1.9}$ shows good agreement with previous results on thermally grown a-SiO$_2$ allowing to take into consideration some central results, in particular the saturation of the width under the same irradiation energy. The thickness of the intermediate layer was chosen considering that the NP can elongate further than 100 nm at fluences above 1 $\times$ 10^{14} cm^{-2} [123]. For the given size the NPs can be expected to reach a length between 100-120 nm considering a mean width of 10 nm allowing to study the confinement process at higher fluences [152]. To study the system and to demonstrate the applicability of a-SiN$_{1.06}$ as a diffusion barrier an a-SiO$_{1.9}$ layer of 140.2 $\pm$ 0.1 nm thickness was chosen. The design and fabrication of the samples is depicted in Figure7.11 and consists of two a-SiN$_{1.06}$ layers (top and bottom) with

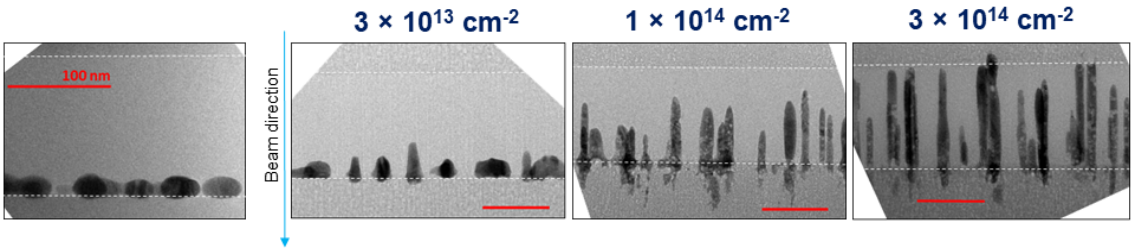

Figure 7.12: *Evolution of the ion-shaping process of Au NPs in a multilayer system with fluence. Dashed white lines were added to outline the location of the a-SiN$_{1.06}$/a-SiO$_{1.9}$ interface.*

thickness of around 160 nm and an intermediate a-SiO$_{1.9}$ layer deposited by PECVD. The synthesis of a single Au NP layer was carried out under the same conditions as for the previous samples. A 5 nm thick Au layer deposited between the bottom a-SiN$_{1.06}$ and the intermediate a-SiO$_{1.9}$ layers.

Figure7.12 shows the transformation from nearly spherical Au NPs into high aspect-ratio nano-rods located at the interface of a-SiN$_{1.06}$/a-SiO$_{1.9}$ layer as expected, while very limited diffusion is observed towards the bottom a-SiN$_{1.06}$ layer. After irradiation with 1×10^{14} cm^{-2}, we observed that the elongated Au NPs exhibit similar width and length values as in the previous section, with a mean length around 75 nm, and without reaching the top layer. When the fluence increases to 3×10^{14} cm^{-2}, the intermediate layer shows that elongated Au NPs reach or are within 5 nm from the top a-SiN$_{1.06}$ layer. Also, for 1 and 3×10^{14} cm^{-2}, the formation of small nano-rods accompanying the larger elongated NPs is apparent, which can be the result of the variation in the original NPs size or due to mass redistribution. Due to the presence of the a-SiN$_{1.06}$ layer, the intermediate a-SiO$_{1.9}$ layer develops the formation of defective regions aligned with the beam direction from fluences as low as 3×10^{13} cm^{-2}. After irradiation with 1 and 3×10^{14} cm^{-2}, the Au NPs exhibit nano-porosity too, which seems to originate near the a-SiO$_{1.9}$/a-SiN$_{1.06}$ interface after irradiation with 1×10^{14} cm^{-2} and extending through the whole elongated NPs at the highest fluence. Furthermore, the NPs that reach, or nearly reach the top layer, show

a narrow width distribution with a mean value of 9.1 ± 0.5 nm where no observable difference in width of the NPs is observed for irradiation with 1 and 3 × 10^{14} cm^{-2}. This suggests that mass redistribution between NPs is involved in the ion-shaping process. If we consider mass conservation, it is possible to approximately calculate the maximum length (L_M) of a nano-rod in terms of their original volume: [160]

$$L_M = \frac{4}{3R_{width}^2} R_w^2 \cdot R_l, \tag{7.1}$$

where the saturation of the width is represented by R_{width}. As the NP is initially a spheroid, we take into account the initial minor R_w and major R_l axes. Considering the initial values as estimated for the Au NP at the a-$SiO_{1.9}$/a-$SiN_{1.06}$ interface, the maximum length possible for a saturation of the width of 9 nm corresponds to L_M=65 nm. The observation of the shorter and longer NPs thus supports the hypothesis that, under the current experimental conditions, Au NPs can elongate beyond the expected length by aggregation of the monomers ejected during the process by neighbour NPs, as previously observed by Dawi *et al.* [68], and Singh *et al.* [315] in the case of Ag NPs[1]. The mass redistribution, together with the presence of nano-porosity, allows Au NPs to reach aspect-ratios larger than 15 at the highest irradiation fluence, while the top layer allows the top end of those NPs to be located almost at the same position within the sample (within 5 nm from the interface with the upper a-$SiN_{1.06}$ layer) demonstrating that a-$SiN_{1.06}$ can be used to confine the ion-shaping process to the intermediate a-$SiO_{1.9}$ layer. We do not rule out the effect of nano-porosity of the Au NPs, which can let them elongate further without the necessity of extra material.

7.6 Summary

In this chapter, experimental observations of the shape transformation of nearly spherical Au NPs about 20 nm in width and 16 nm in length, upon irradiation with

[1]the ripening process cannot be attributed to Ostwald ripening as it is not driven by a chemical potential gradient [315].

185 MeV Au ions in a-$SiO_{1.9}$, a-$SiN_{1.06}$ and when located at the interface of the two dielectric materials are presented. When the NPs are embedded in a single layer, a difference in the geometry of the elongated NPs, as well as a higher deformation rate for NPs in a-$SiO_{1.9}$ compared to a-$SiN_{1.06}$ is observed. The differences have been discussed in terms of calculations performed using the 3D-iTS model. Clear differences in the thermal profile experienced by the Au NPs due to the specific combination of electron-phonon coupling strength and thermal conductivity in the two host materials are apparent. Furthermore, such differences become more relevant when the NPs are located at the interface of a-$SiO_{1.9}$ and a-$SiN_{1.06}$, where preferential elongation towards the a-$SiO_{1.9}$ layer was observed for all configurations studied. The comparison of the calculated thermal environments for the four cases studied suggests that the thermal conductivity plays a major role for the local temperature profile at the metal/dielectric boundary, which should have a major influence on the shape transformation process and the formation of nano-satellites around the elongated NPs. The presence of such nano-satellites in a-$SiO_{1.9}$ while being absent in a-$SiN_{1.06}$ suggests that the Au mobility is highly reduced in a-$SiN_{1.06}$. Thus, the resulting elongations process occurs preferentially towards the a-$SiO_{1.9}$ layer while creating a high density of very small nano-satellites with an average of 2 nm near the NPs surface. Furthermore, the elongated Au NPs embedded in, or in contact with, the a-$SiN_{1.06}$ layer present the formation of nano-porous regions, in particular near the a-$SiO_{1.9}$/a-$SiN_{1.06}$ boundary. In addition, defective regions are formed in a-$SiN_{1.06}$ at higher fluences, and to lesser extent in a-$SiO_{1.9}$ when in contact with a-$SiN_{1.06}$, while retaining the directionality along the ion beam direction. These are possibly formed by empty regions or voids but without excluding the possibility of N_2 nano-bubble formation. Thus, the formation of the defective region in a-$SiO_{1.9}$ and inside the Au NPs can be the result of damage diffusion from the a-$SiN_{1.06}$ layer. Finally, it is demonstrated that a-$SiN_{1.06}$ can be used as a material to confine the ion-shaping process into an intermediate a-$SiO_{1.9}$ layer, where the dimensions of the layer can be varied. The latter represent a step-forward for device engineering and applications.

Chapter 8

Conclusions and future work

This work presented a first systematic study of the use of ion irradiation to modify the physical and chemical properties of a-SiO_xN_y thin layers deposited by PECVD, with special aim on the binary components (a-SiO_2 and a-Si_3N_4) to get a better insight.

First, it was studied the ion track morphology and formation process after irradiation with 185 MeV and 2.3 GeV Au ions at low fluences, that lead to the following conclusions:

- The ion tracks were characterised using SAXS. The corresponding extracted scattering intensities, after appropriate background subtraction, were fitted with a core-shell model with a smooth transition showing better agreement at high q-values than a core-shell model.
- The SAXS results, in combination with MD simulations, suggests that the morphology of the formed ion tracks in a-SiO_2, a-Si_3N_4 and a-SiO_xN_y corresponds to an under-dense core surrounded by an over-dense shell connected by a linear transition.
- Besides a higher energy deposition in a-Si_3N_4 (S_e = 20.7 keV/nm) the ion track radius is smaller 4.1 $\pm$ 0.1 nm, than in a-SiO_2 (S_e = 16.3 keV/nm) where the corresponding ion track radius is 5.3 $\pm$ 0.1 nm. The difference in radial dimensions was mainly ascribed to the difference in the electron-phonon coupling. Which was deduced from the empirical correlation between the electron-mean-free path and the optical band gap, being the bandgap experimentally determined.
- The absolute density variation was determined for all materials. A nearly five

times larger density change was determined for a-Si_3N_4 with respect to a-SiO_2. It was suggested that the greater thermal conductivity of a-Si_3N_4 lead to a decrease in the duration of the corresponding thermal spike, limiting the relaxation process.

- A comparison with stoichiometric a-SiO_2 and nearly stoichiometric a-Si_3N_4 was carried out too. A similar behaviour was observed for the two a-SiO_2 samples, while for a-Si_3N_4 we observe an increase in the ion track radius and decrease of the absolute density change for the near-stoichiometric sample.

- The velocity effect in a-SiO_2 and a-Si_3N_4 was also presented.

- For a-SiO_xN_y samples, we observe an increasing ion track radius and decrease of the absolute density change with increasing O content. However, when the O/N ratio is greater than or equal to 1 the ion track dimensions saturate with a value similar to a-SiO_2 but with a progressive decrease of the absolute density change towards the value of a-SiO_2.

Afterwards, the synthesis of Au NPs embedded in a-SiO_2, a-Si_3N_4 and at the interface of the two materials was explored using two methods, ion beam synthesis and by a dielectric/metal/dielectric multilayer deposition followed by RTA. Based on the presented observations it is possible to conclude:

- The synthesis of Au NPs was studied in a-Si_3N_4 for PECVD and nearly-stoichiometric samples by ion implantation with 2 MeV Au ions. For the former, Au NPs with diameters close to 2 nm were synthesised. For the later, a phase transition from amorphous-to-polycristalline was observed accompanied by the nearly homogeneous diffusion of the implanted Au along through the layer.

- For a-SiO_2, the two materials exhibit similar Au NPs dimensions.

- The synthesis of Au NPs in the multilayer system showed that for a-SiO_2 and a-Si_3N_4 it was possible to produce NPs with dimensions larger than those obtained by ion beam synthesis with a narrower distribution.

- At the interface of the two materials, the synthesised Au NPs showed an asymmetric behaviour, being embedded preferentially by the layer deposited at the top, possibly due to a de-wetting process during the deposition of the top layer.

Finally, the ion shaping process of Au NPs by swift heavy-ion irradiation with 185 MeV Au ion of Au NPs in a-SiO_2, a-Si_3N_4 and at the interface of the two materials was carried out. From the carried out experiments it is concluded that:

- The ion shaping process occurs too in a-Si_3N_4.
- It was characterise the ion shaping process of Au NPs in a-SiO_2 and a-Si_3N_4 as a function of fluence.
- When the Au NPs are located at the a-SiO_2/a-Si_3N_4 interface, we observe a preferential elongation towards the a-SiO_2 region. This was explained based on the thermal profile calculated by the 3D-iTS model. From the numerical results a longer duration of the thermal spike in the a-SiO_2 region with respect to the a-Si_3N_4 was observed while reaching higher temperatures.
- TEM and HAADF in STEM mode micrographs showed the formation of porous Au NPs after swift heavy-ion irradiation, in particular when in contact with a-Si_3N_4. While this process is still not well understood, it is possible that the porous structures formed in a-Si_3N_4 can diffuse through the Au NPs.
- It was demonstrated the use of a-Si_3N_4 as a material to confine the ion-shaping process into an intermediate a-SiO_2 layer, where the dimensions of the layer can be varied.

8.1 Future work

While good insight into the modification of the physical and chemical properties of a-SiO_xN_y materials, there are still some open questions remaining. The use of X-ray photoelectron spectroscopy (XPS) can provide with a quantitative analysis of the elemental composition, as well as information regarding the bond configuration. It has been shown that it is possible to determine the bond concentration from this

analysis, which can complement the information extracted from FTIR. Also, TEM characterisation of a-SiO_xN_y materials after irradiation would help to clarify if porous structures are formed when Au NPs are not present and if the O content plays a relevant role in their formation.

As suggested, it is an important step forward to carry out 3D i-TS calculations for off-centre cases to compare the minimum pathway required to induce the NP melting between a-SiO_2 and a-Si_3N_4. While one potential difference is the lower value of the electron-phonon coupling for the latter, the effect of the thermal conductivity could also be a factor affecting this process. If a larger pathway is required for the ion to induced melting in a-Si_3N_4 with respect to a-SiO_2, this would suggest less events involved in the ion shaping process at the same nominal fluence thus, suggesting another parameter needed to be taken into account to engineer anisotropic NPs (besides the bulk thermal conductivity of the matrix). Such study is expected to be done in the short term.

Regarding the potential formation of porous structures in a-SiO_xN_y materials with low O content, two techniques are proposed to clarify if they are empty regions or voids, or N_2 nano-bubbles. It is proposed to carry out energy dispersive X-ray (EDX) analysis with a double aberration corrected TEM to obtain information of the elemental content at a very local level. The mapping might potential resolve if there is an increase concentration of Si or N inside the sample, that can demonstrate the dissociation of the SiN_4 molecule. A second method is the use of positron annihilation lifetime spectroscopy (PALS), as it can resolve the mean size of the porous and if the porous structures are empty or not.

Another important step forward to the results we have obtained is the characterisation of the linear and non linear optical properties of the spherical and ion-shaped Au NPs. To do so, it is necessary to repeat the fabrication process using an optically transparent substrate, such as α-Al_2O_3 or quartz, to allow the carry out of transmission experiments, such as optical absorption (OA), second harmonic generation. The later becomes relevant as the presence of nano-porous Au NPs breaks the centro-symmetric symmetry which can potentially lead to a very interesting second harmonic signal.

Bibliography

[1] M. Toulemonde, C. Dufour, A. Meftah, and E. Paumier, "Transient thermal processes in heavy ion irradiation of crystalline inorganic insulators," *Nuclear Instruments and Methods in Physics Research Section B: Beam Interactions with Materials and Atoms*, vol. 166-167, pp. 903–912, 2000.

[2] C. Dufour, V. Khomenkov, G. Rizza, and M. Toulemonde, "Ion-matter interaction: the three-dimensional version of the thermal spike model. application to nanoparticle irradiation with swift heavy ions," *J. Phys. D: Appl. Phys.*, vol. 45, no. 6, p. 065302, 2012.

[3] W. Wesch and E. Wendler, *Ion Beam Modification of Solids*. Springer International Publishing, 2016.

[4] C. D'Orléans, J. P. Stoquert, C. Estournès, C. Cerruti, J. J. Grob, J. L. Guille, F. Haas, D. Muller, and M. Richard-Plouet, "Anisotropy of co nanoparticles induced by swift heavy ions," *Physical Review B*, vol. 67, no. 22, pp. 2201011–2201014, 2003.

[5] E. Snoeks, A. V. Blaaderen, T. V. Dillen, C. M. Kats, M. L. Brongersma, and A. Polman, "Colloidal ellipsoids with continuously variable shape," *Adv. Mat.*, vol. 12, no. 20, pp. 1511–1514, 2000.

[6] "Snics."

[7] "Alphatross source rf-charge exchange ion source."

[8] "Tools & capabilities."

[9] R. Hellborg, *Electrostatic Accelerators*. Berlin: Springer, 2005.

[10] M. D. Cesare, *Origin and Detection of Actinides: Where Do We Stand with the Accelerator Mass Spectrometry Technique?*, pp. 167–186. London: IntechOpen, 2011.

[11] C. Schmelzer and D. Bohne, "Gsi, a new heavy-ion research facility," (Batavia, Illinois, USA), Proton Linear Accelerator Conference, 1970.

[12] B. Fultz and J. M. Howe, *Transmission Electron Microscopy and Diffractometry of Materials*. Berlin: Springer, 2008.

[13] A. Thomson, I. Lindau, Y. Liu, D. Attwood, P. Pianetta, E. Gullikson, M. Howells, A. Robinson, K.-J. Kim, J. Scofield, J. Kirz, J. Underwood, J. Kortright, G. Williams, and H. Winick, *X-ray Data Book by the Center for X-ray Optics and Light Source, Lawrence Berkeley National Laboratory*. Center for X-ray Optics and Light Source, 2009.

[14] N. M. Kirby, S. T. Mudie, A. M. Hawley, D. J. Cookson, H. D. T. Mertens, N. Cowieson, and V. Samardzic-Boban, "A low-background-intensity focusing small-angle x-ray scattering undulator beamline," *Appl. Cryst.*, vol. 46, pp. 1670–1680, 2013.

[15] D. S. Sivia, *Elementary scattering theory*. New York: Oxford University Press, 2011.

[16] F. Giorgis, F. Giuliani, C. F. Pirri, E. Tresso, C. Summonte, R. Rizzoldi, R. Galloni, A. Desalvo, and P. Rava, "Optical, structural and electrical properties of device-quality hydrogenated amorphous silicon-nitrogen films deposited by plasma-enhanced chemical vapour deposition," *Phil. Mag. B*, vol. 77, no. 4, pp. 925–944, 1998.

[17] B. Hallam, B. Tjahjono, and S. Wenham, "Effect of pecvd silicon oxynitride film composition on the surface passivation of silicon wafers," *Solar Energy Materials & Solar Cells*, vol. 96, pp. 173–179, 2012.

[18] P. Mazzodi and G. W. Arnold, *Ion Beam Modification of Inxulators*. Amsterdam: Elsevier, 1987.

[19] M. Nastasi, J. W. Mayer, and J. K. Hirvonen, *Ion-Solid Interactions: Fundamentals and Applications.* Cambridge: Cambridge University Press, 1996.

[20] W.-K. Chu, J. W. Mayer, and M.-A. Nicolet, *Backscattering Spectrometry.* New York: Academic Press, 1978.

[21] M. Nastasi, J. W. Mayer, and Y. Wang, *Ion Beam Analysis: Fundamentals and Applications.* Boca Raton, FL: CRC Press, 2015.

[22] J. S. Williams, "Ion implantation of semiconductors," *Mater. Sci. Eng. A*, vol. 253, no. 1, pp. 8–15, 1998.

[23] C. Chen, I. C. Cho, H. S. Jian, and H. Niu, "Fe doped magnetic nanodiamods made by ion implantation," *Sci. Rep.*, vol. 7, p. 41938, 2017.

[24] Y. Tan, X. Liu, Z. He, M. Zhao, H. Zhang, and F. Chen, "Tuning of interlayer coupling in large-area graphene/wse2 van der waals heterostructure via ion irradiation: optical evidences and photonic applications," *ACS Photonics*, vol. 4, no. 6, pp. 1531–1538, 2017.

[25] T. Sharma, R. Singhal, R. Vishnoi, G. Lakshmi, S. Chand, D. K. Avasthi, A. Kanjilal, and S. K. Biswas, "Ion irradiation induced modifications of p3ht: a donor material for organic photovoltaic devices," *Vacuum*, vol. 13, pp. 73–85, 2017.

[26] O. Sánchez-Dena, P. Mota-Santiago, L. Tamayo-Rivera, E. V. García-Ramírez, A. Crespo-Sosa, and J. A. Reyes-Esqueda, "Size-and shape-dependent nonlinear optical response of au nanoparticles embedded in sapphire," *Optical Materials Express*, vol. 4, no. 1, pp. 92–100, 2014.

[27] A. Benyagoub and M. Toulemonde, "Ion tracks in amorphous silica," *J. Mater. Res.*, vol. 30, no. 9, pp. 1529–1543, 2015.

[28] A. Nadzri, D. Schauries, P. Mota-Santiago, C. Trautmann, A. Gleadow, A. Hawley, and P. Kluth, "Composition and orientation dependent annealing of ion tracks in apatite - impliocations for fission track thermochronology," *Chem. Geology*, vol. 451, pp. 9–16, 2017.

[29] D. Schauries, P. Mota-Santiago, E. Gilbert, N. Kirby, C. Trautmann, and P. Kluth, "Structure, morphology and annealing behaviour of ion tracks in polycarbonate," *Eur. Polym. J.*, vol. 108, pp. 406–411, 2018.

[30] A. Hadley, C. Notthoff, P. Mota-Santiago, U. Hossain, N. Kirby, M. Toimil-Molares, C. Trautmann, and P. Kluth, "Etched ion tracks in amorphous sio2 characterized by small angle x-ray scattering: influence of ion energy and etching conditions," *Nanotechnology*, vol. 30, p. 274001, 2019.

[31] P. Apel, "Track etching technique in membrane technology," *Radiat. Meas.*, vol. 34, pp. 559–566, 2001.

[32] C. Dekker, "Solid-state nanopores," *Nature Nanotech.*, vol. 2, pp. 209–215, 2007.

[33] B. Venkatesan and R. Bashir, "Nanopore sensor for nucleic acid analysis," *Nature Nanotech.*, vol. 6, pp. 615–624, 2011.

[34] M. T.-M. and, "Characterization and properties of micro- and nanowires of controlled size, composition, and geometry fabricated by electrodeposition and ion-track technology," *J. Nanotechnol.*, vol. 3, p. 860, 2012.

[35] "Capacitors including track-etched separator materials," 2004.

[36] D. Fink, H. Hu, R. Klett, M. Muller, J. Zhu, C. Li, Y. Sun, F. Ma, and L. Wang, "Conductivity of aged non-overlapping and overlapping tracks in ion irradiated polymide," *Radiat. Meas.*, vol. 25, pp. 51–54, 1995.

[37] N. Strickland, S. Wimbush, P. Kluth, P. Mota-Santiago, M. Ridgway, J. Kennedy, and N. Long, "Effect of annealing high-dose heavy-ion irradiated high-temperature superconductor wires," *Nucl. Inst. and Meth. B*, vol. 409, pp. 351–355, 2017.

[38] C. Notthoff, P. Mota-Santiago, A. Hadley, U. Hossain, S. Jordan, C. Glover, S. Mudie, and P. Kluth, "Structural properties of nano-porous gasb prepared by swift heavy-ion irradiation," *Nucl. Inst. and Meth. B*, vol. 435, pp. 126–132, 2018.

[39] N. C. Tombs, F. A. S. Jr., and J. J. Comer, "Solid solution in the silicon nitride - silicon dioxide system," *J. Electrochem. Soc.*, vol. 116, no. 6, pp. 862–863, 1969.

[40] T. L. Chu, J. R. Szedon, and C. H. Lee, "Films of silicon nitride - silicon dioxide mixtures," *J. Electrochem. Soc.*, vol. 115, no. 3, pp. 318–322, 1968.

[41] T. Baak, "Silicon oxynitride; a material for grin optics," *Appl. Opt.*, vol. 21, no. 6, pp. 1069–1072, 1982.

[42] V. A. Gritsenko, J. B. Xu, R. W. M. Kwok, Y. H. Ng, and I. H. Wilson, "Short range order and the nature of defects and traps in amorphous silicon oxynitride governed by the mott rule," *Phys. Rev. Lett.*, vol. 81, no. 5, pp. 1054–1057, 1998.

[43] V. A. Gritsenko, "Atomic structure of the amorphous nonstoichiometric silicon oxides and nitrides," *Physics-Uspekhi*, vol. 51, no. 7, pp. 699–708, 2008.

[44] A. N. Sorokin, A. A. Karpushin, V. A. Gritsenko, and H. Wong, "Electronic structure of amorphous silicon oxynitride with different compositions," *J. Appl. Phys.*, vol. 105, p. 073706, 2009.

[45] N. Brinkmann, D. Sommer, G. Micard, G. Hahn, and B. Terheiden, "Electrical, optical and structural investigation of plasma-enhanced chemical-vapor-deposited amorphous silicon oxynitride films for solar cell applications," *Solar Energy Materials & Solar Cells*, vol. 108, pp. 180–188, 2013.

[46] V. A. Gritsenko, Y. G. Shavalgin, P. A. Pundur, H. Wong, and W. M. Kwok, "Short-range order and luminescence in amorphous silicon oxynitride," *Phil. Mag. B*, vol. 80, no. 10, pp. 1857–1868, 2000.

[47] L. D. Negro, J. H. Yi, M. Miltunen, J. Michel, L. C. Kimerling, S. Hamel, A. J. Williamson, G. Galli, T.-W. F. Chang, V. Sukhovatkins, and E. H. Sargents, "Light-emitting silicon-rich nitride systems and photonic structures," *J. Exp. Nanosci.*, vol. 1, no. 1, pp. 29–50, 2006.

[48] R. Huang, Z. Lin, Y. Guo, C. Song, X. Wang, H. Lin, L. Xu, J. Song, and H. Li, "Bright red, orange-yellow and white switching photoluminescence from silicon

oxynitride films with fast decay dynamics," *Opt. Mat. Exp.*, vol. 4, no. 2, p. 212, 2014.

[49] T. Milek, *Silicon Nitride for Microelectronic Applications: Part 2 Applications and Device*. New York: Springer, 2013.

[50] C. Noguez, "Surface plasmons on metal nanoparticles: The influence of shape and physical environment," *Journal of Physical Chemisctry C*, vol. 111, no. 10, pp. 3806–3819, 2007.

[51] A. A. Leino, O. H. Pakarinen, F. Djurabekova, K. Nordlund, P. Kluth, and M. C. Ridgway, "Swift heavy ion shape transformation of au nanocrystals mediated by molten material flow and recrystallization," *Materials Research Letters*, vol. 2, no. 1, pp. 37–42, 2014.

[52] H. Amekura, N. Okubo, D. Tsuya, and N. Ishikawa, "Counterevidence to the ion hammering scenario as a driving force for the shape elongation of embedded nanoparticles," *AIP Advances*, vol. 7, no. 8, p. 085304, 2017.

[53] K. Awazu, S. Ishii, K. Shima, S. Roorda, and J. L. Brebner, "Structure of latent tracks created by swift heavy-ion bombardment of amorphous sio2," *Phys. Rev. B*, vol. 62, no. 6, pp. 3689–3698, 2000.

[54] B. Canut, A. Ayari, K. Kaja, A. L. Deman, M. Lemiti, A. Fave, A. Souifi, and S. Ramos, "Ion-induced tracks in amorphous si3n4 films," *Nucl. Instr. Meth. Phys. Res. B*, vol. 266, pp. 2819–2923, 2008.

[55] C. Trautmann, S. Klaumünzer, and H. Trinkaus, "Effect of stress on track formation in amorphous iron boron alloy: Ion tracks as elastic inclusions," *Phys. Rev. Lett.*, vol. 85, no. 17, p. 3648, 2000.

[56] P. Kluth, C. S. Schnohr, O. H. Pakarinen, F. Djurabekova, D. J. Sprouster, R. Giulian, M. C. Ridgway, A. P. Byrne, C. Trautmann, D. J. Cookson, K. Nordlund, and M. Toulemonde, "Fine structure in swift heavy ion tracks in amorphous sio2," *Physical Review Letters*, vol. 101, no. 17, p. 175503, 2008.

[57] J. E. Shelby, *Introduction to Glass Science and Technology.* Cambridge: The Royal Society of Chemistry, second edition ed., 1997.

[58] T. Kitayama, Y. Morita, K. Nakajima, K. Narumi, Y. Saitoh, M. Matsuda, M. Sataka, M. Tsujimoto, S. Isoda, M. Toulemonde, and K. Kimura, "Formation of ion tracks in amorphous silicon nitride films with mev c60 ions," *Nuclear Instruments and Methods in Physics Research Section B: Beam Interactions with Materials and Atoms*, vol. 356-357, pp. 22–27, 2015.

[59] M. Toulemonde, A. Benyagoub, C. Trautmann, N. Khalfaoui, M. Boccanfuso, C. Dufour, F. Gourbilleau, J. J. Grob, J. P. Stoquert, J. M. Constantini, F. Haas, E. Jacquet, K.-O. Voss, and A. Meftah, "Dense and nanometric electronic excitations induced by swift heavy ions in an ionic caf2 crystal: Evidence for two thresholds of damage creation," *Phys. Rev. B*, vol. 852, no. 5-1, p. 054112, 2012.

[60] R. F. H. Jr., L. Yang, R. H. M. III, C. W. White, R. A. Zuhr, L. Yang, R. Dorsinville, and R. R. Alfano, "Nonlinear optical properties of metal-quantum-dot composites synthresized by ion implantation," *Nulc. Inst. and Meth. B*, vol. 91, pp. 493–504, 1994.

[61] G. D. Marchi, G. Mattei, P. Mazzoldi, C. Sada, and A. Miotello, "Two stages in the kinetics of gold cluster growth in ion-implanted silica during isothermal annealing in oxidizing atmosphere," *J. Appl. Phys.*, vol. 92, p. 4249, 2002.

[62] G. Rizza, Y. Ramjauny, T. Gacoin, L. Vieille, and S. Henry, "Chemically synthesized gold nanoparticles embedded in a sio2 matrix: a model to give insights into nucleation and growth under irradiation," *Phys. Rev. B*, vol. 76, p. 245414, 2007.

[63] S. Mirzaei, F. Kremer, R. Feng, C. J. Glover, and D. J. Sprouster, "Evidence for the formation of sige nanoparticles in ge-implanted si3n4," *J. Appl. Phys.*, vol. 121, p. 105702, 2017.

[64] S. Mirabella, S. Cosentino, A. Gentile, G. Nicotra, N. Piluso, L. V. Mercaldo, F. Simone, C. Spinella, and A. Terrasi, "Matrix role in ge nanoclusters embedded

in si3n4 or sio2," *Appl. Phys. Lett.*, vol. 101, p. 011911, 2012.

[65] M. Bayle, C. Bonafos, P. Benzo, G. Benassayag, B. Pecassou, L. Khomenkova, F. Gourbilleau, and R. Carles, "Ag doped silicon nitride nanocomposites for embedded plasmonics," *Appl. Phys. Lett.*, vol. 107, no. 10, p. 101907, 2015.

[66] A. Oliver, J. A. Reyes-Esqueda, J. C. Cheang-Wong, C. E. Román-Velázquez, A. Crespo-Sosa, L. Rodríguez-Fernández, J. A. Seman, and C. Noguez, "Controlled anisotropic deformation of ag nanoparticles by si ion irradiation," *Physical Review B*, vol. 74, no. 24, p. 245425, 2006.

[67] S. Klaumunzer, "Modification of nanostructures by high-energetic ion beams," *Nuclear Instruments and Methods in Physics Research, Section B: Beam Interactions with Materials and Atoms*, vol. 244, no. 1, pp. 1–7, 2006.

[68] E. A. Dawi, G. Rizza, M. P. Mink, A. M. Vredenberg, and F. P. Habraken, "Ion beam shaping of au nanoparticles in silica: Particle size and concentration dependence," *Journal of Applied Physics*, vol. 105, no. 7, 2009.

[69] H. Goldstein, *Classical Mechanics.* Addison-Wesley, 1980.

[70] J. F. Ziegler, J. P. Biersack, and U. L. Littmark, *The stopping and range of ions in solids.* New York: Pergamon Press, 1985.

[71] J. Lindhard, "Influence of crystal lattice on motion of energetic charged particles," *Mat. Fys. Medd. Dan. Vid. Selsk.*, vol. 34, pp. 1–64, 1965.

[72] W. H. Barkas, *Nuclear Research Emulsions-I. Techniques and Theory.* New York, Academic Press, 1963.

[73] O. B. Firsov, "A qualitative interpretation of the mean electron excitation energy in atomic collisions," *Sov. Phys. JETP*, vol. 36, p. 1076, 1959.

[74] J. Lindhard and M. Scharff, "Energy dissipation by ions in the kev region," *Phys. Rev.*, vol. 124, no. 1, pp. 128–130, 1961.

[75] J. F. Ziegler, "Stopping of energetic light ions in elemental matter," *J. Appl. Phys.*, vol. 85, no. 3, p. 1249, 1999.

[76] H. A. Bethe, "Zur theorie des durchgangs schneller korpuskularstrahlen durch materie," *Ann. Phys.*, vol. 397, no. 3, pp. 325–400, 1930.

[77] H. A. Bethe, "Braking formula for electrons of relativistic speed," *Z. Phys.*, vol. 76, p. 293, 1932.

[78] F. Bloch, "Zur bremsung rasch bewegter teilchen beim durchgang durch materie," *Ann. Phys.*, vol. 408, no. 3, pp. 285–320, 1933.

[79] F. Bloch, "Bremsvermogen von atomen mit mehreren elektronen," *Z. Phys.*, vol. 81, no. 5-6, pp. 363–376, 1933.

[80] W. H. Bragg and R. Kleeman, "On the alpha particles of radium, and their loss of range in passing through various atoms and molecules," *Phil. Mag.*, vol. 10, no. 57, pp. 318–340, 1905.

[81] G. H. Kinchin and R. S. Pease, "The displacement of atoms in solids by radiation," *Rept. Prog. Phys.*, vol. 18, p. 1, 1955.

[82] Z. Stachurski, "A theoretical model of an ideal amorphous solid," *Phys. Proc.*, vol. 48, pp. 55–58, 2013.

[83] E. Wendler, A. Heft, and W. Wesch, "Ion-beam induced damage and annealing behaviour in sic," *Nucl. Inst. and Meth. B*, vol. 141, no. 1-4, pp. 105–117, 1998.

[84] M. R. Pascucci, J. L. Hutchison, and L. W. Hobbs, "The metamict transformation in alpha-quartz," *Rad. Eff.*, vol. 74, no. 1-4, pp. 219–226, 2006.

[85] K. Nordlund, M. Ghaly, and R. S. Averback, "Mechanism of ion beam mixing in metals and semiconductors," *J. Appl. Phys.*, vol. 83, no. 3, pp. 1238–1246, 1998.

[86] M. C. Busch, A. Slaoui, P. Siffert, M. Dooryhee, and M. Toulemonde, "Structural and electrical damage induced by high-energy heavy ions in sio2/si structures," *J. Appl. Phys.*, vol. 71, no. 6, p. 2596, 1992.

[87] E. Zarkadoula, M. Toulemonde, and W. J. Webber, "Additive effects of electronic and nuclear energy losses in irradiation-induced amorphization of zircon," *Appl. Phys. Lett.*, vol. 107, p. 261902, 2015.

[88] T. Som, O. P. Spinha, J. Ghatank, B. Satpati, and D. Kanjilal, "Mev heavy ion induced recrustallization of buried silicon nitride layer: role of energy loss processes," *J. Appl. Phys.*, vol. 101, p. 034912, 2007.

[89] M. Toulemonde, W. J. Webber, G. Li, V. Shutthanandan, P. Kluth, T. Yang, Y. Wang, and Y. Zhang, "Synergy of nuclear and electronic energy losses in ion-irradiation processes: the case of vitreous silicon dioxide," *Phys. Rev. B*, vol. 83, p. 054106, 2011.

[90] M. Sall, I. Monnet, C. Grygiel, B. B. D'Etat, H. Lebius, S. Leclerc, and E. Balanzat, "Synergy between electronic and nuclear energy losses for color center creation in aln," *EPL*, vol. 102, p. 26002, 2013.

[91] W. J. Webber, E. Zarkadoula, O. H. Pakarinen, R. Sachan, M. F. Chisholm, P. Liu, H. Xue, K. Jin, and Y. Zhang, "Synergy of elastic and inelastic energy loss on ion track formation in srtio3," *Sci. Rep.*, vol. 5, p. 07726, 2015.

[92] J. F. Ziegler, M. D. Ziegler, and J. P. Biersack, "Srim-the stopping and range of ions in matter (2010)," *Nucl. Inst. and Meth. B*, vol. 268, no. 11-12, pp. 1818–1823, 2010.

[93] J. P. Biersack and L. Haggmark, "A monte carlo computer program for the transport of energetic ions in amorphous targets," *Nucl. Inst. and Meth.*, vol. 174, pp. 257–269, 1980.

[94] J. P. Biersack, "New projected range algorithm as derived from transport equations," *Z. Phys. A*, vol. 305, pp. 95–101, 1982.

[95] P. Mota-Santiago, H. Vazquez, T. Bierschenk, F. Kremer, A. Nadzri, D. Schauries, F. Djurabekova, K. Nordlund, C. Trautmann, S. Mudie, M. C. Ridgway, and P. Kluth, "Nanoscale density variations induced by high energy heavy ions in amorphous silicon nitride and silicon dioxide," *Nanotechnology*, vol. 29, no. 14, p. 144004, 2018.

[96] T. Bierschenk, R. Giulian, B. Afra, M. D. Rodriguez, D. Schauries, S. Mudie, O. H. Pakarinen, F. Djurabekova, K. Nordlund, O. Osmani, N. Medvedev,

B. Rethfeld, M. C. Ridgway, and P. Kluth, "Latent ion tracks in amorphous silicon," *Phys. Rev. B*, vol. 88, no. 17, p. 174111, 2013.

[97] J. Jensen, A. Razpet, M. Skupinski, and G. Possnert, "Ion tracks in amorphous sio2 irradiated with low and high energy heavy ions," *Nucl. Inst. and Meth. B*, vol. 245, no. 1, pp. 269–273, 2006.

[98] J. Jensen, A. Razpet, M. Skupinski, and G. Possnert, "Ion track formation below 1 mev/u in thin films of amorphous sio2," *Nucl. Instr. and Meth. B*, vol. 243, no. 1, pp. 119–126, 2006.

[99] A. Meftah, F. Brisard, J. M. Constantini, M. Hage-Ali, J. P. Stowuert, F. Studer, and M. Toulemonde, "Swift heavy ions in magnetic insulators: A damage-cross-section velocity effect," *Phys. Rev. B*, vol. 48, no. 2, pp. 920–925, 1993.

[100] H. Amekura, P. Kluth, P. Mota-Santiago, I. Sahlberg, V. Jantunen, A. A. Leino, H. Vazquez, K. Nordlund, F. Djurabekova, N. Okubo, and N. Ishikawa, "Vapor-like phase of amorphous sio2 is not a prerequisite for the core/shell ion tracks or ion shaping," *Phys. Rev. Mat.*, vol. 2, no. 9, p. 096001, 2018.

[101] F. F. Komarov, "Defect and track formation in solids irradiated by superhigh-energy ions," *Physics-Uspekhi*, vol. 46, no. 12, pp. 1253–1282, 2003.

[102] N. Itoh, D. M. Duffy, S. Khakshouri, and A. M. Stoneham, "Making tracks: electronic excitation roles in forming swift heavy ion tracks," *J. Phys.: Condens. Matter*, vol. 21, p. 474205, 2009.

[103] M. R. Waligorski, R. N. Hamm, and R. Katz, "The radial distribution of dose around the path of a heavy ion in liquid water," *Nuclear Tracks and Radiation Measurement*, vol. 11, no. 6, pp. 309–319, 1986.

[104] O. H. Pakarinen, F. Djurabekova, and K. Nordlund, "Density evolution in formation of swift heavy ion tracks in insulators," *Nucl. Instr. Meth. Phys. Res. B*, vol. 268, pp. 3163–3166, 2010.

[105] R. L. Fleischer, P. B. Price, and R. M. Walker, "Ion explosion spike mechanism for formation of charged-particle tracks in solids," *J. Appl. Phys.*, vol. 36, no. 11, p. 3645, 2004.

[106] G. Schiwietz, K. Czerski, M. Roth, F. Staufenbiel, and P. L. Grande, "Femtosecond dynamics-snapshots of the early ion-track evolution," *Nucl. Inst. and Meth. B*, vol. 225, no. 4, pp. 4–26, 2004.

[107] M. Toulemonde, W. Assmann, C. Dufour, A. Meftah, and C. Trautmann, "Nanometric transformation of the matter by short and intense electronic excitation: Experimental data versus inelastic thermal spike model," *Nucl. Inst. and Meth. B*, vol. 277, pp. 28–39, 2012.

[108] Z. G. Wang, C. Dufour, E. Paumier, and M. Toulemonde, "The se sensitivity of metals under swift-heavy-ion irradiation: a transient thermal process," *J. Phys. D*, vol. 6, pp. 6733–6750, 1994.

[109] M. Toulemonde, J. M. Constantini, C. Dufour, A. Meftah, E. Paumier, and F. Studer, "Track creation in sio2 and bafe12o19 by swift heavy ions: a thermal spike description," *Nuclear Instruments and Methods in Physics Research Section B: Beam Interactions with Materials and Atoms*, vol. 116, no. 1-4, pp. 37–42, 1996.

[110] J. Zhang, M. Lang, R. C. Ewing, R. Devanathan, W. J. Weber, and M. Toulemonde, "Nanoscale phase transitions under extreme conditions within an ion track," *J. Mater. Res.*, vol. 25, no. 7, pp. 1344–1351, 2010.

[111] K. Awazu, S. Roorda, J. L. Brebner, S. Ishii, and K. Shima, "Structure of latent tracks created by swift heavy ions in amorphous sio2 and zinc phosphate glass," *Jpn. J. Appl. Phys.*, vol. 42, no. 6, pp. 3950–3957, 2003.

[112] G. S. Martin, O. A. Bernaola, and G. G. Bermudez, "Comparative study of in track profiles in amorphous sio2 by tem and afm observations," *Nucl. Inst. and Meth. B*, vol. 245, no. 1, pp. 247–276, 2006.

[113] G. Szenes, "General features of latent track formation in magnetic insulators irradiated with swift heavy ions," *Phys. Rev. B*, vol. 51, no. 13, p. 8026, 1995.

[114] I. M. Lifshitz and V. V. Slyozov, "The kinetics of precipitation from supersaturated solid solutions," *J. Phys. Chem. Solids*, vol. 19, no. 1-2, pp. 35–50, 1961.

[115] M. I. Kaganov, I. M. Lifshitz, and L. V. Tanatarov, "Relaxation between electrons and the crystalline lattice," *J. Exptl. Theoret. Phys.*, vol. 4, no. 2, pp. 232–237, 1956.

[116] S. L. Daraszewicz and D. M. Duffy, "Extendind the inelastic thermal spike model for semiconductors and insulators," *Nucl. Inst. and Meth. B*, vol. 269, pp. 1646–1649, 2011.

[117] K. Awazu, X. Wang, M. Fujimaki, J. Tominaga, H. Aiba, Y. Ohki, and T. Komatsubara, "Elongation of gold nanoparticles in silica glass by irradiation with swift heavy ions," *Physical Review B*, vol. 78, no. 5, p. 054102, 2008.

[118] G. Szenes, "Comparison of two thermal spike models for ion-solid interaction," *Nucl. Inst. and Meth. B*, vol. 269, pp. 174–179, 2011.

[119] H. Trinkaus and A. I. Ryazanov, "Viscoelastic model for the plastic flow of amorphous solids under energetic ion bombardment," *Phys. Rev. Lett.*, vol. 74, no. 25, pp. 5072–5075, 1995.

[120] A. I. Ryazanov, A. E. Volkov, and S. Klaumünzer, "Model of track formation," *Phys. Rev. B*, vol. 51, no. 18, pp. 12107–12115, 1995.

[121] W. F. Ames, *Numerical Methods por Partial Differential Equations.* Boston: Academic Press, Inc, 1992.

[122] K. W. Morton and D. F. Mayers, *Numerical Solutions of Partial Differential Equations: An Introduction.* Cambridge: Cambridge University Press, 1994.

[123] G. Rizza, P. E. Coulon, V. Khomenkov, C. Dufour, I. Monnet, M. Toulemonde, S. Perruchas, T. Gacoin, D. Mailly, X. Lafosse, C. Ulysse, and E. A. Dawi,

"Rational description of the ion-beam shaping mechanism," *Phys. Rev. B*, vol. 86, no. 3, p. 035450, 2012.

[124] B. J. Alder and T. E. Wainwright, "Phase transition for a hard sphere system," *J. Chem. Phys.*, vol. 27, p. 1208, 1957.

[125] B. J. Alder and T. E. Wainwrigth, "Studies in molecular dynamics. i. general method," *J. Chem. Phys.*, vol. 31, no. 2, p. 459, 1959.

[126] K. Nordlund, "Molecular dynamics simulation of ion ranges in the 1-100 kev energy range," *Comp. Mater. Sci.*, vol. 3, no. 4, pp. 448–456, 1995.

[127] K. Albe, K. Nordlund, and R. S. Averback, "Modeling the metal-semiconductor interaction: analytical bond-order potential for platinum-carbon," *Phys. Rev. B*, vol. 65, no. 19, p. 195124, 2002.

[128] A. A. Leino, S. L. Daraszewicz, O. H. Pakarinen, K. Nordlund, and F. Djurabekova, "Atomistic two-tempreature modelling of ion track formation in silicon dioxide," *EPL*, vol. 110, no. 1, p. 16004, 2015.

[129] X. Zhang and C. P. Grigoropoulos, "Thermal conductivity and diffusivity of free-standing silicon nitride thin films," *Rev. Sci. Instrum.*, vol. 66, no. 2, p. 1115, 1995.

[130] M. Bogner, A. Hofer, G. Benstetter, H. Gruber, and R. Fu, "Differential 3w method for measuring thermal conductivity of aln and si3n4 thin films," *Thin Solid Films*, vol. 597, pp. 267–270, 2015.

[131] A. J. G. Jr. and F. R. Brotzen, "The effective transverse thermal conductivity of amorphous si3n4 thin films," *J. Appl. Phys.*, vol. 76, no. 7, p. 4007, 1994.

[132] Y. Ben-Hai and C. Dong, "Predictions of pressure-induced structural transition, mechanical and thermodynamic properties of alpha- and beta-si3n4 ceramics: ab initio and quasi-harmonic debye modeling," *Chinese Physics B*, vol. 21, no. 6, p. 060508, 2012.

[133] F. de Brito Mota, J. F. Justo, and A. Fazzio, "Structural properties of amorphous silicon nitride," *Phys. Rev. B*, vol. 58, no. 13, pp. 8323–8328, 1998.

[134] T. Watanabe, D. Yamasaki, K. Tatsumara, and I. Ohdomari, "Improved interatomic potential for stressed si, o mixed systems," *Appl. Surf. Sci.*, vol. 234, no. 1-4, pp. 207–213, 2004.

[135] J. Samela, K. Nordlund, V. N. Popok, and E. E. Campbell, "Origin of complex impact craters on native oxide coated silicon surfaces," *Phys. Rev. B*, vol. 77, no. 7, p. 075309, 2008.

[136] S. Munetoh, T. Motooka, K. Moriguchi, and A. Shintani, "Interatomic potential for si-o systems using tersoff parameterization," *Comput. Mater. Sci.*, vol. 39, no. 2, pp. 334–339, 2007.

[137] K. Nordlund, M. Ghaly, R. S. Averback, M. Caturla, T. D. de la Rubia, and J. Tarus, "Defect production in collision cascades in elemental semiconductors and fcc metals," *Phys. Rev. B*, vol. 57, no. 13, pp. 7556–7570, 1998.

[138] H. J. C. Berendsen, J. P. M. Postma, W. F. van Gunsteren, A. DiNola, and J. R. Haak, "Molecular dynamics with coupling to an external bath," *J. Chem. Phys.*, vol. 81, no. 8, p. 3684, 1984.

[139] D. A. Porter, *Phase Transformations in Metals and Alloys.* New York: CRC Press, 2009.

[140] L. Ratke and P. W. Voorhees, *Growth and Coarsening.* New York: Springer, 2002.

[141] M. Strobel, S. Reiss, and K. H. Heining, "Evolution of nanocluster ensembles: Computer simulation of diffusion and reaction controlled ostwald ripening," *Nucl. Inst. and Meth. B*, vol. 120, no. 1-4, pp. 216–220, 1996.

[142] C. Wagner, "Theory of precipitate change by redissolution," *Z. Electrochem.*, vol. 65, pp. 581–591, 1961.

[143] F. Ruffino, M. G. Grimaldi, F. Giannazzo, F. Roccaforte, V. Raineri, C. Bongiorno, and C. Spinella, "Kinetic mechanisms of the in situ electron beam-induced self-organization of gold nanoclusters in sio2," *J. Phys. D: Appl. Phys.*, vol. 42, p. 075304, 2009.

[144] A. Miotello, G. D. Marchi, G. Mattei, P. Mazzoldi, and C. Sada, "Clustering of gold atoms in ion-implanted silica after thermal annealing in different atmospheres," *Phys. Rev. B*, vol. 63, no. 7, p. 075409, 2001.

[145] M. M. Timm, Z. E. Fabrim, C. Marin, D. L. Baptista, and P. F. Fichtner, "Electron irradiation effects on the nucleation and growth of au nanoparticles in silicon nitride membranes," *J. Appl. Phys.*, vol. 122, p. 165301, 2017.

[146] S. Roorda, T. van Dillen, A. Polman, C. Graf, A. van Blaaderen, and B. J. Kooi, "Aligned gold nanorods in silica made by ion irradiation of core-shell colloidal particles," *Adv. Mater.*, vol. 16, p. 235, 2004.

[147] J. J. Penninkhof, T. van Dillen, S. Roorda, C. Graf, A. van Blaaderen, A. M. Vredenber, and A. Polman, "Anisotropic deformation of metallo-dielectric core-shell colloids under mev ion irradiation," *Nucl. Inst. and Meth. B*, vol. 242, no. 1-2, pp. 523–529, 2006.

[148] T. van Dillen and A. Polman, "Ion beam-induced anisotropic plastic deformation at 300 kev," *Appl. Phys. Lett.*, vol. 83, no. 21, p. 4315, 2003.

[149] G. Rizza, E. A. Dawi, A. M. Vredenberg, and I. Monnet, "Ion engineering of embedded nanostructures: from spherical to facetted nanoparticles," *Appl. Phys. Lett.*, vol. 95, p. 043105, 2009.

[150] E. A. Dawi, A. M. Vredenberg, G. Rizza, and M. Toulemonde, "Ion-induced elongation of gold nanoparticles in silica by irradiation with ag and cu swift heavy ions: track radius and energy loss threshold," *Nanotechnology*, vol. 22, no. 21, p. 215607, 2011.

[151] Y. K. Mishra, F. Singh, and D. K. Avasthi, "Synthesis of elongated au nanoparticles in silica matrix by ion irradiation," *Appl. Phys. Lett.*, vol. 91, no. 6, p. 063103,

2007.

[152] P. Kluth, R. Giulian, D. J. Sprouster, C. S. Schnor, A. P. Byrne, D. J. Cookson, and M. C. Ridgway, "Energy dependent saturation width of swift heavy ion shaped embedded au nanoparticles," *Appl. Phys. Lett.*, vol. 94, no. 11, p. 113107, 2009.

[153] O. Peña-Rodriguez, J. Olivares, M. Carrascosa, A. Garcia-Cabañes, A. Rivera, and F. Agullo-Lopez, *Optical Waveguides Fabricated by Ion Implantatio/Irradiation: A review*, pp. 267–314. InTech, 2012.

[154] H. Kumar, S. Ghosh, D. Avasthi, D. Kabiraj, A. Mucklich, S. Zhou, H. Schmidt, and J. P. Stoquert, "Ion beam-induced shaping of ni nanoparticles embedded in a silica matrix: from spherical to prolate shpae," *Nanoscale Res. Lett.*, vol. 6, p. 155, 2011.

[155] M. C. Ridgway, R. Giulian, R. Sprouster, P. Kluth, L. L. Araujo, D. J. Llewellyn, A. P. Byrne, F. Kremer, P. Fichtner, G. Rizza, H. Amekura, and M. Toulemonde, "Role of thermodynamics in the shape transformation of embedded metal nanoparticles induced by swift heavy-ion irradiation," *Physical Review Letters*, vol. 106, no. 9, p. 095505, 2011.

[156] H. Amekura, N. Ishikawa, N. Okubo, M. C. Ridgway, R. Giulian, K. Mitsuishi, Y. Nakayama, C. Buchal, S. Mantl, and N. Kishimoto, "Zn nanoparticles irradiated with swift heavy ions at low fluences: Optically-detected shape elongation induced by nonoverlapping ion tracks," *Physical Review B*, vol. 83, no. 20, 2011.

[157] H. Amekura, N. Ishikawa, N. Okubo, Y. Nakayama, and K. Mitsuishi, "Asynchronous melting of embedded metal nanoparticles and silica matrix for shape elongation induced by swift heavy ion irradiation," *Nucl. Inst. and Meth. B*, vol. 269, p. 2730, 2011.

[158] H. Amekura, N. Okubo, and N. Ishikawa, "Optical birefringence of zn nanoparticles embedded in silica induced by swift heavy-ion irradiation," *Opt. Express*, vol. 22, p. 29888, 2014.

[159] H. Amekura, M. L. Sele, N. Ishikawa, and N. Okubo, "Thermal stability of embedded metal nanoparticles elongated by swift heavy ion irradiation: Zn nanoparticles in a molten state but preserving elongated shapes," *Nanotechnology*, vol. 23, no. 9, p. 095704, 2012.

[160] G. Rizza, F. Attouchi, P. E. Coulong, S. Perruchas, T. Gacoin, I. Monnet, and L. Largeau, "Rayleigh-like instability in the ion-shaping of au-ag allow nanoparticles embedded within a silica matrix," *Nanotechnology*, vol. 22, p. 175305, 2011.

[161] M. Shirai, K. Tsumori, M. Kutsuwada, K. Yasuda, and S. Matsumara, "Morphological change in fept nanogranular thin films induced by swift heavy ion irradiation," *Nucl. Inst. and Meth. B*, vol. 267, no. 10, p. 1787, 2009.

[162] B. Schimdt, K. H. Heining, A. Mucklich, and C. Akhmadaliev, "Swift-heavy-ion-induced shaping of spherical ge nanoparticles into disks and rods," *Nucl. Inst. and Meth. B*, vol. 267, pp. 1345–1348, 2009.

[163] "Plasmatherm."

[164] "Oxford instruments," 2003.

[165] N. Jehanathan, M. Saunders, Y. Liu, and J. Dell, "Crystallization of silicon nitride thin films synthesized by plasma-enhanced chemical vapour depostion," *Scr. Mater.*, vol. 57, pp. 739–742, 2007.

[166] R. M. A. Azam and N. M. Bashara, *Ellipsometry and polarized light.* Amsterdam, North Holland Publishing Co., 1987.

[167] G. E. J. Jr., *Ellipsometry*, pp. 402–411. London: Academic Press, 1999.

[168] V. M. Airaksinen, *Silicon Wafer and Thin Film Measurements*, pp. 289–298. Elsevier, 2010.

[169] T. E. Jenkins, "Multiple-angle-of-incidence ellipsometry," *J. Phys. D: Appl. Phys.*, vol. 32, pp. R45–R56, 1999.

[170] R. M. A. Azzam and N. M. Bashara, *Ellipsometry and Polarised Light.* Amsterdam, North-Holland, 1986.

[171] G. E. J. Jr. and F. A. Modine, "Parametrization of the optical functions of amorphous materials in the interband region," *Appl. Phys. Lett.*, vol. 69, p. 371, 1996.

[172] "Erratum," *Appl. Phys. Lett.*, vol. 69, p. 2137, 1996.

[173] M. Conte and W. W. Mackay, *An introduction to the physics of particle accelerators*. World Scientific, 2008.

[174] J. H. Billen, "A radio frequency he- source and a source of negative ions by cesium sputtering," *IEEE Trans. Nucl. Sci.*, vol. 28, no. 2, pp. 1535–1539, 1981.

[175] M. Conway, "Ibmam."

[176] "Pelletron charging system."

[177] D. C. Weisser, "Resistor assemblies, their development and performance," *Nucl. Inst. and Meth. A*, vol. 328, no. 1-2, pp. 138–145, 1993.

[178] M. Sarkar, N. Shukla, N. Banerji, and Y. N. Mohapatra, "Transmission and charge state distribution of carbon ions emerging from nitrogen gas target in a tandem accelerator: Impact of stripper gas pressure," *Phys. Rev.*, vol. 15, p. 100101, 2012.

[179] T. R. Ophel, J. S. Harrison, J. O. Newton, R. H. Spear, E. W. Titterton, and D. C. Weisser, "The 14 ud pelletron accelerator at the australian national university," *Nucl. Inst. and Meth.*, vol. 122, pp. 227–234, 1974.

[180] T. R. Ophel, "A history of accelerators in australia," *Nucl. Inst. and Meth. A*, vol. 382, no. 1-2, pp. 20–31, 1996.

[181] D. C. Weisser and M. D. Malev, "Nec accelerator tube upgrade: 16.7 mv in a 14 ud," *Nucl. Inst. and Meth. B*, vol. 287, no. 1-2, pp. 64–67, 1990.

[182] "Source of negative ions by cesium sputtering-snics ii."

[183] "Multi-cathode source of negative ions by cesium sputtering (mc-snics)."

[184] D. C. Weisser and M. D. Malev, "Gridded buncher-far field extension using carbon coated teflon sleeves," *Nucl. Inst. and Meth. A*, vol. 268, no. 2-3, pp. 488–489, 1988.

[185] "Accelerator operations."

[186] J. L. Duff, "Dynamics and acceleration in linear structures," (Loutraki, Greece), CERN Accelerator School: Introduction to Accelerator Physics, 2000.

[187] B. Santiago, *A Practical Introduction to Beam Physics and Particle Accelerators*. Bristol: IOP Publishing, 2016.

[188] I. Brown and J. Washburn, "The mevva ion source for high current metal ion implantation," *Nucl. Inst. and Meth. Phys. B*, vol. 21, no. 1-4, pp. 201–204, 1987.

[189] C. Xiao, L. Groening, and O. K. Kester, "Collimation and decoupling of ecr source beams for brilliance optimization," *Nucl. Inst. and Meth. Phys. A*, vol. 738, pp. 167–176, 2014.

[190] C. Xiao, L. Groening, H. Vormann, S. Mickat, R. Hollinger, A. Adonin, A. Orzhekhovskaya, M. Maier, H. Al-Omari, W. Barth, O. K. Kester, and S. Yaramyshev, "Straight low energy beam transport for intense uranium beams," *Nucl. Inst. and Meth. A*, vol. 788, pp. 173–181, 2015.

[191] W. Barth, W. Bayer, L. Dahl, L. Groening, S. Richter, and S. Yaramyshev, "Upgrade program of the high current heavy ion unilac as an injector for fair," *Nucl. Inst. and Meth. Phys. A*, vol. 577, no. 1-2, pp. 211–214, 2007.

[192] I. M. Kapchinskii and V. A. Teplvakov *Prib. Teckh. Eksp.*, vol. 19, no. 2, 1970.

[193] U. Ratzinger and R. Tiede, "Status of the hiif rf linac study based on h-mode cavities," *Nucl. Inst. and Meth. A*, vol. 415, pp. 229–235, 1998.

[194] M. Mayer, "Simnra, a simulation program for the analysis of nra, rbs and erda," *AIP Conf. Proceedings*, vol. 475, no. 1, p. 541, 1999.

[195] L. R. Doolittle, "Algorithms for the rapid simulation of rutherford backscattering spectra," *Nucl. Inst. and Meth. B*, vol. 9, no. 3, pp. 344–351, 1985.

[196] L. R. Doolittle, "A semiatuomatic algorth for rutherford backscattering analysis," *Nucl. Inst. and Meth. B*, vol. 15, no. 1-6, pp. 227–231, 1986.

[197] J. F. Ziegler, *Helium Stopping Powers and Ranges in All Elements.* New York: Pergamon, 1977.

[198] J. R. Tesmer and M. Nastasi, *Handbok of Modern ion Beam Materials Analysis.* Michigan: Materials Research Society, 1995.

[199] W. M. Arnold and F. H. P. M. Habraken, "Elastic recoil detection," *Rep. Prog. Phys.*, vol. 56, pp. 859–903, 1993.

[200] B. Stuart, *Infrared spectroscopy: fundamentals and applications.* Wiley, 2004.

[201] M. H. Brodsky, M. Cardona, and J. J. Cuomo, "Infrared and raman spectra of the silicon-hydrogen bonds in amorphous silicon prepared by glow discharge and sputtering," *Physical Review B*, vol. 16, no. 8, pp. 3556–3571, 1977.

[202] E. Bustarret, M. Bensouda, M. C. Habrard, and J. C. Bruyere, "Configurational statistics in a-sixnyhz alloys: a quantitative bonding analysis," *Phys. Rev. B*, vol. 38, no. 12, p. 8171, 1988.

[203] M. H. Drodsky, M. Cardona, and J. J. Cuomo, "Infrared and raman spectra of the silicon-hydrogen bonds in amorphous silicon prepared by glow discharge and sputtering," *Phys. Rev. B*, vol. 16, no. 8, p. 3556, 1977.

[204] B. J. G. de Aragao and Y. Messaddeq, "Peak separation by derivative spectroscopy applied to ftir analysis of hydrolized silica," *J. Braz. Che. Soc.*, vol. 19, no. 8, pp. 1582–1594, 2008.

[205] J. Coates, *Interpretation of infrared spectra, a practical approach.* Chichester: John Wiley & Sons Ltd, 2000.

[206] "1500 c heavy duty tube furnace."

[207] "Aet thermal - rapid therxal processor rx."

[208] "Lesker nano 36 thermal evaporator standard operating procedure."

[209] "Beyond the diffraction limit," *Nature Photonics*, vol. 3, p. 361, 2009.

[210] C. Hetherington, "Aberration correction for tem," *Mater. Today*, vol. 7, no. 12, pp. 50–55, 2004.

[211] Y. Jiang, Z. Chen, Y. Han, P. Deb, H. Gao, S. Xie, P. Purohit, M. W. Tate, J. Park, S. M. Gruner, V. Elser, and D. A. Muller, "Electron ptychography of 2d materials to deep sub-angstrom resolution," *Nature*, vol. 559, pp. 343–349, 2018.

[212] H. Rose, "Aberration correction in electron microscopy," *Int. J. Mater. Res.*, vol. 97, no. 7, p. 885, 2006.

[213] D. B. Williams and C. B. Carter, *Transmission Electron Microscopy A Textbook for Materials Science*. New York: Springer, 2009.

[214] L. Reimer and H. Kohl, *Transmission Electron Microscopy Physics of Image Formation*. New York: Springer, 2008.

[215] W. C. Röntgen, "Ueber eine neue art von strahlen. vorläufige mitteilung," *Aus den Sitzungsberichten der Würzburger Physik.-medic. Gesellschaft Würzburg*, pp. 1–11, 1895.

[216] W. C. Röntgen, "On a new kind of rays," *Nature*, vol. 53, pp. 274–276, 1896.

[217] O. Glatter and O. Kratky, *Small angle X-ray scattering*. New York: Academic Press, 1982.

[218] W. H. Bragg and W. L. Bragg, "The reflection of x-rays by crystals," *The Royal Society*, vol. 88, no. 605, pp. 428–438, 1913.

[219] A. Guinier and G. Fournet, *Small-Angle Scattering of X-rays*. New York: John Wiley & Sons, 1955.

[220] P. Krishnamurti, "Studies in x-ray diffraction. part i: The structure of amorphous scattering. part ii: Colloidal solutions and liquid mixtures.," *Indian J. Phys.*, vol. 5, pp. 473–500, 1930.

[221] B. E. Warren, "X-ray diffraction study of carbon black," *J. Chem. Phys.*, vol. 2, pp. 551–555, 1934.

[222] H. Winick, G. Brown, K. Halbach, and J. Harris, "Wiggler and undulator magnets," *Physics Today*, vol. 34, no. 5, pp. 50–63, 1981.

[223] F. R. Elder, A. M. Gurewitsch, R. V. Langmuir, and H. C. Pollock, "Radiation from electrons in a synchrotron," *Phys. Rev.*, vol. 71, no. 11, pp. 829–830, 1947.

[224] F. R. Elder, A. M. Gurewitsch, R. V. Langmuir, and H. C. Pollock, "A 70-mev synchrotron," *J. Appl. Phys.*, vol. 18, no. 9, pp. 810–818, 1947.

[225] H. C. Pollock, "The discovery of synchrotron radiation," *Am. J. Phys.*, vol. 51, no. 3, p. 278, 1983.

[226] A. Lienard, "Champ electrique et magnetique produit par une charge concentree en un point et animee d'un mouvement quenconque," *L'Eclairage Electrique*, vol. 16, p. 5, 1898.

[227] G. A. Schiott *Ann. Phys.*, vol. 24, p. 635, 1907.

[228] J. Schwinger *Phys. Rev.*, vol. 70, p. 798, 1946.

[229] D. Ivanenko and A. A. Sokolov *Dokl. Akad. Nauk.*, vol. 59, p. 1551, 1948.

[230] J. Schwinger *Proc. Nat. Acad. Sci.*, vol. 40, p. 132, 1954.

[231] A. A. Sokolov, N. P. Klepikov, and I. M. Ternov *Dokl. Akad. Nauk.*, vol. 89, p. 665, 1953.

[232] K. R. Lea, "Highlights of synchrotron radiation," *Phys. Rep.*, vol. 43, no. 8, pp. 337–375, 1978.

[233] A. S. Schlachter, *Third-generation synchrotron light sources*, pp. 1–22. Dordrecht: Springer, 1994.

[234] M. Engel, B. Stühn, J. J. Schneider, T. Cornelius, and M. Naumann, "Small-angle x-ray scattering (saxs) off parallel, cylindrical, well-defined nanopores: from

random pore distribution to highly ordered samples," *Applied Physics A*, vol. 97, pp. 99–108, 2009.

[235] T. N. Blanton, C. L. Barnes, and M. Lelental, "Preparation of silver behenate coatings to provide low- to mid-angle diffraction calibration," *J. Appl. Cryst.*, vol. 33, pp. 172–173, 2000.

[236] F. Zhang, J. Ilavsky, G. G. Long, J. P. G. Quintana, A. J. Allen, and P. R. Jemian, "Glassy carbon as an absolute intensity calibration standad for small-angle scattering," *Metall. Mater. Trans.*, vol. 41, no. 5, pp. 1151–1158, 2009.

[237] B. Afra, K. Nordlund, M. D. Rodriguez, T. Bierschenk, C. Trautmann, S. Mudie, and P. Kluth, "Thermal response of nanoscale cylindrical inclusions of amorphous silica embedded in alpha-quartz," *Phys. Rev. B*, vol. 90, p. 224108, 2014.

[238] J. Ilavsky and P. R. Jemian, "Irena: tool suite for modeling and analysis of small-angle scattering," *J. Appl. Cryst.*, vol. 42, p. 349, 2009.

[239] P. J. W. Debye, "Zerstreuung von röntgenstrahlen," *Ann. Phys.*, vol. 351, no. 6, pp. 809–823, 1915.

[240] G. Arfken, *Mathematical Methods for Physicists.* Orlando: Academic Press, 1985.

[241] R. M. Aarts and A. J. Janssen, "Approximation of the struve function h1 occurring in impedance calculations," *J. Acoust. Soc. Am.*, vol. 113, no. 5, pp. 2635–2637, 2003.

[242] R. M. Aarts and A. J. Janssen, "Efficient approximation of the struve functions hn occurring in the calculation of sound radiation quantities," *J. Acoust. Soc. Am.*, vol. 140, no. 6, pp. 4154–4160, 2016.

[243] M. Abramowitz and I. Stegun, *Handbook of Mathematical Functions.* Nuew York: Dover, 1972.

[244] J. W. Pratt, "On interchanging limits and integrals," *Ann. Math. Stat.*, vol. 31, no. 1, pp. 74–77, 1960.

[245] V. A. Borodin, A. E. Volkov, and D. N. Korolev, "Viscous flow of amporphous metals in swift heavy ion tracks," *Nucl. Instr. Meth. Phys. Res. B*, vol. 209, pp. 122–130, 2003.

[246] A. A. Langford, M. L. Fleet, B. P. Nelson, W. A. Lanford, and N. Maley, "Infrared absorption strength and hydrogen content of hydrogenated amorphous silicon," *Phys. Rev. B*, vol. 45, no. 23, p. 13367, 1992.

[247] J. Dupuis, E. Fourmond, J. F. Lelievre, D. Ballutaud, and M. Lemiti, "Impact of pecvd sion stoichiometry and post-annealing on the silicon surface passivation," *Thin Solid Films*, vol. 516, pp. 6954–6958, 2008.

[248] J. Viard, E. Beche, D. Perarnau, R. Berjoan, and J. Durand, "Xps and ftir study of silicon oxynitride thin films," *J. Eur. Ceram. Soc.*, vol. 17, no. 15-16, pp. 2025–2028, 1997.

[249] M. I. Alayo, I. Pereyra, W. L. Scopel, and M. C. A. Fantini, "On the nitrogen and oxygen incorporation in plasma-enhanced chemical vapor deposition (pecvd) sioxny films," *Thin Solid Films*, vol. 402, pp. 154–161, 2002.

[250] D. L. Smith, A. S. Alimonda, C.-C. Chen, S. E. Ready, and B. Wacker, "Mechanism of sinxhy deposition from nh3-sih4 plasma," *J. Electrochem. Soc.*, vol. 2, no. 614-623, p. 137, 1990.

[251] K. C. Lin and S. C. Lee, "The structural and optical properties of a-sinx:h prepared by plasma-enhanced chemical-vapor deposition," *J. Appl. Phys.*, vol. 72, no. 11, pp. 5474–5482, 1992.

[252] F. Karouta, K. Vora, J. Tian, and C. Jagadish, "Structural, compositional and optical properties of pecvd silicon nitride layers," *Journal of Physics D: Applied Physics*, vol. 4, no. 445301, p. 10, 2012.

[253] S. Hasegawa, L. He, Y. Amano, and T. Inokuma, "Analysis of sih and sin vibrational absorption in amorphous sinx:h films in terms of a charge-transfer model," *Phys. Rev. B*, vol. 45, no. 8, p. 5315, 1993.

[254] L. He, T. Inokuma, Y. Kurata, and S. Hasegawa, "Vibrational properties of sio and sih in amorphous siox:h films (0¡x¡2.0) prepared by plasma-enhanced chemical vapor deposition," *J. Non-Cryst. Solids*, vol. 185, pp. 249–261, 1995.

[255] L.-N. He, D.-M. Wang, and S. Hasegawa, "A study of plasma-deposited amorphous siox:h (0¡x¡2) films using infrared spectroscopy," *J. Non-Cryst. Solids*, vol. 261, no. 1-3, pp. 67–71, 2000.

[256] M. C. Ridgway, T. Bierschenk, R. Giulian, B. Afra, M. D. Rodriguez, L. L. Araujo, A. P. Byrne, N. Kirby, O. H. Pakarinen, F. Djurabekova, K. Nordlund, M. Schleberger, O. Osmani, N. Medvedev, B. Rethfeld, and P. Kluth, "Tracks and voids in amorphous ge induced by swift heavy-ion irradiation," *Phys. Rev. Lett.*, vol. 110, no. 24, p. 245502, 2013.

[257] P. Kluth, O. H. Pakarinen, F. Djurabekova, R. Giulian, M. C. Ridgway, A. P. Byrne, and K. Nordlund, "Nanoscale density fluctuations in swift heavy ion irradiated amorphous sio2," *J. Appl. Phys.*, vol. 110, no. 12, p. 123520, 2011.

[258] N. Tomozeiu, *Silicon Ixide (SiOx, 0¡x¡2): a Challenging Material for Optoelectronics*, pp. 55–100. InTech, 2011.

[259] F. Djurabekova and K. Nordlund, "Atomistic simulation of the interface structure of si nanocrystals embedded in amorphous silica," *Phys. Rev. B*, vol. 77, no. 11, p. 115325, 2008.

[260] I. Mariella and S. Meloni, "Atomistic structure of amorphous silicon nitride from classical molecular dynamics simulations," *Phys. Rev. B*, vol. 83, no. 16, p. 165209, 2011.

[261] O. Debieu, R. P. Nalini, J. Cardin, X. Portier, J. Perrière, and F. Gourbilleau, "Structural and optical characterization of pure si-rich nitride thin films," *Nanoscale Res. Lett.*, vol. 8, no. 31, p. 13, 2013.

[262] G. Dupont, H. Caquineau, B. Despax, R. Berjoan, and A. Dollet, "Structural properties of n-rich a-si-n:h films with a low electron-trapping rate," *J. Phys. D*, vol. 30, pp. 1064–1076, 1997.

[263] G. Scardera, T. Puzzer, G. Conibeer, and M. A. Green, "Fourier transform infrared spectroscopy of annealed silicon-rich silicon nitride thin films," *J. Appl. Phys.*, vol. 104, no. 10, p. 104310, 2008.

[264] J. Fu, H. Shang, Z. Li, W. Wang, and D. Chen, "Thermal annealing effect of the stress stability in silicon dioxide films grown by plasma-enhanced chemical vapor deposition," *Microsys. Technol., In Press*, pp. 1–5, 2016.

[265] A. Kushima, X. Lin, J. Li, X. Qian, J. Eapen, J. Mauro, P. Diep, and S. Yip, "Computing the viscosity of supercooled liquids. ii. silica and strong-fragile crossover behaviour," *J. Chem. Phys.*, vol. 131, p. 164505, 2009.

[266] T. M. Haddad, *Advanced Multilayered and Fibre-Reinforced Composites*. Netherlands: Springer Netherlands, 2012.

[267] K. V. Loiko, I. V. Peidous, Y. Zu, and H. M. Ho, "Experimental study of si3n4 viscosity for calibration of stress-dependent models of silicon oxidation," *J. Electrochem. Soc.*, vol. 146, no. 11, pp. 4226–4229, 1999.

[268] P. G. Pai, S. S. Chao, Y. Takagi, and G. Lucovsky, "Infrared spectroscopic study of siox films produced by plasma enhanced chemical vapor deposition," *J. Vac. Sci. Technol. A*, vol. 4, no. 3, p. 689, 1986.

[269] D. V. Tsu, G. Lucovsky, and M. J. Mantini, "Local atomic structure in thin films of silicon nitride and silicon diimide produced by remote plasma-enhanced chemical-vapor deposition," *Physical Review B*, vol. 33, no. 10, pp. 7069–7076, 1986.

[270] H. R. Philipp, "Optical and bonding model for non-crystalline siox and sioxny materials," *J. Non-Cryst. Mat.*, vol. 8-10, pp. 627–632, 1972.

[271] U. Kreibig and M. Vollmer, *Optical properties of metal clusters*. Berlin: Springer, 1995.

[272] P. E. Mota-Santiago, A. Crespo-Sosa, J. L. Jiménez-Hernández, H. G. Silva-Pereyra, J. A. Reyes-Esqueda, and A. Oliver, "Size characterisation of noble-

metal nano-crystals formed in sapphire by ion irradition and subsequent thermal annealing," *Applied Surface Science*, vol. 259, no. 15, pp. 574–581, 2012.

[273] A. Benami, Y. E. Hassouani, A. Oliver, and A. Lopez-Suarez, "Effect of silver nanoparticles on the photoluminescence of silicon nanocrystals," *Spectrosc. Lett.*, vol. 47, pp. 411–414, 2014.

[274] D. J. Sprouster, R. Giulian, L. L. Araujo, P. Kluth, B. Johannessen, N. Kirby, and M. C. Ridgway, "Formation and structural characterization of ni nanoparticles embedded in sio2," *J. Appl. Phys.*, vol. 96, pp. 317–325, 2011.

[275] Y. Chen, "Nanofabrication by electron beam lithography and its applications: A review," *Microelectron. Eng.*, vol. 135, pp. 57–72, 2015.

[276] U. Burghaus, "Applications of electron beam lithography in surface science and catalysis-mode-nano-array catalysts," *Catal.*, vol. 25, pp. 141–171, 2013.

[277] A. Slablab, T. J. Isotalo, J. Makitalo, L. Turquet, P. E. Coulon, T. Niemi, C. Ulysse, M. Kociak, D. Mailly, G. Rizza, and M. Kauranen, "Fabrication of ion-shaped anisotropic nanoparticles and their orientational imaging by second-harmonic generation microscopy," *Sci. Rep.*, vol. 6, p. 37469, 2016.

[278] K. Matsuoka, H. Tahara, T. Akiyama, and S. Yamada, "Effects of capping layers on the photoelectrochemical property of silver nanoparticle-modified indium-tin-oxide electrode," *J. Photochem. Photobio. A*, vol. 221, no. 2–3, pp. 239–243, 2011.

[279] D. Lantiat, D. Babonneau, S. Camelio, F. Pailloux, and M. F. Denanot, "Evidence for cappin-layer effects on the morphology and plasmon excitation of ag nanoparticles," *J. Appl. Phys.*, vol. 102, p. 113518, 2007.

[280] S. B. Kalidindi, U. Sanyal, and B. R. Jagirdar, "Chemical synthesis of metal nanoparticles using amino-boranes," *Chem. Sus. Chem.*, vol. 4, no. 3, pp. 317–324, 2011.

[281] K. Awazu, X. Wang, M. Fujimaki, J. Tominaga, S. Fuji, H. Aiba, Y. Ohki, and T. Komatsubara, "Mechanism of elongaton of gold or silver nanoparticles in silica by irradiation with swift heavy-ions," *Nucl. Inst. and Meth. B*, vol. 267, pp. 941–943, 2009.

[282] P. E. Coulon, J. Amici, M. C. Clochard, V. Khomenkov, C. Dufour, I. Monet, C. Grygiel, S. Perruchas, C. Ulysse, L. Largeau, and G. Rizza, "Ion-shaping of embedded gold hollow nanoshells into vertical aligned prolate morphologies," *Sci. Rep.*, vol. 6, p. 21116, 2016.

[283] F. Feng, X. H. Xiao, G. X. Cai, J. B. Wang, and C. Z. Jiang, "Engineering embedded metal nanoparticles with ion beam technology," *Appl. Phys. A*, vol. 105, pp. 317–325, 2009.

[284] R. Giulian, L. L. Araujo, P. Kluth, D. J. Sprouster, C. S. Schnohr, B. Johannessen, G. J. Foran, and M. C. Ridgway, "The influence of annealing conditions on the growth and structure of embedded pt nanocrystals," *J. Appl. Phys*, vol. 105, p. 044303, 2009.

[285] P. Kluth, B. Johannessen, G. J. Foran, D. J. Cookson, S. M. Jluth, and M. C. Ridgway, "Disorder and cluster formation during ion irradiation of au nanoparticles in sio2," *Phys. Rev. B*, vol. 74, p. 014202, 2006.

[286] P. Mota-Santiago, F. Kremer, A. Nadzri, M. C. Ridgway, and P. Kluth, "Elongation of metallic nanoparticles at the interface of silicon dioxide and silicon nitride," *Nucl. Inst. and Meth. B*, vol. 409, pp. 328–332, 2017.

[287] R. Giulian, *Pt Nanocrystals Formed by Ion Implantation and Modified by Swift Heavy Ion Irradiation.* PhD Thesis: The Australian National University, 2009.

[288] P. R. Jemian, J. R. Weertman, G. G. Long, and R. D. Sparl, "Characterization of 9cr-movnb steel by anomalous small-angle x-ray scattering," *Acta Metall. Mater.*, vol. 39, pp. 2477–2487, 1991.

[289] D. J. Sprouster, R. Giulian, L. L. Araujo, P. Kluth, B. Johannessen, D. J. Cookson, and M. C. Ridgway, "Swift heavy-ion irradiation-induced shape and struc-

tural transformation in co nanoparticles," *J. Appl. Phys.*, vol. 109, p. 113504, 2011.

[290] D. S. Smith, A. Alzina, J. Bourret, B. Nait-Ali, F. Pennec, N. Tessier-Doyen, K. Otsu, H. Matsubara, P. Elser, and U. T. Gonzenbach, "Thermal conductivity of porous materials," *J. Mater. Res.*, vol. 28, no. 17, pp. 2260–2272, 2013.

[291] S. Mirzaei, *Study of the structural properties of Ge nanoparticles formed by ion implanttion and thermal annealing in nitride-base dielectric matrices.* PhD Thesis: The Australian National University, 2016.

[292] A. M. Mahamad and G. K. Mamidipudi, *Metal Induced Crystalization.* Crystallization Science and Technology, London: IntechOpen, 2012.

[293] B. Schimdt, A. Mucklich, L. Rontzsch, and K. H. Heining, "Ho do high energy heavy-ions shape ge nanoparticles embedded in sio2," *Nucl. Inst. and Meth. B*, vol. 257, pp. 30–32, 2007.

[294] "Surface plasmon resurrection," *Nat. Photonics*, vol. 6, p. 707, 2012.

[295] R. Zia, J. A. Schuller, A. Chandran, and M. L. Brongersma, "Plasmonics: the next chip-scale technology," *Mat. Today*, vol. 9, no. 7-8, pp. 20–27, 2006.

[296] V. M. Shalaev, W. Cai, U. K. Chettiar, H.-K. Yuan, A. K. Sarychev, V. P. Drachev, and A. V. Kildishev, "Negative index of refraction in optical metamaterials," *Opt. Lett.*, vol. 30, p. 3356, 2005.

[297] S. Zhang, W. Fan, N. C. Panoiu, K. J. Malloy, R. M. Osgood, and S. R. J. Brueck, "Experimental demonstration of near-infrared negative-index metamaterials," *Phys. Rev. Lett.*, vol. 95, p. 137404, 2005.

[298] F. J. Garcia-Vidal, L. Martin-Moreno, and J. B. Pendry, "Surfaces with holes in them: new plasmonic metamaterials," *J. Opt. A*, vol. 7, p. S97, 2005.

[299] R. Guo, M. Decker, F. Setzpfandt, X. Gai, D.-Y. Choi, R. Kiselev, A. Chipouline, I. Staude, T. Pertsch, D. N. Neshev, and Y. S. Kivshar, "High-bit rate ultra-

compact light routing with mode-selective on-chip nanoantennas," *Sci. Adv.*, vol. 3, p. 1700007, 2017.

[300] M. Jahn, S. Patze, I. J. Hidi, R. Knipper, A. J. Radu, A. Muhlig, S. Yuksel, V. Peksa, K. Weber, T. Mayerhofer, D. Cialla-May, and J. Popp, "Plasmonic nanostructures for surface enhanced spectroscopic methods," *Analyst*, vol. 141, p. 756, 2016.

[301] J. N. Anker, W. P. Hall, O. Lyandres, N. C. Shah, J. Zhao, and R. P. V. Duyne, "Biosensing with plasmonic nanosensors," *Nat. Mater.*, vol. 7, p. 442, 2008.

[302] A. G. Brolo, "Plasmonics for future biosensors," *Nat. Photonics*, vol. 6, no. 11, p. 709, 2012.

[303] N. Fang, H. Lee, C. Sun, and X. Zhang, "Sub-diffraction-limited optical imaging with a sulver super-lens," *Science*, vol. 308, p. 534, 2005.

[304] H. A. Atwater and A. Polman, "Plasmonics for improved photovoltaic devices," *Nat. Mater.*, vol. 9, p. 205, 2010.

[305] H. F. Lu, S. Mokkapati, L. Fu, G. Jolley, H. H. Tan, and C. Jagadish, "Plasmonic quantum dot solar cells for enhanced infrared response," *Appl. Phys. Lett.*, vol. 100, no. 10, p. 103505, 2012.

[306] T. Zhang, S. Callard, C. Jamois, C. Chevalier, D. Feng, and A. Belarouci, "Plasmonic-photonic crystal coupled nanolaser," *Nanotechnology*, vol. 25, p. 315201, 2014.

[307] D. Sarker, S. Bhattacharya, H. Kumar, P. Srivastava, and G. S, "Evidence of local structural influence on the shape driven magnetic anisotropy in electronically excited ni nanoparticles embedded in sio2 matrix," *Sci. Rep.*, vol. 8, p. 1040, 2018.

[308] J. C. Pivin, F. Singh, O. Angelov, and L. Vincent, "Perpendicular magnetization of fept particles in silica induced by swift heavy ion irradiation," *J. Phys. D: Appl. Phys.*, vol. 42, p. 025005, 2009.

[309] J. A. Reyes-Esqueda, C. Torres-Torres, J. C. Cheang-Wong, A. Crespo-Sosa, L. Rodriguez-Fernandez, C. Noguez, and A. Oliver, "Large optical birefringence by anisotropic silver nanocomposites," *Optics Express*, vol. 16, no. 2, pp. 710–717, 2008.

[310] A. A. Leino, O. H. Pakarinen, F. Djurabekova, and K. Nordlund, "A study on the elongation of embedded au nanoclusters in sio2 by swift heavy ion irradiation using md simulations," *Nucl. Inst. and Meth. B*, vol. 282, pp. 76–80, 2012.

[311] P. Mota-Santiago, T. Bierschenk, F. Kremer, A. Nadzri, H. Vazquez, F. Djurabekova, K. Nordlund, C. Trautmann, S. Mudie, M. C. Ridgway, and P. Kluth, "Nanoscale density fluctuations induced by energetic heavy ions in silicon nitride and silicon dioxide," In preparation.

[312] G. R, F. Kremer, L. L. Araujo, D. J. Sprouster, P. Kluth, P. F. P. Fichtner, A. P. Byrne, and M. Ridgway, "Shape transformation of sn nanocrystals induced by swift heavy-ion irradiation and the necessity of a molten ion track," *Phys. Rev. B*, vol. 82, no. 11, p. 113410, 2010.

[313] W. R. Tyson and W. A. Miller, "Surface free energies of solid metals: Estimation from liquid surface tension measurements," *Surf. Sci.*, vol. 62, no. 1, pp. 267–276, 1977.

[314] P. Kluth, B. Johannessen, V. Giraud, A. Cheung, C. J. Glover, G. d. M. Azevedo, G. J. Foran, and M. C. Ridgway, "Bond length contraction in au nanocrystals formed by ion implatnation into thin sio2," *Appl. Phys. Lett.*, vol. 85, no. 16, pp. 3561–3563, 2004.

[315] F. Singh, S. Mohapatra, J. P. Stoquert, D. K. Avasthi, and J. C. Pivin, "Shape deformation of embedded metal nanoparticles by swift heavy ion irradiation," *Nucl. Inst. and Meth. B*, vol. 267, pp. 936–940, 2009.